

# **Renewable Energy – Low Temperature Thermionic Emission from Modified Diamond Surfaces**

**Fabian Fogarty**

A dissertation submitted to the University of Bristol in accordance with the requirements for the award of the degree of Doctor of Philosophy in the Faculty of Science, School of Chemistry, February 2020.

Word count ~ 32k

exc. prelim pages, references,  
appendices, tables and figures

## Abstract

Thermionic energy conversion holds great promise for effective and clean energy production. Diamond has a unique set of properties that distinguish it as an excellent potential thermionic emitter, a crucial component of thermionic energy converters. In particular, the hydrogen-terminated diamond surface exhibits a negative electron affinity, which allows for efficient emission of electrons. The hydrogen termination is not stable at elevated temperatures, which necessitates investigating alternative candidates such as titanium. This work is primarily concerned with the investigation of the electronic properties and surface stability of titanium containing diamond surface terminations to assess their potential as a thermionic emitter.

*Ab initio* computational modelling of various titanium surface terminations showed that titanium nitride, titanium oxide, and titanium carbide all have the potential to exhibit negative electron affinities. The titanium nitride surface termination showed similar stability as the hydrogen termination, while the titanium oxide surfaces exhibited better stability. The titanium carbide terminations proved the most stable, with promising electronic properties.

Titanium-oxide- and titanium-nitride-terminated diamond surfaces were prepared using techniques such as acid and plasma treatment, chemical vapour deposition, and e-beam evaporation. The fabricated surfaces were annealed at temperatures of up to 1000 °C and analysed primarily using X-ray and ultraviolet photoelectron spectroscopy. For most of the titanium surfaces, the oxygen or nitrogen desorbed by 1000 °C while the titanium did not, resulting in titanium-carbide-terminated diamond. Though these titanium carbide surfaces typically exhibited moderately higher work functions than the equivalent titanium oxide or nitride terminations, they still exhibited negative electron affinities.

Therefore, titanium-carbide-terminated diamond surfaces were found to be stable at elevated temperatures while also exhibiting favourable electronic properties.

## **Acknowledgments**

Firstly, I would like to thank Professor Paul May and Dr Neil Fox for the opportunity and resources that enabled me to conduct this research in the first place, as well as their support and guidance throughout this endeavour. I particularly appreciate Dr Mattia Cattelan and Dr James Smith for their patience and invaluable guidance in the diamond lab and the NanoESCA lab. I would also like to thank the whole diamond research group for their companionship and insights over the last three years. Max and Gary deserve a special mention for their very useful discussions on the finer points of English grammar during the writing of this thesis. Lastly, and most importantly, I am most grateful for the unconditional love and support of my wife, Martine, without whom I would have surely been lost to insanity some time ago.

I declare that the work in this dissertation was carried out in accordance with the requirements of the University's *Regulations and Code of Practice for Research Degree Programmes* and that it has not been submitted for any other academic award. Except where indicated by specific reference in the text, the work is the candidate's own work. Work done in collaboration with, or with the assistance of, others, is indicated as such. Any views expressed in the dissertation are those of the author.

SIGNED: ..... DATE: .....

# Table of Contents

<b>Table of Contents .....</b>	<b>IV</b>
<b>List of Figures and Tables.....</b>	<b>IX</b>
<b>List of Abbreviations .....</b>	<b>XVIII</b>
<b>Outline .....</b>	<b>XIX</b>
<b>1 Introduction.....</b>	<b>1</b>
<b>1.1 Climate Change.....</b>	<b>2</b>
<b>1.2 Thermionic Energy Conversion .....</b>	<b>3</b>
1.2.1 History.....	4
1.2.2 Background .....	5
1.2.3 Challenges .....	6
<b>1.3 Diamond.....</b>	<b>8</b>
1.3.1 Why Diamond for TEC devices? .....	9
<b>1.4 Doping.....</b>	<b>11</b>
1.4.1 Common Dopants.....	11
1.4.2 Effect of Doping on Thermionic Emission .....	12
<b>1.5 Surface Terminations.....</b>	<b>15</b>
1.5.1 Hydrogen.....	15
1.5.2 Oxygen .....	16
1.5.3 Nitrogen .....	16
1.5.4 Other Single-Element Terminations .....	17
1.5.5 Group I and II Metal Oxide Terminations .....	18
1.5.6 Transition Metal Oxides.....	19
1.5.7 Termination Summary .....	19

<b>2</b>	<b>Computational Modelling</b> .....	<b>20</b>
<b>2.1</b>	<b>Theoretical Background</b> .....	<b>21</b>
2.1.1	Born-Oppenheimer Approximation .....	22
2.1.2	Hartree-Fock Approximation.....	22
2.1.3	Density Functional Theory (DFT).....	23
2.1.3.1	The Kohn-Sham Approach .....	24
2.1.3.2	Correlation Interaction .....	24
2.1.3.3	Exchange Interaction .....	24
2.1.4	Exchange-Correlation Energy (XC) Functionals .....	25
2.1.4.1	Local and Semi-local Approximations .....	25
2.1.4.2	Hybrid Functionals .....	26
2.1.5	Basis Sets .....	28
<b>2.2</b>	<b>Experimental Details</b> .....	<b>29</b>
2.2.1	Geometry Optimization .....	29
2.2.2	Adsorption Energy .....	30
2.2.3	Electron Affinity.....	31
<b>2.3</b>	<b>Results</b> .....	<b>33</b>
2.3.1	Titanium Carbide.....	34
2.3.2	Oxygen and TiO.....	39
2.3.3	Nitrogen and TiN.....	44
2.3.4	Summary .....	49
<b>3</b>	<b>Experimental Techniques</b> .....	<b>51</b>
<b>3.1</b>	<b>Photoemission Spectroscopies</b> .....	<b>52</b>
3.1.1	Surface Sensitivity.....	52
3.1.2	X-ray Photoelectron Spectroscopy .....	53
3.1.3	Ultraviolet Photoelectron spectroscopy .....	57
3.1.4	Analysis of XPS data .....	59
3.1.4.1	Background .....	59
3.1.4.2	Line Shapes.....	63
3.1.4.3	Parameter constraints.....	65

3.1.4.4	Binding Energies of Functional Groups .....	67
3.1.4.5	Limit of detection.....	69
3.1.4.6	Errors .....	70
3.1.4.7	Contamination .....	70
3.1.4.8	Summary.....	71
<b>3.2</b>	<b>Chemical Vapour Deposition .....</b>	<b>72</b>
<b>3.3</b>	<b>Raman Spectroscopy .....</b>	<b>74</b>
<b>3.4</b>	<b>Summary .....</b>	<b>74</b>
<b>4</b>	<b>Methodology and Instrumentation .....</b>	<b>76</b>
<b>4.1</b>	<b>Introduction.....</b>	<b>77</b>
<b>4.2</b>	<b>Sample Preparation.....</b>	<b>77</b>
<b>4.3</b>	<b>Hot Filament CVD Reactor.....</b>	<b>78</b>
<b>4.4</b>	<b>Raman .....</b>	<b>78</b>
<b>4.5</b>	<b>Terminations.....</b>	<b>79</b>
4.5.1	Hydrogen.....	79
4.5.2	Oxygen and Nitrogen .....	80
4.5.2.1	UV-Ozone Treatment .....	80
4.5.2.2	Acid Treatment .....	80
4.5.2.3	Plasma Treatment .....	80
4.5.3	Titanium.....	81
<b>4.6</b>	<b>NanoESCA.....</b>	<b>82</b>
4.6.1	Preparation and Analysis Chamber .....	83
4.6.2	Fabrication Chamber .....	84
4.6.3	X-ray Photoelectron Spectroscopy .....	84
4.6.4	Work Function Maps and UV-Photoelectron Spectroscopy .....	86
<b>4.7</b>	<b>Summary .....</b>	<b>87</b>

<b>5</b>	<b>Simple Terminations</b> .....	<b>88</b>
5.1	Introduction.....	89
5.2	H-terminated Diamond .....	90
5.2.1	C 1s Core-level Spectra.....	93
5.3	O-terminated Diamond .....	97
5.3.1	UV-Ozone and Acid Oxidation.....	98
5.3.2	Oxygen Plasma Oxidation.....	100
5.3.3	Summary .....	102
5.4	N-terminated Diamond.....	104
5.5	Summary .....	107
<b>6</b>	<b>TiO/TiN Terminations</b> .....	<b>108</b>
6.1	Introduction.....	109
6.2	Titanium.....	109
6.3	Titanium Oxide .....	114
6.3.1	QML TiO .....	115
6.3.2	HML TiO .....	121
6.3.3	FML TiO .....	127
6.3.4	TiO Work Functions.....	132
6.4	Titanium Nitride .....	135
6.4.1	QML TiN .....	136
6.4.2	HML TiN .....	142
6.4.3	FML TiN .....	147
6.4.4	TiN Work Functions.....	153
6.5	Summary .....	156

<b>7</b>	<b>Comparison and Future Work.....</b>	<b>158</b>
7.1	Comparison of Modelling and Experimental Data.....	159
7.2	Conclusion.....	160
7.3	Future Work .....	160
<b>8</b>	<b>References .....</b>	<b>163</b>
	<b>Appendix A – Electrostatic Potentials Graphs .....</b>	<b>178</b>
	TiC Section 2.3.1 .....	178
	TiO Section 2.3.2.....	182
	TiN Section 2.3.3 .....	187
	<b>Appendix B – Work Function Maps.....</b>	<b>195</b>
	Sample #2.7, section 6.2 .....	195
	Titanium sample, section 6.2 .....	195
	TiO QML, section 6.3.1 .....	196
	TiO HML, section 6.3.2.....	198
	TiO FML, section 6.3.3.....	200
	TiN QML, section 6.4.1 .....	202
	TiN HML, section 6.4.2.....	204
	TiN FML, section 6.4.3.....	206
	<b>Appendix C – UPS SPectra .....</b>	<b>208</b>
	TiO QML, section 6.3.1 .....	208
	TiO HML, section 6.3.2.....	209
	TiO FML, section 6.3.3.....	210
	TiN QML, section 6.4.1 .....	211
	TiN HML, section 6.4.2.....	212
	TiN FML, section 6.4.3.....	213

# List of Figures and Tables

Figure 1-1 – A schematic diagram of a TEC device. ....	3
Figure 1-2 – A band diagram of a semiconductor-vacuum interface defining a variety of material properties. (a) shows a PEA (or high WF) while (b) shows an NEA. ....	10
Figure 1-3 – Band diagrams of various band-bending scenarios. CBM is the conduction band minimum, VBM is the valence band maximum, $E_{vac}$ is the vacuum level, WF is the work function, and EA is the electron affinity. (a) a semiconductor with no band bending, (b) a p-type semiconductor where the vacuum level is higher than the CBM at the surface but lower than the bulk CBM, i.e. an ‘effective’ NEA, (c) a p-type semiconductor with the vacuum level lower in energy than the CBM at the surface, i.e. a ‘true’ NEA, such as H-terminated boron-doped diamond, (d) an n-type semiconductor where the vacuum level is lower than the CBM at the surface but higher in energy than the bulk CBM, i.e. an ‘effective PEA’ such as H-terminated N-doped diamond. ....	14
Figure 2-1 – An example of an electrostatic potential graph along the $z$ -axis of the slab. The $x$ -axis shows the distance in fraction of unit cell with the unit cell being centred upon the middle of the slab. The green arrow illustrates how $V_{vac} - V_{av, slab}$ is calculated. ....	31
Figure 2-2 – (a) Side view of the non-reconstructed (100) diamond surface, (b) the same surface, rotated $90^\circ$ about the $z$ -axis, (c) the top-down view of the same surface, and (c) an angled view of the bulk diamond structure.....	33
Figure 2-3 – The optimised structures of the various clean, H-, and Ti-terminated diamond (100) surfaces investigated. (a) – (h) are sample identifiers corresponding to Table 2-1. Each structure is displayed as top-down followed by a side view. Green are the C atoms, yellow are the Ti atoms and grey are H atoms. ....	35
Figure 2-4 – An ideal (100) diamond surface showing the two dangling bonds.....	37
Figure 2-5 – Two $2 \times 1$ reconstructed (100) diamond surfaces. The different layers are colour coded to aid in visualization. Green is the top most layer, red is the second from the top layer, blue is the third, and black is the fourth layer. ....	36

Figure 2-6 – The optimised structures of the various O- and TiO-terminated diamond (100) surfaces investigated. (a) – (h) are sample identifiers corresponding to Table 2-2. Each structure is displayed as top-down followed by a side view. Green are the C atoms, red are O atoms, and yellow are the Ti atoms.....	40
Figure 2-7 – The optimised structures of two TiO-terminated diamond (100) surfaces investigated. (i) – (k) are sample identifiers corresponding to Table 2-2. Each structure is displayed as top-down followed by a side view. Green are the C atoms, red are O atoms, and yellow are the Ti atoms. ....	41
Figure 2-8 –The variation of the EA with Ti coverage for O- and TiO-terminated diamond surfaces. ....	43
Figure 2-9 – The optimised structures of the various N-, N-hydride-, and TiN-terminated diamond (100) surfaces investigated. (a) – (h) are sample identifiers corresponding to Table 2-3. Each structure is displayed as top-down followed by a side view. Green are the C atoms, red are O atoms, and yellow are the Ti atoms. ....	46
Figure 2-10 – The optimised structures of the various N-hydride- and Ti-terminated diamond (100) surfaces investigated. (i) – (p) are sample identifiers corresponding to Table 2-3. Each structure is displayed as top-down followed by a side view. Green are the C atoms, red are O atoms, and yellow are the Ti atoms.....	47
Figure 2-11 – variation of EA with ML coverage for N-, NH <sub>x</sub> -, and TiN-terminated diamond surfaces. ....	48
Figure 2-12 – Box plots showing the surface stability of the three Ti-containing surface terminations. The boxes represent the interquartile range, the line is the mean, and × is the median. ....	50
Figure 3-1 – An example curve of the inelastic mean free path of an electron through a solid. ....	53
Figure 3-2 – An energy level diagram (a) depicting the origin of the various emission lines, and a table (b) of the most intense emission lines for common anode materials. <sup>155</sup> .....	54
Figure 3-3 – A schematic diagram of a hemispherical electron analyser. ....	55
Figure 3-4 – An example of the UPS spectrum of a typical NEA surface (e.g. H-terminated diamond). The dotted line shows a typical UPS spectrum without the NEA	

peak, i.e. for a PEA surface (e.g. O-terminated diamond). The inset shows how the WF is determined where the secondary electron cut-off (SECO) and the baseline intersect (4.49 eV in this example). $E_k$ is the kinetic energy of the photoelectrons $E_{\text{Fermi}}$ is the energy of the Fermi level. ....	58
Figure 3-5 A linear background on a C 1s spectrum.....	60
Figure 3-6 – Various backgrounds computed on a Ti 2p spectrum. (a) a separate Shirley background for each peak, (b) a single Shirley background across both peaks, (c) a linear background, and (d) a Tougaard background. (e) is an overlay of the different peaks showing the difference in size as a result of the various backgrounds. The FWHM values shown in the inset table are for the Ti 2p <sub>3/2</sub> peaks. ....	62
Figure 3-7 – Various centred Voigt profiles. Each case has the same area and the same full width at half maximum of 1. ....	64
Figure 3-8 – (a) a peak fitting with the appropriate constraints, (b) a peak fitting without constraints, and (c) a peak fitting with the FWHM constrained, but too many components added. The 15 components shown in (c) were the minimum required to get the RSTD below 1. ....	66
Figure 3-9 – A Bachmann C-H-O phase diagram for diamond depositon. The area between the dotted lines indicates where diamond growth will occur. Recreated from <sup>174</sup> .....	73
Figure 3-10 – (a) Energy level diagram of the various scattering processes involved in Raman spectroscopy and (b) a Raman spectrum of single crystal diamond. ....	75
Figure 4-1 – A top-down view, colour-coded schematic diagram of the NanoESCA at the University of Bristol. ....	82
Figure 4-2 – The schematics (a) and image (b) of the IDEA (imaging double hemispherical energy analyser).....	84
Figure 5-1 – (a) The XPS widescan survey spectrum of H-terminated (100) diamond, and (b) the associated UPS spectrum giving a WF of $3.8 \pm 0.1$ eV, as shown in the inset. This type of spectrum is discussed in more detail in section 3.1.3. ....	91
Figure 5-2 – The WF map of H-terminated diamond (a), and one of the PEEM images used to construct it (b). The field of view is $\sim 78 \mu\text{m}$ .....	92

Figure 5-3 – (a) A H-terminated C 1s spectrum fitted with a symmetric SGL(12) line shape, and (b) a higher magnification of the shoulder region of that same spectrum where the black line is the sum of all the components. The inset shows the black envelope overlapping with the experimental data (red line) which can be difficult to see when the data fits well, except at high magnification. ....	94
Figure 5-4 – (a) A C 1s XPS spectrum from H-terminated diamond fitted with an asymmetric SGL(12)T(1.7) line shape, and (b) a higher magnification of the shoulder regions of that same spectrum where the black line is the sum of all the components. ....	95
Figure 5-6 – The O 1s core-level scan of a H-terminated diamond sample. ....	96
Figure 5-6 – Experimental and simulated C 1s core-level spectrum of a H-terminated (100) surface showing a band bending value of 1.65 eV. From <sup>46</sup> .....	96
Figure 5-7 – A box plot of the O percentage from Table 5-2. The Interquartile range is from 5.6 – 6.0 %, the mean (X) is 5.8 %, and the median is 5.7 %. ....	101
Figure 5-8 – The WF maps of samples #2.7 (top) #2.8 (middle left), #2.9 (middle right), and #2.10 (bottom). ....	103
Figure 5-9 – A summary of the N content achieved through the various N termination experiments where the first four experiments were performed in the Terminator and the last two in the Microwave plasma reactor. The labels of the individual points refer to the sample id in Table 5-3. ....	106
Figure 6-1 – The ratio of the signal intensities of Ti to C as a function of the quantity of Ti deposited. Each point in the plot corresponds to 100 s of Ti deposition. ....	110
Figure 6-2 – The XPS survey spectrum of Ti after 5 h of Ti deposition. ....	111
Figure 6-3 – (a) The XPS C 1s and (b) Ti 2p core-level spectra of Ti after 5 h of Ti deposition.....	112
Figure 6-4 – QML TiO – The O 1s core-level spectrum after the 1000 °C anneal. ....	116
Figure 6-5 – QML TiO – An overlay of the O 1s spectra (left) after the different temperature anneals and the areas of the corresponding component peaks (right). ....	117
Figure 6-6 – QML TiO – An overlay of the C 1s spectra (top left) after the different temperature anneals, a bar chart of the areas of the corresponding component peaks (top right), and another overlay of the C 1s spectra on a logarithmic vertical-axis (bottom	

right) to enable the visualisation of the smaller components in the shoulders. The bar chart is also on a logarithmic scale for the same reason.....	119
Figure 6-7 – QML TiO – An overlay of the Ti 2p spectra after the different temperature anneals.....	120
Figure 6-8 – HML TiO – An overlay of the O 1s spectra (left) after the different temperature anneals and the areas of the corresponding component peaks (right)...122	
Figure 6-9 – HML TiO – An overlay of the C 1s spectra (top left) after the different temperature anneals, a bar chart of the areas of the corresponding component peaks (top right), and another overlay of the Cls spectra on a logarithmic vertical-axis (bottom right) to enable the visualisation of the smaller components in the shoulders. The bar chart is also on a logarithmic scale for the same reason.....	124
Figure 6-10 – HML TiO – An overlay of the Ti 2p spectra after the different temperature anneals.....	125
Figure 6-11 – Periodic table showing the values and trends in the electronegativity of the elements. <sup>151</sup> .....	126
Figure 6-12 – FML TiO – An overlay of the O 1s spectra (left) after the different temperature anneals and the areas of the corresponding component peaks (right)...128	
Figure 6-13 – FML TiO – An overlay of the C 1s spectra (top left) after the different temperature anneals, a bar chart of the areas of the corresponding component peaks (top right), and another overlay of the Cls spectra on a logarithmic vertical-axis (bottom right) to enable the visualisation of the smaller components in the shoulders. The bar chart is also on a logarithmic scale for the same reason.....	129
Figure 6-14 – FML TiO – An overlay of the Ti 2p spectra after the different temperature anneals.....	131
Figure 6-15 – TiO – How the WF of the three TiO-terminated samples evolves as a function of annealing temperature. 0 °C is the O-terminated samples before Ti deposition while 400 °C is the WF after Ti deposition as this is the deposition temperature.....	132
Figure 6-16 – TiO – Evolution of the WFs of the (a) QML, (b) HML, and (c) FML Ti oxide-terminated samples in relation to the O content. ....	133

- Figure 6-17 – QML TiN – An overlay of the O 1s spectra (left) after the different temperature anneals and the areas of the corresponding component peaks (right)...138
- Figure 6-18 – QML TiN – An overlay of the C 1s spectra (top left) after the different temperature anneals, a bar chart of the areas of the corresponding component peaks (top right), and another overlay of the Cls spectra on a logarithmic vertical-axis (bottom right) to enable the visualisation of the smaller components in the shoulders. The bar chart is also on a logarithmic scale for the same reason.....139
- Figure 6-19 – QML TiN – An overlay of the N 1s spectra (left) after the different temperature anneals and the areas of the corresponding component peaks (right).. 140
- Figure 6-20 – QML TiN – An overlay of the Ti 2p spectra after the different temperature anneals..... 141
- Figure 6-21 – HML TiN – An overlay of the O 1s spectra (left) after the different temperature anneals and the areas of the corresponding component peaks (right)...143
- Figure 6-22 – HML TiN – An overlay of the C 1s spectra (top left) after the different temperature anneals, a bar chart of the areas of the corresponding component peaks (top right), and another overlay of the Cls spectra on a logarithmic vertical-axis (bottom right) to enable the visualisation of the smaller components in the shoulders. The bar chart is also on a logarithmic scale for the same reason.....144
- Figure 6-23 – HML TiN – An overlay of the N 1s spectra (left) after the different temperature anneals and the areas of the corresponding component peaks (right)...145
- Figure 6-24 – HML TiN – An overlay of the Ti 2p spectra after the different temperature anneals.....146
- Figure 6-25 – FML TiN – An overlay of the O 1s spectra (left) after the different temperature anneals and the areas of the corresponding component peaks (right)...149
- Figure 6-26 – FML TiN – An overlay of the C 1s spectra (top left) after the different temperature anneals, a bar chart of the areas of the corresponding component peaks (top right), and another overlay of the Cls spectra on a logarithmic vertical-axis (bottom right) to enable the visualisation of the smaller components in the shoulders. The bar chart is also on a logarithmic scale for the same reason.....150
- Figure 6-27 – FML TiN – An overlay of the N 1s spectra (left) after the different temperature anneals and the areas of the corresponding component peaks (right)...151

Figure 6-28 – FML TiN – An overlay of the Ti 2p spectra after the different temperature anneals.....	152
Figure 6-29 – TiN – How the WF of the three TiN-terminated samples evolves as a function of annealing temperature. 0 °C is the O-terminated samples before Ti deposition while 400 °C is the WF after Ti deposition as this is the deposition temperature.....	153
Figure 6-30 – TiN – Showing how the WFs of the (a) QML, (b) HML, and (c) FML TiN-terminated samples evolve in relation to the O content. ....	154
Table 2-1 – The computed surface energy and EA of the various clean, H-, and Ti-terminated (100) diamond surfaces investigated. Column 2 describes the initial state of each system before structure optimisation while the (a) – (h) in column 1 refer to the optimised structures displayed in Figure 2-3. ....	34
Table 2-2 – The computed surface energy and EA of the various O- and TiO-terminated (100) diamond surfaces investigated. Column 2 describes the initial state of each system before structure optimisation while the (a) – (h) in column 1 refer to the optimised structures displayed in Figure 2-6 and Figure 2-7. ....	39
Table 2-3 – The computed surface energy and EA of the various N-, N-hydride-, and TiN-terminated (100) diamond surfaces investigated. Column 2 describes the initial state of each system before structure optimisation while the (a) – (p) in column 1 refer to the optimised structures displayed in Figure 2-9 and Figure 2-10. ....	44
Table 3-1 – Pressure dependence of the mean free path and time to form a monolayer (ML). ....	56
Table 3-2 – A summary of the most intense emission lines for common gases used in a gas discharge lamp. I – light emitted from neutral atoms, II – light emitted from singly ionized atoms. ....	58
Table 3-3 – Binding energies of common functional groups present in the C 1s peak. <sup>61,71,156–161</sup> .....	67
Table 3-4 – Binding Energies of common functional groups present in the O 1s peak. <sup>156,157,162–164</sup> .....	67

Table 3-5 – Binding Energies of common functional groups present in the N 1s peak. <sup>156,157,165–169</sup> .....	68
Table 3-6 – Binding energies of the different oxidation states of Ti in the Ti 2p <sub>3/2</sub> peak. <sup>156,157,166,167,170–173</sup> .....	68
Table 3-7 – Spin-orbit splitting values for various oxidation states of Ti in the the Ti 2p peak. <sup>156,157,170–173</sup> .....	68
Table 3-8 – Relative sensitivity factors of some commonly encountered elements.....	69
Table 5-1 – A summary of the percentage composition of the survey scans and the component peaks of the O 1s core-level scans of diamond oxidised by UV-ozone or acid treatment.....	98
Table 5-2 – A summary of the percentage composition of the survey scans and the component peaks of the O 1s core-level scans of diamond oxidised by an O plasma.	100
Table 5-3 – A summary of the percentage composition of the survey and the component peaks of the N 1s core-level scans of N-terminated diamond. NH <sub>3</sub> /N <sub>2</sub> in the prep column indicates the feed gas used for the plasma treatment, while T/MW indicates the reactor used, either the Terminator (T) or the Microwave (MW) plasma reactor. ....	105
Table 6-1 – Spin-orbit splitting <i>j</i> values and peak area ratios for the various subshells. ....	113
Table 6-2 – QML TiO – Summary of the elemental composition after annealing at different temperatures where 0 °C represents before deposition, and 400 °C is after deposition, as this is the deposition temperature.....	115
Table 6-3 – HML TiO – Summary of the elemental composition after annealing at different temperatures where 0 °C represents before deposition, and 400 °C is after deposition, as this is the deposition temperature.....	121
Table 6-4 – FML TiO – Summary of the elemental composition after annealing at different temperatures where 0 °C represents before deposition, and 400 °C is after deposition, as this is the deposition temperature.....	127
Table 6-5 – QML TiN – Summary of the elemental composition after annealing at different temperatures where 0 °C represents before deposition, and 400 °C is after deposition, as this is the deposition temperature.....	136

Table 6-6 – HML TiN – Summary of the elemental composition after annealing at different temperatures where 0 °C represents before deposition, and 400 °C is after deposition, as this is the deposition temperature.....142

Table 6-7 – FML TiN – Summary of the elemental composition after annealing at different temperatures where 0 °C represents before deposition, and 400 °C is after deposition, as this is the deposition temperature.....147

# List of Abbreviations

CBM	- conduction band minimum
CVD	- chemical vapour deposition
DFT	- density functional theory
EA	- electron affinity ( $\chi$ )
ESCA	- electron spectroscopy for chemical analysis
FML	- full monolayer
GGA	- generalised gradient approximation
GTO	- gaussian-type orbital
HF	- Hartree-Fock
HFCVD	- hot filament chemical vapour deposition
HML	- half monolayer
HPHT	- high-pressure high-temperature
IMFP	- inelastic mean free path
IPCC	- intergovernmental panel on climate change
LDA	- local density approximation
ML	- monolayer
MWCVD	- microwave assisted chemical vapour deposition
NEA	- negative electron affinity
PEA	- positive electron affinity
PEEM	- photoemission electron microscopy
QMB	- quartz microbalance
QML	- quarter monolayer
SCD	- single-crystal diamond
SECO	- secondary electron cut-off
SPA-LEED	- spot profile analysis – low energy electron diffraction
STO	- slater-type orbitals
TEC	- thermionic energy conversion
UEG	- uniform electron gas
UHV	- ultra-high vacuum
UPS	- ultraviolet photoelectron spectroscopy
VBM	- valence band maximum
WF	- work function ( $\varphi$ )
XC	- exchange-correlation energy
XPS	- X-ray photoelectron spectroscopy
$\mu$ ARPES	- micro angle resolved photoelectron spectroscopy

# Outline

## **Chapter 1**

This chapter provides the motivation, theoretical background, and context for this work.

## **Chapter 2**

This chapter explores the theoretical modelling undertaken in parallel with experimental work to yield a deeper understanding of the surfaces studied.

## **Chapter 3**

This chapter discusses the theoretical and practical aspects of the fabrication and analysis techniques underpinning this work.

## **Chapter 4**

This chapter expounds the experimental methods and instruments used to prepare and analyse the samples.

## **Chapter 5**

This chapter investigates diamond surfaces-terminated by non-metals such as hydrogen, oxygen and nitrogen.

## **Chapter 6**

This chapter delves into metal deposition on diamond surfaces, and the stability and properties of these surfaces at elevated temperatures.

## **Chapter 7**

This chapter summarises the most pertinent results, compares the experimental and computational studies, and suggests further avenues of exploration.

# CHAPTER



## Introduction

Western civilization, it seems to me, stands by two great heritages. One is the scientific spirit of adventure — the adventure into the unknown, an unknown which must be recognized as being unknown in order to be explored; the demand that the unanswerable mysteries of the universe remain unanswered; the attitude that all is uncertain; to summarize it — the humility of the intellect. The other great heritage is Christian ethics — the basis of action on love, the brotherhood of all men, the value of the individual — the humility of the spirit.

These two heritages are logically, thoroughly consistent. **But logic is not all; one needs one's heart to follow an idea.** If people are going back to religion, what are they going back to? Is the modern church a place to give comfort to a man who doubts God — more, one who disbelieves in God? Is the modern church a place to give comfort and encouragement to the value of such doubts? So far, have we not drawn strength and comfort to maintain the one or the other of these consistent heritages in a way which attacks the values of the other? Is this unavoidable? How can we draw inspiration to support these two pillars of western civilization so that they may stand together in full vigour, mutually unafraid? Is this not the central problem of our time?

Richard Feynman - remarks (2 May 1956) at a Caltech YMCA lunch forum

## 1.1 Climate Change

According to a report published by the Intergovernmental Panel on Climate Change (IPCC)<sup>i</sup> in October 2018, “rapid, far-reaching and unprecedented changes in all aspects of society” were needed to stave of what many media outlets dubbed the ‘climate catastrophe’.<sup>1</sup> With the sensationalist tendencies of modern news reporting, one may wonder whether this is merely overdramatization. Essentially, the report states that limiting global warming to 1.5 °C compared to 2 °C (previous target) would significantly reduce the damaging impact on both the ecosystem and human health. To accomplish this, global net human-caused emissions of carbon dioxide would need to fall by about 45 % from 2010 levels by 2030, reaching ‘net zero’ by 2050.<sup>1</sup> To put into perspective how challenging this will be to achieve, even if all conditional and unconditional ‘nationally determined contributions’ of the Paris Agreement<sup>ii</sup> were met, the result is estimated to be a 3 °C increase by 2100, and is likely to grow further. This highlights the need for drastic action.

The higher global temperatures rise, the stronger and more frequent extreme weather events such as droughts, wildfires, storms, or flooding become, in addition to rising sea levels. The impact this will have on humanity, such as famine, disease, and mass-migration of people, is difficult for most to imagine. However, whilst it will be challenging and require commitment and extensive changes on a global scale, it is possible to meet the goals of the IPCC report.<sup>1,2</sup>

Numerous pathways to achieving the 1.5 °C goal have been proposed, including shifting to zero-emission energy production, shifting away from land- and emission-intensive meat-based diets towards environmentally friendlier plant-based diets, electrifying transport and infrastructure, increasing energy efficiency, carbon capture technologies, or geoengineering such as reforestation.<sup>3</sup> The work presented in this thesis is aimed towards cleaner energy production.

---

<sup>i</sup> The IPCC is the UN’s intergovernmental body dedicated to providing governments with assessments of the scientific basis for climate change, its impacts and future risks, and options for adaptation and mitigation.<sup>153</sup>

<sup>ii</sup> The Paris Agreement is the world’s first comprehensive climate agreement within the United Nations Framework Convention on Climate Change which seeks to reduce the impact of human-caused climate change. Considering President Trump announced in 2017 his intention to withdraw the United States (the 2<sup>nd</sup> largest emitter of CO<sub>2</sub>) from the agreement, its effectiveness may not be as far-reaching as hoped.

## 1.2 Thermionic Energy Conversion

Controlled electron emission is a crucial component in several technological applications, including but not limited to electron microscopy, X-ray sources, electron-beam lithography, high-power microwave amplifiers, emissive flat panel displays, ion engines for long-distance spacecraft, and, of course, thermionic energy conversion.<sup>4-11</sup>

A thermionic energy conversion (TEC) device is a solid-state device which directly converts heat into electricity. Thermionic emission is electron emission whereby the energy required for the electrons to overcome the potential barrier at the surface is provided by thermal energy. A TEC device, as shown in Figure 1-1, consists of a hot cathode (emitter) which emits electrons across a small gap to the cooler anode (collector) thereby creating a self-bias which can be used to drive a load. TEC devices have many advantages over other power-generating techniques, such as their simple design, compact size, no moving parts, and high theoretical efficiency. A plethora of possible heat sources exist, ranging from solar, burning fuels such as hydrogen or coal, nuclear reactors, to waste heat from a variety of sources such as car exhausts or the human body. Because of this, the potential for direct thermal-to-electrical energy conversion is vast, and a wide range of temperatures and powers are possible.<sup>12</sup>

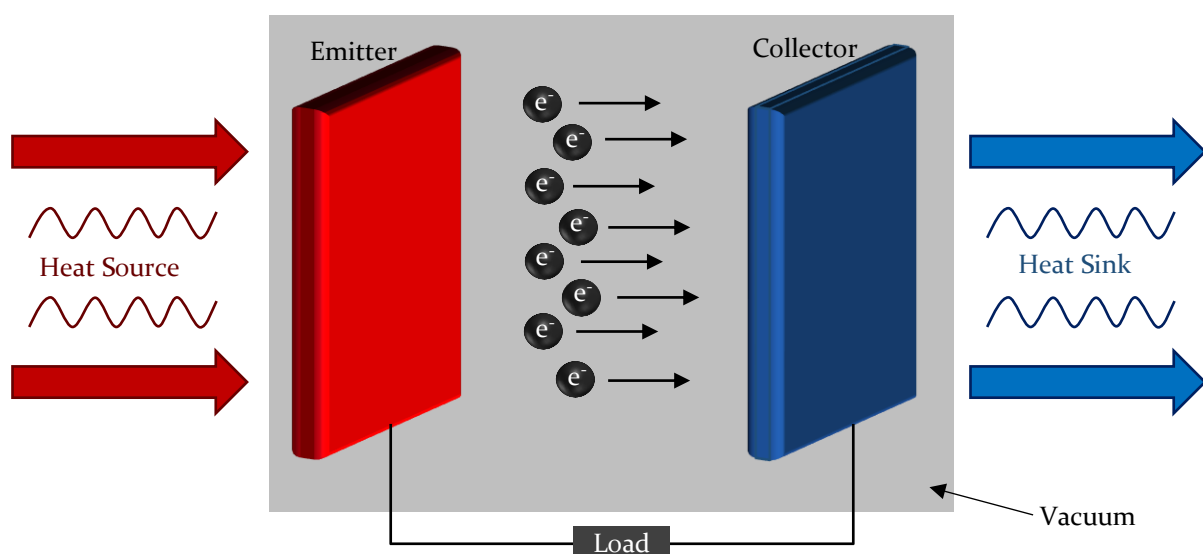


Figure 1-1 – A schematic diagram of a TEC device.

### 1.2.1 History

The idea of TEC devices is not new, having been first proposed by Schlichter in 1915.<sup>13</sup> Extensive investigations were carried out in the 1950s through to the 1980s, with several test reactors being created for space applications. The US created a solar-energy converter that operated at  $\sim 1,600$  °C and  $\sim 150$  W with 7 – 11 % efficiency for up to  $\sim 11,000$  h.<sup>12</sup> The former Soviet Union created several thermionic nuclear reactors and used two 6 kW reactors on some of their satellites.<sup>14</sup> Ultimately, progress was slow, and TEC technology was eclipsed by alternative direct-conversion technologies such as photovoltaic and thermoelectric. This led to a decrease in funding, which combined with the lack of availability of sufficiently advanced materials, technologies, and fabrication techniques, resulted in little progress.<sup>15,16</sup> In 2001, a report by the American National Research Council stated that “the thermionic technology base and infrastructure stand close to extinction”, and provided a rather stark view of the future for TEC devices.<sup>17</sup> However, recent developments in material science, as well as the understanding of the underlying physical processes involved, have led to a renewed interest, as well as new approaches and strategies being developed. For more information, several reviews of the subject are available.<sup>12,18–23</sup>

### 1.2.2 Background

Thermionic emission is described by the Richardson-Dushman equation (also known as the Richardson or Richardson-Laue-Dushman equation), which relates the emission current density ( $J$ ) to the emitter temperature ( $T$ ):

$$J = AT^2 \exp\left(-\frac{\varphi}{k_B T}\right)$$

Equation 1-1

where  $A$  is the emission constant (Richardson constant) of the material,  $\varphi$  is the work function (WF) of the emitter, and  $k_B$  is the Boltzmann constant. The  $A$  factor is given by:

$$A = A_0 \lambda$$

Equation 1-2

where  $\lambda$  is a material-dependent correction factor, and  $A_0$  is the theoretical Richardson constant:

$$A_0 = \frac{4\pi m k_a^2 q_e}{h^3} = 120.2 \text{ A cm}^{-2} \text{ K}^2$$

Equation 1-3

where  $m$  is the mass of an electron,  $q_e$  is the charge of an electron, and  $h$  is the Planck constant. From Equation 1-1, it can be seen that the WF is a critical parameter due to the exponential nature of the  $\left(-\frac{\varphi}{k_a T}\right)$  term. Most materials have WF values of several eV, resulting in high temperatures (>1500 °C) being necessary to achieve reasonable emission currents. Diamond, however, can have very low WF values (depending on the surface and its functionalisation) making it an excellent candidate for TEC devices, as discussed in section 1.3.1.

### 1.2.3 Challenges

The maximum voltage achievable in a TEC device is essentially the difference in the WF values ( $\Delta\phi$ ) of the emitter and the collector. Therefore, for high output power, the WF of the emitter needs to be low to create significant emission currents, but the WF of the collector needs to be even lower to generate a large  $\Delta\phi$ . If the emitter had a WF of 1 eV, the WF of the collector is required to be  $\sim 0.5$  eV at most, which is extremely small compared to that of most materials ( $\sim 2 - 5$  eV). If differently terminated diamond were used as both the emitter and the collector, then the high secondary electron emission of diamond would be problematic as this would lead to significant electron backscatter. Furthermore, to prevent thermionic emission from the collector, it requires cooling, which additionally impacts the efficiency.

Another significant challenge that needs to be overcome is the space-charge effect. As electrons are emitted into vacuum, they leave behind a positive charge. Therefore, the material needs to be conducting to be able to neutralize this charge. However, at sufficient emission current densities, this positive charge creates an effective attraction on the emitted electrons, leading to a cloud of electrons near the emitter surface. These electrons in turn create an additional emission barrier for subsequent electrons. Therefore, mitigation of the space-charge effect is a critical aspect of device design.

Several approaches have been suggested to address the space-charge effect, including filling the gap with an easily ionizable vapour, reducing the interelectrode gap, or using a small voltage to accelerate electrons through the gap.<sup>19</sup> However, each of these approaches has its own advantages and challenges and no clear winner exists at present. Filling the interelectrode gap with an easily ionizable vapour such as caesium would create positive ions that prevent the space-charge cloud from forming, but collision with these ions would also reduce the energy of the emitted electrons, and hence the overall power of the TEC device. Reducing the interelectrode gap to below 10  $\mu\text{m}$  would mean there was insufficient space between the electrodes for the space-charge cloud to form, however, being in such close proximity to the hot emitter would make it challenging to cool the collector sufficiently. And finally, using a small voltage to accelerate the electrons across the interelectrode gap, either through applying a bias to the collector or a grid between the electrodes, would prevent the space-charge effect, but as this

requires power, it also reduces the overall efficiency of the device. For more information on device configurations and recent progress, see this review by Khalid *et al.*<sup>19</sup>

Despite these challenges, TEC remains an attractive solution to electricity production. Like other direct-conversion technologies, the lack of moving parts offers long lifetimes with little-to-no maintenance. Furthermore, TEC devices offer very high theoretical efficiency, being able to, in theory, operate near the Carnot limit. The Carnot theorem (also known as the Carnot rule, limit, or efficiency), is a principle which specifies the maximum efficiency ( $\eta_{max}$ ) with which a heat engine may operate. It is a consequence of the second law of thermodynamics<sup>iii</sup> and depends only on the temperature difference between the heat source ( $T_H$ ) and heat sink ( $T_C$ ), as defined by:

$$\eta_{max} = 1 - \frac{T_C}{T_H}$$

Equation 1-4

A theoretical TEC device operating with the emitter at 1800 K, and the collector at 1000 K, could operate near the Carnot efficiency of 44 %.<sup>12</sup> A graphene based TEC device has been proposed which, with an emitter temperature of 900 K and a collector temperature of 425 K, could achieve an efficiency of 45 % (Carnot efficiency = 53 %).<sup>24</sup> Perhaps most importantly, is that none of the challenges mentioned previously are insurmountable. There are no chemical/physical reasons why a TEC device cannot operate near Carnot efficiency with high power generation.<sup>12</sup>

---

<sup>iii</sup> The entropy of an isolated system can only increase over time for irreversible processes or remain constant for reversible processes. Carnot's theorem predates the second law of thermodynamics, as heat was not well understood at the time (1824) and is said to be one of the first formulations of the second law.

## 1.3 Diamond

Diamond has been valued as a gemstone since antiquity due to its outstanding optical properties. The well-known hardness of diamond coupled with its ability to disperse light give diamonds the brilliance that made them so sought-after. Although diamond is not the most thermodynamically stable allotrope of carbon, the presence of a large energy barrier makes the conversion of diamond to the more energetically stable graphite extremely slow. It would take longer than the lifetime of the universe (13.8 billion years) for a 1-carat diamond to be converted to graphite under standard conditions, so therefore, on any useful timescale, diamonds are indeed forever.<sup>25,26</sup>

More recently however, diamond has garnered interest for a variety of science and technology applications due to its many other extreme properties. Though it is well known that diamond is the hardest naturally occurring material, it also has exceptional thermal conductivity<sup>iv</sup>, high electron mobility, a broad potential window, excellent biocompatibility, is extremely resistant to heat, chemical, pressure, and radiation damage, as well as having an uncommonly wide transparency band, ranging from deep UV through the visible to the far infrared light. For more details about the properties and potential applications, refer to the review by May.<sup>27</sup>

---

<sup>iv</sup> Natural diamond has a thermal conductivity more than 5 times that of copper, which is often seen as an excellent conductor of heat, while diamond has been synthesised with more than 8 times the thermal conductivity of copper. Isotopically enriched diamond (0.07 % <sup>13</sup>C as opposed to the natural 1 % <sup>13</sup>C) has been shown to have a thermal conductivity of 33.2 W cm<sup>-1</sup> K<sup>-1</sup> while copper has a thermal conductivity of 4 W cm<sup>-1</sup> K<sup>-1</sup>.<sup>154</sup>

### 1.3.1 Why Diamond for TEC devices?

The elevated temperature regimes at which TEC devices operate eliminate most semiconductors as viable candidates. Diamond, on the other hand, has a unique set of properties that distinguish it for TEC applications, as mentioned above, and discussed in more detail by Wort *et al.*<sup>28</sup> Furthermore, a H-terminated diamond surface has a negative electron affinity (NEA). Electron affinity (EA,  $\chi$ ) has two definitions. In chemistry it is the amount of energy released when an electron is added to an atom or molecule. However, the definition of interest here is from physics, where it is defined as:

$$\chi = E_{\text{vac}} - E_{\text{CBM}}$$

Equation 1-5

where  $E_{\text{vac}}$  is the energy of the vacuum level, and  $E_{\text{CBM}}$  is the energy of the conduction band minimum (CBM). Therefore, if the vacuum level is lower in energy than the CBM, then any electrons in the conduction band are easily emitted into vacuum with minimal energy loss, and importantly, have no energy barrier to overcome.

As mentioned previously, this NEA is a well-known property of H-terminated diamond. However, the H-terminated surface is not stable at elevated temperatures. Above  $\sim 700$  °C, the H atoms desorb, and if cooled and exposed to air, the surface will be re-terminated by O atoms.<sup>18</sup> O-terminated diamond, on the other hand, has a positive electron affinity (PEA), which introduces an additional potential barrier to electron emission, thereby limiting its usefulness for TEC devices. It is therefore of great interest to create a diamond surface that exhibits an NEA similar to the H-terminated surface, which is stable at elevated temperatures.<sup>29-32</sup>

The difference in EA for the two elements discussed above is due to the surface electric dipole.<sup>33,34</sup> Terminating diamond with an element which is less electronegative than C (e.g. H) will create a surface dipole with the outermost layer being slightly positively charged, which leads to an NEA. Conversely, terminating atoms which are more electronegative than C (e.g. O, F), will lead to a slight negative charge on the outermost layer, producing a PEA. It is for this reason that elements with very low electronegativity, such as alkali and alkaline earth metals (group 1 and 2), excel as coatings for reducing the WF of a material.<sup>35-37</sup> For multi-element terminations

(e.g. OH, NH, or NH<sub>2</sub>), the surface dipole may be less trivial, but can be calculated using *ab initio* methods.<sup>38</sup>

The WF of a material is closely linked to, but distinct from, its EA. The WF is defined as the energy difference between the Fermi level and the vacuum level. So, although both the EA and the WF are a measure of where the vacuum level lies, they are in relation to different points, as shown in Figure 1-2. Furthermore, it is not straight-forward to convert between the two, as the position of the Fermi level is not fixed in semiconductors and varies with doping. For example, although two n-type and p-type doped diamond samples may have the same EA, the p-type sample would exhibit a higher WF as discussed in section 1.4.2.

Primarily, diamond is an excellent candidate as a thermionic emitter because of its excellent thermal properties and the potentially very low (<1 eV) WF values, dependant on doping and surface termination.

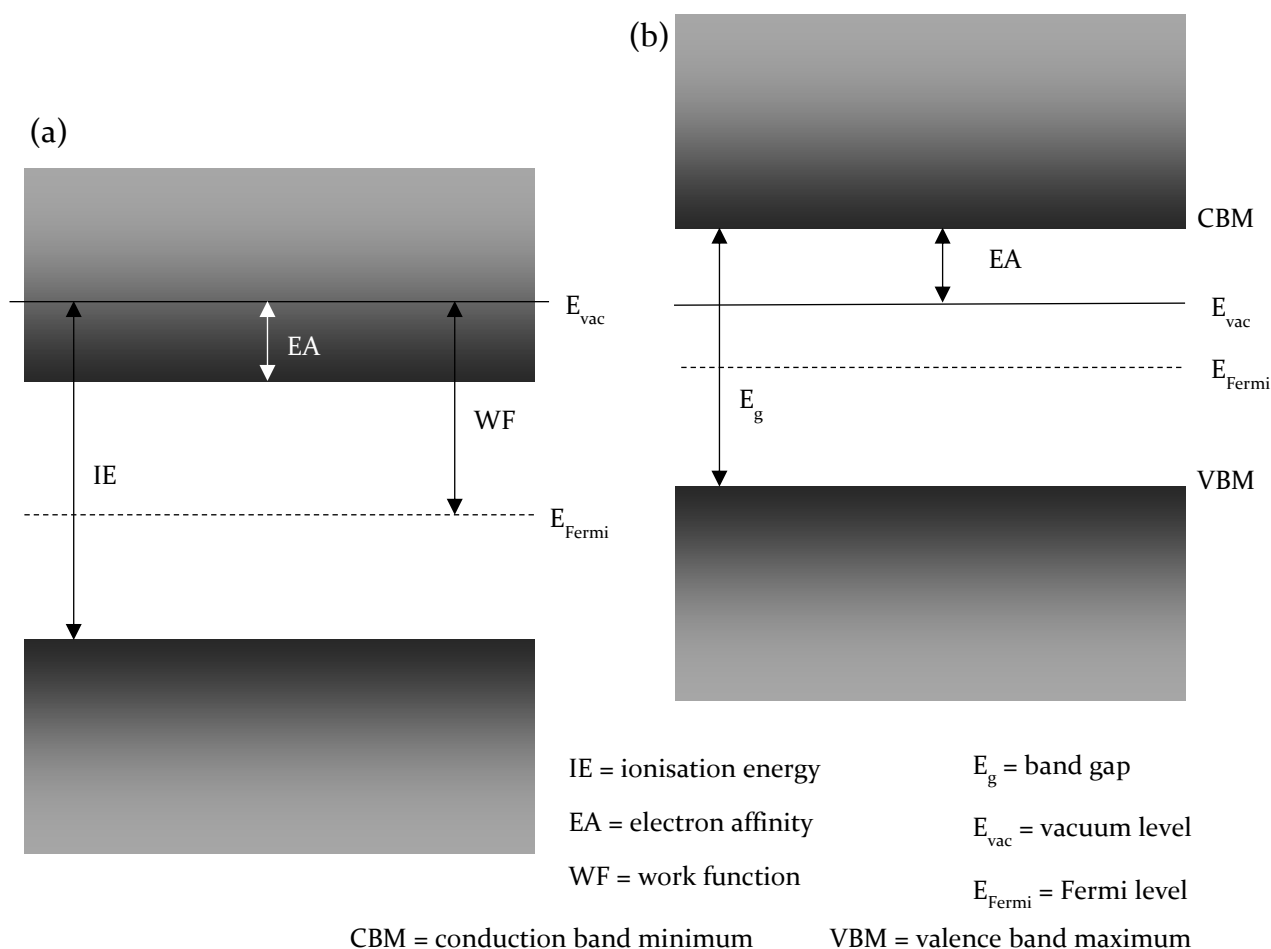


Figure 1-2 – A band diagram of a semiconductor-vacuum interface defining a variety of material properties. (a) shows a PEA (or high WF) while (b) shows an NEA.

## 1.4 Doping

An important distinction between the EA and the WF is the fact that while the EA is independent of doping, the WF is not. This is because doping affects the position of the Fermi level, while the position of the bulk CBM, and hence the EA, remain unaffected by doping. In theoretical work, the EA is typically discussed as it is easier to calculate and ignores the effects of doping. This is because doping is expensive to simulate as it typically requires large unit cells (>500 atoms) in comparison to the slab calculations performed in this work (~60 atoms). In experimental studies however, it is easier, and more appropriate, to measure the WF of the sample.

### 1.4.1 Common Dopants

The p-type doping of diamond can be easily achieved by incorporating boron into the growth process. Boron introduces an acceptor level 0.4 eV above the valence band maximum (VBM). However, because p-type doping pins the Fermi level near the VBM, thereby increasing the WF, it is of limited use for TEC devices. n-type doping is more desirable, because this pins the Fermi level closer to the CBM and thereby lowers the WF. However, n-type doping is challenging for diamond. Boron, inhabiting the same row in the periodic table as carbon but with one less electron, is a suitable p-type dopant. Although nitrogen, also a second-row element but with one additional electron, would theoretically be an ideal n-type dopant, this is not the case. This is because the N defect relaxes, leading to the donor level being 1.7 eV below the CBM. This deep donor level is therefore difficult to access and leads to nitrogen-doped diamond not being conductive at room temperature, unlike boron-doped diamond. Whilst this is problematic for most electronic applications, TEC devices operate at elevated temperatures, where N-doped diamond is conductive. However, as room-temperature conductivity was necessary for XPS and UPS, boron-doped diamond was utilised for the work presented here. Another candidate for n-type doping of diamond is phosphorus, which is in the same group as N, with a donor level 0.6 eV below the conduction band. The main challenge of using phosphorus is its larger atom size, making it difficult to incorporate into the diamond lattice in sufficient quantities, i.e. it is challenging to

achieve high doping concentrations, which can lead to poor conductivity.<sup>35</sup> Unless stated otherwise, the experiments discussed below, on the impact of doping on the electronic properties of diamond, are performed using H-terminated diamond.

#### 1.4.2 Effect of Doping on Thermionic Emission

As discussed in section 1.2.2, electron emission is not only dependent on the WF. While the EA and WF are surface properties, and hence are highly dependent on the surface termination, the Richardson constant is a material property. It is therefore influenced significantly by the bulk, and thereby doping, of the diamond crystal. An ideal thermionic emitter would exhibit a low WF and high Richardson constant.

N-doped polycrystalline diamond has been found to have a WF of 2.0 – 2.9 eV with associated Richardson constants of 68 – 70 A cm<sup>-2</sup> K<sup>-2</sup>.<sup>35,39</sup> Emission currents of 1 – 5 mA cm<sup>-2</sup> have been achieved at temperatures between 500 – 700 °C.<sup>39-41</sup> Ultra-nanocrystalline N-doped diamond has been determined to have even lower WF values of 1.3 – 1.7 eV, but unfortunately also exhibited low Richardson constants of 0.7 – 3.7 A cm<sup>-2</sup> K<sup>-2</sup>.<sup>42-44</sup> No explanation of these low values of the Richardson constants were offered.

Phosphorus-doped polycrystalline and single-crystal (100) diamond have been found to have lower WF values than N-doped diamond, with 0.9 eV and 0.7 eV, respectively.<sup>29,35</sup> Richardson constants were very low at 10<sup>-5</sup> A cm<sup>-2</sup> K<sup>-2</sup> for polycrystalline and 10<sup>-7</sup> A cm<sup>-2</sup> K<sup>-2</sup> for single crystal diamond samples. This was attributed to low mobility and high resistivity as a result of the difficulties of doping the diamond lattice with the considerably larger phosphorus atoms. While these studies attained doping concentrations of ~10<sup>17</sup> cm<sup>-3</sup>, another study with a higher doping concentration of 5×10<sup>20</sup> cm<sup>-3</sup>, achieved a Richardson constant of 15 A cm<sup>-2</sup> K<sup>-2</sup>, resulting in a current density of 8 mA cm<sup>-2</sup> at 600 °C.<sup>45</sup> More details about the effects of n-type doping on thermionic emission can be found in a review by Koeck *et al.*<sup>35</sup>

Another consideration is the substrate upon which the polycrystalline diamond is grown. A study investigating the effects of different substrates on N-doped diamond, found that the non-carbide forming rhenium achieved superior emission values versus the commonly used carbide forming molybdenum and tungsten substrates. The

molybdenum and tungsten substrate samples, with Richardson constants of 0.7 and 1.2 A cm<sup>-2</sup> K<sup>-2</sup>, respectively, and WFs of 1.4 eV, achieved emissions currents of 0.25 and 0.55 mA cm<sup>-2</sup> at 500 °C respectively. The diamond grown on the rhenium substrate, with a Richardson constant of 53.1 A cm<sup>-2</sup> K<sup>-2</sup> and a WF of 1.3 eV, achieved emission currents of 32 mA cm<sup>-2</sup> at 500 °C.<sup>44</sup>

When considering the band structure, the bands (energy states) of a material can bend up or down at interfaces. This band bending is not a physical effect, but rather a representation of the energy offset due to a charge imbalance at the interface. Interfaces between different materials experience this charge imbalance for different reasons. For the conductor/vacuum interface (such as in thermionic emitters), the position of the vacuum level is determined by the WF of the material and is fixed in relation to the conduction band. Therefore, if the material is p-type doped, and the Fermi level is pinned near the VBM, both the vacuum level and the conduction band are pulled downwards at the surface. Because the vacuum level does not bend, this can lead to an 'effective' NEA where the vacuum level is lower in energy in relation to the bulk CBM, as shown in Figure 1-3(b). This is the case for most semiconductors. Diamond is exceptional in that it can exhibit a 'true' NEA, as shown in Figure 1-3(c). Despite n-type doping being desirable because the pinning of the Fermi level near the CBM decreases the WF, the upward band bending can lead to scenarios where, despite having an NEA, the vacuum level is higher in energy than the bulk conduction band leading to an 'effective' PEA, as shown in Figure 1-3(d).<sup>46</sup>

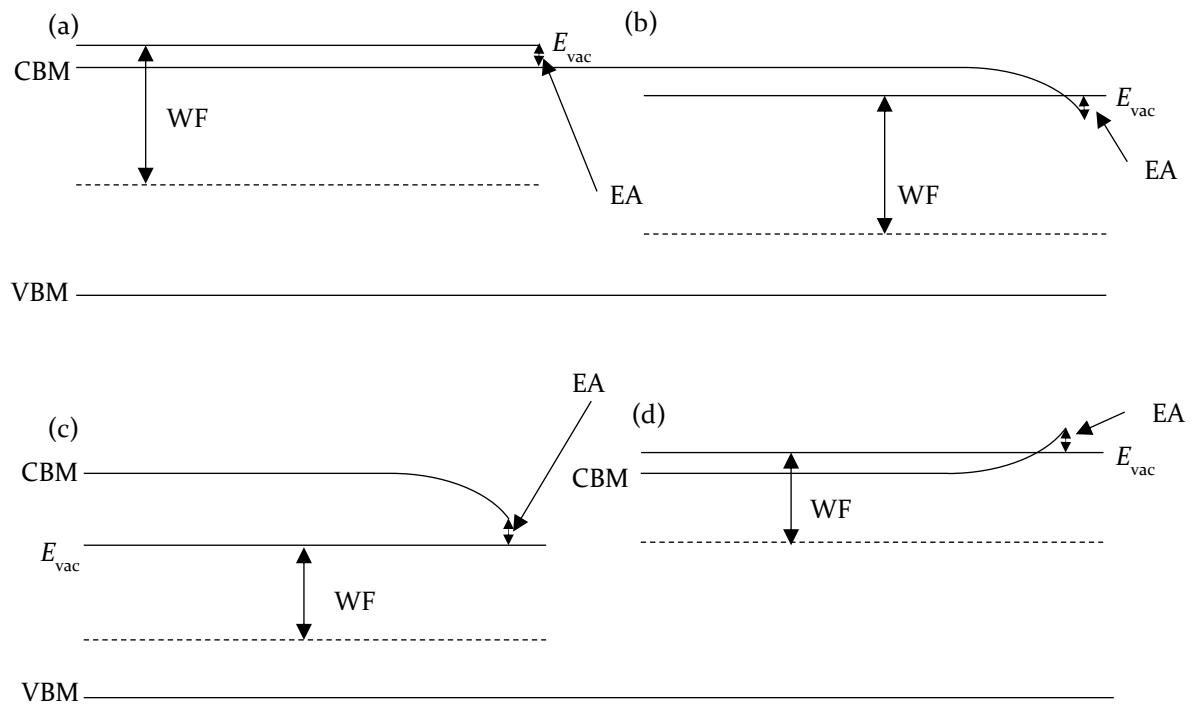


Figure 1-3 – Band diagrams of various band-bending scenarios. CBM is the conduction band minimum, VBM is the valence band maximum,  $E_{vac}$  is the vacuum level, WF is the work function, and EA is the electron affinity. (a) a semiconductor with no band bending, (b) a p-type semiconductor where the vacuum level is higher than the CBM at the surface but lower than the bulk CBM, i.e. an ‘effective’ NEA, (c) a p-type semiconductor with the vacuum level lower in energy than the CBM at the surface, i.e. a ‘true’ NEA, such as H-terminated boron-doped diamond, (d) an n-type semiconductor where the vacuum level is lower than the CBM at the surface but higher in energy than the bulk CBM, i.e. an ‘effective’ PEA’ such as H-terminated N-doped diamond.

## 1.5 Surface Terminations

Naturally, diamond is either H- or O-terminated. Although diamond is typically seen as chemically inert, there are many ways to functionalise the surface. Considering diamond is made of carbon, standard organic chemistry techniques can be applied to terminate the surface. Various chemical, electrochemical, and photochemical methods are available, ranging from the photolysis of perfluoroazooctane to DNA micropatterning via direct amination.<sup>47,48,57,49-56</sup> For more information on possible functionalisation routes, refer to these reviews.<sup>58,59</sup> Plasma treatments, such as those used in this work, are also highly effective. Though several of the crystal faces of diamond [predominantly (100), (110), and (111)] have been studied, both computationally and experimentally, the following discussion is primarily concerned with the (100) diamond surface. Practical methods of achieving H, O, and N terminations will be discussed here, along with results from literature on EA and surface stability for these terminations, as well as other terminations of interest.

### 1.5.1 Hydrogen

Diamond grown through chemical vapour deposition (CVD) is naturally H-terminated due to the excess H used in this process. Otherwise, exposure to a H plasma or annealing in H<sub>2</sub> can be used to H-terminate the diamond surface. The H-terminated (100) diamond surface is known to exhibit an NEA of -0.8 to -1.3 eV.<sup>60-66</sup> Boron-doped H-terminated diamond, both single crystal and polycrystalline, has been shown experimentally to exhibit a WF of 3.7 – 4.2 eV.<sup>46,66-69</sup>

For thermionic emission, threshold temperatures and maximum current densities are in the range of 300 – 600 °C and 0.1 – 1 mA cm<sup>-2</sup>, respectively.<sup>29,30,35,39,40,42,70</sup>

### 1.5.2 Oxygen

There are several options available for the O-termination of a diamond surface. These include plasma, UV-ozone, electrochemical, and acid treatment.<sup>61,71</sup> Although heating in a pure O<sub>2</sub> atmosphere leads to graphitisation of the surface, mixtures of oxygen and argon along with careful temperature control, or reduced pressures have been used to thermally oxidise diamond surfaces.<sup>59,72-74</sup>

Theoretical calculations of the O-terminated (100) surface have yielded an EA of 2.6 – 2.7 eV for ether-like O, 3.6 – 3.8 eV for ketone-like O, and -0.6 to 2.1 eV for the hydroxyl (OH) termination.<sup>38,75-78</sup> The variation in NEA values of the OH-termination may be attributed to the difficulties of density functional theory (DFT) to accurately model H bonding interactions.

Experimental studies on UV-ozone-, acid-, and plasma-oxidised diamond surfaces have yielded an EA of 1.6 – 1.8 eV.<sup>60,61</sup> Boron-doped O-terminated diamond has been determined to exhibit a WF of 4.9 – 5.2 eV, or 3.8 eV for the hydroxyl termination.<sup>66,68</sup>

When O desorbs, it predominantly departs as CO or CO<sub>2</sub>, thereby damaging the surface by removing carbon atoms.<sup>79,80</sup>

### 1.5.3 Nitrogen

N termination can be achieved using a variety of methods, similar to those for O termination. These range from UV-ammonia, electrochemical, to plasma treatments.<sup>47,57,62,81-84</sup> In some instances, the surface was chlorine-terminated prior to photochemical or thermal treatment.<sup>56,85,86</sup>

N-terminated diamond has been calculated to have a PEA of 3.2 – 3.5 eV.<sup>62,87</sup> The primary-amine termination (-NH<sub>2</sub>), has been experimentally shown to exhibit an NEA of unknown magnitude.<sup>88</sup> As these surfaces have been less widely studied than H- or O-terminated diamond, no WF data could be found for N-terminated diamond surfaces within the literature.

#### 1.5.4 Other Single-Element Terminations

Metal deposition can be achieved using a variety of techniques. The sample is typically annealed in vacuum to yield a clean surface, and the metal is then deposited using techniques such as evaporation, sputtering, or chemical reactions (e.g. atomic layer deposition). Various theoretical studies have shown that lithium, aluminium and various 1<sup>st</sup>-row transition metals are all expected to yield NEAs of -0.3 to -2.7 eV.<sup>78,89,90</sup> However, all but two of these metals (titanium and vanadium) are calculated to be less stable than H-terminated diamond.

Experimentally, cobalt, copper, and zirconium have been determined to exhibit NEA values of -0.2 to -0.7 eV, though these experiments did not include thermal stability or thermionic emission testing.<sup>91-93</sup> Similarly, silicon and germanium were found to exhibit NEAs of -0.9 and -0.7 eV respectively. Silicon was stable upon further oxidation, which is useful for TEC devices operating in ambient conditions.<sup>94-97</sup> Similarly, these experiments did not include thermal stability or emission testing.

Though no electron affinities were measured, a thermionic-emission study on Ti-terminated diamond showed that while at similar temperatures, the Ti termination exhibited a lower emission current than the H termination ( $\sim \times 0.5$ ), but because the Ti termination was stable up to a higher temperatures, a higher emission current was ultimately possible. The emission current of the H termination decreased rapidly at 725 °C due to the desorption of the H. The Ti termination on the other hand was heated up to 950 °C, where the emission current was higher ( $\sim \times 2$ ) than that of the H termination. This is due to the elevated temperature, as thermionic emission increases with temperature. It should be noted, though, that while the H termination was examined over a period of 10 minutes to show the degradation, no such tests were performed on the Ti termination. Therefore, it is unknown whether the Ti termination is stable for longer time periods at these temperatures.<sup>98</sup>

The trends seem to indicate that carbide forming metals (e.g. Ti, vanadium, aluminium) not only have more negative NEA values, but are also more stable, due to the strength of the metal carbide bond.

Other terminations, though not of interest in electron emission due to their PEA values, include sulphur and various halogens.<sup>33,58,99-101</sup>

### 1.5.5 Group I and II Metal Oxide Terminations

A common challenge with metal terminations on diamond is the weak metal-carbon bond which leads to poor surface stability at elevated temperatures. A possible alternative is to use metal oxides as the surface termination. While the O termination is fairly stable and exhibits a PEA, if a sufficiently low electronegativity metal is deposited on the O layer, causing the polarity of dipole to reverse, it may provide an NEA. Furthermore, the coverage of metal could be tuned to provide the optimum coordination to the metal, thereby making it air stable.

With caesium having one of the lowest electronegativities, caesium-oxide-terminated diamond was one of the earliest and most extensively studied systems. Caesium-oxide-terminated diamond has been theoretically and experimentally shown to have an NEA (-0.9 eV) and a WF of 1.3 eV, but is not stable above 400 °C.<sup>36,102-105</sup>

Lithium-oxide-terminated diamond has been calculated to have an NEA lower than that of the H-terminated surface with -3.9 eV and -4.0 eV for the (100) and (111) surfaces, respectively. At the same time, the calculated stability of the surface is similar to that of H-terminated diamond.<sup>78,106</sup> It has also been shown experimentally that lithium oxide leads to an NEA surface with a large electron yield increase.<sup>106,107</sup> It should be noted, however, that this comparison of electron emission is versus a PEA surface, which is naturally expected to have a lower electron yield due to the increased potential barrier for electron emission.

Magnesium-oxide-terminated diamond was calculated to have an EA and surface stability comparable to that of lithium-oxide- and H-terminated diamond.<sup>108</sup> Experimentally, the magnesium-oxide-terminated surface was determined to have an NEA of -2.0 eV.<sup>109</sup> Interestingly, while the lithium oxide surface required a 600 °C anneal to activate the NEA, this was not necessary for the magnesium oxide.

Computational studies of various group I and group 2 metals on O-terminated diamond surfaces suggest that the WF (and therefore NEA) is not directly proportional to electronegativity, with less electronegative elements not necessarily yielding lower WF values.<sup>78,108,110</sup> There is, however, a clear trend for the stability of these elements. The lighter elements are calculated to be more stable, which is attributed to the fact that the smaller atoms are held closer to the surface, and hence are less likely to desorb.

### 1.5.6 Transition Metal Oxides

Theoretical calculations on titanium, vanadium, nickel, copper, and zinc oxide show that all five metals have the potential for NEA. Various monolayer (ML) coverages of metal were investigated, from quarter monolayer (QML, 1 metal atom per 4 O atoms) to full monolayer (FML, 1 metal atom per O atom). The most stable surface with the lowest EA was the Ti QML scenario, with an NEA of -3.1 to -3.6 eV. Only the vanadium and titanium oxide surfaces were calculated to be more stable than the H termination.<sup>90,111,112</sup> It should be noted that this was also the case for the metal-diamond surfaces discussed above in section 1.5.4.

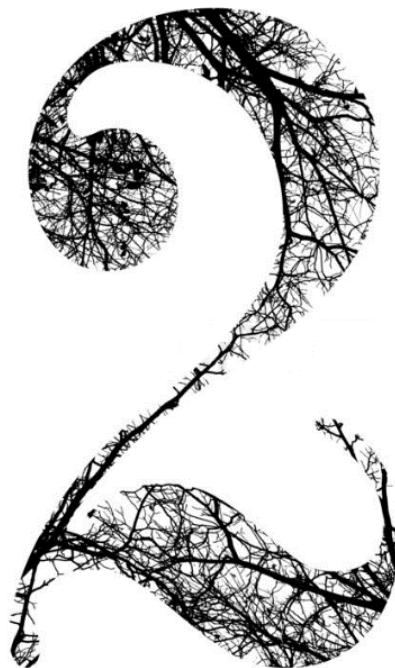
Several experimental studies on cobalt, copper, and zirconium determined that both cobalt and copper reduce the electron affinities of O-terminated (100) surfaces, but not sufficiently to yield an NEA. Zirconium, on the other hand, was found to produce an NEA of undetermined magnitude. No measurements of surface stability at elevated temperatures were performed in these studies.<sup>91,113,114</sup>

Though not a transition metal, silicon-oxide-terminated diamond was found to exhibit an NEA of -0.3 eV.<sup>97</sup> Similarly, the aluminium-oxide termination was calculated to have an NEA of -1.4 eV.<sup>89</sup>

### 1.5.7 Termination Summary

Following CVD diamond growth, the surface is typically H-terminated, and exhibits an NEA. Despite the chemical inertness of diamond, the surface can be modified with a wide range of elements using a variety of techniques. Single element terminations range from halides, through non-metals such as oxygen, nitrogen, silicon, and sulphur, to transition metals and group one and two metals. Most of these surfaces either exhibit positive electron affinities or suffer from lack of stability at elevated temperatures. In response to this, metal-oxide terminations have gathered significant interest. Trends from several studies suggest that smaller carbide-forming metals are prime candidates for NEA surfaces that are stable at elevated temperatures. As titanium is amongst the smallest carbide-forming metals, with a low theoretical NEA, it has been selected as the focus of this work to investigate the electronic properties and stability of the TiO-terminated diamond surface at elevated temperatures.

## CHAPTER



# Computational Modelling

“The underlying physical laws necessary for the mathematical theory of a large part of physics and the whole of chemistry are thus **completely known**, and the difficulty is only that the exact application of these laws leads to equations much **too complicated to be soluble**. It therefore becomes desirable that **approximate** practical methods of applying quantum mechanics should be developed, which can lead to an explanation of the main features of complex atomic systems without too much computation.”

Paul Dirac - Proceedings of the Royal Society of London. Series A, Containing Papers of a Mathematical and Physical Character, Vol. 123, No. 792 (6 April 1929)

## 2.1 Theoretical Background

The main goal of electronic structure calculations is to determine the ground-state energy of electrons in molecules. From this, a wide variety of properties can be determined, such as adsorption energies, bond lengths, or the band structure. Empirical models built from experimental data can be used to predict various properties accurately. However, in practice, modern systems of interest are too complex, and experiments to determine the necessary parameters would be too numerous and time consuming. Thus, there is extensive interest in *ab initio* (from first principles) electronic structure calculations which use only physical constants, i.e. the positions of the nuclei and number of electrons.

Quantum Mechanics was developed during the early part of the twentieth century as a result of the shortcomings of classical mechanics. As this predates the modern computer, the fact that so many of the methods used today are based on the works of those early pioneers is extraordinary. With over 80 years of experience, it is reasonable to say that quantum mechanics has been very successful in describing the behaviour of matter on an atomic scale. One of the most well-known and fundamental equations is the Schrödinger equation, more specifically the time-independent nonrelativistic Schrödinger equation:

$$\left[ -\frac{\hbar^2}{2m} \left( \frac{\partial^2}{\partial x^2} + \frac{\partial^2}{\partial y^2} + \frac{\partial^2}{\partial z^2} \right) + V \right] \Psi(r) = E\Psi(r)$$

Equation 1.1

where  $\hbar$  is the Planck constant divided by  $2\pi$  (also known as the Dirac constant),  $m$  is the mass,  $x, y$  and  $z$  are the cartesian coordinates,  $V$  is the potential energy (in the absence of an external field, this depends only on the charges and positions of all the nuclei),  $\Psi$  is the wavefunction,  $r$  is the position vector, and  $E$  is the energy of the particles. The left-hand side is usually abbreviated to  $\hat{H}\Psi$  where  $\hat{H}$  is the Hamiltonian operator. To solve the Schrödinger equation, values of  $E$  and  $\Psi$  need to be determined such that when the wavefunction is operated upon by the Hamiltonian operator, it returns the original wavefunction multiplied by its energy. The wavefunction is a function of the position coordinates of the particle, the time, and some quantum

variables that determine the particle's spin. The wavefunction is the goal when solving the Schrödinger equation because it contains the complete information about a system, much as position and momentum do in classical mechanics. However, the wavefunction itself is not observable. Rather, the square of the wavefunction provides a probability density, i.e. the probability of finding an electron in a particular location. The Schrödinger equation is so complex however, that it is not actually solvable except for the simplest of cases. The difficulty lies in the fact that not only does each particle have 3 degrees of freedom, but all the particles interact with each other. Consequently, the many-electron wavefunction has to be solved simultaneously for all particles<sup>v</sup>. This is similar to the  $n$ -body problem which concerns the orbits of celestial objects and how they are influenced by each other's gravity to yield complex orbits.

Because the Schrödinger equation is usually too complicated to be solved, assumptions and approximations must be made to enable the equation to be solved numerically.

### 2.1.1 Born-Oppenheimer Approximation

The Born-Oppenheimer approximation states that the wavefunctions of the electrons and the nuclei can be separated. This is because of the difference in nuclear and electron masses; even the lightest nuclei, a proton, is  $\sim 1800$  times heavier than an electron. For a more typical atom such as C, this mass ratio exceeds 20,000. Because the electron is significantly lighter, it responds considerably faster to external stimuli, such that the nucleus can be treated as stationary on an electronic timescale. Therefore, the wavefunction can be split into an electron wavefunction and nuclear wavefunction that can be computed independently.

### 2.1.2 Hartree-Fock Approximation

The Hartree-Fock (HF) approach approximates the multi-electron wavefunction as a linear combination of an antisymmetrized product of one-electron wavefunctions. The

---

<sup>v</sup> For a relatively simple molecule such as Benzene ( $C_6H_6$ ), which consists of 12 nuclei (6 carbon and 6 hydrogen) and 42 electrons (1 from each hydrogen and 6 from each carbon), this results in  $(12 + 42) \times 3 = 162$  variables which need to be solved simultaneously. This is not currently possible.

one-electron wavefunctions are known as atomic spin orbitals and the product is referred to as the Slater determinant. The wavefunction of one electron depends on the electric fields produced by all the other atoms. Therefore, if the wavefunctions of all but one electron are known, the wavefunction of the last electron can be calculated precisely. To solve this problem, an initial guess of the wavefunctions of the electrons is made. The wavefunctions of all but one electron are then averaged, and hence the wavefunction of the last electron, i.e. how it moves in the average electric field generated by the others, can be calculated. This wavefunction is then added to the average wavefunction of all the electrons, and another electron is chosen to repeat the process. This continues until the multi-electron wavefunction obtained is the same as in the previous step, within some tolerance, i.e. the solution is self-consistent.

### 2.1.3 Density Functional Theory (DFT)

In this context, a functional is a function of a function, also known as a higher-order function. In DFT, the functional is the electron density, which is a function of time and space. The electron density is the fundamental property in DFT, unlike HF theory which deals directly with the multi-electron wavefunction. The electron density, i.e. the probability of an electron occupying a certain point in space, depends only on three variables ( $x$ ,  $y$ , and  $z$ ) rather than the  $3N$  variables (the coordinates of  $N$  particles in the system) needed for HF. This results in easier scaling and DFT being significantly faster than HF methods.

Modern DFT was born in 1964 when Hohenberg and Kohn published their landmark paper in the *Physical Review*.<sup>115</sup> According to the Hohenberg-Kohn theorems, the external potential is a unique functional of the electron density in the ground state, and therefore the total energy is also a functional of the ground-state electron density. Consequently, all properties of a system can be determined from only the ground-state electron density. Furthermore, unlike the wavefunction, the electron density is observable and can be measured experimentally.

Simple and powerful though the theorems are, they do not provide a method of constructing the functionals or of calculating the ground state density. In particular, the functionals for the kinetic energy and the electron-electron interactions are not known.

### 2.1.3.1 The Kohn-Sham Approach

A paper published by Kohn and Sham in 1965 forms the second pillar of modern DFT.<sup>116</sup> Instead of trying to compute the energy of the interacting electrons as a functional of the density, they proposed to instead utilise a system of non-interacting electrons. Typically, the wavefunction, and hence the electron density, of non-interacting electrons, is different to that of the interacting electrons. In the Kohn-Sham approach, however, a fictitious system of non-interacting electrons is constructed in such a way as to have the same density as that of the interacting electrons. This significantly simplifies the problem because the expression for the kinetic energy of non-interacting electrons is known, and hence does not need to be approximated. This changes the challenge from determining the Hohenberg-Kohn functional to finding the fictitious system of non-interacting electrons which has the same electron density as the 'real' system and leaves only the electron-electron interactions to be approximated.

### 2.1.3.2 Correlation Interaction

As electrons all have negative charges, an electron experiences the electrostatic repulsion of nearby electrons, preventing them from coming too close to each other. This is known as the correlation interaction, electron correlation, or Coulomb correlation, and is independent of the spin of the electrons. Because the HF method uses an average electric field to calculate the one-electron wavefunction, this electron correlation is not accounted for in classical HF. There are, however, a variety of post-HF methods that incorporate this interaction, using HF as the starting point.

### 2.1.3.3 Exchange Interaction

As a consequence of the Pauli exclusion principle, which states that two identical Fermions cannot occupy the same quantum state, if two electrons have parallel spin, they cannot occupy the same space at the same time. This phenomenon gives rise to an effective repulsion between electrons with parallel spin. Therefore, electrons with parallel spins do not move independently of each other. This is known as the exchange interaction, or Fermi correlation.

### 2.1.4 Exchange-Correlation Energy (XC) Functionals

The electron-electron interactions are combined into a single entity called the exchange-correlation energy (XC) functional. When one discusses the ‘failings of DFT’, it is actually the failings of the approximations used that is in question, as DFT is, in principle, exact. Except in very simple cases (e.g. uniform electron gas, UEG) however, it is not known what the XC functional looks like, and even if it were known, it would probably be too complicated to be of practical use. Hence, it is not possible to treat the electron-electron interactions exactly and approximations are necessary. The level of theory chosen for this is one of the largest factors in both the computational expense and accuracy of the calculation. Higher levels of theory may give better results but will take significantly longer to perform the more complex calculations.

#### 2.1.4.1 Local and Semi-local Approximations

The oldest and one of the simplest (and most popular) XC functionals, the linear density approximation (LDA, sometimes referred to as local spin-density approximation, LSDA), assumes a simple linear functional of the density. It is based on the UEG (also known as jellium) which is an ideal model where interacting electrons and positive charges are uniformly distributed in a solid, and hence the electron density is also a uniform quantity. The XC is linearly decomposed into exchange and correlation terms which are solved separately. The exchange term is then relatively simple as this is well known for the UEG, leaving only the correlation term to be approximated. Because LDA assumes that the electron density is the same everywhere, it has a tendency to overestimate the correlation interaction while underestimating the exchange interaction.

The next rung on ‘Jacob’s ladder’<sup>vi</sup> is the generalised gradient approximation (GGA), which is a step up from the LDA. It depends not only on the value of the electron density at a particular point (as in LDA), but also on its first derivative (the gradient). This allows

---

<sup>vi</sup> ‘Jacob’s ladder’ is a theoretical construct used to describe the various levels of theory employed by different XC functionals. Each level up represents an increase in the complexity of the functional, and commonly an increase in chemical accuracy. It was introduced by Perdew in 2001 and is named after the ladder to heaven allegedly encountered by Jacob in the Bible (Genesis 28:10-19).<sup>155</sup>

for corrections due to the inhomogeneity of real systems as opposed to the UEG. Most GGA functionals are constructed from the LDA functional with an additional correction term. There are numerous functionals of this type available, either containing some empirically determined parameters (e.g. BLYP [composed of the Becke88 exchange and the Lee-Yang-Parr correlation]), or not (e.g. PBE [Perdew–Burke–Ernzerhof]). These functionals are sometimes jokingly referred to as either chemists (empirical) or physicists (non-empirical) functionals. Good non-empirical functionals are, perhaps, not the most accurate but are universal in that they will give reasonable results for most systems. Empirical functionals, on the other hand, tend to be more accurate within the systems and properties that they were designed for.

Meta-GGA functionals are another step further and additionally depend on the second derivative (the kinetic energy density). With this additional information (resulting from the extra computational cost involved), these functionals are typically more accurate. They attempt to perform almost as well as hybrid functionals, without the high computational cost. Kurth *et al.* provide good overview of LDA, GGA and meta-GGA functionals.<sup>117</sup>

#### 2.1.4.2 Hybrid Functionals

Difficulties in accurately expressing the exchange interaction for local (LDA) and semi-local functionals (GGA) can be alleviated by incorporating a fraction of the exact exchange energy calculated from HF theory, as shown below:

$$E_{xc} = \alpha E_x^{HF} + (1 - \alpha) E_x^{local} + E_c^{local}$$

Equation 2-1

where  $\alpha$  is the mixing parameter, typically 0.15 – 0.25,  $E_x^{HF}$  is the exact Hartree-Fock exchange,  $E_x^{local}$  is the DFT exchange from LDA, GGA, or meta-GGA functionals, and  $E_c^{local}$  is the DFT correlation. The value of  $\alpha$ , i.e. how much HF exchange is incorporated, is an important parameter for the various functionals available. This mixing of the HF and DFT exchange correlation is useful because, although HF fails to account for the correlation interaction, it calculates the exchange energy exactly, not approximately. These type of functionals are known as hybrid functionals. Naturally, as these functionals use both DFT and HF, they are amongst the most computationally

expensive, because the HF exchange is non-local, depending not only on the density but also on the density matrix functionals. This is especially true for larger molecules and periodic systems because HF does not scale as well as DFT. The first successful, and one of the most commonly used, functional of this type was introduced by Becke in 1993 with his semi-empirical three-parameter exchange combined with the Lee-Yang-Parr correlation to create the B3LYP functional. PBE0 is a non-empirical hybrid functional based on the GGA functional PBE, with  $\alpha = 0.25$ .

Calculating the exact Hartree-Fock exchange is quite computationally expensive, as discussed previously. The HSE (Heyd-Scuseria-Ernzerhof) suite of functionals<sup>118</sup> use a screened Coulomb potential to control the extent of the short-range exchange leading to increased computational efficiency, especially for larger systems:

$$E_{xc}^{HSE} = \alpha E_x^{HF,SR}(\omega) + (1 - \alpha) E_x^{PBE,SR}(\omega) + E_x^{PBE,LR}(\omega) + E_c^{PBE}$$

Equation 2-2

where  $\alpha$  is the mixing parameter,  $\omega$  is an adjustable parameter that controls the extent of short-range interaction,  $E_x^{HF,SR}$  is the short-range HF exchange,  $E_x^{PBE,SR}$  and  $E_x^{PBE,LR}$  are the short- and long-range PBE exchange respectively, and  $E_c^{PBE}$  is the PBE correlation. When  $\omega = 0$ , the long-range term becomes zero, and the functional degenerates into the PBE0 functional, as shown in Equation 2-1, while the inverse is true for  $\omega \rightarrow \infty$ , and the functional asymptotically reaches PBE. The HSE06 functional ( $\alpha = 0.25$  and  $\omega = 0.2$ ) has been shown to yield excellent results, particularly for the electronic properties of periodic metal and semiconductor systems, such as those of interest in this work.<sup>119-122</sup>

It should be noted that using a higher level of theory does not necessarily yield better results. Different functionals are optimised for different systems and properties, and hence may yield unsatisfactory results if used outside of those regimes. Therefore, the literature should be consulted to determine the optimal functional to be used. Furthermore, consideration should be given to which functional is 'good enough' i.e. which functional delivers reasonable results with minimal computational cost.

### 2.1.5 Basis Sets

In a well-thought-out calculation, the largest error should originate from the choice of XC functional, but this is of course not the only approximation used. As discussed previously, the wavefunction of a single non-interacting electron is an atomic orbital, and these are known. However, atomic orbitals are, in principle, infinite, and hence approximations are once again necessary to allow efficient computation. A basis set is a set of functions (basis functions) used to represent the atomic orbitals in order to convert the partial differential equations of the DFT model into algebraic equations that can be solved. The best physical representations are Slater-type orbitals (STO), but they are computationally difficult to implement. Instead, Gaussian-type orbitals (GTO) can be used to mimic STOs. A single gaussian is a poor fit for an STO, but multiple gaussian functions are a closer match, and much easier to implement.

Basis sets are characterised by the number of GTOs per atomic orbital, where minimal basis sets have one, double-zeta sets have two, triple-zeta have three, etc. Furthermore, basis sets may include polarization. As atoms approach each other, the atomic orbitals may shift to one side of the atom (polarization) to create an instantaneous dipole. To polarise a basis function with angular momentum  $l$ , it is mixed with a basis function of angular momentum  $l + 1$ , e.g. an s-orbital can be polarizable if it is mixed with a p-orbital. Typically, the bigger the basis set (more functions) the better result it will yield, though there is little benefit above triple-zeta basis sets to justify the additional computational expense.

## 2.2 Experimental Details

The *ab initio* quantum-mechanical simulations in this work were primarily performed using the CRYSTAL17 package to calculate the ground-state energies, electronic wavefunctions, and properties of some periodic systems. The fundamental approximation made is the expansion of the single-particle wavefunctions as a linear combination of Bloch functions defined in terms of local functions. In turn, the local functions are linear combinations of Gaussian-type functions whose exponents and coefficients are defined by input.<sup>123</sup>

Being a Gaussian basis-set code, as opposed to a planewave code, CRYSTAL17 is ideally suited for using hybrid DFT and HF exchange-correlation functionals. The HSE06 exchange-correlation functional and the pop-TZVP-rev2 basis sets were used.<sup>124-126</sup>

All surface calculations were performed on a symmetrical 12-atom-thick slab, with a surface on either side. A 2×2 supercell was used to yield 4 C atoms on the surface, thereby enabling variations in the coverage of Ti from quarter-, to half-, to full monolayer coverage by including one, two, or four Ti atoms, respectively. All surfaces (Ti, O, N, etc.) were created by adding the relevant atoms to the clean, non-reconstructed, 48-atom diamond slab. Several parameters including slab thickness, energy tolerances, and size of the *k*-point grid were converged prior to other calculations being performed.

### 2.2.1 Geometry Optimization

The first calculation to be performed is a geometry optimisation, sometimes called energy minimisation. In this process, the approximate structure created by the user is optimised to be closer to the ‘true’ structure. This iterative process moves the atoms in the system to find the ‘ideal’ lowest-energy state where the net inter-atomic force on each atom is below a certain tolerance. For example, if the user was unfamiliar with the geometric properties of a water molecule (H<sub>2</sub>O) and thus assumed a linear (180°) molecule with bond lengths of 100 pm, the resulting O-H bonds would be quite strained; any property calculation performed on this molecule would yield results which deviate significantly from actual water molecules. The geometry optimisation of this

molecule would move the H atoms until they were close to their ideal bond length (95.84 pm) and angle (104.5°).<sup>127</sup> In many systems, such as those of interest here, it is necessary to optimise the lattice parameter and the atomic positions separately. The optimised theoretical lattice parameter differs from the experimental lattice parameter. Therefore, if the experimental lattice parameter was used for the calculations, the lattice would be strained, and the calculated properties would not correspond to a relaxed and ground-state crystal structure. The lattice parameter is first optimised using bulk diamond, and is then kept constant for the slab calculations, while allowing the atoms to move.

### 2.2.2 Adsorption Energy

While adsorption energies are typically calculated in relation to the lowest-energy surface, which for O-terminated non-reconstructed (100) diamond is the ether-like O-terminated surface, in this work the adsorption energies are calculated relative to the clean (unterminated, non-reconstructed) diamond surface to enable a comparison between the various terminations. The adsorption energies ( $\gamma$ ) are calculated according to the following equation:

$$\gamma = \frac{E_T - E_0 - (N_A \times E_{iso,A} + N_B \times E_{iso,B})}{N_T}$$

Equation 2-3

where  $E_T$  is the total energy of the slab,  $E_0$  is the energy of the clean diamond surface,  $N_A$  and  $N_B$  are the number of adsorbate atoms of element A and B respectively, while  $E_{iso,A}$  and  $E_{iso,B}$  are the energies of an isolated adsorbate atom of element A and B respectively, and  $N_T$  is the total number of adsorbate atoms. As the computed values for  $E_T$ ,  $E_0$  and  $E_{iso}$  are negative, convention states that exothermic adsorption energies are negative.

### 2.2.3 Electron Affinity

The EA ( $\chi$ ) is calculated according to the following equations:

$$\chi = I - E_g$$

Equation 2-4

$$I = (V_{vac} - V_{av,slab}) - (V_{VBM,bulk} - V_{av,bulk})$$

Equation 2-5

where  $I$  is the ionisation energy and  $E_g$  is the computational band gap.  $(V_{vac} - V_{av,slab})$  is the energy difference between the vacuum potential and the average potential in the middle of the slab where the diamond is 'bulk-like', which can be obtained by performing an electrostatic potential calculation on the slab, as shown in Figure 2-1.  $(V_{VBM,bulk} - V_{av,bulk})$  is the energy separation between the average electrostatic potential energy in the bulk and the bulk valence-band maximum, which can be obtained by performing a band structure calculation on bulk diamond. By convention, the sign for the ionisation energy is positive.

While this was initially attempted using the CRYSTAL17 code, due to technical difficulties these calculations were instead performed using the Cambridge Serial Total

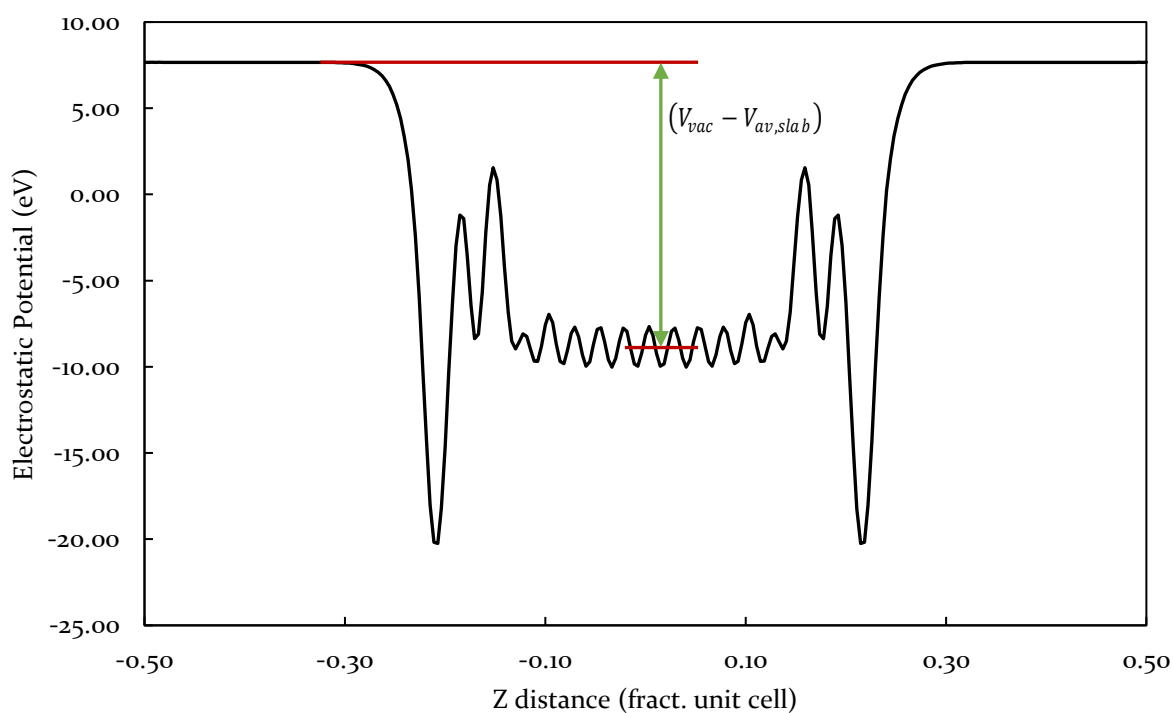


Figure 2-1 – An example of an electrostatic potential graph along the z-axis of the slab. The x-axis shows the distance in fraction of unit cell with the unit cell being centred upon the middle of the slab. The green arrow illustrates how  $(V_{vac} - V_{av,slab})$  is calculated.

Energy Package (CASTEP). CASTEP uses planewave basis sets rather than the Gaussian basis sets used by CRYSTAL17. Due to the extreme computational cost of hybridising planewaves, planewave codes such as CASTEP are not ideally suited for the hybrid functionals necessary for this work. Performing this calculation with a pure DFT exchange-correlation functional will have a significant impact on the accuracy of the EA calculation. However, as the purpose of this work was to compare trends in the systems analysed, rather than absolute values, any offset should affect all systems equally and could therefore be disregarded.

Due to the nature of EA, and an NEA being preferential here and in similar work, care must be taken when discussing the magnitude of the EA. In some publications, when discussing NEA, one system may be referred to as having a greater (meaning more negative) NEA than another. To avoid such confusion, in this work positive and negative electron affinities are compared and discussed in terms of being higher or lower than each other, with lower being more desirable.

## 2.3 Results

A wide variety of diamond (100) surfaces were investigated, split into three categories. Firstly, the O-terminated surfaces, both ether- and ketone-like, as well as surfaces derived from these, primarily TiO with differing degrees of Ti coverage. Secondly, the N-terminated surfaces, and surfaces derived therefrom, primarily TiN but also including  $\text{NH}_x$ -terminated surfaces. And finally, TiC surfaces, as well as the clean (100) diamond surface and the H-terminated surface.

A description of each system investigated can be found in the relevant table, followed by a visual representation in subsequent figures. One important thing to note is that the description in the tables describes how the system was constructed prior to geometry optimisation while the visuals are of the optimised systems. The two rarely differ significantly, except in the matter of the  $2 \times 1$  surface reconstruction.

All the systems were constructed on a non-reconstructed (100) diamond surface, as shown in Figure 2-2. The ML coverage refers to the quantity of Ti in relation to the unit cell. The unit cells used were 12-atom-thick  $2 \times 2$  slabs, resulting in four surface C atoms at each end of the slab. Therefore, four atoms of Ti equate to a full monolayer (FML),

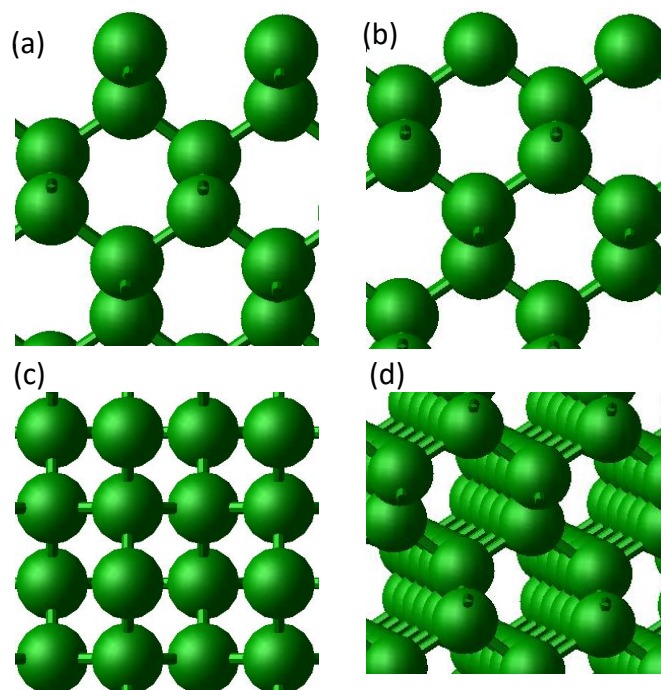


Figure 2-2 – (a) Side view of the non-reconstructed (100) diamond surface, (b) the same surface, rotated  $90^\circ$  about the z-axis, (c) the top-down view of the same surface, and (d) an angled view of the bulk diamond structure.

two atoms a half monolayer (HML), and a single atom a quarter monolayer (QML) coverage.

### 2.3.1 Titanium Carbide

The various titanium carbide (TiC) surfaces investigated are summarised in Table 2-1, along with the H-terminated and clean (100) diamond surface. The primary intention was to vary the coverage of Ti, from QML to FML.

In the case of QML, there is only one position where the Ti atom can be, between the four surface C atoms. For the HML and FML surfaces however, there are multiple positions where the Ti atoms may reside. The Ti atom can either be between two C atoms, effectively bridging them, such as (d) or (g), or directly above a C atom such as scenario (e) or (h). It should be noted that scenario (e), while initially each of the two Ti atoms are above one C atom, the optimised structure, as shown in Figure 2-3, actually shows the Ti atoms bridging two C atoms, as in scenario (d). This is to be expected, as each C atom can only form two bonds, while Ti prefers to have four bonds. Two interesting differences between the optimised structures of (d) and (e) are that the Ti atoms in (e) are not in a row, but rather alternate to form a zigzag pattern across the surface. Furthermore, in scenario (d), the surface carbons underneath the Ti atoms reconstructed while those in scenario (e) did not. The fact that (e) did not reconstruct may be due to the alternating nature of the Ti atoms, because it is energetically more favourable to have the reconstructed bonds in a row, as shown in Figure 2-4.<sup>128</sup> As such,

	Description	Name	ML Coverage	$\gamma$ (J m <sup>-2</sup> N <sup>-1</sup> )	EA (eV)
(a)	H-terminated	C-H	-	-1.9	-1.6
(b)	Clean diamond surface	Clean	-	-	1
(c)	One Ti atom bonded to four C atoms	C-Ti1	QML	-3.1	-0.7
(d)	Two Ti atoms bridging two C atoms each	C-Ti2br	HML	-2.5	-1.6
(e)	Two Ti atoms on top of one C atom each	C-Ti2t	HML	-2.2	-0.4
(f)	Two Ti atoms bonded to four C atoms each	C-Ti2b4	HML	-3.0	0.8
(g)	Four Ti atoms bridging two C atoms each	C-Ti4br	FML	-2.5	0.0
(h)	Four Ti atoms on top of one C atom each	C-Ti4t	FML	-2.3	-0.1

Table 2-1 – The computed surface energy and EA of the various clean, H-, and Ti-terminated (100) diamond surfaces investigated. Column 2 describes the initial state of each system before structure optimisation while the (a) – (h) in column 1 refer to the optimised structures displayed in Figure 2-3.

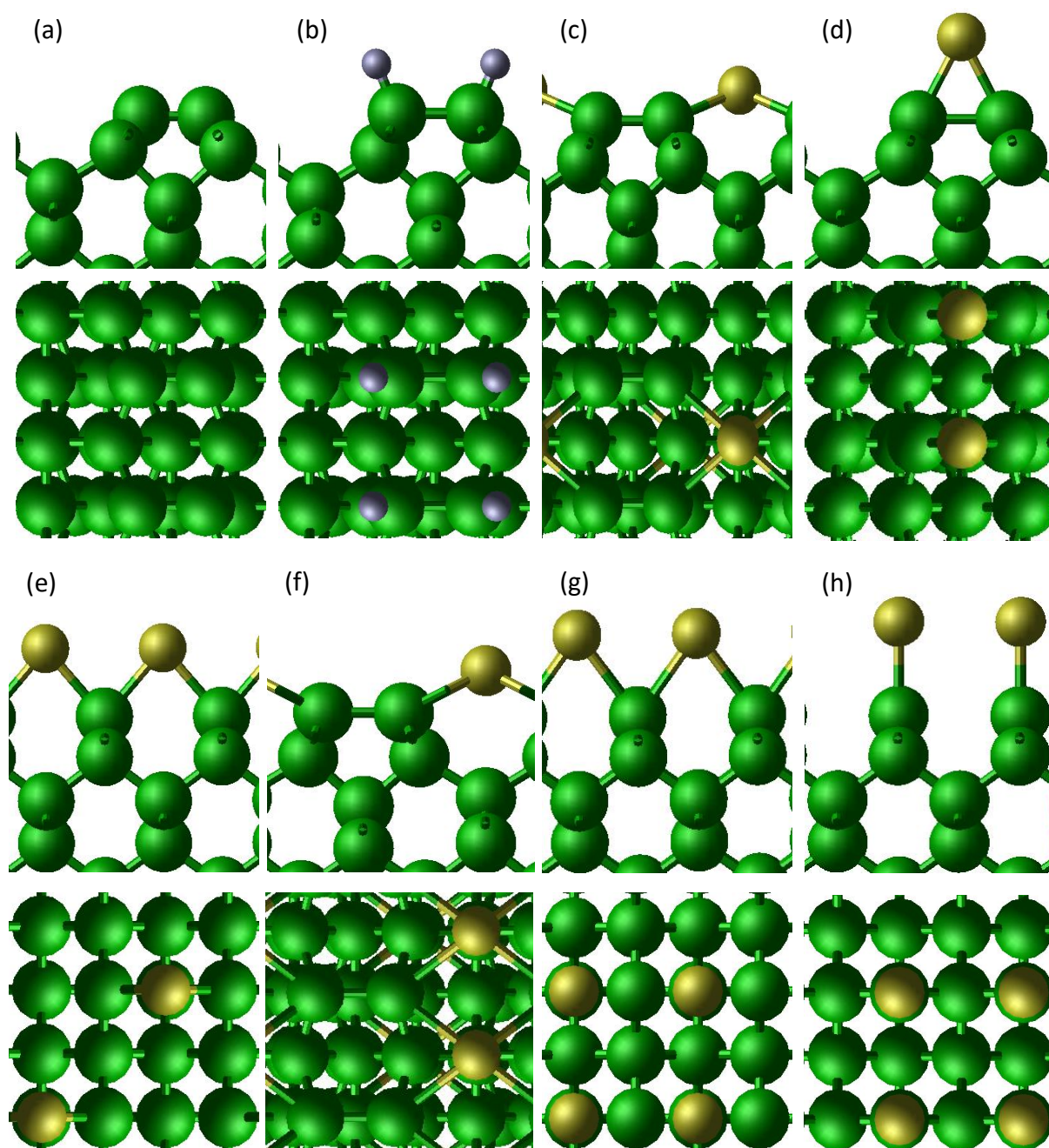


Figure 2-3 – The optimised structures of the various clean, H-, and Ti-terminated diamond (100) surfaces investigated. (a) – (h) are sample identifiers corresponding to Table 2-1. Each structure is displayed as a side view followed by a top-down view. Green are the C atoms, yellow are the Ti atoms and grey are H atoms.

if the C atoms in scenario (e) had reconstructed, this would have resulted in the high energy alternating structure. As scenario (d) is reconstructed, while (e) is not, (d) is lower in energy as seen in Table 2-1.

In the bulk of an ideal crystal (no defects), the position of each atom depends only on the forces exerted by the surrounding atoms. As the forces on all atoms are the same, the crystal can easily be represented by a small unit cell repeated infinitely in all directions. However, if a surface is introduced, those atoms at the surface do not experience the same force from every direction. Furthermore, the atoms at the surface will have fewer bonds. In the case of the diamond (100) surface, each atom is only bonded to two other C atoms underneath. The resulting dangling bonds, as shown in Figure 2-5, are energetically unfavourable. As a consequence, the surface C atoms reconstruct so that some of them are closer together and can therefore bond with each other. This can be seen in scenario (a), which began as a non-reconstructed surface, as shown in Figure 2-2, but reconstructed during the geometry optimisation. Whilst a single dangling bond per C atom remains, this is preferential to the initial state. This dangling bond being energetically unfavourable is reflected by all the surfaces investigated in this work having a lower adsorption energy than the clean surface in

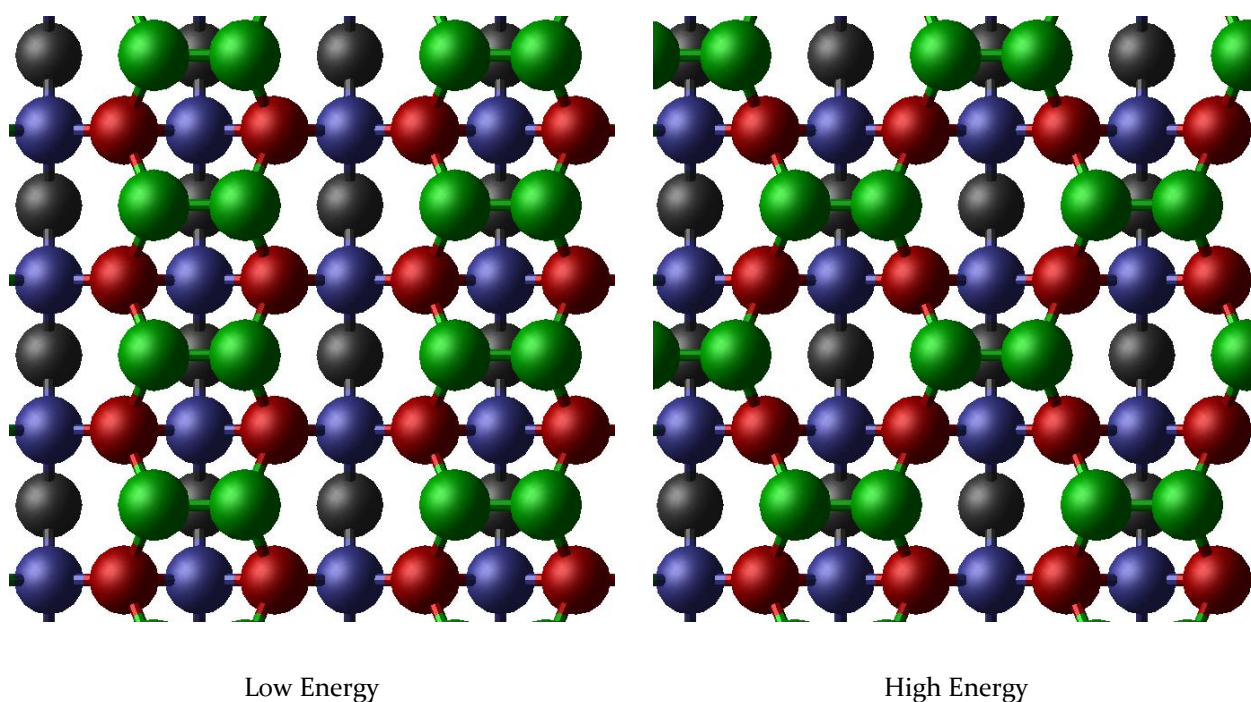


Figure 2-4 – Two 2x1 reconstructed (100) diamond surfaces. The different layers are colour coded to aid in visualization. Green is the top most layer, red is the second from the top layer, blue is the third, and black is the fourth layer.

scenario (a). This can be seen from the penultimate column in Table 2-1, Table 2-2, and Table 2-3, where all the adsorption energies relative to the clean diamond surface are negative. This  $2 \times 1$  surface reconstruction of the C atoms can be seen in several scenarios [(a) – (d) and (f)].

One particularly interesting result is that out of the three reconstructed scenarios featuring Ti, the reconstructed bond is underneath the Ti for one of them, scenario (d), while scenarios (c) and (f) feature the reconstructed bond between the Ti atoms. As a consequence, the Ti atoms in scenario (c) and (f) are closer to the surface than in scenario (d), or any of the other TiC-terminated surfaces. The more a Ti atom ‘sticks out’ above the surface, the more likely it is to be impacted upon by another particle, and hence desorb. This is reflected in the fact that these two scenarios, (f) and (c), where the Ti atoms are almost in line with the topmost C layer, are significantly more stable than the other surfaces. The three non-reconstructed TiC surfaces [(e), (g), and (h)], where the atoms are similarly ‘sticking out’, are amongst the least stable TiC surfaces. The reconstructed bond in scenario (d) being underneath the Ti atom, rather than between the Ti atoms, coupled with the decrease in stability, indicates that this structure is perhaps only a local minimum as opposed to the true minimum.

Scenario (b) is the H-terminated diamond surface that was discussed in Chapter 1 as being a common surface termination used in the thermionic energy converters, upon

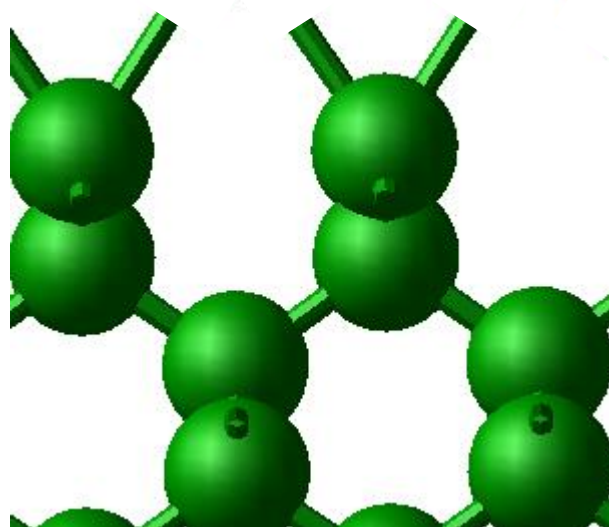


Figure 2-5 – An ideal (100) diamond surface showing the two dangling bonds.

which we are aiming to improve. The calculated EA of -1.6 eV is close to the literature values discussed in section 1.5.1. All the TiC scenarios are more stable than the H-terminated surface. This is most likely because the titanium carbide bond is much stronger than the C-H bond.<sup>129</sup>

Out of the three HML surfaces, scenario (f) is the most stable with an adsorption energy of  $-3.0 \text{ J m}^{-2} \text{ N}^{-1}$ , most likely due to each Ti atom being bonded to four C atoms, rather than two C atoms as in the other two HML scenarios. However, it also exhibits the highest EA of all the TiC surfaces investigated. Scenario (c), the QML surface, is the only surface exhibiting greater stability, with a surface energy of  $-3.1 \text{ J m}^{-2} \text{ N}^{-1}$ . The structure of this surface is almost identical to scenario (f), where each Ti atom is bonded to four C atoms, which most likely accounts for their similar surface stability.

Though scenario (c) is the most stable of the TiC-terminated diamond surfaces, it only has the second-lowest EA. The EA, while being higher than that of the H-terminated surface, is still negative at -0.7 eV, which, combined with the high stability, makes this a promising surface for further study. The lowest EA is exhibited by scenario (d), equalling that of the H-terminated surface at -1.6 eV. Whilst not the most stable of the TiC surfaces, it exhibits greater stability than the H-terminated surface and is therefore also a promising candidate for further study.

### 2.3.2 Oxygen and TiO

The various O- and TiO-terminated surfaces investigated in this work are summarised in Table 2-2. They can broadly be divided into two categories, ether-like O-terminated diamond [(a) – (e)] and ketone-like O-terminated diamond [(f) – (k)], and surfaces derived therefrom. For both of these types of surfaces, the Ti coverage was varied from QML, through HML, to FML. In both instances there are two variations of the HML coverage.

Looking at the trends in adsorption energy between the ether- and ketone-like surfaces, it can be seen that the clean ether-like O-terminated surface is more stable than the ketone-like O surface, which agrees with literature (section 1.5.2). For the TiO surfaces however, the opposite is true, where those surfaces built upon ketone-like O-terminated diamond are lower in energy. Furthermore, it should be noted that in most cases, the TiO-terminated surface is more stable than the related O-terminated surface. This is because upon addition of Ti onto these surfaces, while the ether-like O atoms need to break one of the C-O bonds in order to bond with the Ti, the ketone-like surfaces merely reduces the C=O bond to a C-O bond. This can, to some extent, be seen in the optimised structures presented in Figure 2-6 and Figure 2-7, in particular by comparing scenarios (b) and (g), which both contain one Ti atom bonded to four O atoms. In scenario (b), the two O atoms to the left of the Ti have broken one of their bonds while

	Description	Name	ML Coverage	$\gamma$ (J m <sup>-2</sup> N <sup>-1</sup> )	EA (eV)
(a)	Ether-like O	Oe	-	-2.1	3.0
(b)	One Ti atom bonded to four ether-like O atoms	Oe-Ti1	QML	-2.3	-0.9
(c)	Two Ti atoms bridging two ether-like O atoms each	Oe-Ti2br	HML	-2.3	-0.3
(d)	Two Ti atoms on top of one ether-like O atoms each	Oe-Ti2t	HML	-2.1	1.3
(e)	Four Ti atoms on top of one ether-like O atoms each	Oe-Ti4	FML	-2.0	4.1
(f)	Ketone-like O	Ok	-	-1.9	3.7
(g)	One Ti bonded to four ketone-like O atoms	Ok-Ti1	QML	-2.5	-2.9
(h)	Two Ti atoms bridging two ketone-like O atoms each	Ok-Ti2br	HML	-2.4	-0.1
(i)	Two Ti atoms on top of one ketone-like O atoms each	Ok-Ti2t	HML	-2.3	1.4
(k)	Four Ti atoms on top of one ketone-like O atoms each	Ok-Ti4	FML	-2.3	1.1

Table 2-2 – The computed surface energy and EA of the various O- and TiO-terminated (100) diamond surfaces investigated. Column 2 describes the initial state of each system before structure optimisation while the (a) – (h) in column 1 refer to the optimised structures displayed in Figure 2-6 and Figure 2-7.

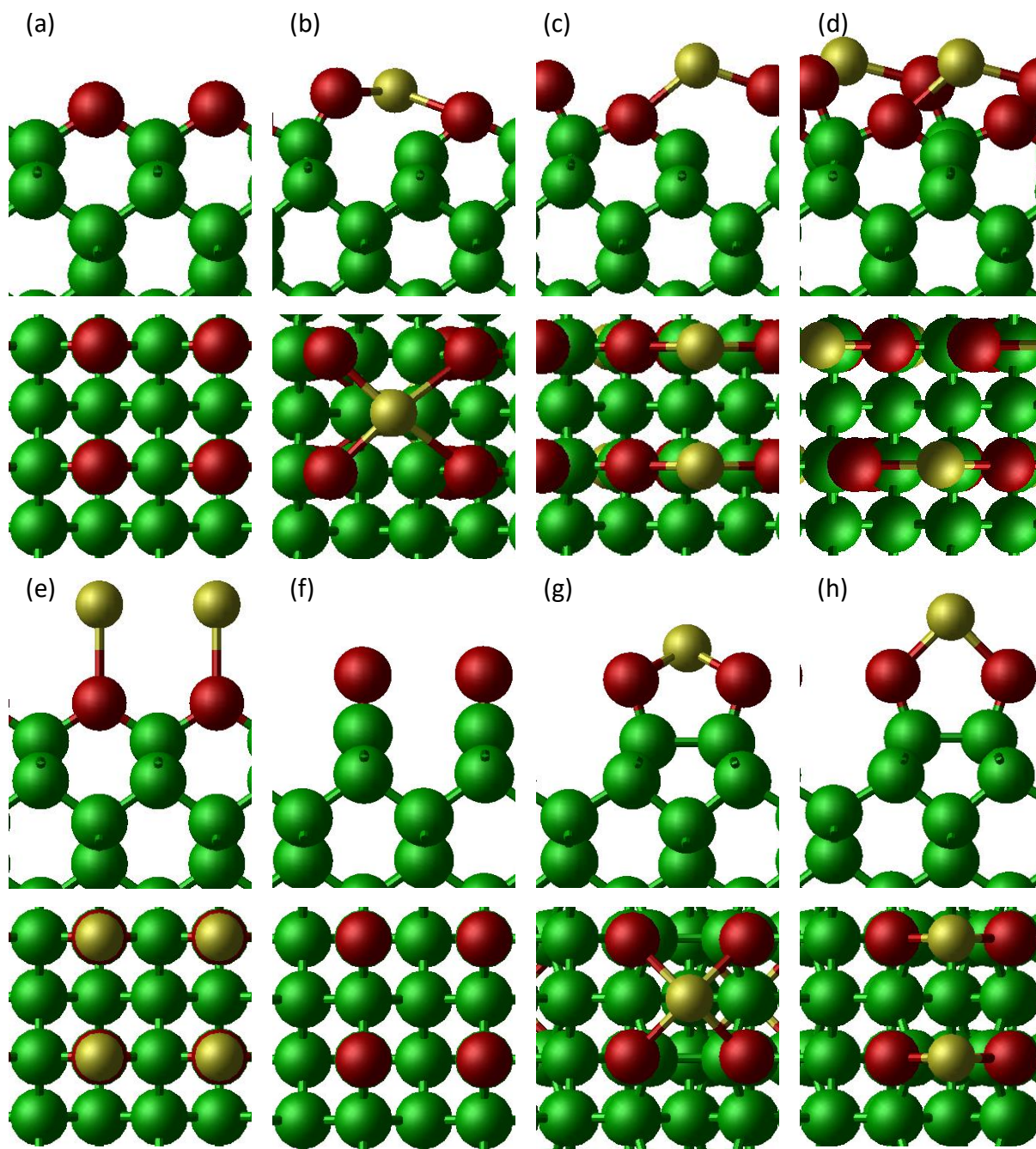


Figure 2-6 – The optimised structures of the various O- and TiO-terminated diamond (100) surfaces investigated. (a) – (h) are sample identifiers corresponding to Table 2-2. Each structure is displayed as a side view followed by a top-down view. Green are the C atoms, red are O atoms, and yellow are the Ti atoms.

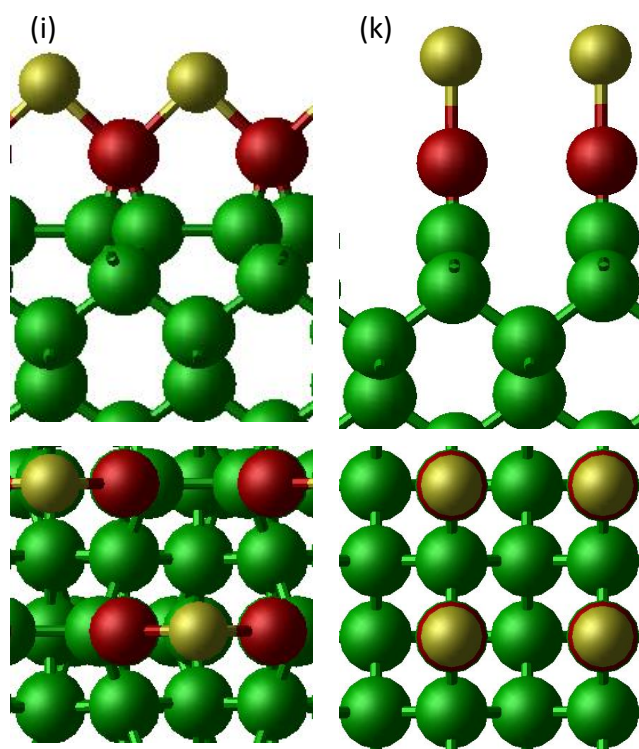


Figure 2-7 – The optimised structures of two TiO-terminated diamond (100) surfaces investigated. (i) – (k) are sample identifiers corresponding to Table 2-2. Each structure is displayed as a side view followed by a top-down view. Green are the C atoms, red are O atoms, and yellow are the Ti atoms.

the other two O atoms on the right are still bridging two C atoms, thereby making it appear as though the O is forming 3 bonds. In scenario (g), on the other hand, each O is bonded only to one C, as they would be in the absence of Ti, as represented in scenario (f). Furthermore, in scenario (g) the surface C atoms have reconstructed, as they are now only single bonded to the O atoms and hence would otherwise have a dangling bond.

For the ether-like O surface, the same behaviour as in scenario (b) can be seen in the two HML scenarios, (c) and (d). For scenario (d), though the optimised structure shows the Ti atoms bridging two O atoms, the structure was initially constructed with the Ti atoms directly above one O atom. The same is true for scenario (i), as was the case for scenario (e) of the TiC scenarios in the previous section. This indicates that Ti does not readily bond to a single atom, which is supported by the +4 oxidation state being the most stable.<sup>130</sup> For the FML scenarios, (e) and (k), on the other hand, the Ti atoms do not rearrange in the same way as the HML samples. While this may be partially due to no surface atoms being available to bond, it is most likely due to the steric hinderance of the Ti atoms being in close proximity to each other.

While for the TiC HML scenario (e), the C atoms underneath the Ti did not reconstruct, the equivalent ketone-like TiO scenario (i) does show a reconstruction. This is interesting because it allows the comparison of the surface stability across the HML scenarios in regard to reconstruction. For the two TiC scenarios, (d) and (e), the energy difference is 0.3 eV while the energy difference of the two reconstructed TiO scenarios, (h) and (i), is only 0.1 eV. This is to be expected because the reconstruction is energetically favourable. Furthermore, the TiO surface with the reconstructed bonds in a row [(h)] is lower in energy compared to the surface where the reconstructed bonds zigzag [(i)], as discussed in the previous section and illustrated in Figure 2-4.

The two clean O-terminated surfaces, (a) and (f), have relatively high electron affinities which agree closely with literature values as discussed in section 1.5.2. For the ketone-like surfaces, once a QML of Ti is added to the clean O surface, there is a significant decrease in the EA from 3.7 eV to -2.9 eV. This is to be expected considering the reversal of the surface dipole as discussed in sections 1.3.1 and 1.5.5. This EA (-2.9 eV) calculated for scenario (g) is the lowest EA of all the surfaces investigated in this work. Upon increasing the coverage to HML, the EA increases. In scenario (h), where the Ti atoms are in a row, a lower EA (-0.1 eV) is observed in comparison to scenario (i), where the Ti atoms alternate to form a zigzag pattern, with EA = 1.4 eV. This was also the case for the TiC scenarios (d) and (e). Upon increasing the coverage to an FML, there is little difference in both the adsorption energy and the EA, as illustrated in Figure 2-8.

For the ether-like surfaces, once a QML of Ti is added there is a significant decrease in the EA resulting in an NEA of -0.9 eV. This is the lowest value for the ether-like O-terminated surfaces, as can be seen from Figure 2-8. The HML scenarios have a higher EA than the QML scenarios, and again, the surface with the Ti atoms in a row presents the lower EA.

Upon increasing the Ti coverage to an FML (e) the EA increases to 4.1 eV, which is the second highest EA obtained across all scenarios. The FML scenario exhibits a higher EA than that of the clean surface [(a)], while also being the only TiO-terminated surface to be less stable than the equivalent O-terminated surface. This is particularly interesting because the same is not observed for the ketone-like FML surface, (k). The reason for this can be deduced by inspecting the optimised structures in Figure 2-6 and Figure 2-7.

By comparing the two FML scenarios [(e) and (k)], it can be seen that the ether-like O atoms in (e) are forced to make three bonds as opposed to the two bonds of the ketone-like O atoms. Furthermore, by comparing scenario (e) to the three other ether-like TiO-terminated surfaces [(b) – (d)], it can be seen that the FML surface has not rearranged half of the O atoms by breaking a C-O bond.

Interestingly, the most stable TiO-terminated surface, the ketone-like QML scenario (g), also exhibits the lowest EA. On this surface, all adsorbate atoms have their ideal number of bonds. The O atoms are each bonded to a C and a Ti atom, the Ti atoms are each bonded to four O atoms and the C atoms have reconstructed so that there are no dangling bonds.

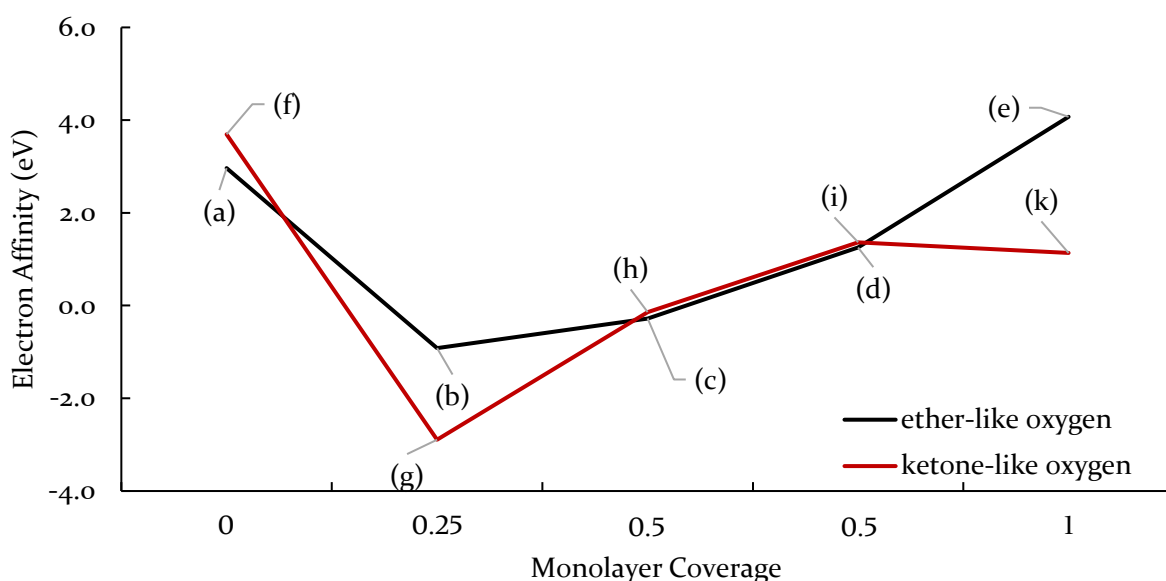


Figure 2-8 –The variation of the EA with Ti coverage for O- and TiO-terminated diamond surfaces.

### 2.3.3 Nitrogen and TiN

As with the TiO and TiC surfaces, the primary objective was to vary the coverage of the Ti on N-terminated surfaces. As with the O-terminated surfaces, these surfaces can be broadly divided into two categories, the ether-like N-terminated diamond surfaces where the N atom is bridging two C atoms, and the ketone-like N-terminated surfaces where the N atoms are directly above a C. However, as N typically forms three bonds, compared to two bonds formed by O, there is a wider variety of structures possible. Furthermore, as the N termination for laboratory experiments is achieved using an ammonia plasma, as will be discussed in sections 4.5.2.3 and 5.4, NH- and NH<sub>2</sub>-terminated surfaces are also investigated. Table 2-3 summarises the various N-

	Description	Name	ML Coverage	$\gamma$ (J m <sup>-2</sup> N <sup>-1</sup> )	EA (eV)
(a)	Ether-like N	Ne	-	-1.4	3.6
(b)	One H atom above each ether-like N atom	Ne-H	-	-1.5	-1.4
(c)	One Ti atom bonded to four ether-like N atoms	Ne-Ti1	QML	-2.0	-1.1
(d)	Two Ti atoms bridging two ether-like N atoms each	Ne-Ti2br	HML	-2.0	0.5
(e)	Two Ti atoms on top of one ether-like N atom each	Ne-Ti2t	HML	-1.8	0.6
(f)	Four Ti atoms above one ether-like N atom each	NeTi4	FML	-2.0	0.8
(g)	Ketone-like N	Nk	-	-1.0	4.7
(h)	One H atom above each ketone-like N	Nk-H1	-	-1.2	-1.5
(i)	Two H atoms bonded to each ketone-like N atom in the x-direction	Nk-H2x	-	-1.2	-2.3
(k)	Two H atoms bonded to each ketone-like N atom in the y-direction	Nk-H2y	-	-1.2	-0.9
(l)	One Ti atom bonded to four ketone-like N atoms	Nk-Ti1	QML	-1.8	-1.7
(m)	Two Ti atoms bridging two ketone-like N atoms each	Nk-Ti2br	HML	-1.9	-0.8
(n)	Two Ti atoms on top of one ketone-like N atom each	Nk-Ti2t	HML	-2.0	-1.1
(o)	Four Ti atoms bridging two ketone-like N atom each	Nk-Ti4br	FML	-2.0	0.7
(p)	Four Ti atoms above one ketone-like N atom each	Nk-Ti4t	FML	-2.0	0.3

Table 2-3 – The computed surface energy and EA of the various N-, N-hydride-, and TiN-terminated (100) diamond surfaces investigated. Column 2 describes the initial state of each system before structure optimisation while the (a) – (p) in column 1 refer to the optimised structures displayed in Figure 2-9 and Figure 2-10. Figure 2-3

terminated surfaces and their derivatives, while the optimised structures are presented in Figure 2-9 and Figure 2-10.

As with the TiC- and TiO-terminated surfaces, there is very little difference between the initial and optimised structures, except for the HML 'on top' scenarios where the two Ti are initially above one C/O/N atom. Particularly interesting however, is the fact that out of the two scenarios presented here, only (n) has rearranged the Ti atoms to bridge two N atoms while (e) has not. This is most likely related to the preference of N to form three bonds, where the two bonds formed in scenario (n) are more stable than the ether-like scenario (e), which after bonding to two C atoms can only form one bond to the Ti. Looking at the stability of the various surfaces, it can be seen that the clean N-terminated scenarios, (a) and (g) are less stable than their respective derivatives. This is similar to the O and TiO terminations, although the energy difference is significantly larger here ( $0.0 - 0.6 \text{ J m}^{-2} \text{ N}^{-1}$ ,  $0.4 - 1.0 \text{ J m}^{-2} \text{ N}^{-1}$  respectively). This is most likely related to the fact that N prefers to form three bonds whereas each of the surface C atoms only has two bonds available, resulting in a dangling bond on the N atom which is energetically unfavourable. However, the  $\text{NH}_x$ -terminated surfaces [(b) and (h) - (k)], where each N atom forms three bonds, are only minimally more stable ( $0.1 - 0.2 \text{ J m}^{-2} \text{ N}^{-1}$ ), which may be due to the low bond energy of the N-H bond as discussed further in section 5.4. Furthermore, there is no difference in the energy of the three ketone-like  $\text{NH}_x$ -terminated surfaces [(h) - (k)], regardless of whether there are one or two H atoms, or which direction the H atoms are facing. The TiN-terminated surfaces are significantly more stable, though interestingly, there is little difference in the energy between the various QML, HML, and FML coverages. There is also minimal difference between the TiN surfaces built upon the ether-like N-terminated surface and those built upon the ketone-like N-terminated surface, with all exhibiting an adsorption energy of  $-1.8$  to  $-2.0 \text{ J m}^{-2} \text{ N}^{-1}$ . This is in contrast to the TiO surfaces, where the ketone-like surfaces were more stable than the ether-like surfaces. This is most likely due to the ether-like N atoms not having to break a C-N bond to allow them to bond to a Ti atom.

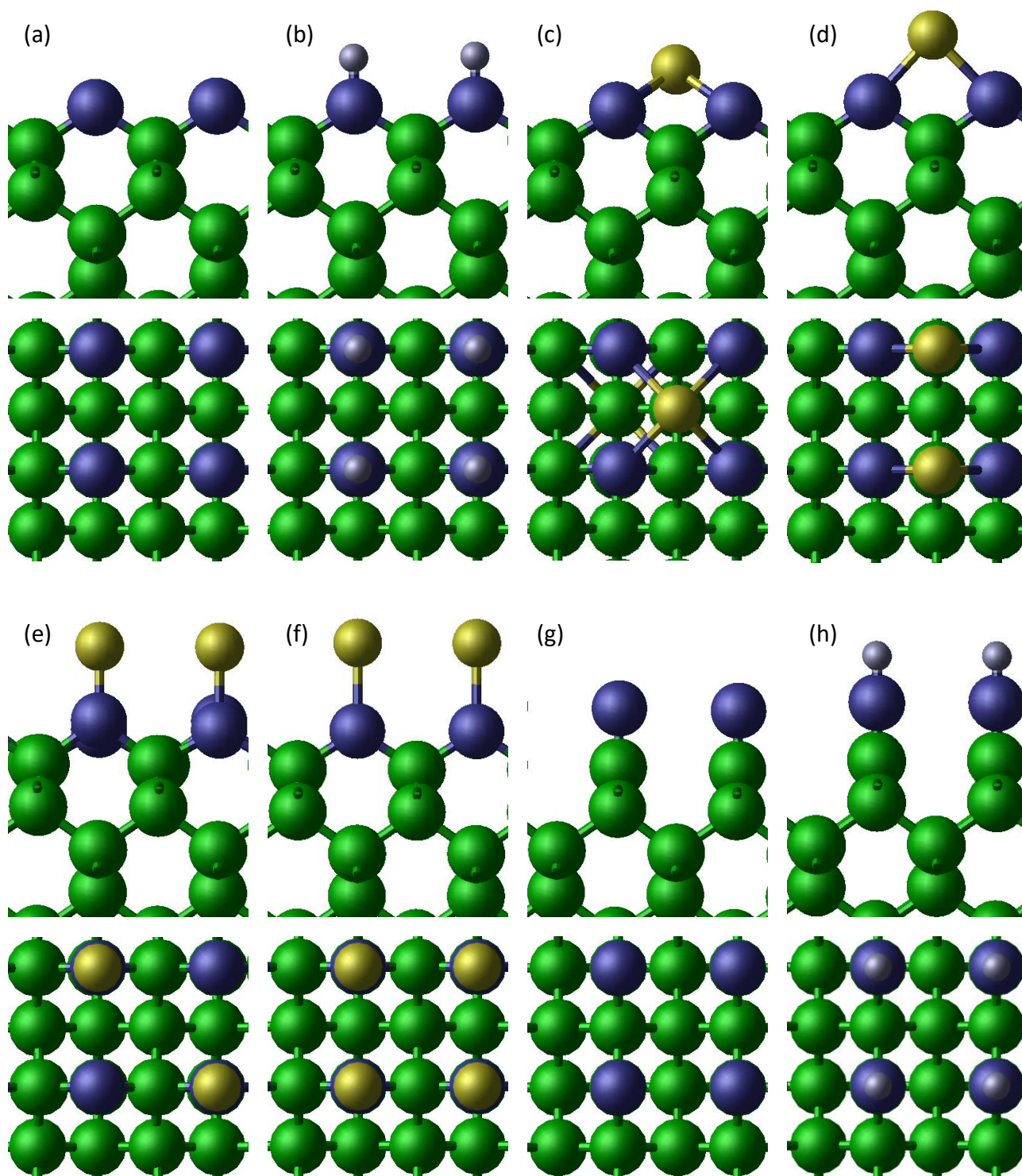


Figure 2-9 – The optimised structures of the various N-, N-hydride-, and TiN-terminated diamond (100) surfaces investigated. (a) – (h) are sample identifiers corresponding to Table 2-3. Each structure is displayed as a side view followed by a top-down view. Green are the C atoms, red are O atoms, and yellow are the Ti atoms.

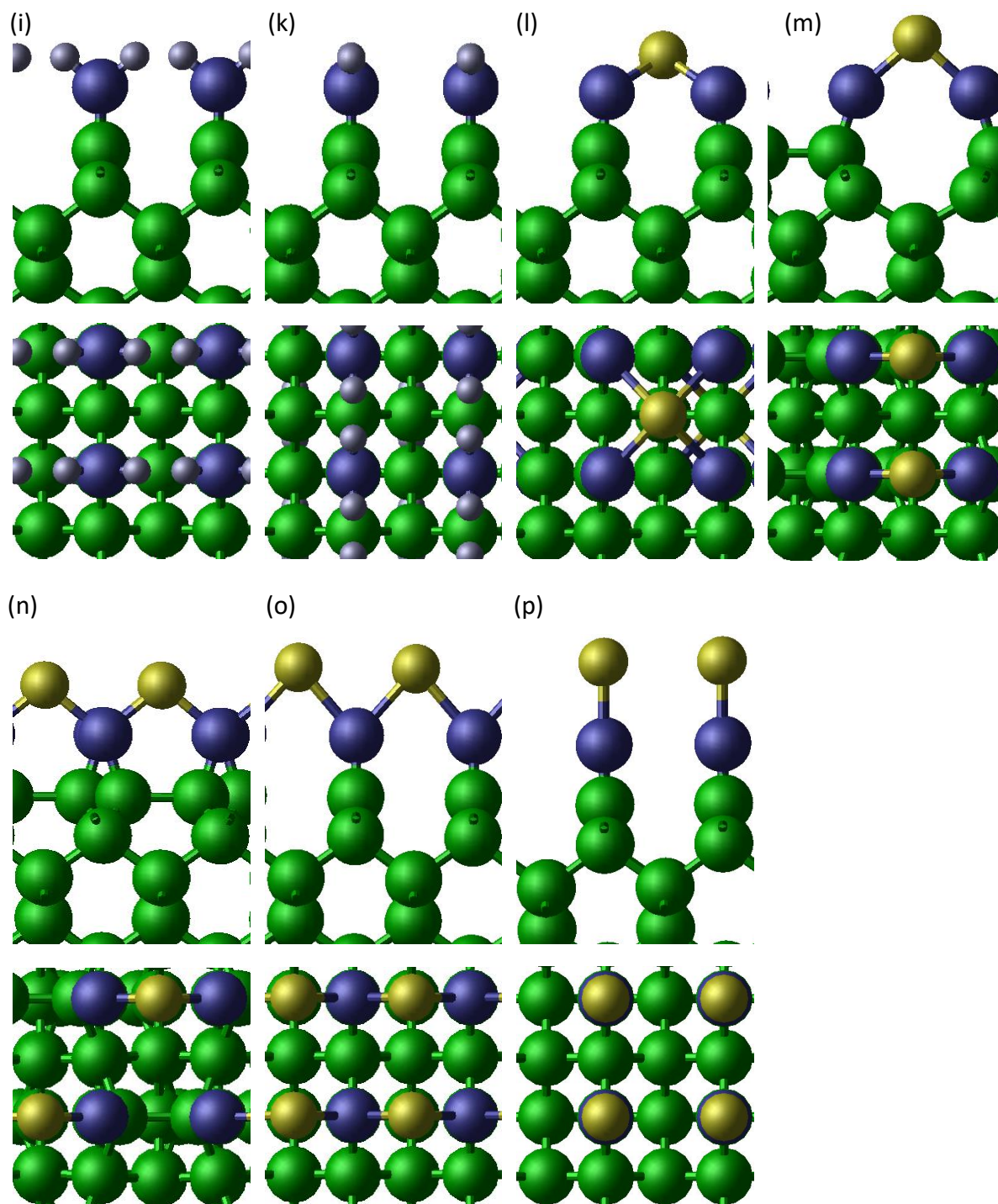


Figure 2-10 – The optimised structures of the various N-hydride- and Ti-terminated diamond (100) surfaces investigated. (i) – (p) are sample identifiers corresponding to Table 2-3. Each structure is displayed as a side view followed by a top-down view. Green are the C atoms, red are O atoms, and yellow are the Ti atoms.



### 2.3.4 Summary

The purely N- and O-terminated surfaces are amongst the highest electron affinities observed in this work, as was expected from the literature, discussed in sections 1.5.2 and 1.5.3. In almost all scenarios, the addition of Ti is predicted to not only greatly improved (i.e. reduced) the EA, but also stabilised the surface.

Of the TiC-terminated surfaces, all have shown greater stability than the H termination, but none of them exhibited lower electron affinities. No direct trend can be observed between stability and Ti coverage, although the two most stable surfaces are both characterised by each Ti atom being bonded to four C atoms.

Furthermore, for TiO surfaces, the most stable surfaces with the lowest adsorption energy were the QML scenarios, while increasing the Ti concentration led to increased electron affinities and adsorption energies. For the TiO scenarios, the most stable surface also exhibited the lowest EA. This was the ketone-like QML TiO-terminated surface.

For the N containing surfaces, the lowest EA values were also the QML TiN-terminated surfaces, however, there was a small decrease in the adsorption energies upon increasing the Ti concentrations. While the  $\text{NH}_x$  scenarios had low electron affinities, they were amongst the least stable surfaces investigated in this work, with adsorption energies significantly higher than the H-terminated diamond surface.

Considering only the surfaces involving Ti, increased stability was observed from the TiN- to the TiO- through to the TiC-terminated surfaces, as shown in Figure 2-12. Of all the scenarios investigated, those where the Ti atoms were closer to the top layer of C atoms tended to be more stable than scenarios with Ti atoms further from the C surface. Only three of the surfaces were found to have lower EA values than the H termination. Two of these, a nitrogen hydride [scenario (i)] and a titanium nitride [scenario (l)] termination, were less stable than the H-terminated surface. The third however, the QML ketone-like TiO-terminated diamond surface, was more stable, as well as exhibiting a lower EA.

In chapter 7, these theoretical studies will be compared to the results of the experimental studies discussed in chapters 5 and 6.

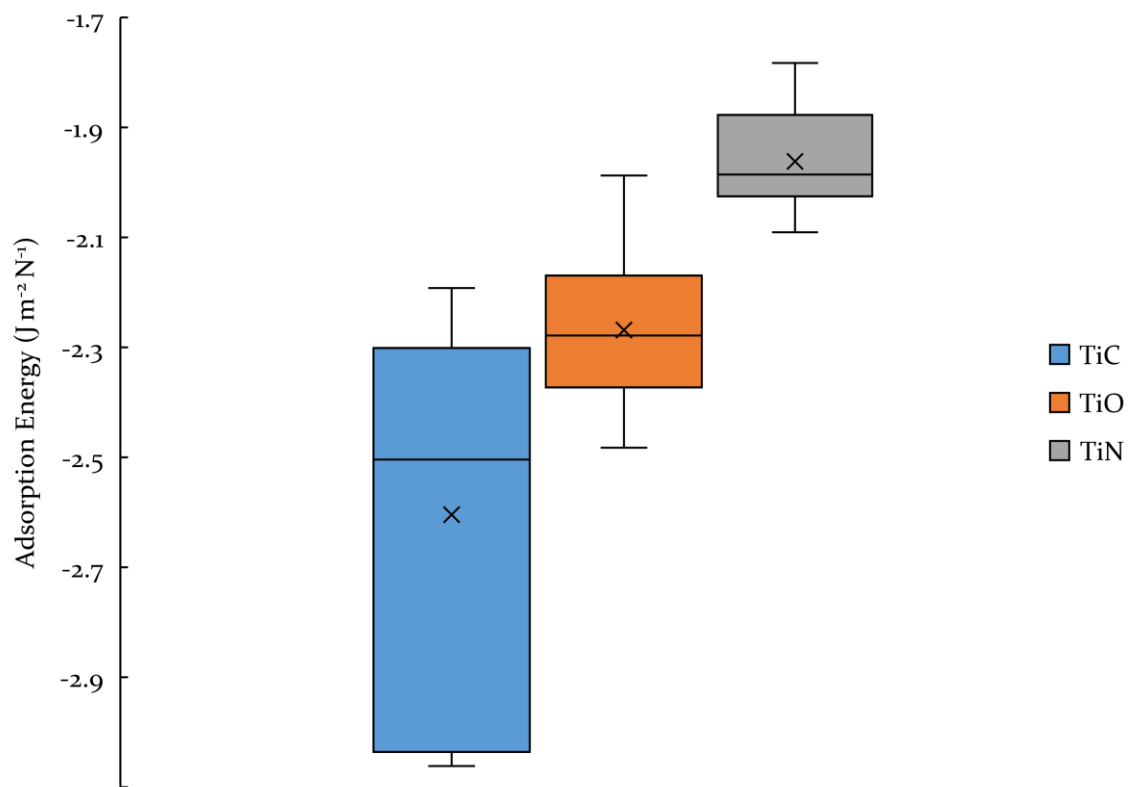


Figure 2-12 – Box plots showing the surface stability of the three Ti-containing surface terminations. The boxes represent the interquartile range, the line is the mean, and × is the median.

## CHAPTER



# Experimental Techniques

“Equipped with his five senses, man explores the universe around him and calls the adventure Science.”

Edwin Hubble - "The Exploration of Space". Harper's Magazine 158: 732. (May 1929).

## 3.1 Photoemission Spectroscopies

When Heinrich Hertz discovered the photoelectric effect in 1887, he neither understood the phenomenon, nor realised its significance.<sup>131</sup> In 1902, it was observed that the kinetic energy of the detected electrons varied not with intensity of the incident radiation, as predicted by the wave theory of light, but with frequency.<sup>132</sup> In 1905, Einstein explained this by postulating the existence of discrete quanta of light, later known as photons. Two years later, the first XPS spectra was recorded, but it wasn't until almost 50 years later that the potential applications were realised when Siegbahn built his high-resolution X-ray photoelectron spectrometer, which he referred to as electron spectroscopy for chemical analyses (ESCA).<sup>133</sup> Photoemission spectroscopy techniques utilise this effect by irradiating a sample with electromagnetic radiation, and measuring the energy of the emitted electrons. Depending on the wavelengths of the incident light, different electrons are emitted, and diverse information is gained.

### 3.1.1 Surface Sensitivity

X-ray photoelectron spectroscopy and ultraviolet photoelectron spectroscopy are both surface sensitive techniques. Even though the incident ionising radiation can penetrate several micrometres into the sample, the ejected electrons must travel through the sample to be emitted into vacuum and reach the detector. Therefore, only those electrons that originate from the top few layers are able to escape and be analysed. There are a variety of processes that lead to electrons losing their energy, such as inelastic collisions, recapture, recombination, trapping, or excitation of the sample. These processes lead to an exponential attenuation of the signal as depth increases, as the further the electron has to travel, the less likely it is to have enough energy to escape the sample. Figure 3-1 shows an example of an inelastic mean free path (IMFP) through a solid, which is the average distance an electron travels before losing energy in an inelastic collision. From this, it can be seen that, at the typical energies for XPS (0-1400 eV), the IMFP is on the order of several nanometres.

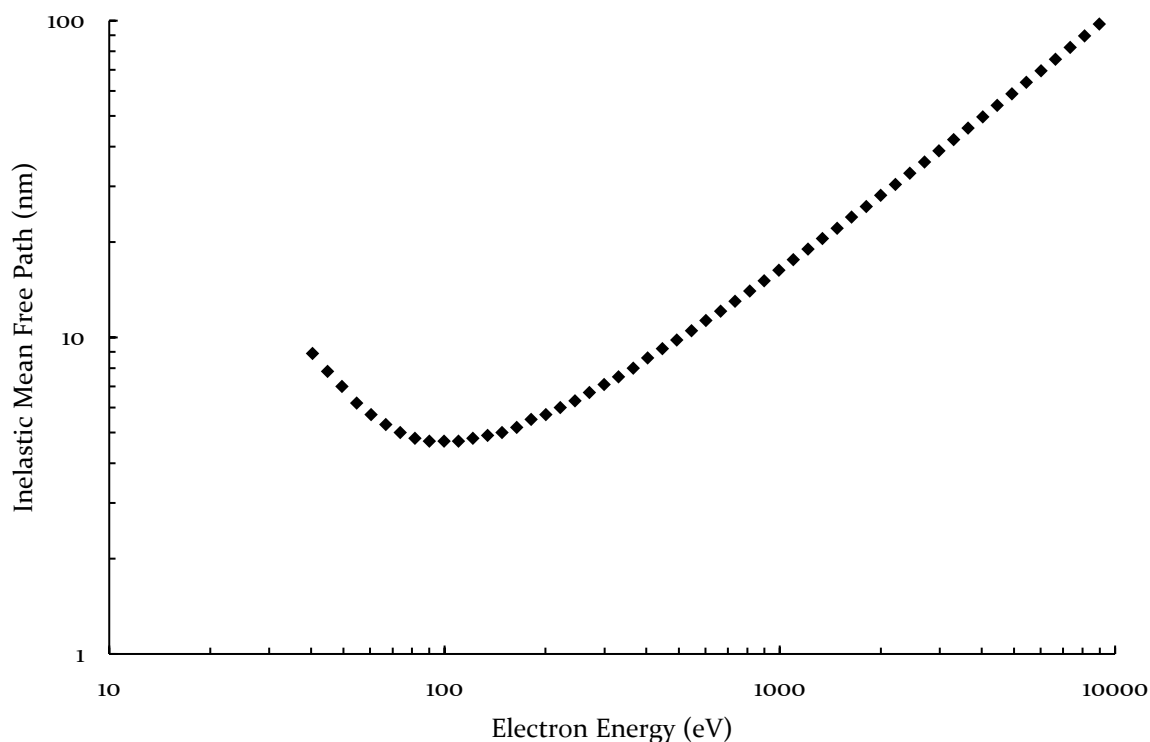


Figure 3-1 – An example curve of the inelastic mean free path of an electron through a solid.

### 3.1.2 X-ray Photoelectron Spectroscopy

In XPS, the incident photons are X-rays. These photons dislodge core-level electrons from the sample, which are then emitted and detected. The kinetic energy of the detected electron can be converted to the binding energy, as shown by:

$$E_B = h\nu - (E_k + \phi)$$

Equation 3-1

where  $E_B$  is the binding energy of the electron,  $h\nu$  is the energy of the photon,  $E_k$  is measured kinetic energy of the electron, and  $\phi$  is the WF of the analyser. The binding energy is the amount of energy required to remove an electron from its atom, and is highly dependent on the nucleus, and the sub-shell that the electron originates from. This allows us to determine which element the electron originated from, and therefore, sample composition. As larger atoms often have electrons in several different sub-shells, there are commonly several peaks in the spectrum which correspond to one element. These different shells will have different likelihoods of emitting an electron, and therefore, there is a standard peak for each element that is used for analysis, usually the most intense peak. For C and O, for example, this is the 1s peak, and for Ti the 2p peak.

In cases where peaks from different elements overlap, a different peak may be used for analyses.

There are small differences in the initial and final state of an atom when an electron is excited by X-rays, which affect the binding energy of an electron. These variations in initial and final state energy are due to the environment of the atom, i.e. what other elements the atom is bonded to, but also how the atoms are bonded. This surface-sensitive chemical-state identification makes XPS a powerful analytical tool.

An XPS system consists of three main parts, the X-ray source, the electron analyser and detector, and the vacuum chamber. The light source generates X-rays by bombarding a metallic anode with high-energy electrons. When the electrons interact with the anode material, two effects can occur. Either the electron is slowed down by the electric field of the atoms, and emits electromagnetic radiation known as *bremstrahlung*, or a core-level electron is ejected, and an electron from a higher energy level replaces that electron, emitting the difference in energy as the characteristic X-rays of the anode material. Figure 3-2 shows some of the potential emission lines, and the energy of the strongest emission line for some common anode materials. Magnesium and aluminium are the most common anode materials. Despite some of the other materials having a higher energy, and therefore, being able to scan across a larger energy range, they also have wider line widths and therefore lower energy resolutions. Modern XPS systems use monochromatic  $K\alpha$  radiation to achieve a higher energy resolution. This is achieved

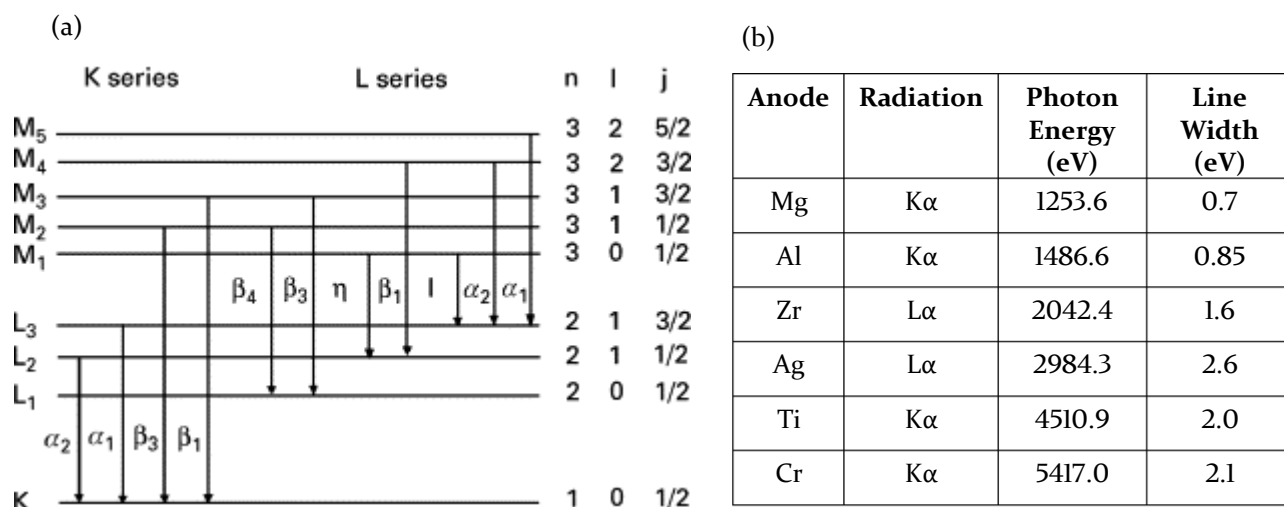


Figure 3-2 – An energy level diagram (a) depicting the origin of the various emission lines, and a table (b) of the most intense emission lines for common anode materials.<sup>156</sup>

using diffraction and constructive interference by focusing the beam onto a quartz crystal.

There are several designs of electron analysers for separating the emitted photoelectrons according to their energy. The most widely used design is the hemispherical analyser as shown in Figure 3-3. It consists of two hemispheres which are biased to establish an electrostatic field that allows only electrons of certain energy,  $E_0$ , to reach the detector. If the electron has too much energy,  $E_H$ , it would not be able to follow the path  $E_0$  and would instead hit the outer hemisphere. The same applies for electrons with too little energy,  $E_L$ , except these would hit the inner hemisphere. By varying the bias of the two hemispheres, one can control the energy resolution of the analyser and scan through the energy range.

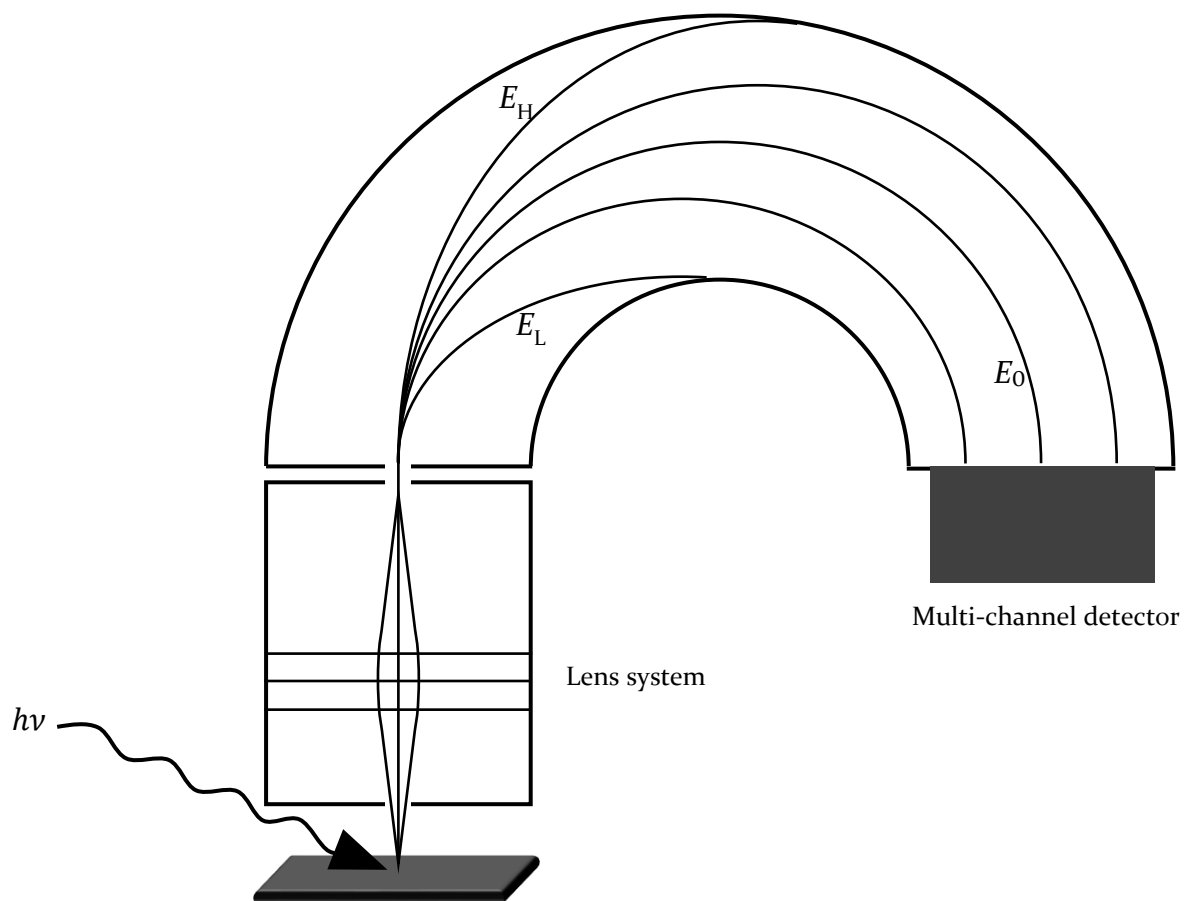


Figure 3-3 – A schematic diagram of a hemispherical electron analyser.

Because of the relatively long path-lengths of the electrons inside the analyser, the whole system needs to be at minimum under high vacuum ( $<1 \times 10^{-6}$  mbar), as can be seen from Table 3-1. At atmospheric pressure, an electron can only travel an average of 50 nm before colliding with a gas molecule and lose energy. This would mean none of the emitted photoelectrons would reach the detector. However, most systems usually operate at significantly lower pressure, at least ultra-high vacuum ( $<1 \times 10^{-9}$  mbar), because XPS is a surface sensitive technique. The last column in Table 3-1 shows how long it takes for a monolayer of unwanted adsorbates to form on a clean sample surface based on the number of atoms striking each surface atom per second. It can be seen that to prepare a clean surface for a practical measurement duration, at least ultra-high vacuum is required.

Degree of Vacuum	Pressure (mbar)	Inelastic mean free path of electrons (m)	Atoms striking surface atoms ( $s^{-1}$ )	Time to ML coverage (s)
Atmospheric	1000	$5 \times 10^{-8}$	$4 \times 10^8$	$2.5 \times 10^{-9}$
Low	$<1$	$5 \times 10^{-5}$	$4 \times 10^5$	$2.5 \times 10^{-6}$
Medium	$<1 \times 10^{-3}$	0.05 (5 cm)	400	$2.5 \times 10^{-3}$
High	$<1 \times 10^{-6}$	50	0.4	2.5
Ultra-High	$<1 \times 10^{-9}$	$5 \times 10^4$	$4 \times 10^{-4}$	$2.5 \times 10^3$ (40 min)

Table 3-1 – Pressure dependence of the mean free path and time to form a monolayer (ML).

### 3.1.3 Ultraviolet Photoelectron spectroscopy

Ultraviolet photoelectron spectroscopy (UPS) was developed several years after XPS and utilises ultraviolet electromagnetic radiation as the light source. Compared to XPS, UPS probes the valence electrons instead of the core electrons but does so more accurately. As the valence molecular orbitals often exhibit a high degree of hybridisation, the small shifts in binding energy due to the chemical state of the atom are more varied and subtle. Therefore, UPS spectra tend to be used for material characterisation through spectral fingerprinting rather than individual peak assignment. UPS is also often more surface sensitive than XPS because the emitted photoelectrons are of a lower energy, and therefore usually have a shorter IMFP, as shown in Figure 3-1. This is of course dependent on the material, as different materials have different IMFPs. UPS is particularly useful for determining the WF ( $\phi$ ) of a material, as per:

$$\phi = h\nu - (\text{SECO} - E_{\text{Fermi}})$$

Equation 3-2

where  $h\nu$  is the incident photon energy, SECO is the secondary electron cut-off, and  $E_{\text{Fermi}}$  is the energy of the Fermi level. Figure 3-4 shows a typical UPS spectrum, with the inset showing how the SECO is determined, i.e. the value where the baseline and the SECO peak intersect. One thing to note, is that a UPS spectrum usually has kinetic energy as the horizontal axis, with 21.2 eV at the origin, and finishing at 0 eV (the Fermi level). This horizontal axis has been converted to  $E_k - E_{\text{Fermi}}$ , so that the secondary electron cut-off is equal to the WF. The valence band peaks between 10 – 15 eV in this example are fairly muted. Typically, it is necessary to apply a small bias to the sample to be able to distinguish the sample WF from the analyser WF.

A UPS system has the same base components as an XPS system except for the light source. The most common type of source is a gas discharge lamp, usually filled with helium to produce 21.2 eV photons. The gas discharge lamp can also be filled with other gases such as hydrogen, neon, or argon, as shown in Table 3-2. However, because these emit either significantly lower photons and/or closely spaced multiplets, which are harder to filter out, helium is the most common choice. A key difference between X-ray and UV-sources is that no material is transparent to the UV photons, and hence no window can be placed between the plasma of the gas discharge lamp and the chamber. UPS sources, therefore, require differential pumping, typically 2- or 3-stage. As an

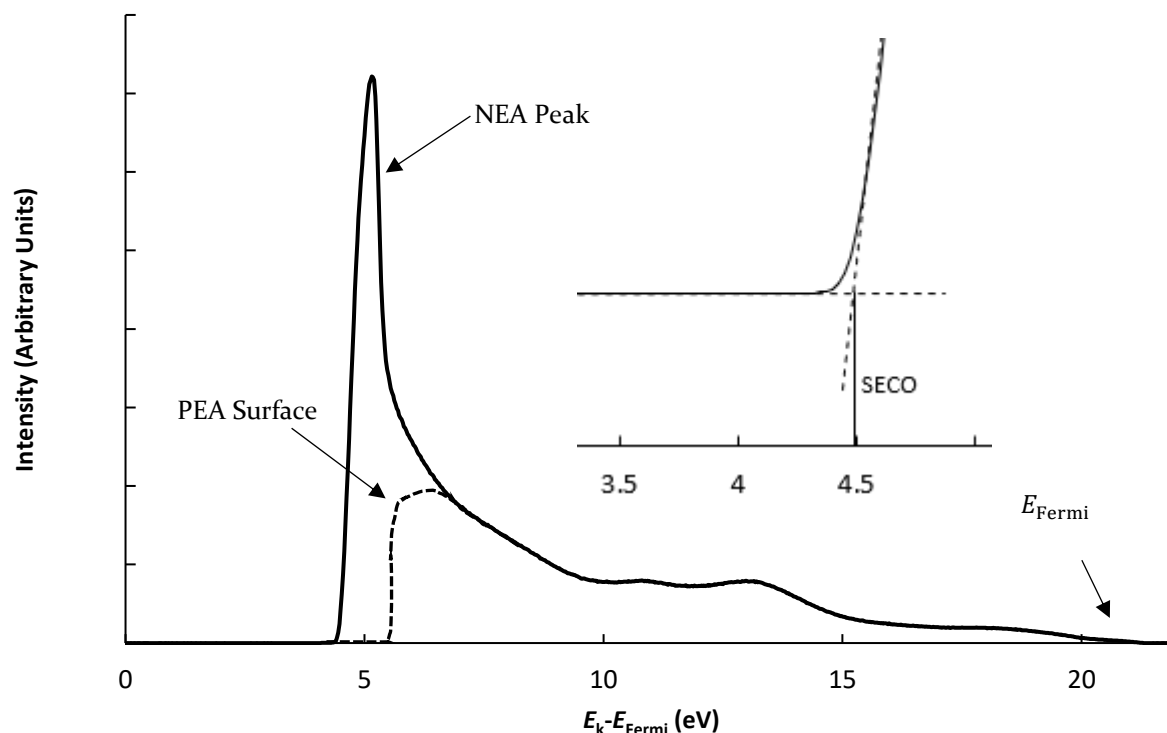


Figure 3-4 – An example of the UPS spectrum of a typical NEA surface (e.g. H-terminated diamond). The dotted line shows a typical UPS spectrum without the NEA peak, i.e. for a PEA surface (e.g. O-terminated diamond). The inset shows how the WF is determined where the secondary electron cut-off (SECO) and the baseline intersect (4.49 eV in this example).  $E_k$  is the kinetic energy of the photoelectrons and  $E_{\text{Fermi}}$  is the energy of the Fermi level (21.2 eV).

example, the NanoESCA at the University of Bristol originally had a gas discharge lamp with 2-stage differential pumping. The base pressure of the chamber when the light source was not in operation was  $2 \times 10^{-11}$  mbar. During operation, the pressure inside the light source was  $\sim 10^2$  mbar, while the pressure in the chamber was  $\sim 10^{-7}$  mbar. Upon upgrading the light source to 3-stage differential pumping, a pressure of  $\sim 10^{-9}$  mbar was achieved during operation.

Gas	Radiation	Photon Energy (eV)
Helium	I $\alpha$	21.2
	II $\alpha$	40.8
Neon	I $\alpha$	16.85
	II $\alpha$	26.8
	II $\alpha$	26.9
Argon	I	11.6
	I	11.8
H	Lyman $\alpha$	10.2

Table 3-2 – A summary of the most intense emission lines for common gases used in a gas discharge lamp. I – light emitted from neutral atoms, II – light emitted from singly ionized atoms.

### 3.1.4 Analysis of XPS data

During XPS, there are two main types of spectra. Firstly, a scan across the whole energy range yields a survey spectrum to determine the elemental composition of the sample. Then, a high-resolution scan across a smaller energy range (i.e. a particular peak of interest) can be performed to provide more in-depth information. As mentioned earlier, the binding energy of an electron is affected by the bonding environment of the parent atom. Therefore, the high-resolution core-level spectrum of a peak is usually made up of an ensemble of component peaks representing the various functional groups, that together make up the envelope of the peak seen in the experimental data. The fitting of these component peaks is not trivial, and care must be taken to ensure that the fitting is representative of the real system.

#### 3.1.4.1 Background

The first challenge when fitting XPS data is the nature of the background signal surrounding the photoelectric peak. As shown earlier in Equation 3-1, the binding energy of a detected electron is determined by subtracting the kinetic energy from the photon energy. This is accurate for the electrons which escaped the sample surface having encountered only elastic collisions, i.e. they did not lose any kinetic energy in those collisions. The deeper an electron originates from, the more likely that it will have experienced inelastic collisions and lost its kinetic energy before it reaches and escapes the surface. This is why the signal decays exponentially with the depth of origin. However, some electrons may experience inelastic collisions and still have enough kinetic energy to escape the surface and reach the detector. Because these electrons have lost some of their kinetic energy, they will contribute to the spectrum at a higher binding energy. Thus, the background signal increases at higher binding energies. Furthermore, as the electrons can experience multiple random inelastic collisions, the background is continuous, increasing with each peak. In simple cases, where the background has a relatively small step in the energy range of the peak, such as the C 1s peak shown in Figure 3-5, the choice of background has little effect and a simple linear background approximation may be used.

To address the issue of more complex backgrounds, a wide variety of approximations exist. The most commonly used are either the Shirley or Tougaard backgrounds.<sup>B4-B6</sup> The Shirley background is an empirical technique that iteratively adjusts the background as a function of the intensity of the photoelectric peak. The background intensity,  $S(E)$ , is computed at the energy  $E$  according to:

$$S(E) = I_2 + \kappa \frac{A2(E)}{[A1(E) + A2(E)]}$$

Equation 3-3

where  $I_1$  and  $I_2$  are the intensities at the higher and lower binding energy background limits, respectively,  $\kappa$  defines the step in the background (equal to  $I_1 - I_2$ ), and  $A1(E)$  and  $A2(E)$  are the integrated areas of the peak above or below the binding energy  $E$ , respectively. Thus, if the intensity of the background signal,  $S(E)$ , is known, then  $A1(E)$  and  $A2(E)$  are also known quantities. However, as  $S(E)$  is initially unknown,  $A1(E)$  and  $A2(E)$  must be computed using an approximation to  $S(E)$ , and then refined iteratively. The Tougaard background on the other hand, is a non-empirical background based on the inelastic scattering cross section. This is based on the dielectric response function and describes the electron-electron interaction of an emitted electron with the electrons in the solid. The electrons in a solid redistribute in the presence of a moving electron, inducing a small electric field which interacts with the moving electron. The inelastic scattering cross section is not known in most cases, so a generalized universal cross

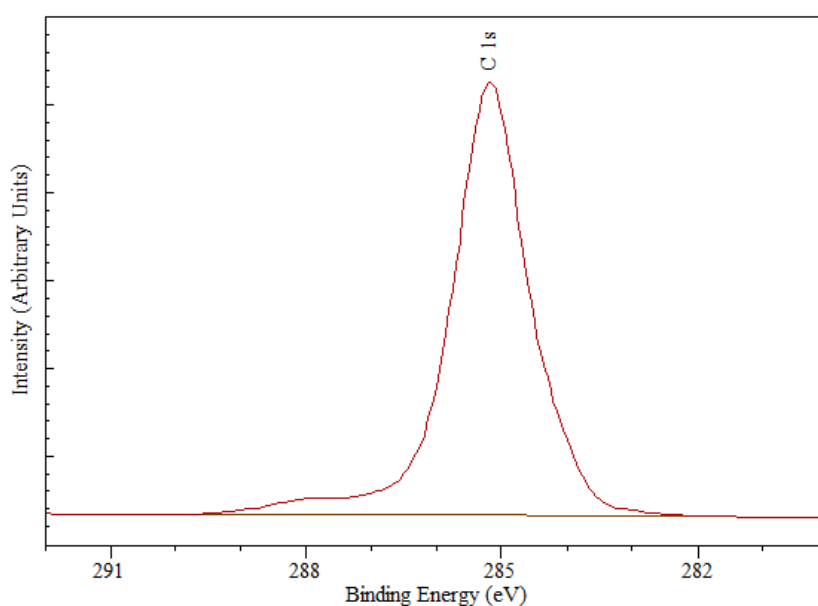


Figure 3-5 A linear background on a C 1s spectrum.

section has been introduced. This is controlled by two parameters and is known as the universal two-parameter Tougaard background (U2T). The main challenge with the Tougaard approximation is the assumption that there are no instrumental artefacts. As such for practical purposes, few spectra are refined enough to enable use of the Tougaard background appropriately.

To effectively evaluate a core-level spectrum, the choice of background is crucial, as the wrong background causes incorrect peak intensities, and hence leads to misinterpretation of data, as shown in Figure 3-6. Here, a Ti 2p peak is fitted with a variety of different background approximations. Due to the difference in background on either side of the peak, the choice of background has a significant impact on the resulting shape and area of the peak. Scenario (a) and (b) both use a Shirley background, either individually or across both parts of the peak. For elements where the spin-orbital splitting value (the distance between the two peaks) is larger, separate backgrounds may be appropriate. The fact that the smaller, higher-energy component in (a) exhibits a much smaller change in background than the lower-energy component suggests that the two peaks overlap. Therefore, a single background across both parts of the peak should be used. Typically, the Shirley background approximation is the background of choice over the Tougaard approximation. This is because the Shirley background encompasses the fundamental idea of why backgrounds are not flat (electron scattering) and tend to agree well with literature standards.<sup>134,137,138</sup> Furthermore, for the Shirley background, there are fewer parameters that are varied by the user, and hence it is easier (and less prone to errors) for an inexperienced user to implement effectively.

As noted in the CasaXPS software manual, “The truth is that none of the background types on offer are correct and therefore selection of one background type over another is essentially chosen as the least wrong rather than the most right.”<sup>139</sup>

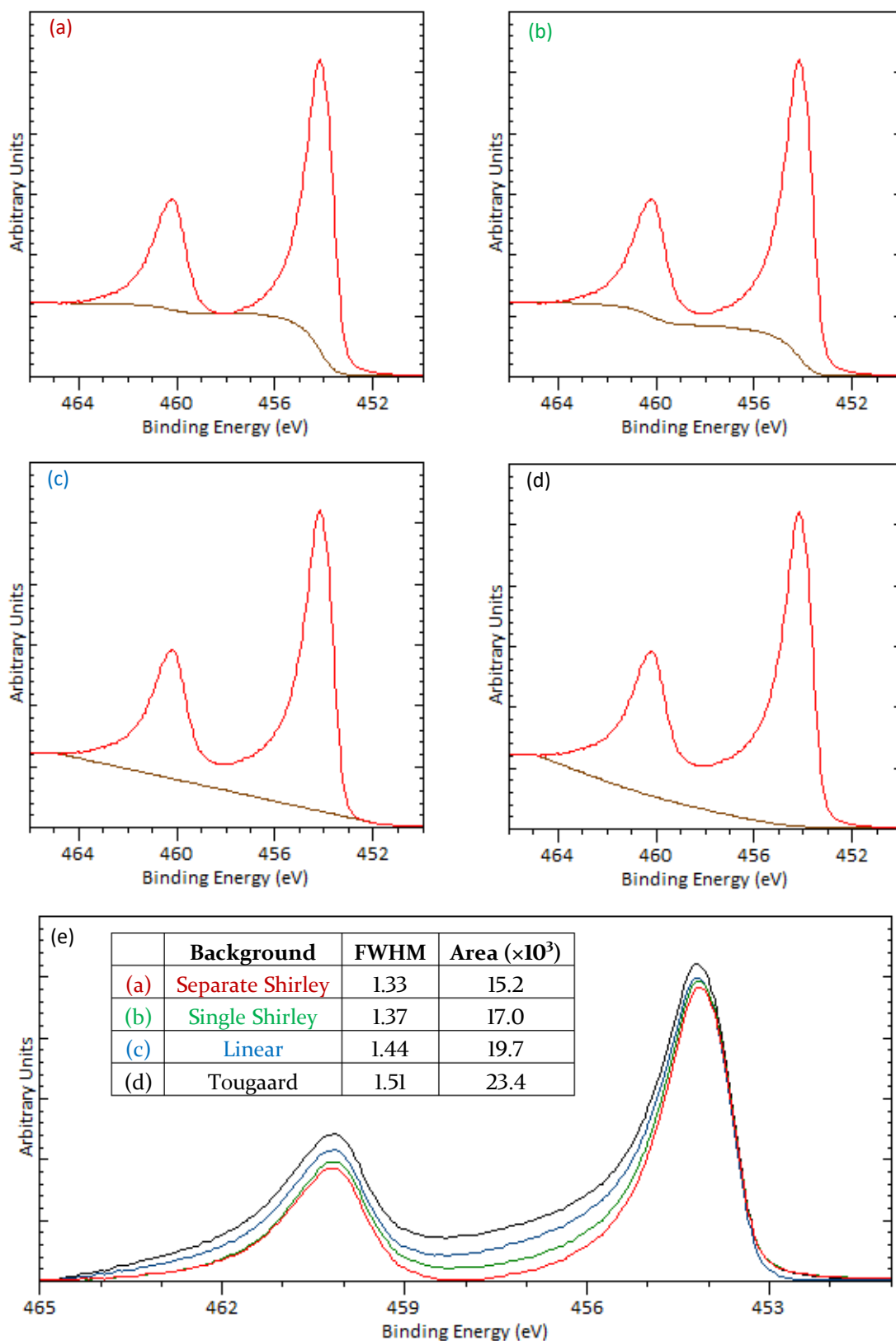


Figure 3-6 – Various backgrounds computed on a Ti 2p spectrum. (a) a separate Shirley background for each peak, (b) a single Shirley background across both peaks, (c) a linear background, and (d) a Tougaard background. (e) is an overlay of the different peaks showing the difference in size as a result of the various backgrounds. The FWHM values shown in the inset table are for the Ti 2p<sub>3/2</sub> peaks.

### 3.1.4.2 Line Shapes

The peaks produced by ejected core-level electrons appear in a variety of shapes. These shapes are influenced by a combination of the processes involved in the ionisation, and distortions due to the measurement process. In general, various effects of the measurement process (such as Doppler broadening or instrumental response) result in a Gaussian distribution while uncertainties in the emission energy of the electron (due to Heisenberg's uncertainty principle) result in a Lorentzian distribution. An idealised model of these influences is a Voigt profile ( $V$ ), which is a convolution of a Gaussian (also known as normal distribution) function and a Lorentzian (also known as Cauchy distribution) function, as shown below:

$$V(x; \sigma, \gamma) = \int_{-\infty}^{\infty} G(x'; \sigma) L(x - x'; \gamma) dx'$$

Equation 3-4

where  $x$  is the shift from the centre of the peak,  $\sigma$ ,  $\gamma$ ,  $G(x; \sigma)$  and  $L(x; \gamma)$  correspond to the centred Gaussian and Lorentzian profiles, respectively:

$$G(x; \sigma) = \frac{e^{-x^2/(2\sigma^2)}}{\sigma\sqrt{2\pi}}$$

Equation 3-5

$$L(x; \gamma) = \frac{\gamma}{\pi(x^2 + \gamma^2)}$$

Equation 3-6

Voigt profiles are mathematically very complex, and so approximations are typically used, the most common being either the Gaussian-Lorentzian product function (GLP) or the Gaussian-Lorentzian sum function (SGL), also known as pseudo-voigt function. Figure 3-7 shows 4 different SGL profiles, from the blue, which is purely Gaussian ( $\gamma = 0$ ), to the purple, which is purely Lorentzian ( $\sigma = 0$ ). The SGL function has 'wings' while, due to the more compact nature of the Gaussian function, the GLP function does not. Thus, there are fundamental differences between the SGL and GLP functions, and they are not interchangeable. Although SGL is mathematically a better approximation of the the Voigt profile, ultimately, how effectively the synthetic line shape matches real data is paramount. Although typically SGL is a better fit, there are some scenarios where GLP is more accurate.<sup>140</sup>

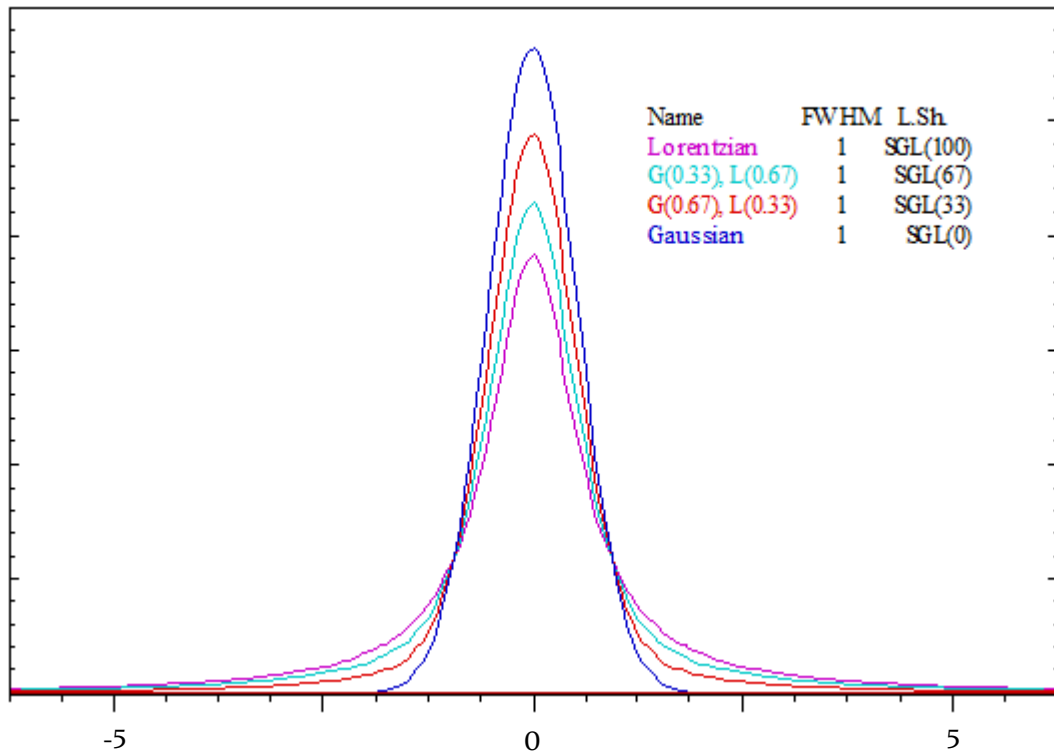


Figure 3-7 – Various centred Voigt profiles. Each case has the same area and the same full width at half maximum of 1.

### 3.1.4.3 Parameter constraints

The fitting of component peaks to the experimental peak envelope to represent various functional groups can be easily performed by software such as CasaXPS. The role of the user is therefore primarily to impose some constraints on the fitting parameters under which the mathematical modelling of the software is carried out. These constraints ensure that the resulting fit is physically meaningful. Figure 3-8 shows the differences between constrained (a) and unconstrained (b) fittings. As can be seen from the residual standard deviation (RSTD), (b) is mathematically a better fit, but considering the blue component has almost four times the FWHM of some of the other components, and that the two largest components are only 0.2 eV apart, this is an unrealistic fit. Despite this, there are many examples of such fits in literature. Furthermore, adding more components to a fitting will ensure a better mathematical fit, as shown in spectrum (c), but again will not necessarily yield useful information.

Thus, knowledge of the system of study is important to know how many components to expect. The constraints to be used depend on the elements and the system in question, so literature should be consulted to ensure a good fit. Two common constraints include fixing the FWHM of all the components of one peak to be the same and imposing a certain energy separation between components.

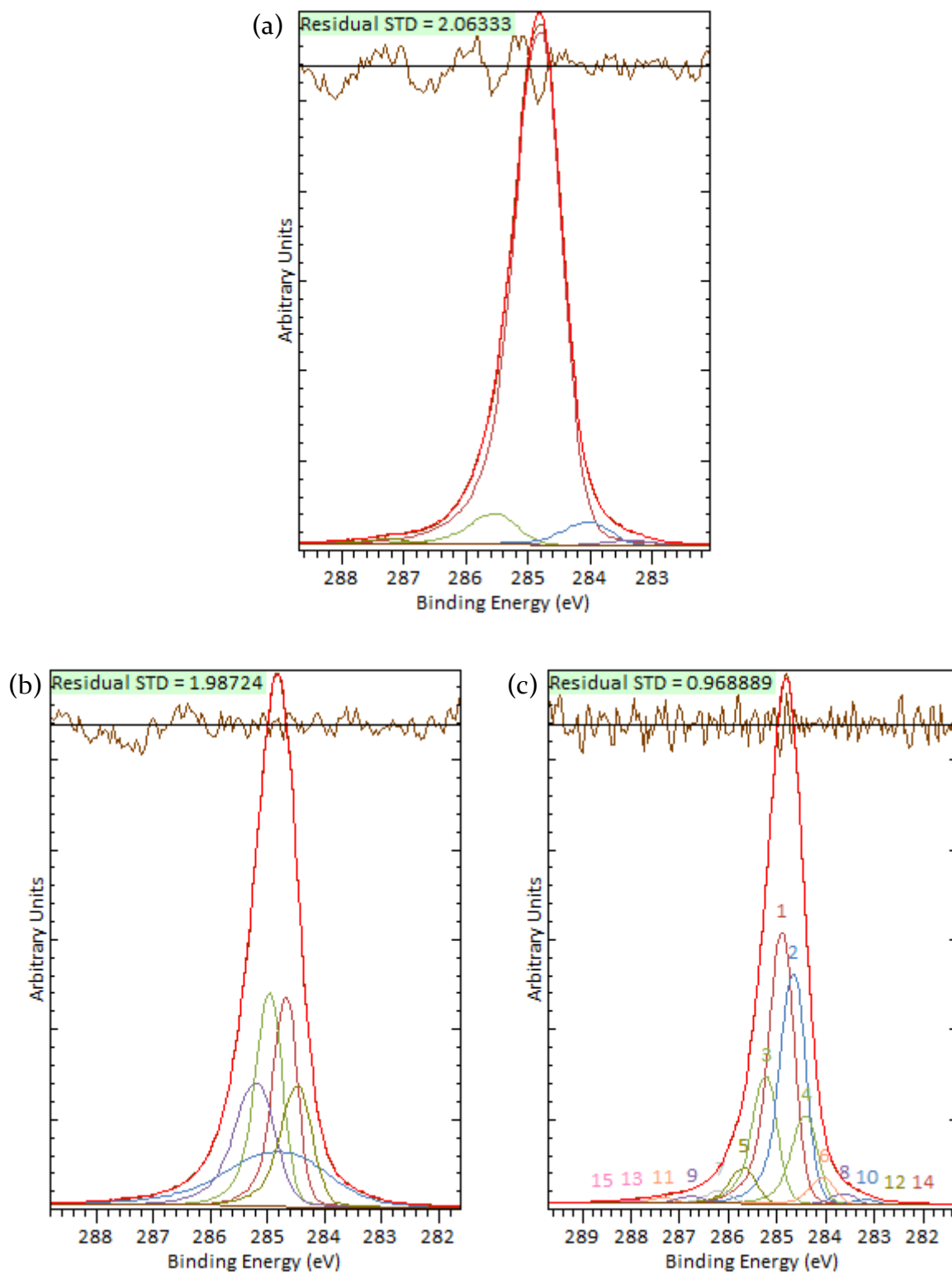


Figure 3-8 – (a) a peak fitting with the appropriate constraints, (b) a peak fitting without constraints, and (c) a peak fitting with the FWHM constrained, but too many components added. The 15 components shown in (c) were the minimum required to get the RSTD below 1.

### 3.1.4.4 Binding Energies of Functional Groups

The binding energies of the various functional groups for C, O, N and Ti are summarised below. Whilst these will predominantly be referenced in chapters 5 and 6, a summary table allows an easier overview.

	<b>Chemical State</b>	<b>Binding Energy (eV)</b>
Metal	Carbide	280.5-283.5
C	sp <sup>2</sup>	~ 284
	sp <sup>3</sup>	284.5-285
H	C-H	~ 285
O	Hydroxyl (C-OH)	286-287
	Ethers (C-O-C)	286-288
	Carbonyls (C=O)	287-289
	Carboxyls	288-289
	Carbonates	289-291.5
Fluorine	C-F <sub>x</sub>	292-294

Table 3-3 – Binding energies of common functional groups present in the C 1s peak.<sup>61,71,157-162</sup>

<b>Chemical State</b>	<b>Binding Energy (eV)</b>
Metal oxides	528-531
Double bond O (ketones, aldehydes)	~ 531
Single bond O (ethers, hydroxyls)	~ 532
Fluorine oxides	534-536

Table 3-4 – Binding Energies of common functional groups present in the O 1s peak.<sup>157,158,163-165</sup>

Chemical State	Binding Energy (eV)
Metal nitrides	396-398
Cyanides (C≡N)	397.5-400
NH <sub>3</sub>	~399
C-NH <sub>x</sub>	399-401
Nitrite (NO <sub>2</sub> <sup>-</sup> )	~404
Nitrate (NO <sub>3</sub> <sup>-</sup> )	405-408

Table 3-5 – Binding Energies of common functional groups present in the N 1s peak.<sup>157,158,166-170</sup>

Chemical State	Binding Energy (eV)
Ti(O)	~454
Ti(II)	~455
Ti(III)	456-457
Ti(IV)	458-459

Table 3-6 – Binding energies of the different oxidation states of Ti in the Ti 2p<sub>3/2</sub> peak.<sup>157,158,167,168,171-174</sup>

Chemical State	Spin-orbit Splitting (eV)
Ti(O)	6.1
Ti(II)	5.7-6.0
Ti(III)/Ti(IV)	5.2-5.9

Table 3-7 – Spin-orbit splitting values for various oxidation states of Ti in the the Ti 2p peak.<sup>157,158,171-174</sup>

### 3.1.4.5 Limit of detection

The limit of detection varies for different elements. The photoelectric effect is one of the possible outcomes of a photon interacting with an atom. Indeed, even if a photon is absorbed, and an electron is excited, there are various relaxation processes that can occur. The probability of a photoelectric event occurring (cross-section) is dependent on the atomic mass of the atom and the energy of the incident photon. For low-energy photons where  $k < 0.9$ , the cross-section ( $\sigma$ ) can be approximated by:

$$\sigma \approx 3 \times 10^{12} \frac{Z^4}{(h\nu)^{3.5}}$$

Equation 3-7<sup>141,142</sup>

where:

$$k = \frac{h\nu}{mc^2}$$

Equation 3-8

where  $Z$  is the atomic number (e.g. 6 for C),  $h\nu$  is the energy of the photon, and  $mc^2$  is the electron mass rest energy ( $5.11 \times 10^5$  eV). For quantitative analysis of the survey spectra, a relative sensitivity factor (RSF), relative to C and dependent on the cross-section, is used to determine elemental composition.<sup>143</sup> From the RSF values in Table 3-8, it can be seen that if a sample was evenly composed of Li, C, and Sn, the C peak would be 17.6 times larger than the Li peak. The Sn peak would be 25.1 times larger than the C peak, or 441 times larger than the Li peak. These are extreme examples as lithium is particularly difficult to detect and tin has a larger than average cross-section, but it demonstrates the differences in the limit of detection for the different elements.

Elemental peak	RSF
Li 1s	0.0568
C 1s	1
N 1s	1.8
O 1s	2.93
F 1s	4.43
Mo 3p	8.66
Sn 3d	25.05

Table 3-8 – Relative sensitivity factors of some commonly encountered elements.

#### 3.1.4.6 Errors

The elemental composition of the sample according to the survey scans is subject to a  $\pm 0.1\%$  error due to the energy resolution of the spectra. It should be noted, that even if a particular element cannot be detected in the survey scan, it may simply be below the limit of detection. Even  $0.01\%$ , which is equivalent to  $100\text{ ppm}$ , is below the detection limit for most elements. Due to the energy resolution of the UPS spectra and the uncertainty of the fitting, the values of the WF calculated are subject to an error of  $\pm 0.1\text{ eV}$ .

The errors on the component fitting for the high-resolution core-level scans are more challenging to quantify. In general, the N 1s and O 1s spectra have a lower associated error than the C 1s and Ti 2p spectra. For carbon, this is due to the asymmetry of the peak, coupled with the relatively large size of the  $sp^2$  and  $sp^3$  components. For Ti, this is due to the large difference in background, and the difficulty in accurately fitting the data due to the Coster-Kronig effect, which will be discussed in more detail in section 6.2.

#### 3.1.4.7 Contamination

One of the most challenging aspects of the XPS analysis of surfaces is the avoidance of contamination, which can affect surface properties or lead to misinterpretation of data. Contamination can originate from a variety of sources, such as sample preparation, transport, or the UHV system itself. The latter is mostly dependent on the system design and can be greatly minimized through the use of oil-free pumps, turbomolecular pumps, and ion pumps.

The user should always wear gloves and/or use tweezers to handle samples to avoid transfer of oils from the skin. Samples should not be stored in plastic containers, particularly with a plastic film as the plasticiser can deposit a variety of contamination onto the sample. Especially problematic are organosilicons because they migrate along surfaces, thereby easily spreading through both transfer and migration onto laboratory benches, tweezers or sample holders. Samples can alternatively be stored in glass containers, or between lint-free microfibre tissue such as lens tissue.

There are many options for cleaning samples such as surfactants, sonication, etching, annealing, or polishing. Which method is chosen depends on the surface of interest. In all cases, high purity reagents or gases should be used to minimize contamination.

If the sample is exposed to air between preparation and insertion into the UHV system, then hydrocarbon (known as adventitious carbon) contamination is unavoidable, as particles from the surrounding atmosphere adsorb onto the sample surface rapidly (discussed in section 3.1.2). Depending on the sample, this can be mitigated either by annealing or noble gas sputtering treatment inside the UHV system.

Most of these issues can be avoided if samples can be cleaned and/or prepared *in situ*, but this is dependent on the capabilities of the UHV system.

#### 3.1.4.8 Summary

Fitting component peaks to XPS core-level spectra is non-trivial and considerable care must be taken to ensure the fitted data are representative of the actual system. Many parameters, such as background type, line shape, or peak position, as well as the constraints imposed upon them, influence the fitting. Due to this, component fitting is rather subjective and can vary drastically from user to user. Care has been taken in this work to ensure that all spectra are fitted with the same procedure and constraints. This ensures a level of consistency that allows for the analyses of trends between the various samples.

## 3.2 Chemical Vapour Deposition

Instead of reproducing nature's way of creating diamonds, using high-pressure high-temperature (HPHT) synthesis, diamond can be produced by adding individual C atoms to a pre-existing template. Chemical vapour deposition (CVD) involves a gas phase chemical reaction with activated C-containing precursor molecules above a suitable solid substrate. While CVD techniques differ in their method of activation, whether that is thermal, such as hot filament reactors, or comes from an electrical discharge, such as during various plasma methods, they share several commonalities. To achieve diamond growth rather than the thermodynamically favoured graphite, typically a large excess of H is required, 99 % by volume. This is because the atomic H in the gas mixture preferentially etches the graphite, rather than diamond. Furthermore, the substrate temperature is usually above 700 °C to favour diamond growth over amorphous carbon. Figure 3-9 shows a phase diagram for diamond growth, also known as a Bachmann diagram, from which can be seen that the regime for diamond growth is relatively small compared to graphitic or no growth.

Hot filament CVD (HFCVD) uses, as the name suggests, a hot filament to activate the gas phase carbon. The filament is heated to temperatures in excess of 2000 °C and therefore, needs to be made of a metal that can withstand such temperatures and not react significantly with the gas mixture. Commonly used metals include tungsten and tantalum, although they do react with C to form metal carbides. This, in turn, makes them brittle, reducing their lifetime. Rhenium is a longer lasting, but more expensive alternative, as it does not carburize as easily. HFCVD is usually performed at pressures of 20 – 40 mbar, although the non-S.I. unit torr is often used for historical reasons. The substrate usually rests on a heater as the filaments provide insufficient heating. Unfortunately, the filaments are particularly sensitive to corrosive or O containing gases and, as such, this limits the variety of gas mixtures that can be used. Furthermore, it is almost impossible to avoid contamination of the diamond film from the filament material. Despite this, HFCVD is relatively cheap and easy to setup and run, achieving growth rates of several  $\mu\text{m h}^{-1}$ .

Microwave plasma assisted CVD (MWCVD) reactors couple microwave energy into gas-phase electrons which then transfer their energy to the precursor molecules through

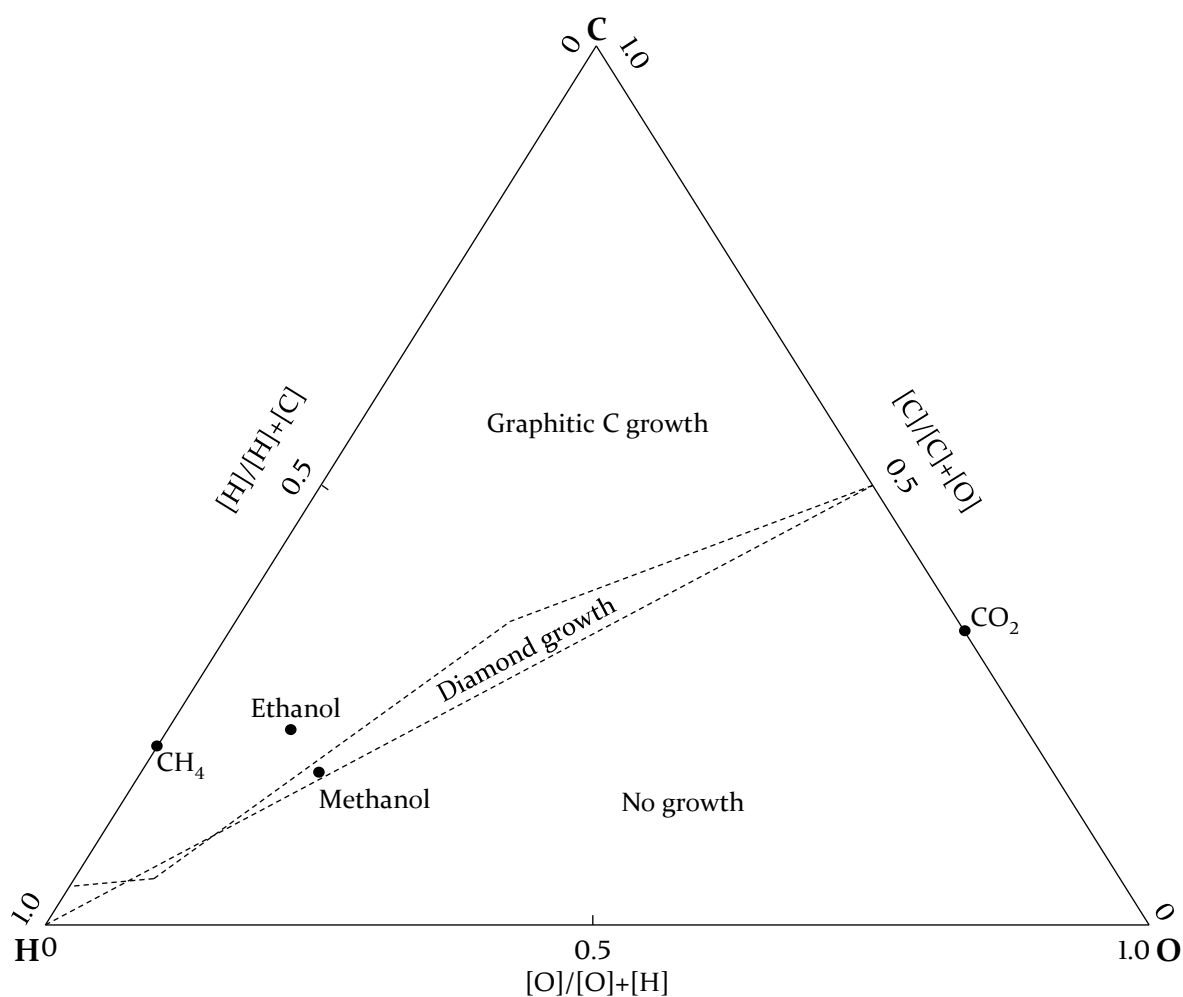


Figure 3-9 – A Bachmann C-H-O phase diagram for diamond deposition. The area between the dotted lines indicates where diamond growth will occur. Recreated from<sup>175</sup>

collisions leading to heating and dissociation of these molecules, before being deposited on the substrate which sits just below the plasma. Because of this, a major difference is that the substrate needs to be cooled rather than heated. Despite being significantly more expensive than HFCVD, MWCVD has several distinct advantages which make it more popular. The lack of filament means that not only is MWCVD cleaner by default, it also allows a wider variety of gas mixtures, including those with O. The inclusion of O in the feed gas mixture can lead to faster growth rates and higher quality diamond with fewer defects. However, it is also more difficult to control O-containing plasmas. MWCVD is also more scalable with input power, allowing higher growth rates of  $>10 \mu\text{m h}^{-1}$ .

### 3.3 Raman Spectroscopy

Raman spectroscopy works on the principle of inelastic scattering of photons, known as Raman scattering, and yields information about the vibrational modes of the system. When photons are scattered by atoms, they are predominantly elastically scattered, which is known as Rayleigh scattering. Such scattered photons have the same energy ( $h\nu$ ) as the incident photons but differ in the direction of travel. A small fraction of scattered photons, approximately 0.1 ppm, however, are scattered inelastically meaning they have a different, usually lower, energy than the incident photons. At the same time, due to conservation of energy, the sample either gains or loses energy, typically vibrational energy. When the photons lose energy, this is known as Stokes Raman scattering, whilst when they gain energy, it is referred to as anti-Stokes Raman scattering, as shown in Figure 3-10(a). Raman spectroscopy is similar and complementary to infra-red spectroscopy, as a vibrational mode that is inactive in one, is often active in the other. A perfect diamond, for example, does not produce an IR spectrum as there is no change in the dipole moment. Raman scattering, on the other hand, requires a change in the polarizability of the vibrational mode, so diamond is Raman active. Raman is particularly sensitive to the ratio of  $sp^2$  to  $sp^3$  carbon and, therefore, is an ideal non-destructive and easy to use method for checking the quality of grown diamond films. Diamond exhibits a sharp, narrow  $sp^3$  peak at a Raman shift of  $1332\text{ cm}^{-1}$ , and a broader  $sp^2$  peak at approximately  $1550\text{ cm}^{-1}$ . A typical Raman spectrum of single crystal diamond is shown in Figure 3-10(b).

### 3.4 Summary

The theoretical aspects of the experimental techniques discussed in this chapter are necessary to gain a proper understanding of the diamond surfaces that are prepared and discussed in chapters 5 and 6. CVD was used to grow the diamond, while Raman spectroscopy was used as an easy and non-destructive method to determine the quality of the grown diamond films. Photoemission spectroscopy (UPS and XPS) was used to analyse these samples, as such special attention is given to the data analyses for these techniques as this significantly affects any conclusions drawn.

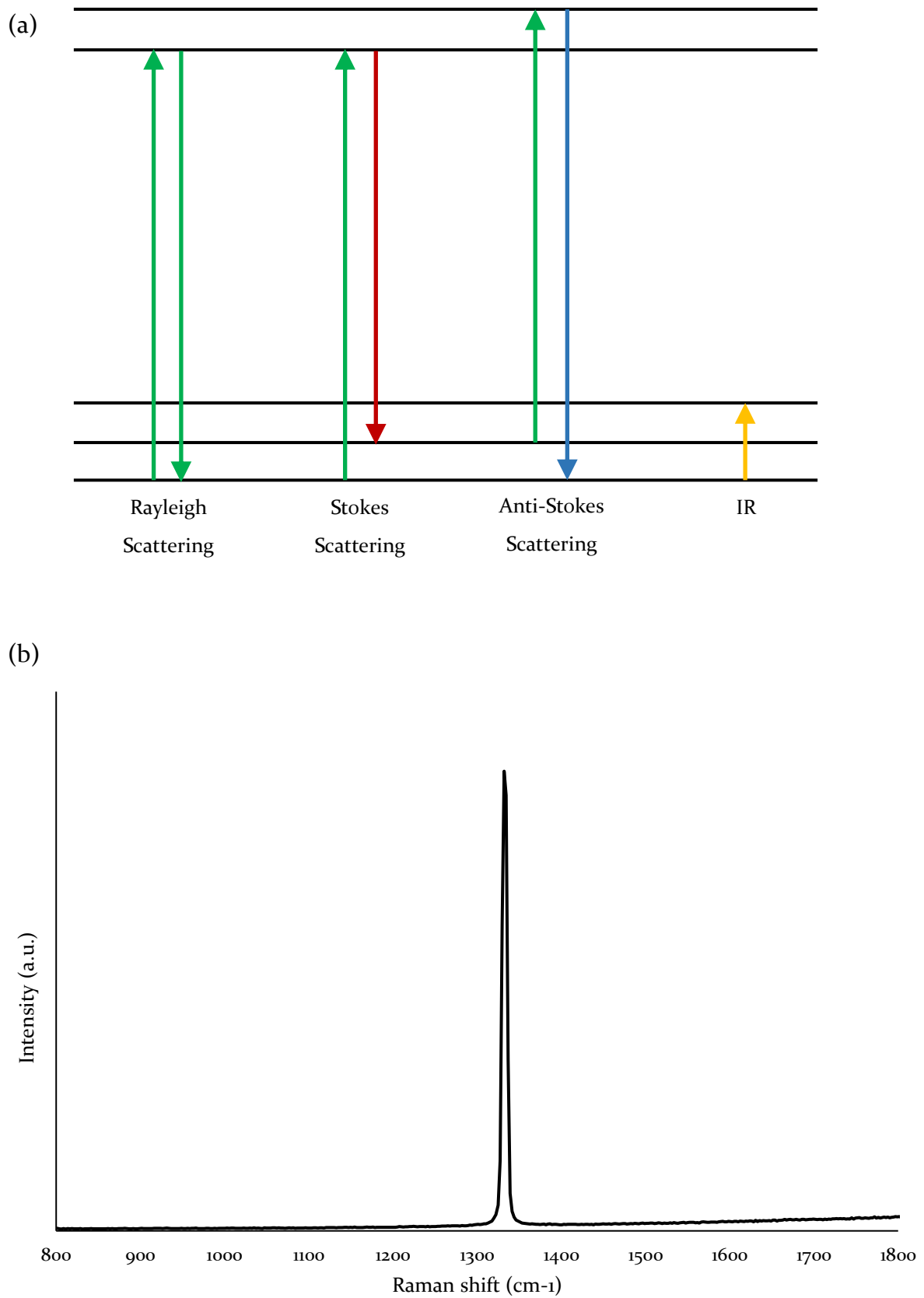


Figure 3-10 – (a) Energy level diagram of the various scattering processes involved in Raman spectroscopy and (b) a Raman spectrum of single crystal diamond.

## CHAPTER



# Methodology and Instrumentation

"Imagination is more important than knowledge. For knowledge is limited, whereas imagination embraces the entire world, stimulating progress, giving birth to evolution."

Albert Einstein - What Life Means to Einstein (1929)

The formulation of a problem is often more essential than its solution, which may be merely a matter of... experimental skill. To raise new questions, new possibilities, to regard old problems from a new angle, requires creative imagination and marks real advance in science.

Albert Einstein and Léopold Infeld - Evolution of Physics (1938, 1966), 92

## 4.1 Introduction

This chapter will discuss the instruments and experimental methodologies used to prepare and analyse the various terminations on the diamond surface. Preparation of these surfaces, from handling, through diamond growth, to surface termination will be discussed. Additionally, the instruments used during the XPS and UPS analysis and subsequent metal deposition will be explored.

## 4.2 Sample Preparation

The surface of the purchased single-crystal diamond (SCD) samples contained metal particles visible under a microscope (Zeiss – AxioLab A, x100 magnification), most likely due to the polishing process. To remove this contamination, the samples were subjected to reflux in conc. sulphuric acid and potassium nitrate (5 g per 100 ml of sulphuric acid used) for 6 hours. When samples were cleaned between experiments to remove terminations, this process was repeated, although shorter times sufficed, typically 30 – 60 min, as confirmed by XPS analysis. Following this, the samples were H-terminated as discussed in section 4.5.1 as the H plasma further cleans and smooths the surface.<sup>46</sup>

When samples were introduced into the ultra-high vacuum (UHV) environment of the NanoESCA, they were first annealed at 300 °C for 30 min. 300 °C is sufficient to desorb any physisorbed atmospheric species caused by the sample being transported in ambient conditions, while not removing any chemically bonded species. Although samples were initially sonicated in acetone, distilled water, and isopropyl alcohol, in accordance with procedures used in the semiconductor industry,<sup>144</sup> this was found to result in contamination such as sodium and silicon, most likely from impure solvents or the walls of the vessels used, as discussed in section 3.1.4.7. As a result, it was decided not to sonicate, or otherwise clean, the samples between the termination procedures and introduction into the NanoESCA. Considering that the samples are cleaned before termination, and with careful sample storage in transit, this was found to yield the cleanest surfaces.

## 4.3 Hot Filament CVD Reactor

During photoemission spectroscopy, as an electron is emitted, a positive charge is left behind which is either neutralised or continues to build up depending on whether the sample is conductive or insulating. A build-up of charge affects the observed binding energies. Because the purchased intrinsic diamond was non-conducting, to avoid charging effects during XPS and UPS, a thin layer ( $\sim 1 \mu\text{m}$ ) of conducting boron-doped single crystal diamond was grown on top of the intrinsic diamond, using a hot-filament chemical vapour deposition (HFCVD) reactor.

The base pressure of the HFCVD system was  $\sim 75$  mtorr and the filaments were typically composed of tantalum wire with a diameter of 0.25 mm. The operating pressure was typically 20 torr (controlled by a manual needle valve), and the gas mixture was composed of 0.05 sccm of diborane (99.995 %), 204.95 sccm of H<sub>2</sub> (99.995 %), and 2 sccm of methane (99.995 %). The filaments were operated at 25 A and 10 V, while the substrate heater was operated at 4 A and 4 V. The purpose of the substrate heating (200 – 300 °C) was primarily to eliminate moisture from the growth surface. The reactor was air cooled using external fans. 1 h of growth resulted in approximately 1  $\mu\text{m}$  of boron-doped diamond.<sup>145</sup>

## 4.4 Raman

To analyse the quality of the grown boron-doped diamond layer, Raman spectroscopy was used. The system was a Renishaw Raman 1000 with a holographic grating of 1200 lines  $\text{mm}^{-1}$  dispersed onto a CCD detector (512x256 pixel array). The system was equipped with three lasers, one helium-cadmium laser which emits UV light (325 nm), and two diode lasers which emit green (514 nm) or near-infrared (785 nm) light. The UV wavelength is more sensitive to  $\text{sp}^3$  carbon, while the nIR wavelength is more sensitive to  $\text{sp}^2$  carbon. The green laser is used most commonly, as this wavelength offers a good compromise between  $\text{sp}^3$  and  $\text{sp}^2$  carbon. For single-crystal diamond, the 25 mW green laser was used at 10 % power to prevent signal saturation.

## 4.5 Terminations

Before terminating samples in preparation for experiments, all samples were acid washed and H-terminated to provide a clean and easily reproducible initial surface. Most of the termination procedures outlined below further clean the surface as well as terminate with the desired species.

### 4.5.1 Hydrogen

Hydrogen termination was performed in a microwave assisted CVD (MWCVD) reactor. The substrate rested on a metallic disk (typically Mo), which was separated from the water-cooled baseplate by a thin circular wire (also typically Mo). By varying the thickness of the wire, the temperature of the substrate could easily be controlled. A wire of 9 mm diameter was typically used for H termination. The reactor was an ASTeX-style MWCVD reactor with a maximum microwave power output of 1.5 kW. The sample temperature was measured using a single-wavelength pyrometer, which had been calibrated with a dual-wavelength pyrometer in a H plasma. This is because the H plasma does not interfere with the pyrometer whereas a methane plasma emits in one of the wavelengths used by the pyrometer. The emissivity setting (i.e. how much light a material emits at a given temperature) was 0.13 for single-crystal diamond. The base pressure of the reactor was ~10 mtorr. The pressure was regulated using a computer-controlled butterfly valve. A flow rate of 300 sccm of H<sub>2</sub> (99.99995 %) was used.

To achieve optimal H termination, three different parameter regimes were used, which had previously been determined by the research group.<sup>146</sup> First, the sample was exposed to a H plasma with a microwave power of 1150 W and a pressure of 80 torr for 2 min to achieve a substrate temperature of ~820 °C. This high-power plasma cleaned the sample by etching surface species, as confirmed by XPS. The power and pressure were then reduced to 650 W and 30 torr, respectively, which achieved a substrate temperature of ~500 °C. This lower temperature facilitated H termination of the diamond surface. The microwave power was then reduced to 0 W until the plasma extinguished while the H flow was maintained at 30 torr for a further 2 min to complete H termination and clean the chamber.

## 4.5.2 Oxygen and Nitrogen

### 4.5.2.1 UV-Ozone Treatment

The sample was exposed to ozone generated by deep ultraviolet radiation for 30 min. This treatment is typically used to clean organic material from glass, metal, or ceramics. For diamond however, this can be used to O-terminate the surface. The system (Jelight, 42A-220) uses ultraviolet light (253.7 nm) to generate ozone at atmospheric pressure. As ozone is very reactive, it removes any surface termination from the diamond, bonds to the diamond and readily dissociates to leave an O-terminated diamond surface.

### 4.5.2.2 Acid Treatment

Powerful oxidising agents are also routinely used to O-terminate diamond. Various acids or combinations of acids are used in the literature.<sup>61,71</sup> In this work, conc. sulfuric acid and potassium nitrate ( $\text{KNO}_3$ ) were used. Approximately 5 g of potassium nitrate were used per 100 ml of sulfuric acid. The sample was refluxed in the acidic mixture at  $>200\text{ }^\circ\text{C}$  for 30 min to yield the O termination.

### 4.5.2.3 Plasma Treatment

The 'Terminator reactor' is a repurposed Edwards sputter coater (SI50A). The reactor is a DC parallel plate plasma reactor with a maximum power of 300 W. The power supply remained unchanged, while the electrode assemblies were modified to change the interelectrode gap, which along with the power and pressure, were optimised to generate a uniform plasma between the electrodes (electrode diameter - 70 mm). The base pressure of the system was below the lower readout limit of the attached pressure gauge ( $<5\text{ mtorr}$ ). The operating pressure was typically 1 torr, which was controlled by a manual needle valve. The flow rate was typically 10 sccm of  $\text{O}_2$  (99.995 %), or 5 sccm for ammonia (99.99 %).

The sample was exposed to a plasma of the relevant gas. For O termination, this was an  $\text{O}_2$  plasma, to which the sample was exposed for 7 seconds. This has previously been determined to be the optimum duration by the research group.<sup>147</sup> Shorter times led to incomplete O coverage while longer times etched and damaged the sample surface. For N termination, the plasma was composed of ammonia ( $\text{NH}_3$ ), though experiments with

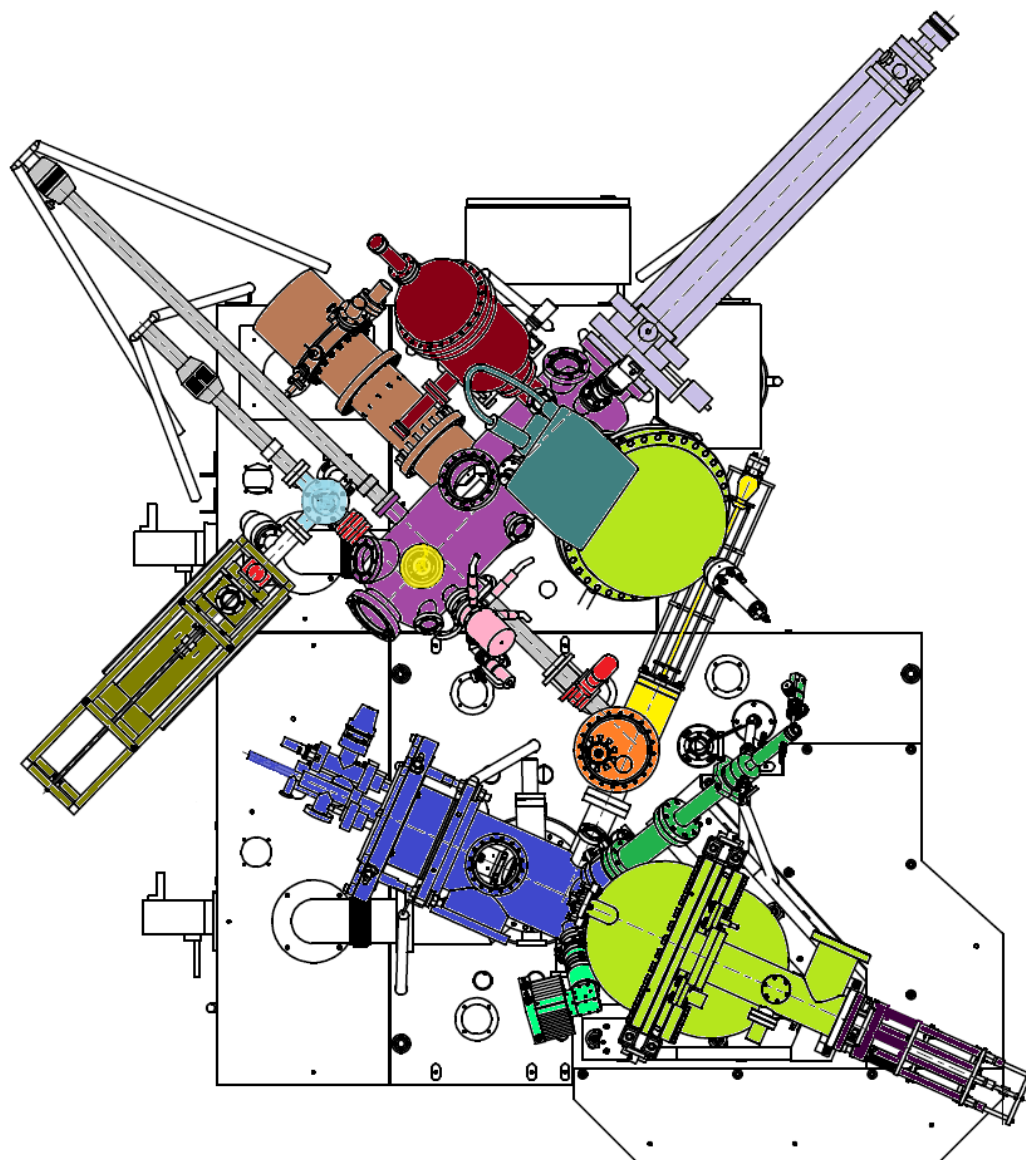
N<sub>2</sub> were also performed, as discussed in section 5.4. For typical N termination, the sample was exposed to the ammonia plasma for 3 min. This reactor was also capable of terminating diamond with other surface terminations such as fluorine by using SF<sub>6</sub> or C<sub>3</sub>F<sub>8</sub>, but these are not relevant to this work.<sup>47</sup>

### 4.5.3 Titanium

Ti was deposited *in-situ* in the fabrication chamber of the NanoESCA. This was achieved using a four-pocket thin-film e-beam evaporator. A high-purity (99.99 %) Ti rod was used. When first inserted into the e-beam evaporator, the tip of the rod was melted to ensure a consistent evaporation rate. The quantity of Ti deposited on the diamond surfaces was primarily monitored using XPS, despite a quartz microbalance being available as discussed in section 4.6.2.

## 4.6 NanoESCA

The NanoESCA is a UHV system equipped with a variety of analysis techniques ideally suited for surface-sensitive experiments. Figure 4-1 shows the schematics for the NanoESCA at the University of Bristol.



Analysis Chamber	Multi-Channel Detector	Wobble Sticks
Preparation Chamber	Monochromatic X-ray Source	Manipulator
Vacuum Suitcase	Helium UV Light Source	Sample Storage Carousel
Electron Analyser	Mercury UV Light Source	Gate Valves
CCD Camera	Magnetic Arms	Fast Entry Load Lock

Figure 4-1 – A top-down view, colour-coded schematic diagram of the NanoESCA at the University of Bristol.

#### 4.6.1 Preparation and Analysis Chamber

As shown in Figure 4-1, the NanoESCA had two main chambers. The first chamber, known as the preparation chamber, performed heating, argon sputtering, X-ray photoelectron spectroscopy (XPS) and spot profile analysis - low energy electron diffraction (SPA-LEED). The second chamber, known as the analysis chamber, allowed ultraviolet photoelectron spectroscopy (UPS), energy filtered photoemission electron microscopy (PEEM), and micro- angle resolved photoemission spectroscopy ( $\mu$ ARPES). The XPS chamber was equipped with a monochromatic aluminium X-ray source (1486.6 eV) and a non-monochromatic aluminium and magnesium (1253.6 eV) twin anode source. The monochromatic source offered excellent energy resolution, whereas the twin anode source offered higher intensity.

Figure 4-2 shows the double hemispherical analyser which made the NanoESCA unique. It enabled different operating modes, from sample navigation (bottom CCD camera) using PEEM, through UPS which uses the channeltron detector, to imaging ESCA mode (top CCD camera). The energy-filtered imaging enabled chemical-state and WF mapping as well as  $\mu$ ARPES, which allowed the direct analysis of the distribution of electrons in reciprocal space.

The analysis chamber was equipped with a non-monochromatic mercury (5.2 eV) and a monochromatic helium gas-discharge (21.2 eV) lamp. For UPS, as spectroscopy is not an imaging technique, both hemispherical analysers were not required. Therefore, the channeltron detector after the first electron analyser, was used, as shown in Figure 4-2.<sup>148</sup>

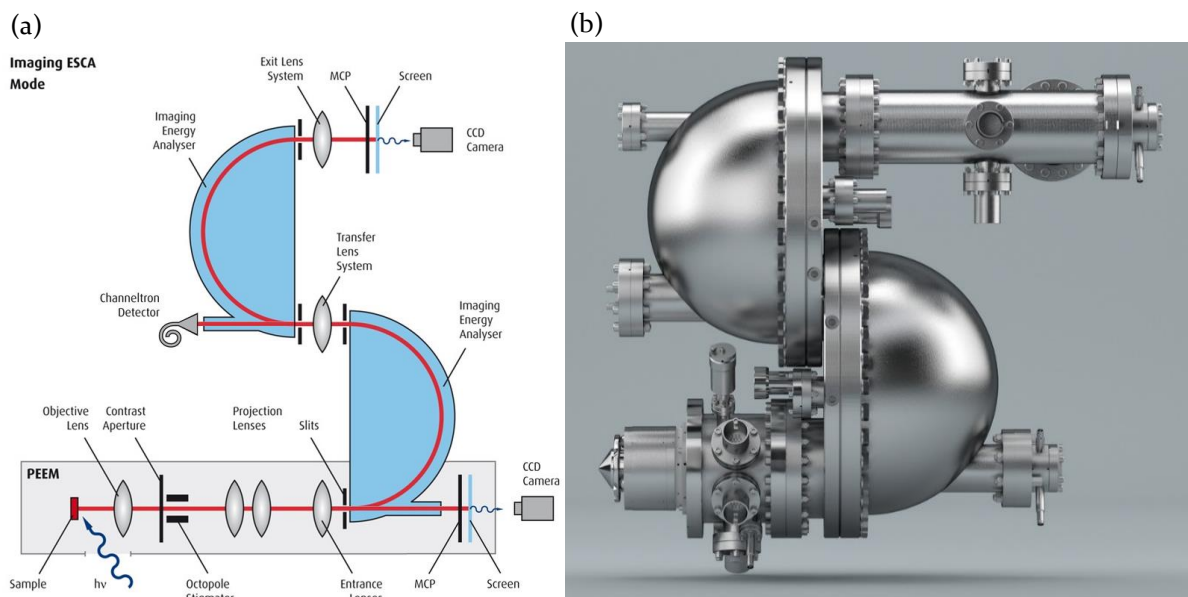


Figure 4-2 – The schematics (a) and image (b) of the IDEA (imaging double hemispherical energy analyser).

#### 4.6.2 Fabrication Chamber

Instead of the vacuum suitcase shown in Figure 4-1, a fabrication chamber for *in situ* sample preparation could alternatively be attached. This chamber consisted of a heated sample stage, a thermal gas cracker, a four-pocket thin-film e-beam evaporator (Mantis QUAD-EV-C), and a quartz microbalance (QMB) to monitor material deposition. The QMB (Infinicon SQM-160) was placed in the same position as the sample for deposition. This meant that the QMB could not be used to monitor the material deposition rate during deposition, as may be possible in other setups, but rather to calibrate the deposition rate prior to sample preparation. Furthermore, this QMB was designed for thick films, rather than the thin films produced in this work, with units of  $\text{k}\text{\AA}$  for layer thickness and  $\text{\AA s}^{-1}$  for deposition rate. This made the monitoring of the low deposition rates required for a monolayer ( $\sim 3 \text{\AA}$ ) of material over several minutes challenging.

#### 4.6.3 X-ray Photoelectron Spectroscopy

All work presented here was performed using the monochromatic aluminium source. To align samples with the detector, a quick scan between 290 – 220 eV with a pass energy of 50 eV, a dwell time of 0.05 s, and step size of 0.5 eV, was performed. This energy range included the C 1s and Mo 3d peak, allowing the C signal from the diamond

to be maximised while eliminating the molybdenum signal from the sample holder. Once the sample was aligned, a fast survey scan across the whole energy range (1200 – 0 eV) was performed with the same parameters as the alignment scan to determine an approximate sample composition. Due to the large step size and small dwell time, this type of scan was fast but yielded a very noisy background, with only the major elements being visible. A regular survey scan, such as those presented in the following chapters, had the same parameters except for the dwell time, which was increased to 0.25 s, for a smoother background signal. This survey scan gave a detailed view of the elements present on the surface.

To analyse the bonding environments of these elements, a high-resolution core-level scan was required. The energy range depended on the element in question. Taking carbon as an example, the C 1s peak was typically between 290 – 280 eV, so a scan between 293 – 277 eV would be performed. 3 eV on either side of the peak allowed for better fitting of the background signal. The pass energy for these types of scans was 20 eV, dwell time 0.5 s, and step size 0.05 eV. The smaller step size increased the resolution, the longer dwell time improved the signal-to-noise ratio, while the decrease in pass energy increased the energy resolution, but also decreased the signal intensity. A further parameter that affected the signal-to-noise ratio was the number of scans performed. A number of repetitions of the same scan were performed and added together to further reduce the background signal. The number of scans necessary depended on the size of the peak in question. For example, the C 1s peaks examined in this work were typically large, as ~90% of the signal came from the diamond substrate. Therefore, this peak was already smooth as the signal-to-noise ratio was already high, so 2 – 3 scans typically sufficed. For elements with much smaller concentrations, such as O or N, a larger number of scans were required. This was because the peaks were relatively small, and therefore a single scan was very jagged due to the low signal-to-noise ratio. The O 1s peaks examined here used between 6 – 16 scans depending on the quantity of O present.

#### 4.6.4 Work Function Maps and UV-Photoelectron Spectroscopy

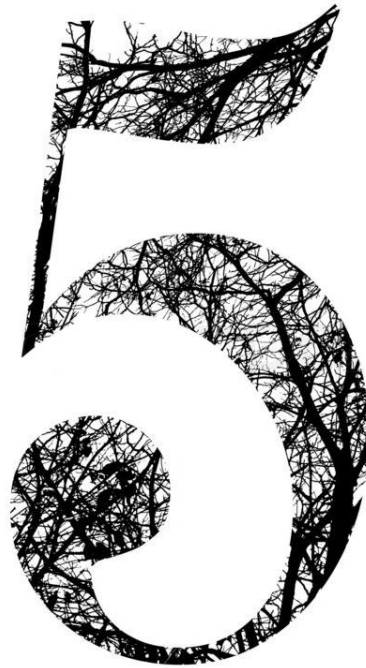
Though the WF maps and UPS gave similar information, they required different procedures, as the maps were an imaging technique while UPS was not. When the instrument had been safely switched on, and the sample was approximately in the correct position, the mercury lamp was used for sample navigation. Whilst this lamp was not monochromatic, it was brighter and had a bigger spot size than the helium light source. The largest field of view was selected ( $\sim 1000 \mu\text{m}$ ) and the sample was slowly moved until the focus was correct and the sample was visible. Next, the light source was switched to the helium lamp, and various parameters such as the stigmators and focus were optimised. The field of view was then changed to  $\sim 78 \mu\text{m}$ , the contrast aperture to  $150 \mu\text{m}$ , and various parameters were once again optimised. To create the images required for the WF map, an image was taken every  $0.025 \text{ eV}$  (dwell time  $10 \text{ s}$ ) for  $1 \text{ eV}$  either side of the WF. An approximate WF was determined by reviewing the energies in snapshot mode (dwell time  $0.2 \text{ s}$ ). As example, if the approximate WF was around  $3 \text{ eV}$ ,  $80$  images were taken at  $0.025 \text{ eV}$  intervals from  $2 - 4 \text{ eV}$ , with a dwell time of  $10 \text{ s}$ . These images were then processed to create the WF maps shown in chapters 5 and Appendix B – Work Function Maps.

For UPS, the contrast aperture was changed to be fully open, and the detector was changed from the CCD camera used for imaging to the channeltron detector. For both the channeltron detector and the camera on this system, care was taken not to exceed the maximum signal intensity as this can result in damage to the detector. For the channeltron detector, this necessitated closing the mechanical iris to restrict the number of photoelectrons reaching the sensor, while for the camera this was achieved by controlling the voltage of the microchannel plate detector. UPS spectra were typically recorded between  $0$  and  $22 \text{ eV}$ .

## 4.7 Summary

In this chapter, the technical details of the experimental techniques and systems used were discussed. These included initial sample preparation, such as cleaning and diamond growth using both hot filament and microwave assisted CVD reactors. Various techniques used to functionalise the surface were discussed, from simple mono-element terminations to metal deposition. The UHV system most commonly used for data analyses (NanoESCA) was discussed in detail, in particular with regard to UPS and XPS.

## CHAPTER



# Simple Terminations

“Nothing in life is to be feared, it is only to be understood. Now is the time to understand more, so that we may fear less.”

Marie Curie - *Our Precarious Habitat* (1973)

## 5.1 Introduction

H-terminated diamond exhibits an NEA, facilitating electron emission at low temperatures, as discussed in Chapter 1. It is one of the most researched diamond terminations because diamond grown by CVD is naturally H-terminated. While the H termination has favourable electronic properties for electron emission, with an NEA of -0.8 to -1.3 eV, as discussed in section 1.5.1, it lacks stability at elevated temperatures. H desorbs at temperatures above 700 °C and leaves behind a surface with a PEA, severely limiting subsequent electron emission. O and N terminations exhibit PEA values, as discussed in sections 1.5.2 and 1.5.3, due to the dipole present on the diamond surface now having the negative charge outermost. Depositing a metal on these oxidised or nitrogenated diamond surfaces reverses the polarity of the surface dipole and therefore, TiO-diamond and TiN-diamond termination schemes are promising candidates for an NEA surface, while the strong covalent bonding between all the surface atoms suggests that the surface is likely to exhibit greater stability at elevated temperatures. The binding energies for the various functional groups referred to in the following chapter are discussed in section 3.1.4.4.

However, before the metal layer is deposited it is beneficial to gain a deeper understanding of diamond surfaces-terminated with a range of simple atoms such as H, O, and N. These studies form the basis of this chapter.

## 5.2 H-terminated Diamond

The following section focuses on H-terminated diamond to facilitate a comparison to literature which can be built upon with subsequent terminations. Figure 5-1(a) shows the XPS survey spectrum of H-terminated diamond, prepared as discussed in sections 3.1.4 and 4.5.1. The spectrum shows only a single peak, the C 1s peak at 284.5 eV. There is no peak for H, as the element does not have any core electrons to emit in XPS. As such, the only way to confirm the H termination is by the absence of any other elements in the spectra, especially O. A clean (100) diamond surface has two dangling bonds per C atom, while a 2x1 surface reconstruction where two of the C atoms bond to each other, there is one dangling bond per surface atom. If the surface was clean (i.e. by removal of all terminating H or other species) as discussed in section 2.3.1, it would immediately oxidise upon exposure to air, because the dangling bonds of a clean surface are energetically unfavourable. Therefore, the absence of any other elements in Figure 5-1(a) suggests that the surface is H-terminated. The spectrum bears a close resemblance to other spectra of H-terminated diamond found in the literature.<sup>37</sup> The broad peaks above the C 1s peak, at approximately 320 and 350 eV, are energy loss features due to the sample interaction with photons producing collective excitations (plasmons) which run as longitudinal charge density oscillations through the volume of the solid and along its surface.<sup>149</sup>

Figure 5-2 shows the work-function map of a H-terminated sample showing values between 3.7 and 3.9 eV, which is in agreement with the value of  $3.8 \pm 0.1$  eV obtained from the UPS spectrum from Figure 5-1(b). These values are also consistent with WF values found in literature (3.7 – 4.2 eV) as discussed in section 1.5.1. While the WF map is from a relatively small sample area (78  $\mu\text{m}$ ), the UPS spectrum is obtained from a significantly larger area, confirming that the sample is uniform, and the WF map is representative of the whole sample. The purple spots indicating regions of higher work-function are a topographical effect of the instrument. While UPS is not usually sensitive to the sample topography, the NanoESCA uses a high voltage extractor (typically 12 kV) to increase the photoemission signal sufficiently for imaging. Therefore, if the sample is uneven, the parts closer to the extractor have a slightly higher energy, as can be seen in

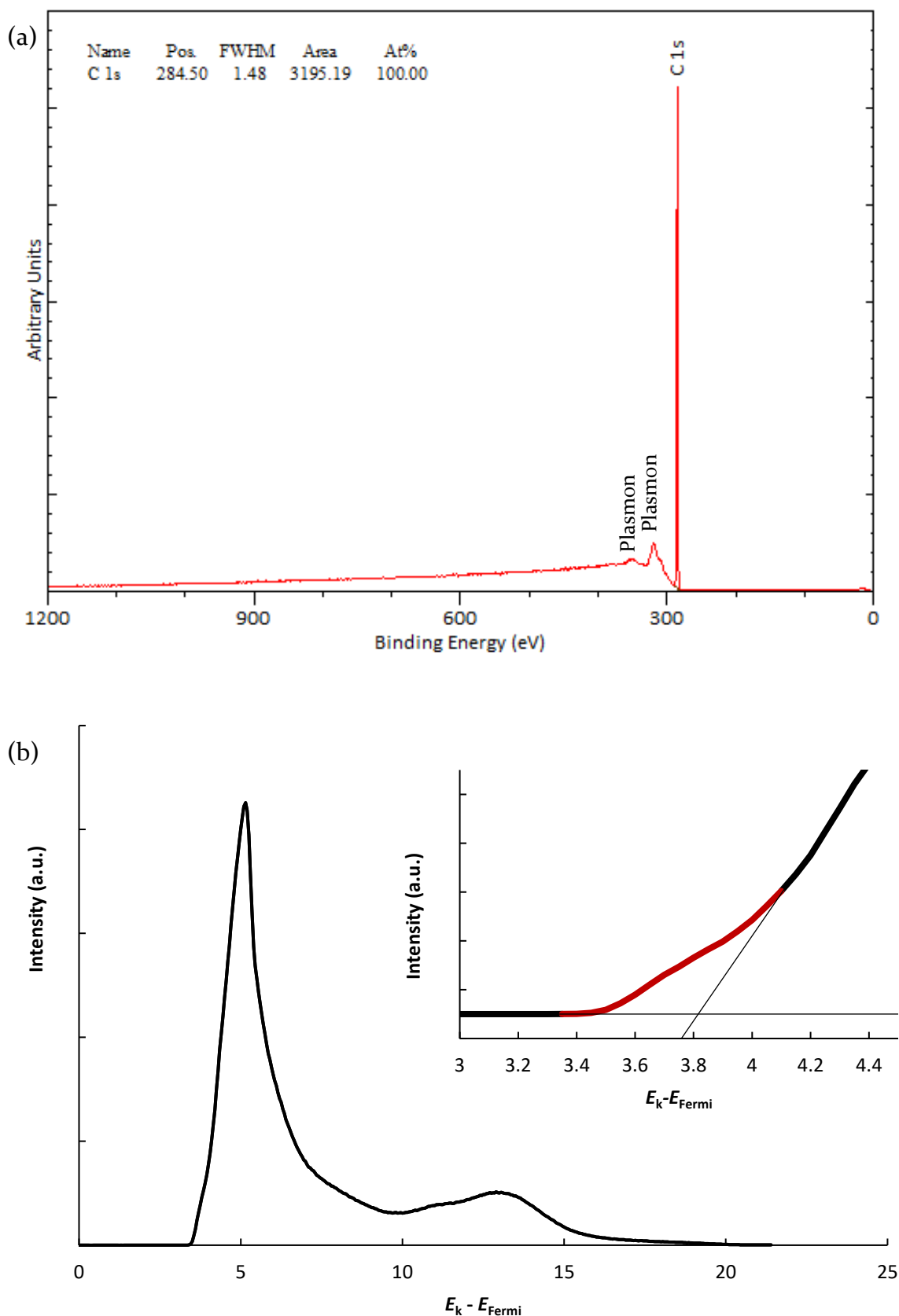


Figure 5-1 – (a) The XPS wide-scan survey spectrum of H-terminated (100) diamond, and (b) the associated UPS spectrum giving a WF of  $3.8 \pm 0.1$  eV, as shown in the inset. This type of spectrum is discussed in more detail in section 3.1.3.

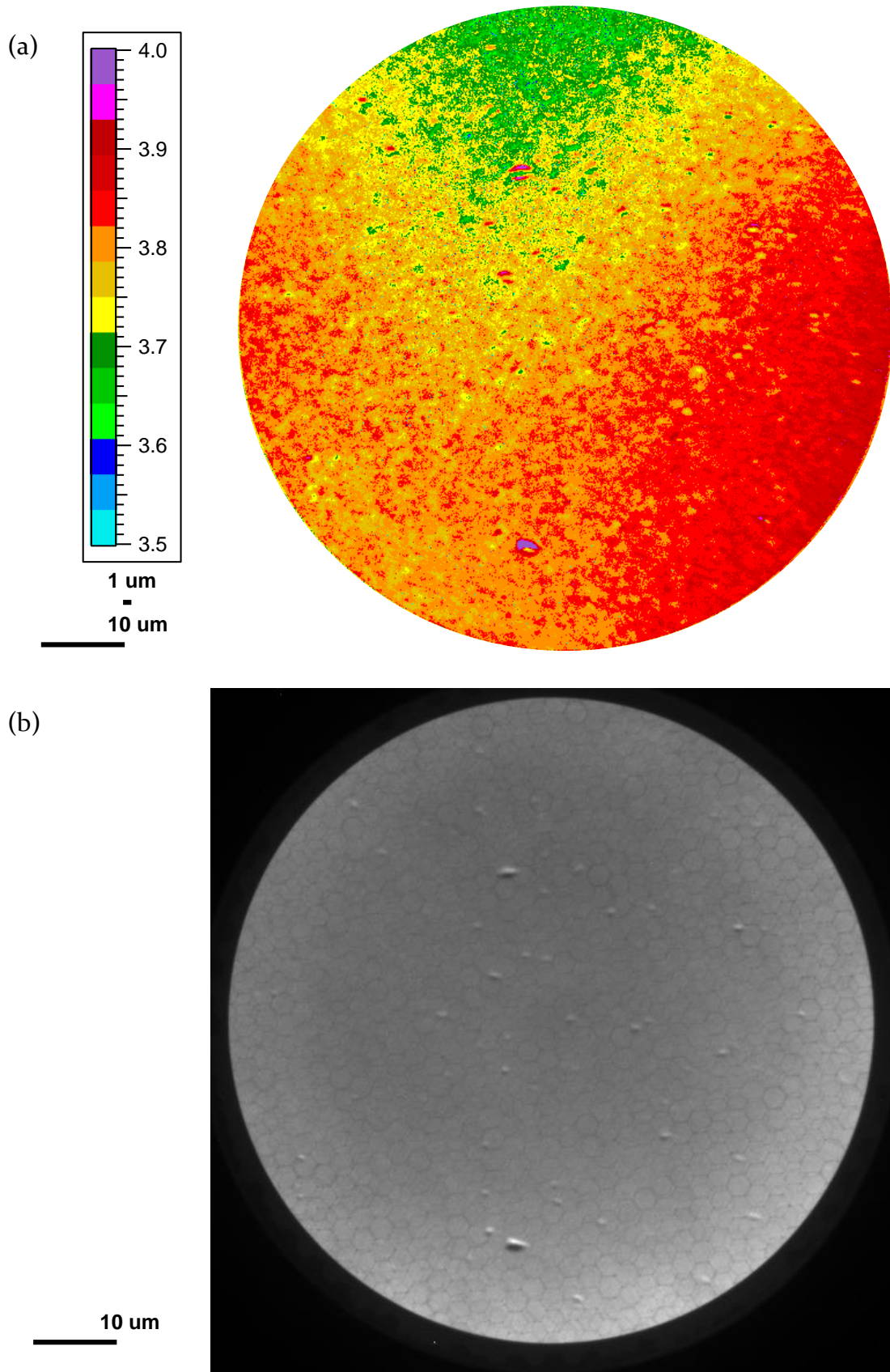


Figure 5-2 - The WF map of H-terminated diamond (a), and one of the PEEM images used to construct it (b). The field of view is  $\sim 78 \mu\text{m}$ . The hexagonal pattern in (b) is due to the multi-capillary packing structure of the MCP.

Figure 5-2 where the purple spots in the work-function map correspond to the peaks in the PEEM image.

### 5.2.1 C 1s Core-level Spectra

The XPS C 1s core-level spectrum of H-terminated diamond was used to determine the best line-shape for fitting the components of the C 1s peak, as this spectrum should be simpler than for other surface terminations. However, as shown in Figure 5-3(a), when trying to fit a typical symmetric line shape commonly used for fitting C, the resulting 9 components seem dubious, and unlikely to be realistic for a sample primarily composed of two elements, C and H. In particular, the presence of 3 large components is questionable. If the component at 284.3 eV was assigned as the  $sp^3$  peak, and 284.7 eV as the C-H peak, the remaining components would have to originate from contamination. It is important to consider that the lack of other elements in the survey spectra may indicate that other elements are present below the limit of detection for this technique, rather than being completely absent from the sample. However, considering the survey spectra presented no other elements, the component at 285.2 eV is too large to arise from a trace contaminant.

Considering the asymmetric nature of metal peaks, and the conductive nature of the examined boron doped single-crystal diamond samples, an asymmetric line shape was fitted to the spectrum, as shown in Figure 5-4. The C 1s peak is thought to be asymmetric because of the particularly strong band bending in diamond leading to the various C layers from the bulk diamond emitting at slightly different energies as shown in Figure 5-5.<sup>46</sup> As such, the final spectrum can be fitted with a total of 5 peaks, 2 large and 3 minor peaks. The largest component at 284.4 eV represents the  $sp^3$  peak, whilst 285.0 eV arises from the C-H peak, and the remaining 3 smaller peaks suggest the presence of other elements below the detection limit of the survey scan.

Due to the core-level-scans having a significantly higher lateral energy resolution than the survey scan, it is possible to see the traces of elements that may not be visible in the survey spectrum. As the three smaller components are in the energy range commonly associated with C-O bonds, an O 1s core-level scan was performed to determine whether there is any trace amounts of O present (Figure 5-6). This is especially pertinent

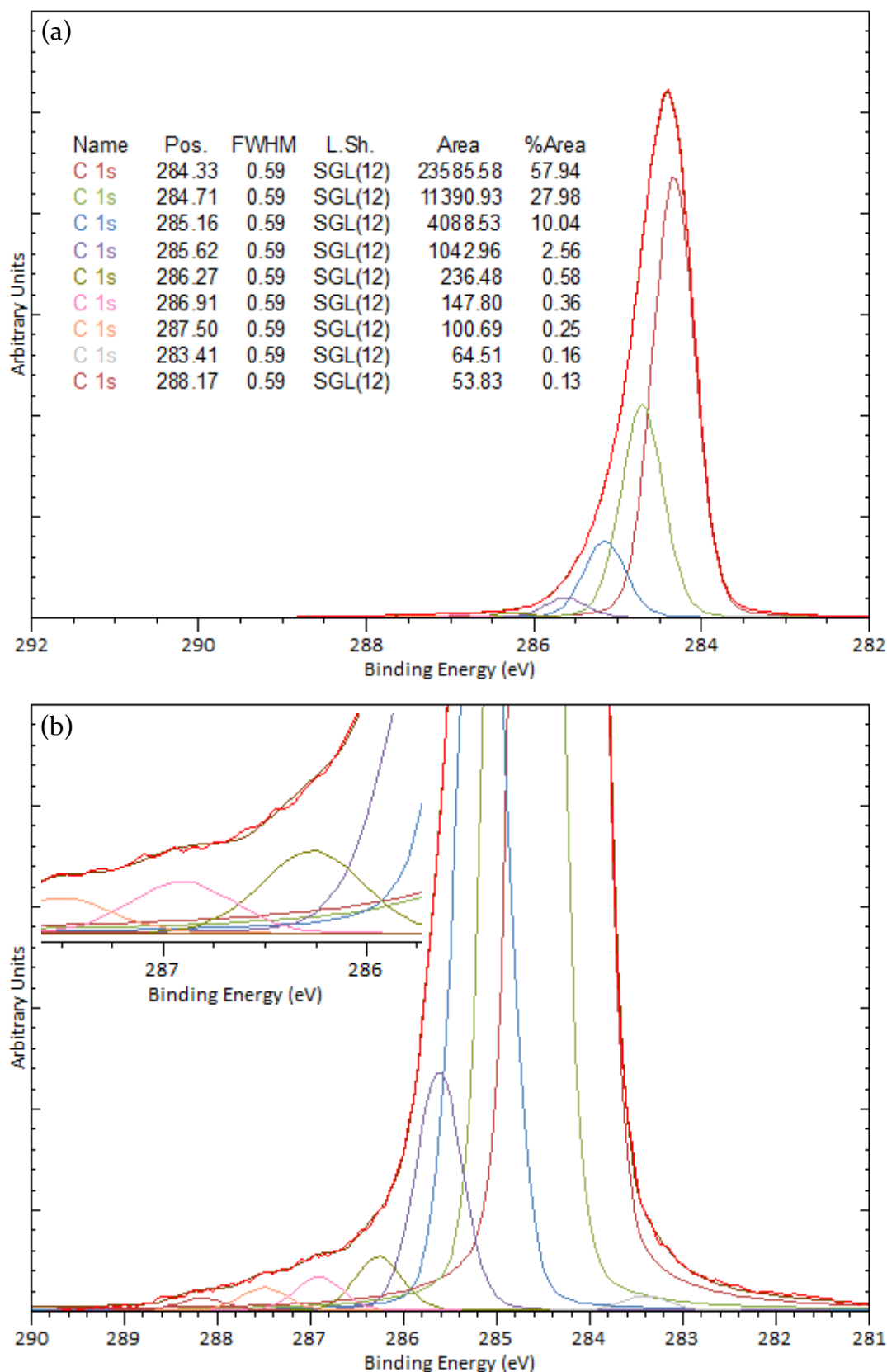


Figure 5-3 – (a) A H-terminated C 1s spectrum fitted with a symmetric SGL(12) line shape, and (b) a higher magnification of the shoulder region of that same spectrum where the black line is the sum of all the components. The inset shows the black envelope overlapping with the experimental data (red line) which can be difficult to see when the data fits well, except at high magnification.

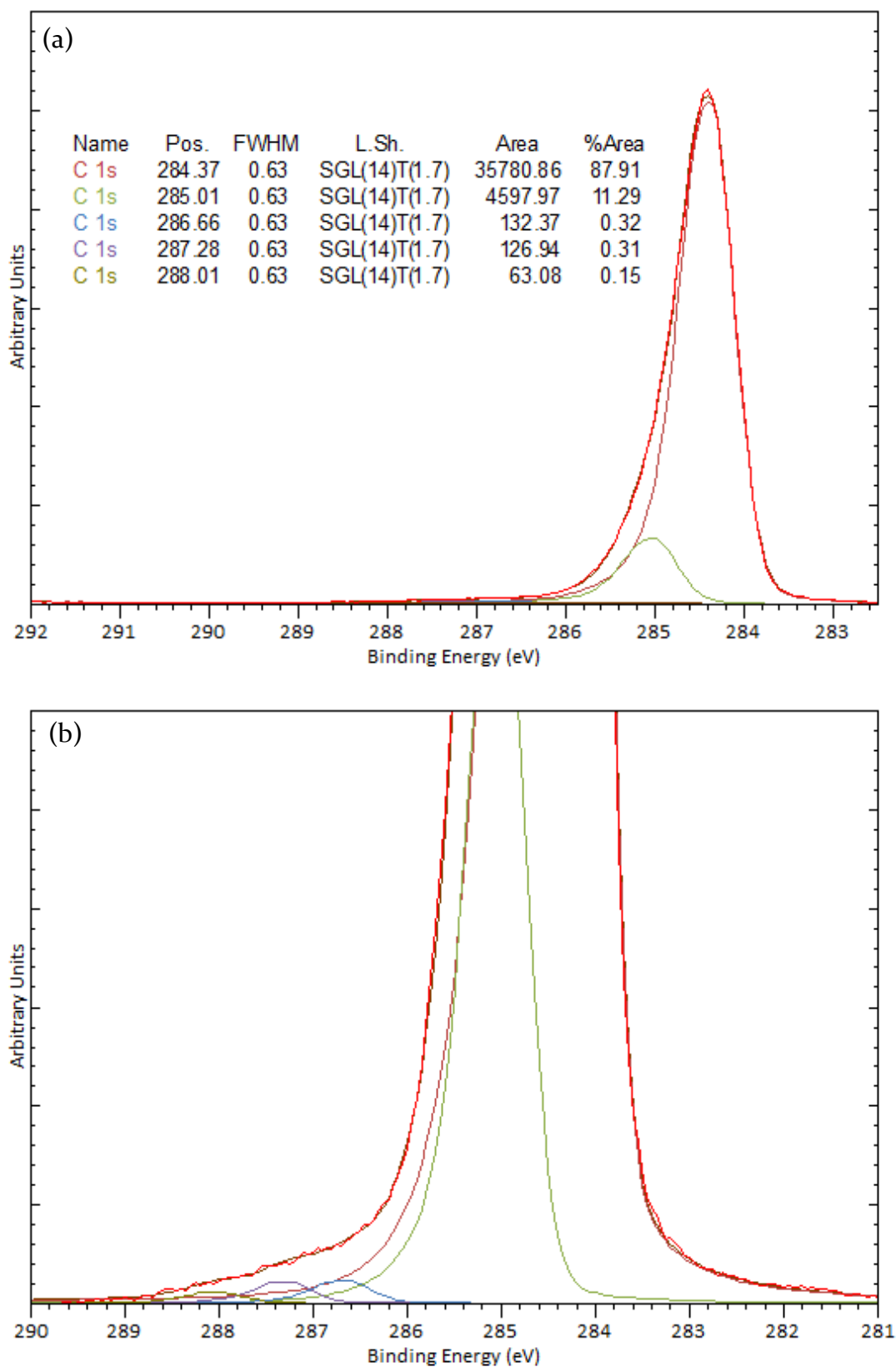


Figure 5-4 - (a) A C 1s XPS spectrum from H-terminated diamond fitted with an asymmetric SGL(12)T(1.7) line shape, and (b) a higher magnification of the shoulder regions of that same spectrum where the black line is the sum of all the components.

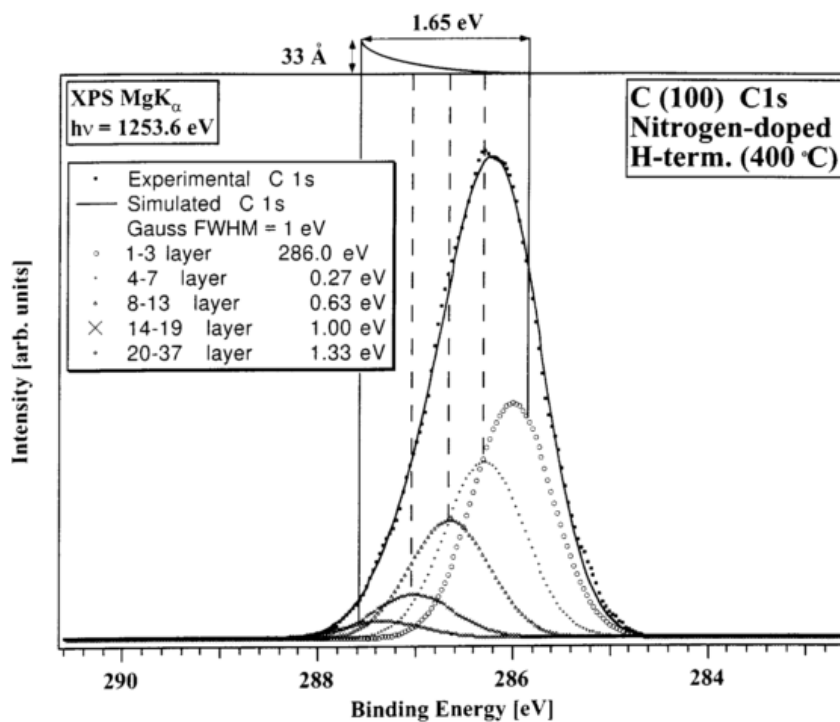


Figure 5-5 – Experimental and simulated C 1s core-level spectrum of a H-terminated (100) surface showing a band bending value of 1.65 eV. From<sup>46</sup>

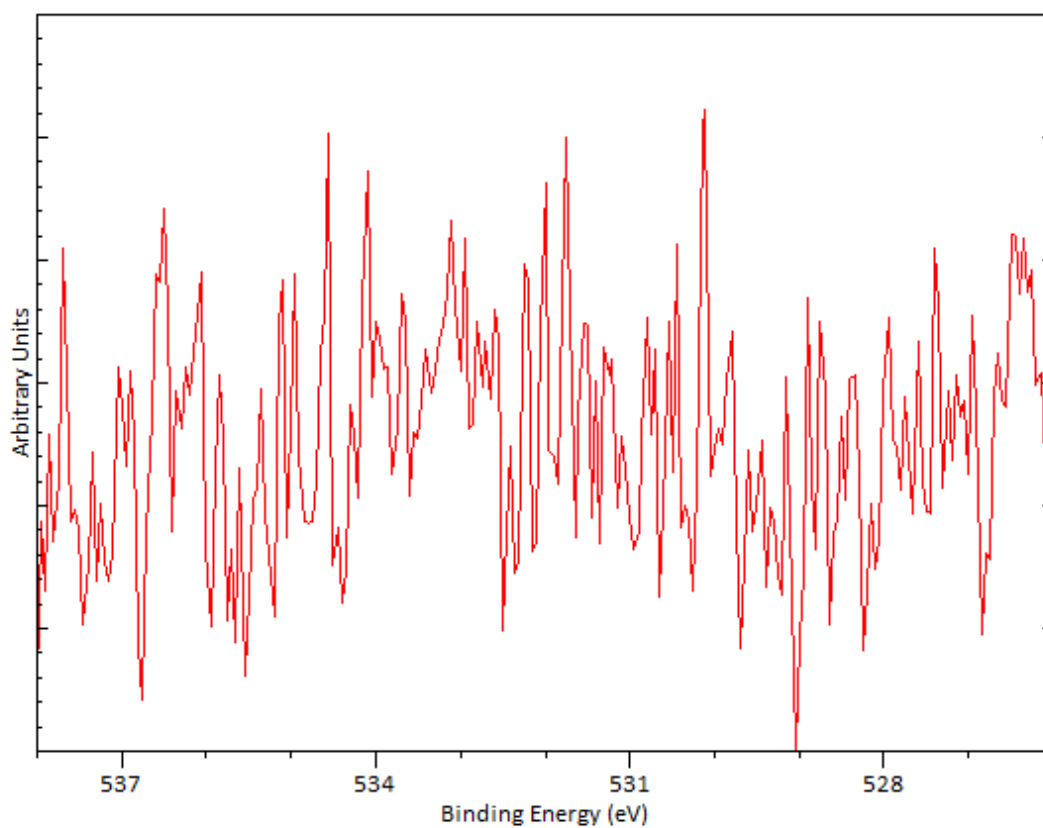


Figure 5-6 – The O 1s core-level scan of a H-terminated diamond sample.

considering O is a very common contaminant of any sample that has been exposed to air. This spectrum contains only background noise, which means that if there is O present, it cannot be detected using XPS even with a high-resolution core-level scan.

### 5.3 O-terminated Diamond

Diamond can be readily oxidised using a variety of methods including plasma or chemical treatment, hot filament cracking, thermal oxidation, UV irradiation in vacuum, ozone treatment, and anodic electrochemical polarization as discussed in section 1.5.2. No significant effort had been made in the literature to compare these different techniques until recently, especially in regard to the quality of the O termination on single crystal diamond. As such, no recommendations were found regarding the best method to utilise.

In this section, three methods for oxidising diamond are considered. Experimental details of the three methods are discussed in section 4.5.2. UV-ozone, acid, and O<sub>2</sub> plasma treatments were evaluated in relation to O coverage and bonding, as well as resulting contamination.

### 5.3.1 UV-Ozone and Acid Oxidation

Table 5-1 shows a summary of the various experiments utilising either UV-ozone or acid treatments to terminate the diamond surface. Samples #1.1 and #1.2 were both exposed to UV-ozone treatment for 30 minutes. However, it can be seen that the results differ drastically. It was assumed that 100 % O coverage corresponds to approximately 5.5 – 6 % O in the survey spectrum of the sample, with the remaining 94 – 94.5 % being C. Examples of what these spectra look like can be seen on page 116 (Section 6.3.1, Figure 6-5). Sample #1.2 shows a similar value (5.0 %) whilst sample #1.1 achieves only 0.2 %. This could be due to the variable sample stage height of the apparatus which could lead to varying degrees of exposure to the ozone created by the UV-lamp. It should be noted that all of these samples were H-terminated prior to oxidation, and that although the H termination is air stable, it will gradually be replaced by O over the course of several weeks when stored in ambient conditions. This would indicate that the UV-ozone treatment was entirely ineffectual for sample 1.1, as the 0.2 % of O found on the surface may simply be the result of exposure to atmospheric O. Furthermore, sample #1.2, yielded the highest WF of any samples investigated in this work. This was problematic as initial sample focusing using the NanoESCA (Figure 4-1) was usually done using the mercury lamp, which produces very bright non-monochromatic light of up to 5.2 eV. As sample #1.2 had a WF of 6.7 eV, no image was forthcoming until the helium light

#	Oxidation method	Elemental Composition (%)				$\phi$ (eV)	O 1s (%)		
		O	Tin	Sodium	Fluorine		533 eV O-F <sub>x</sub>	532 eV ether	531 eV ketone
1.1	UV-ozone	0.2	-	-	-	-	-	-	-
1.2	UV-ozone	5.0	0.1	-	-	6.7	-	79.6	20.4
1.3	Acid	7.1	-	0.4	-	-	-	79.0	21.0
1.4	Acid	7.0	-	1.2	-	-	-	75.8	24.2
1.5	Acid	3.2	0.2	-	0.1	-	8.4	83.2	8.5
1.6	Acid	3.2	0.1	-	0.1	3.5	13.9	75.6	10.5
1.7	Acid	2.7	0.1	-	-	4.6	-	-	-

Table 5-1 – A summary of the percentage composition of the survey scans and the component peaks of the O 1s core-level scans of diamond oxidised by UV-ozone or acid treatment.

source (21.2 eV) was used. This light source has a significantly smaller spot size, which is why it was generally only used once the sample was already in focus.

Samples #1.3 – #1.7 were all oxidised using acid treatment for 30 minutes. The results for O coverage using this method are inconsistent, varying between 2.7 – 7.1 % O. Samples #1.3 and #1.4 produced more than an ML of O, which could be due to oxidised contaminants. Samples #1.5 – #1.7 on the other hand produced rather poor O coverage, ranging from 2.7 – 3.2 %. The ratio of ketone- (531 eV) to ether-like O (532 eV) is fairly consistent at 1:4 – 1:3, except for samples #1.5 and #1.6, which have an extra component peak at 533 eV, due to fluorine contamination.

The WF values of samples #1.6 and #1.7 are lower than the WFs of samples oxidised by other methods. Computational studies in the literature have shown the OH termination to have a lower EA than ether- or ketone-like O terminations, as discussed in section 1.5.2. Furthermore, as the samples are H-terminated before the oxidation, incomplete oxidation, as evidenced by the low O percentage, could lead also to lower WF values.<sup>68</sup>

### 5.3.2 Oxygen Plasma Oxidation

Table 5-2 shows a summary of diamond surfaces oxidised by an O<sub>2</sub> plasma. The O content of the survey scans varies between 5.5 – 6.3 %, a significantly smaller range than the previous oxidation methods. The WF values of samples #2.7 – #2.10 is between 5.3 – 5.6 eV which is slightly higher than values found in the literature (4.9 – 5.2 eV), as discussed in section 1.5.2. As with previous oxidation methods, all the samples have a large ether component at ~532 eV, and a smaller ketone component at ~531 eV. Many of the samples also exhibit a third component at ~530 eV, which corresponds to a metal oxide functional group. The three samples (#2.1, #2.3, and #2.6) with the largest component peaks at 530 eV also have significant amounts of tin contamination from the survey scan, confirming that it is a metal oxide peak. The tin contamination was believed to originate from sample storage, as, after a different storage method was utilised from sample #2.7 onwards, no more tin was observed. These samples also have a higher percentage of ketone present. This is commonly observed in metals due to their lower electronegativity leading to higher oxidation states, as discussed in more detail in section 6.3.3. Sample #2.10 also has a higher percentage of ketone, despite not having tin on the surface. It does however have N, which could account for the increase in double bonded oxygen. Furthermore, samples #2.9 and #2.10, do not have the metal

#	Elemental Composition (%)				$\phi$ (eV)	O 1s (%)			
	O	Tin	Fluorine	N		534 eV O-F <sub>x</sub>	532 eV ether	531 eV ketone	530 eV M-O
2.1	5.8	0.6	-	-	-	-	55.0	41.1	4.0
2.2	5.9	0.1	-	-	-	-	70.0	27.1	2.9
2.3	5.6	0.8	-	-	-	-	56.6	33.2	10.1
2.4	5.9	0.1	-	-	-	-	73.7	25.0	1.2
2.5	5.5	-	-	-	-	-	88.8	11.2	-
2.6	6.3	0.5	-	-	-	-	60.5	29.7	9.8
2.7	5.7	-	-	-	5.3	-	72.7	26.0	1.4
2.8	5.7	-	-	-	5.3	-	76.8	22.1	1.1
2.9	5.6	-	0.3	-	5.4	2.0	76.2	21.8	-
2.10	6.2	-	0.1	0.2	5.6	1.0	60.4	38.6	-

Table 5-2 – A summary of the percentage composition of the survey scans and the component peaks of the O 1s core-level scans of diamond oxidised by an O plasma.

oxide components at 530 eV, but have a third component at 534 eV, which corresponds to the fluoride functional group. This is confirmed by the survey spectra for these two samples containing fluorine. Common contaminants in UHV and surface science studies are discussed in section 3.1.4.7. Sample #2.7 shows a small metal oxide peak despite not showing any tin in the survey spectra, which could indicate the presence of a contaminant below the limit of detection of the survey scan (see sections 3.1.4.5 and 5.2.1).

To determine the quantity of O that corresponds to a perfect ML, it is assumed that the O plasma termination yields a complete ML of O on the diamond surface. Figure 5-7 is a box plot of the percentage of O on the diamond surfaces from the 10 samples in Table 5-2. From this, it can be seen that the distribution is not Gaussian as it is skewed towards the lower values. A better indication of the range of values is the interquartile range, represented by the green box, which excludes the top and bottom 25 % of values. The mean of all the values is 5.8 %, however, because the data do not follow a normal

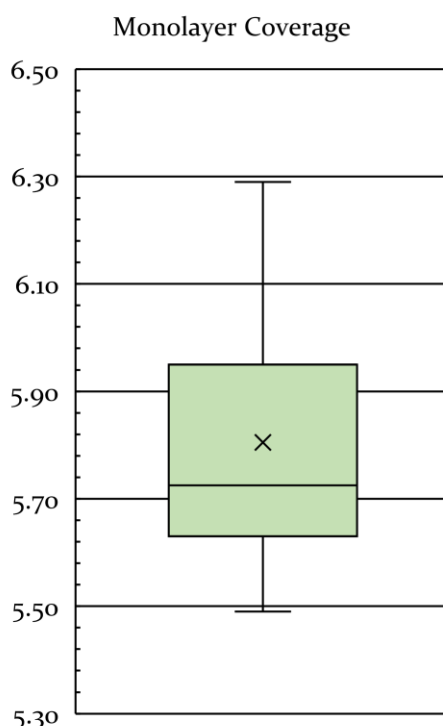


Figure 5-7 – A box plot of the O percentage from Table 5-2. The Interquartile range is from 5.6 – 6.0 %, the mean (X) is 5.8 %, and the median is 5.7 %.

distribution, the median is more applicable due to this being less sensitive to extreme values at either end of the range. The median for this data set is 5.7 %.

Consideration has to be given to the levels of contamination observed in samples #2.1, #2.3, #2.6, and #2.10 due to the possibility of the contaminants also oxidising, and therefore inflating the quantity of O present.

### 5.3.3 Summary

O<sub>2</sub> plasma treatment is the simplest and most robust of the techniques detailed above. Whilst the UV-ozone method takes 30 minutes, and is a quick and uncomplicated treatment, the results were inconsistent and yielded a high WF. For acid treatment, while the actual reflux was performed for 30 minutes, significantly longer was needed to set up and perform the oxidation, as well as involving hazardous substances. The resulting O coverages were also inconsistent. Therefore, O<sub>2</sub> plasma treatment was chosen for further studies, as the simplest, safest, and most reliable method. By analysing the O<sub>2</sub> plasma treated samples, it was determined that  $5.7 \pm 0.1\%$  is equivalent to an ML of O on the diamond surface. The average WF of these O<sub>2</sub> plasma oxidised samples was  $5.4 \pm 0.1$  eV, which, while slightly higher than literature values, is in close agreement with the WF maps of these samples shown in Figure 5-8.

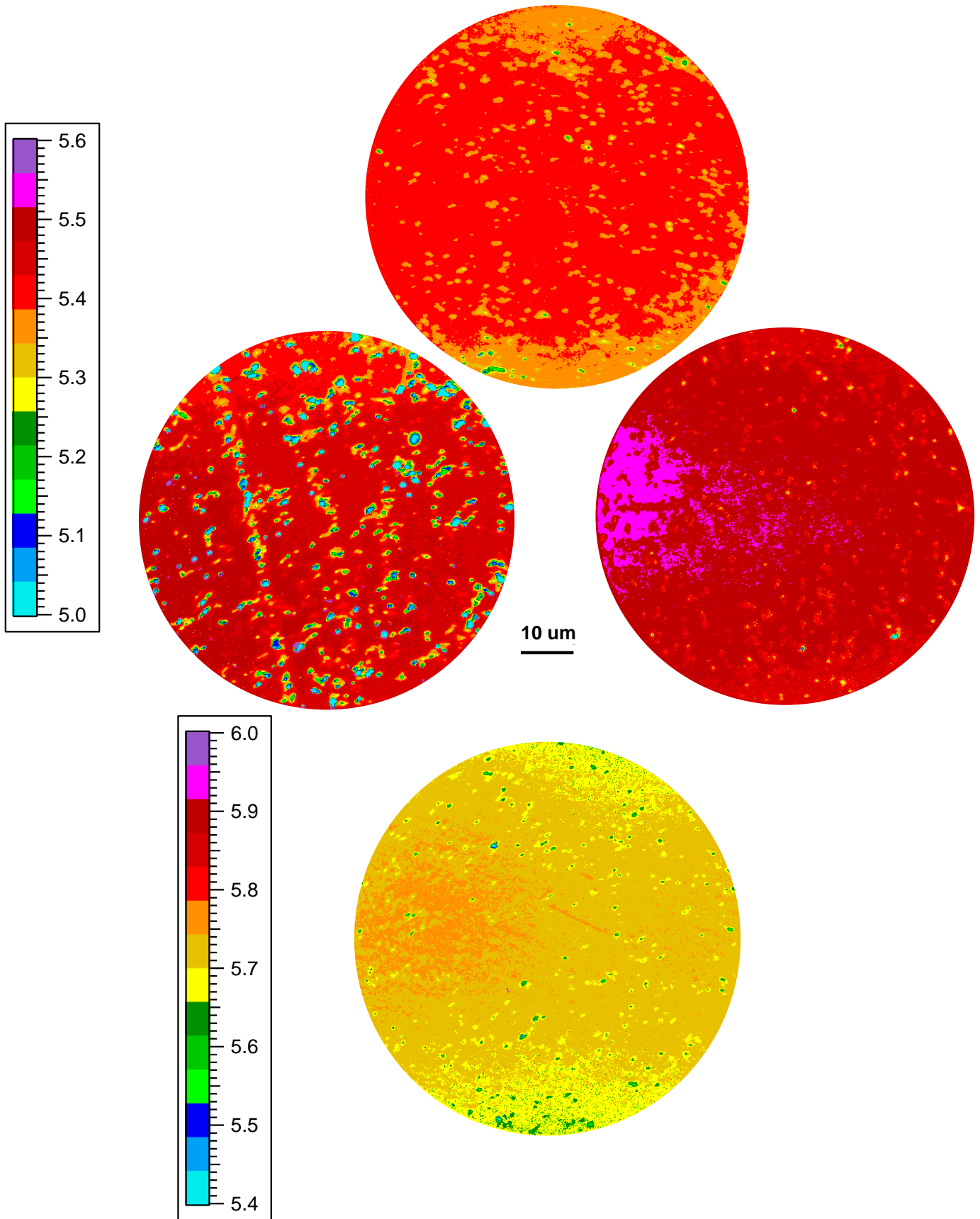


Figure 5-8 – The WF maps of samples #2.7 (top) #2.8 (middle left), #2.9 (middle right), and #2.10 (bottom).

## 5.4 N-terminated Diamond

TiN-terminated diamond was chosen as a good comparison to the TiO terminations, as discussed in chapter 2. N and O atoms are of similar sizes, with an O atom having a radius of 60 pm, or 73 pm when part of a covalent single bond, while N has an atomic radius of 65 pm, or 75 pm when part of a covalent single bond.<sup>150</sup> This means one could expect a similar coverage of both elements on a diamond surface. The fact that O typically forms two bonds, while N typically forms three bonds, leads to interesting differences in their bonding behaviour, as seen in the computational work presented in chapter 2. While O termination is fairly trivial to achieve as described in section 5.3, N-termination presents more of a challenge. While a plasma formed of O<sub>2</sub> works well for oxidising the diamond surface, the choice of feed gas for N is not as simple. A diatomic O<sub>2</sub> molecule has a double bond between the two O atoms, with a bond energy of 498 kJ mol<sup>-1</sup>, while the molecules in N<sub>2</sub> form a triple bond, with a bond energy of 941 kJ mol<sup>-1</sup>.<sup>151</sup> This means that it takes almost twice as much energy to break the N≡N bond than it does to break the O=O bond. Therefore, N<sub>2</sub> plasmas are typically not sufficient to N-terminated diamond unless extremely high powers are used. As such, ammonia (NH<sub>3</sub>) is commonly used as a feed gas instead, as the N-H bonds are significantly easier to break, having a bond energy of 390 kJ mol<sup>-1</sup>.<sup>151</sup>

Table 5-3 summarises various N termination experiments. Sample #3.1 was terminated using an ammonia plasma for 3 minutes. This yielded a surface composition of 2.6 % N, which is a 46 % coverage of the surface using the value of 5.7 % for an ML of O. As discussed previously, the similar size of N and O atoms, especially when in covalent bonds as they would be on the diamond surface, should yield a similar value for ML coverage. An important distinction here is that while the O plasma produces O atoms, an ammonia plasma produces NH or NH<sub>2</sub> radicals. This could explain the lower values of N coverage observed, as steric hindrance, especially in the case of NH<sub>2</sub>, would lead to the maximum N coverage being below an FML. The lower values of N coverage also lead to significant O contamination. The ammonia plasma cleans the surface but cannot populate all the dangling bonds, leading to oxidation upon exposure to air. For sample #3.1, the amount of O and N together is 5.7 % which is consistent with the value

#	Prep	Time (s)	Elemental Composition (%)					$\phi$ (eV)	N 1s (%)		
			O 1s	N 1s	Fe 2p	Sn 3d	Cl 2p		400 eV	399 eV	398/7 eV
3.1	NH <sub>3</sub> (T)	180	3.1	2.6	0.7	-	-	-	13.1	84.9	2.1
3.2	N <sub>2</sub> (T)	10	2.0	1.9	-	0.1	-	-	16.6	83.4	-
3.3	N <sub>2</sub> (T)	20	3.0	1.2	-	0.1	-	-	18.9	81.2	-
3.4	N <sub>2</sub> (T)	30	3.1	0.8	-	0.2	-	-	19.0	81.0	-
3.5	N <sub>2</sub> (MW)	10	1.9	0.5	-	-	-	-	-	-	-
3.6	N <sub>2</sub> (MW)	240	2.7	0.6	-	-	0.9	-	-	-	-
3.7	NH <sub>3</sub> (T)	180	6.1	3.0	1.9	-	-	4.1	-	80.2	19.8
3.8	NH <sub>3</sub> (T)	180	2.7	2.9	0.8	-	-	4.6	-	86.4	13.7
3.9	NH <sub>3</sub> (T)	180	3.7	3.1	0.8	-	-	4.1	16.6	77.1	6.3

Table 5-3 – A summary of the percentage composition of the survey and the component peaks of the N 1s core-level scans of N-terminated diamond. NH<sub>3</sub>/N<sub>2</sub> in the prep column indicates the feed gas used for the plasma treatment, while T/MW indicates the reactor used, either the Terminator (T) or the Microwave (MW) plasma reactor.

for an ML of O. Similar values were obtained for other samples, although contamination has to be taken into account.

To overcome this steric hindrance problem, several experiments with N<sub>2</sub> gas were conducted. Samples #3.2 – #3.4 (Table 5-3) were exposed to a nitrogen plasma for between 10 – 30 s, and the survey scans show N is present. The data collected indicates a deposition rate which is inversely proportional to the duration of the plasma exposure. Conversely, the longer duration runs exhibit a higher O content, which could be an indication the N<sub>2</sub> is not completely dissociating, due to the plasma in the Terminator not providing enough energy to break the strong N≡N triple bond. This results in N<sub>2</sub><sup>+</sup> adsorbing on the surface, which is not air stable and desorbs upon exposure to air, being replaced with atmospheric O. This leads to higher O coverage on the diamond surface with increased plasma exposure time.

To investigate this possibility, N termination in an N<sub>2</sub> plasma was performed in the microwave plasma reactor. This reactor is more powerful (1.5 kW versus 0.3 kW) and can therefore produce hotter plasmas than the Terminator, and it was hoped that this would enable more complete dissociation of the N<sub>2</sub>, and therefore an improved N coverage compared to samples treated in the Terminator. Figure 5-9 shows the results of the various N<sub>2</sub> plasma experiments in comparison to the ammonia plasma sample (#3.1). The two runs in the microwave reactor, 10 seconds (#3.5) and 4 minutes (#3.6)

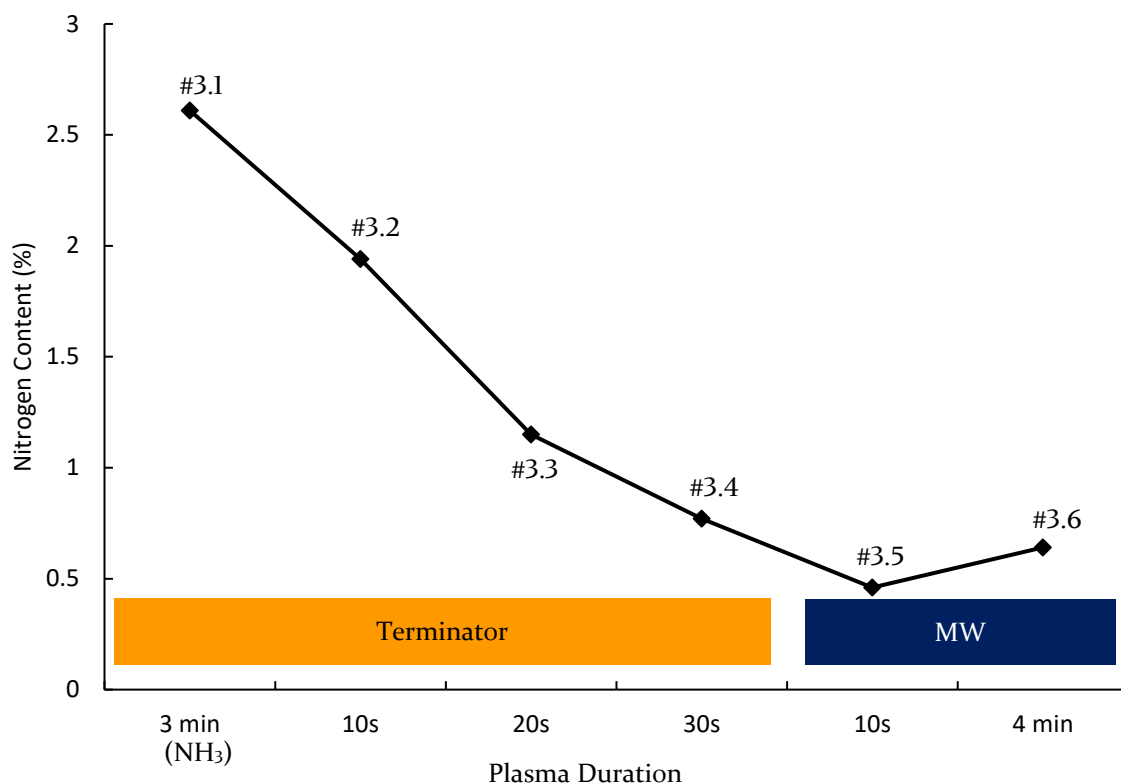


Figure 5-9 – A summary of the N content achieved through the various N<sub>2</sub> termination experiments where the first four experiments were performed in the Terminator and the last two in the Microwave plasma reactor. The labels of the individual points refer to the sample id in Table 5-3.

yielded 0.5 % and 0.6 % respectively, which is significantly lower than the N content achieved using the terminator. It was also observed that the longer exposure time of sample #3.6 severely damaged the diamond surface. All samples are initially mirror smooth (polished with an average roughness,  $R_a$ , of <30 nm), while sample #3.6 was visually significantly rougher after N<sub>2</sub> plasma treatment. This was the first time a pure N plasma had been attempted in this reactor and further work would be required to achieve a robust deposition procedure if at all possible.

In light of this, the ammonia plasma process for N termination was chosen for investigating TiN-terminated surfaces, which are discussed in Chapter 6. Three more samples were terminated using this method (#3.7 – #3.9), the results of which are captured in Table 5-3. These samples have N content (2.9 – 3.1 %) similar to that of sample #3.1, however, there is also significant iron, chromium, and nickel contamination. These elements are sputtered from the stainless-steel electrode of the Terminator used to generate the plasma. Even though these samples are prepared in the same reactor as the O plasma terminations, which do not show this contamination, they

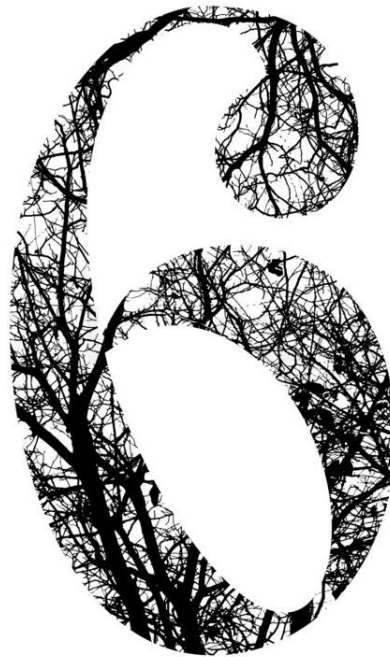
differ significantly in the duration of the plasma exposure. For the O termination, samples are plasma treated for 7 s, while for the N termination, the samples are exposed for 180 s. Table 5-3 shows only the iron contamination, as the nickel and chromium are directly proportional to the iron, and present in significantly smaller quantities.

The four ammonia-terminated samples (#3.1, #3.7 – #3.9) exhibit three components in the N 1s spectra, while those samples-terminated using N<sub>2</sub> exhibit only two components. The third component in the N 1s spectra at an energy of 397-398 eV is indicative of metal nitrides, which is consistent with the observed contamination levels within the samples. The WF values of these three samples range from 4.1 – 4.6 eV, which are lower than those of the O plasma treated diamond (5.3 – 5.6 eV). There are unfortunately no literature values with which to compare this to. Furthermore, it should be noted that, as these samples are contaminated by iron, chromium, and nickel, it cannot be determined whether this lower WF is due to the N termination, or due to the contaminants, as metal coatings are often used to lower the WF, as discussed in section 1.3.1.

## 5.5 Summary

Of the three oxygen termination methods investigated in this chapter, the O<sub>2</sub> plasma treatment was found to be the simplest, safest, and most reliable method. Analyses of the O<sub>2</sub> plasma treated samples, yielded  $5.7 \pm 0.1$  % of O in the XPS survey spectrum to correspond to an ML of O on the diamond surface. The average WF of these O<sub>2</sub> plasma oxidised samples was  $5.4 \pm 0.1$  eV, which is slightly higher than literature values, as discussed in section 1.5.2. Although N and O atoms are of similar sizes and should therefore yield similar ML coverages, there were considerable complications for the N termination of the diamond surfaces. While O<sub>2</sub> is an excellent choice of feed gas for an oxygen plasma, the N≡N bond is much stronger and hence more difficult to break. Therefore, NH<sub>3</sub> is commonly used as a feed gas, but this is deposited on the surfaces as NH or NH<sub>2</sub>. The coverage of N achieved using ammonia was less than 60%, which was believed to be due to the steric hinderance of the NH<sub>x</sub> groups. Furthermore, the increased plasma exposure time compared to oxygen termination resulted in significant contamination due to the sputtering of the stainless-steel electrodes. These challenges would need to be overcome for a higher quality N termination in the future.

## CHAPTER



# TiO/TiN Terminations

“The amazing thing is that every atom in your body came from a star that exploded. And, the atoms in your left hand probably came from a different star than your right hand. It really is the most poetic thing I know about physics: We are all stardust. “

Lawrence M. Krauss - A Universe from Nothing: Why There Is Something Rather Than Nothing

## 6.1 Introduction

In this chapter, diamond surfaces terminated with TiO and TiN are evaluated. Starting with either O- or N-terminated diamond, Ti was deposited on several samples. As with the computational modelling discussed in chapter 2, quarter, half, and full monolayer (QML, HML, and FML) coverages were prepared. These samples were then annealed at increasing temperatures to observe the effect this had on the sample composition and their WF. When discussing annealing temperatures of the samples in this chapter, the 600 °C, 800 °C, and 1000 °C anneals are performed for 15 minutes. The 400 °C anneal however does not refer to the annealing temperature as such, but rather Ti deposition, which was performed while the sample was kept at 400 °C. As such, the amount of time spent at this temperature varies depending on the deposition time needed to achieve the desired Ti coverage. Furthermore, 0 °C is used to denote the sample before Ti deposition, despite this not being strictly accurate as the sample is not cooled and is in fact at room temperature. 0 °C was chosen to aid in visualization and plotting of the data.

## 6.2 Titanium

As discussed in section 3.1.1, the intensity of the XPS signal has an exponential dependency on the depth from which an electron originates. This effect can be used to determine how much deposited Ti corresponds to an ML, as the second layer of Ti would attenuate the signal from the C substrate more than the first. Figure 6-1 shows how the ratio of the signal intensities of C (diamond substrate) and the deposited Ti vary as increasing quantities of Ti are deposited. As a layer of Ti is deposited, the change in the signal intensity for the underlying C is linear, depending only upon how much of the Ti layer is complete, as there is no change in depth for the C atoms while the first layer is being built. When the second layer is being deposited, the C atoms are then positioned two layers below the surface. As such, the C signal decreases faster due to the exponential nature of the signal decay. In Figure 6-1 it can be clearly observed where the gradient of the Ti:C ratio changes, signifying the beginning of the second layer at a Ti coverage of  $4.1 \pm 0.1$  %.

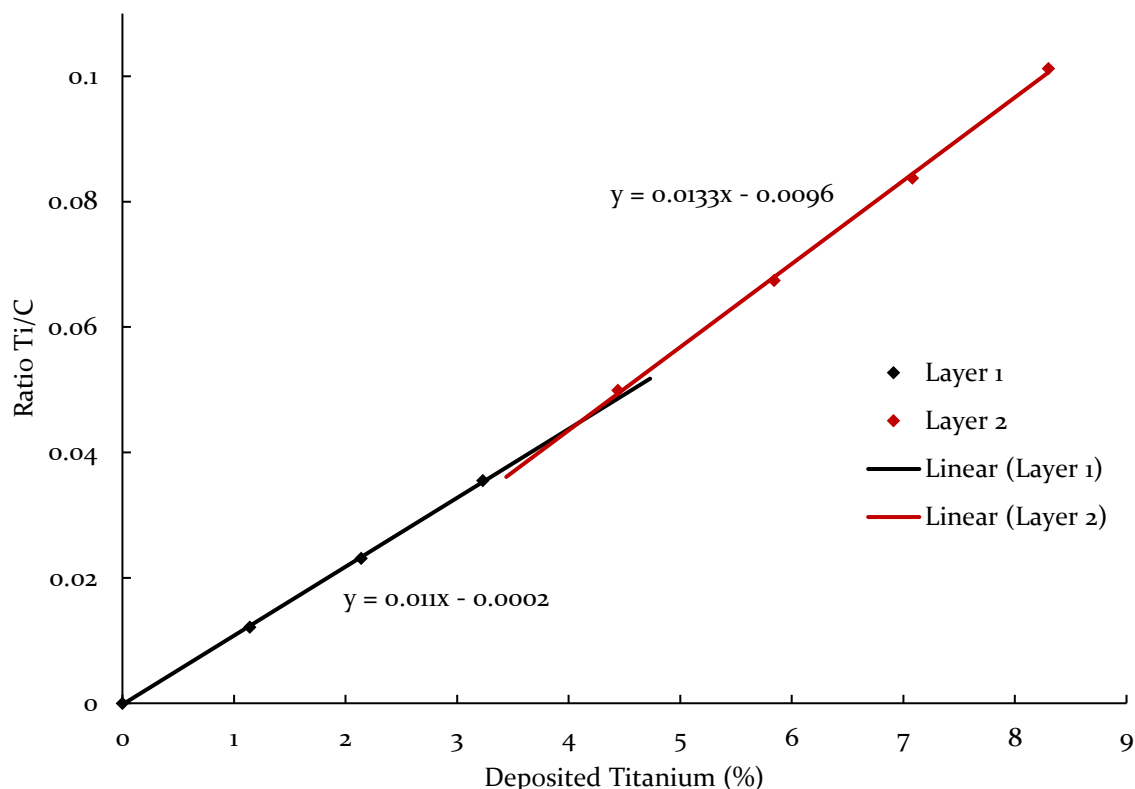


Figure 6-1 – The ratio of the signal intensities of Ti to C as a function of the quantity of Ti deposited. Each point in the plot corresponds to 100 s of Ti deposition.

A pure Ti XPS spectrum was required to allow comparison of the peak shapes in the TiO and TiN spectra discussed in subsequent sections. For this purpose, Ti was deposited using the e-beam evaporator for several hours on a single-crystal diamond sample. The ML of Ti discussed above, 4.1 % of Ti in the survey spectrum, required a deposition duration of 5 min. A duration of 2 h was calculated to yield sufficient coverage to no longer detect the diamond substrate. However, after 2 h, 35 % C remained in the survey spectrum. Therefore, Ti was further deposited for another 3 h, for a total deposition time of 5 h, which again yielded a significant C content. Figure 6-2 shows the survey spectrum after 5 h of Ti deposition, with 23.4 % C present. The C 1s peak in this spectrum is at 282 eV while the higher resolution C 1s core-level spectrum in Figure 6-3(a) shows the peak to be at 281.7 eV. This binding energy corresponds to the metal carbide functionality, whereas the  $sp^2$  and  $sp^3$  carbon from diamond would typically be at 284 – 285 eV. This discrepancy indicates that the C present in the survey spectrum is predominantly in the form of Ti carbide (TiC) and hence does not originate from the diamond substrate, pointing to contamination from the Ti deposition process. This is

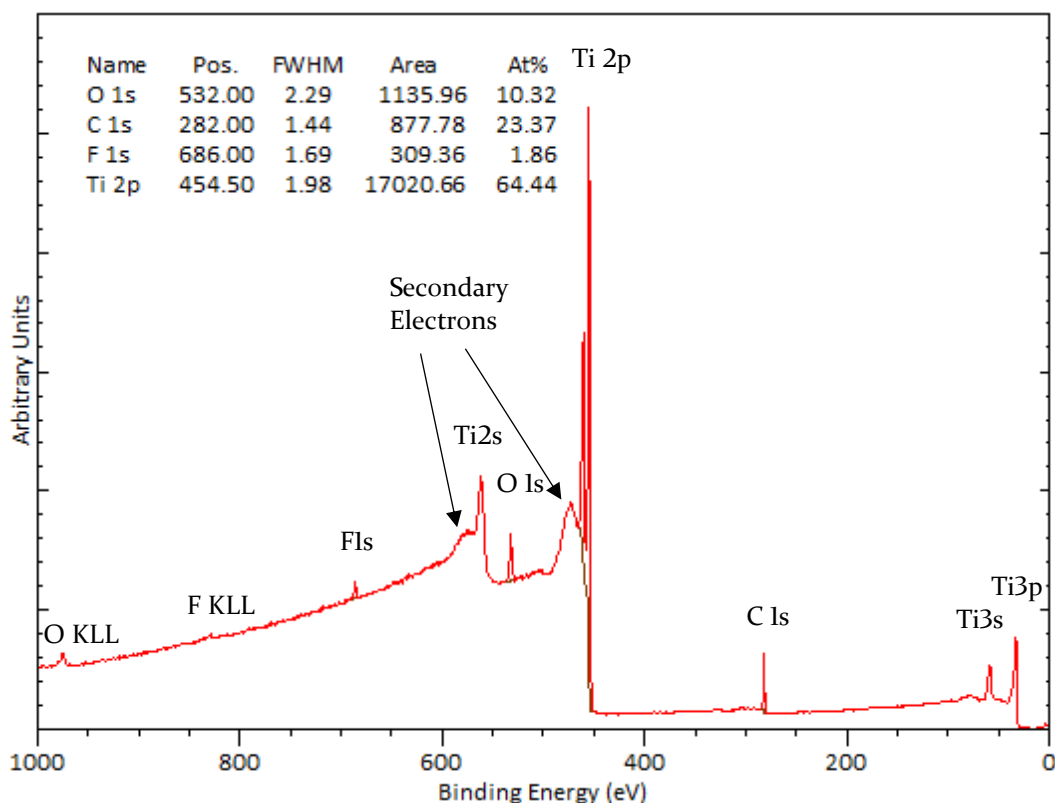


Figure 6-2 – The XPS survey spectrum of Ti after 5 h of Ti deposition.

because atomic Ti is very reactive, which is actually used to lower the pressure of ultra-high vacuum systems. A Ti sublimation pump (TSP) heats a Ti filament causing Ti to sublime and deposit on the chamber walls. This Ti film is very reactive causing any molecules that come into contact with it to ‘stick’, and hence the pressure is reduced. The large increase in the background signal above the Ti 2p peak is discussed in detail in section 3.1.4.1.

The only other significant presence is fluorine, the F 1s peak can be seen at 686 eV in Figure 6-2. The sample had no fluorine present before Ti deposition, 0.9 % after 2 h, and 1.9 % after 5 h. This increasing quantity of fluorine with deposition time is a clear indicator that this contamination is as a result of the deposition process. Whether the fluorine contamination originates from the e-beam evaporator itself or from another component in the chamber, such as the heated sample stage, is unclear at this point, and should be investigated as part of future work.

Figure 6-3(b) shows the XPS Ti 2p core-level spectrum. The Ti 2p<sub>3/2</sub> component is at 454.2 eV, indicating that this Ti is metallic, and it is therefore fitted with an asymmetric line shape. However, in the case of TiO, the Ti would be expected to be at a higher

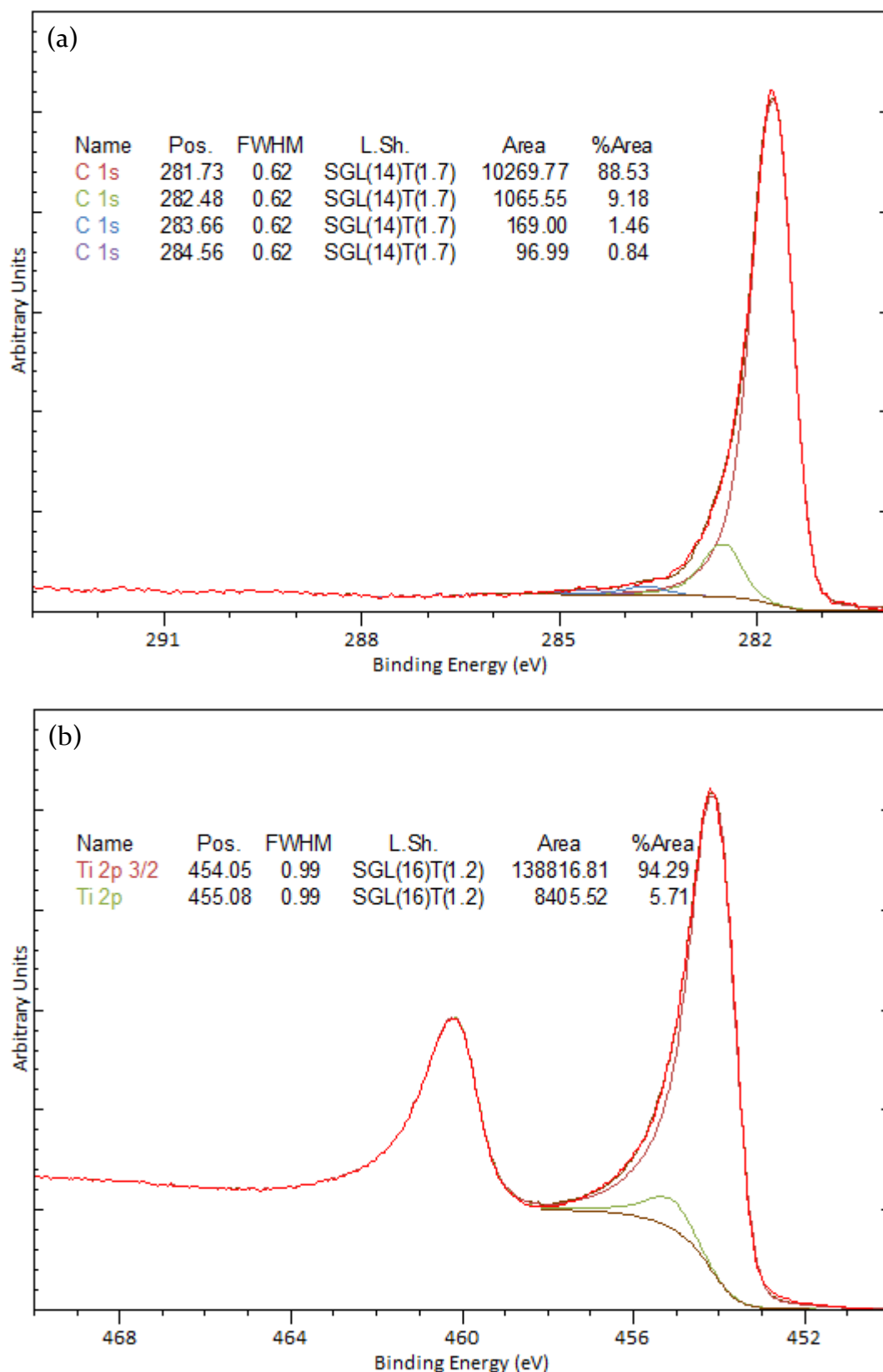


Figure 6-3 – (a) The XPS C 1s and (b) Ti 2p core-level spectra of Ti after 5 h of Ti deposition.

binding energy above 455 eV and be symmetric, because TiO is an insulator. The Ti 2p spectrum also exhibits a small oxide peak at 455.3 eV, which, coupled with the presence of O in the survey spectrum, indicates that some of the deposited Ti is oxidised.

In XPS, peaks are typically labelled  $Enl_j$  where E is the element,  $n$  is the principal quantum number,  $l$  is the orbital angular momentum quantum number, and  $j = |l + s|$ , where  $s$  is the spin angular momentum number and can be  $\pm 1/2$ . Therefore, for  $l = 0$  (s-subshell) the peak is a singlet while  $l > 0$  (the p-, d-, and f-subshells) gives rise to doublet peaks, as seen in Figure 6-3(b), because an unpaired electron can couple its spin and orbital angular momentum either parallel or anti-parallel. The energy separation between the doublet peaks, known as the spin-orbit splitting value, is larger for heavier elements and can be used to aid in element identification. The peaks will also have a specific area ratio dependent on the multiplicity of each spin-orbit state as shown in Table 6-1. Effectively, this means that the doublet peak originating from a 2p subshell should have an area ratio of 1:2.

However, for the Ti  $2p_{1/2}$  and the Ti  $2p_{3/2}$  peaks that is not the case. This is because post-ionisation, the Ti  $2p_{1/2}$  state is short lived compared to the Ti  $2p_{3/2}$  state. This is known as the Coster-Kronig effect and results in the Ti  $2p_{1/2}$  peak being smaller and broader than the typical 2:1 ratio suggests. This results in a complex peak shape, and in an effort to simplify peak fitting, only the Ti  $2p_{3/2}$  peak will be fitted here.

Subshell	$j$ values	Area Ratio
<i>s</i>	1/2	-
<i>p</i>	1/2 3/2	1:2
<i>d</i>	3/2 5/2	2:3
<i>f</i>	5/2 7/2	3:4

Table 6-1 – Spin-orbit splitting  $j$  values and peak area ratios for the various subshells.

## 6.3 Titanium Oxide

To create TiO-terminated diamond surfaces, these samples were first O-terminated using the O<sub>2</sub> plasma method in the Terminator reactor (see section 4.5.2.3). The samples were then characterised in the NanoESCA as discussed in chapter 4. Ti was then deposited *in situ* in varying quantities.

In the computational study (discussed in Chapter 2), the adsorption energy (surface stability) and EA (electron emission) were calculated. The experimental work presented here investigates the same with species desorption as a function of temperature (surface stability) and WF (electron emission). The WF and EA are intrinsically linked as they both define the position of the vacuum level, either relative to the Fermi level or conduction band minimum respectively, as discussed in sections 1.3.1 and 1.4. To enable a comparison of the experimental data to the computational models, a QML, HML, FML of Ti on O-terminated (100) diamond surfaces were prepared. These equate to 1.0 %, 2.1 %, and 4.1 % of Ti in the survey spectrum, respectively. The sample composition is discussed as a function of the annealing temperature, and the impact these had on the observed WF values.

### 6.3.1 QML TiO

As discussed earlier, 4.1 % of Ti in the survey spectrum was determined to equate to an FML. Therefore, to achieve a QML coverage, 1.0 % of Ti was required. Table 6-2 shows a summary of the elemental composition of the QML sample after annealing at various temperatures. Prior to Ti deposition (0 °C), the sample was O-terminated with an ML of O as discussed in section 4.5.2.3. Ti was then deposited while the sample was maintained at 400 °C, resulting in the equivalent of a QML, targeted towards uniform coverage. The Ti 2p core-level spectrum, which shows a large component at 458.5 eV (81.5 %) and a smaller component at 457.4 eV (18.5 %), supports the argument of a uniform Ti layer because these components correspond to TiO. If there was non-uniform growth, i.e. island growth, the Ti 2p spectrum would exhibit a metallic component around 454 eV and/or there would be an increase in the O concentration due to the Ti in the islands oxidising. This oxidation behaviour of Ti, even at pressures of  $1 \times 10^{-8}$  mbar, can be seen in the Ti spectra discussed in section 6.2. As the above scenarios are not observed, it can be assumed that the QML of Ti is uniformly distributed across the sample. The survey spectrum after Ti deposition additionally shows 0.2 % of fluorine, which is believed to originate from the Ti deposition process, as discussed in section 6.2.

After annealing the sample at 600 °C for 15 min, there was a decrease in the O concentration while the Ti concentration remained unchanged, within the margin of error (0.1 %). After annealing the sample at 800 °C for 15 min, there was significantly less O remaining, relative to the ML before deposition. There was also a 0.3 % decrease in the concentration of Ti. However, considering that no corresponding decrease in Ti

<i>T</i> (°C)	Elemental Composition (%)			
	O 1s	Ti 2p	F 1s	Fe 2p
0	5.7	-	-	<0.1
400	5.6	1.0	0.2	<0.1
600	4.6	1.1	-	<0.1
800	0.4	0.8	-	<0.1
1000	<0.1	0.7	-	-

Table 6-2 – QML TiO – Summary of the elemental composition after annealing at different temperatures where 0 °C represents before deposition, and 400 °C is after deposition, as this is the deposition temperature.

concentration was observed after the 1000 °C anneal, and that an increase in temperature would typically result in more of the species desorbing, it is unlikely that this decrease is due to Ti desorption. An example of this can be seen in the 1.0 % decrease of O after the 600 °C anneal, followed by a 4.2 % decrease in O concentration after 800 °C. The decrease in Ti concentration could be because of the Ti atoms on the surface rearranging (e.g. from uniform coverage to nanospheres) or diffusing into the bulk of the diamond.

After the 1000 °C anneal, again for 15 min, most of the O has desorbed. Although no O peaks are visible in the survey spectrum, the O 1s core-level scan revealed a small peak above the background, as shown in Figure 6-4, indicating that there were trace amounts of O present.

Looking at the individual core-level scans, and how they evolve after each annealing process, reveals interesting information about the sample. Figure 6-5 shows an overlay of all the O 1s spectra alongside a bar chart indicating the respective areas of the component peaks. The spectrum before deposition (0 °C) is typical of O-terminated diamond and is very similar to the O 1s spectra discussed in section 5.3.2, with a large

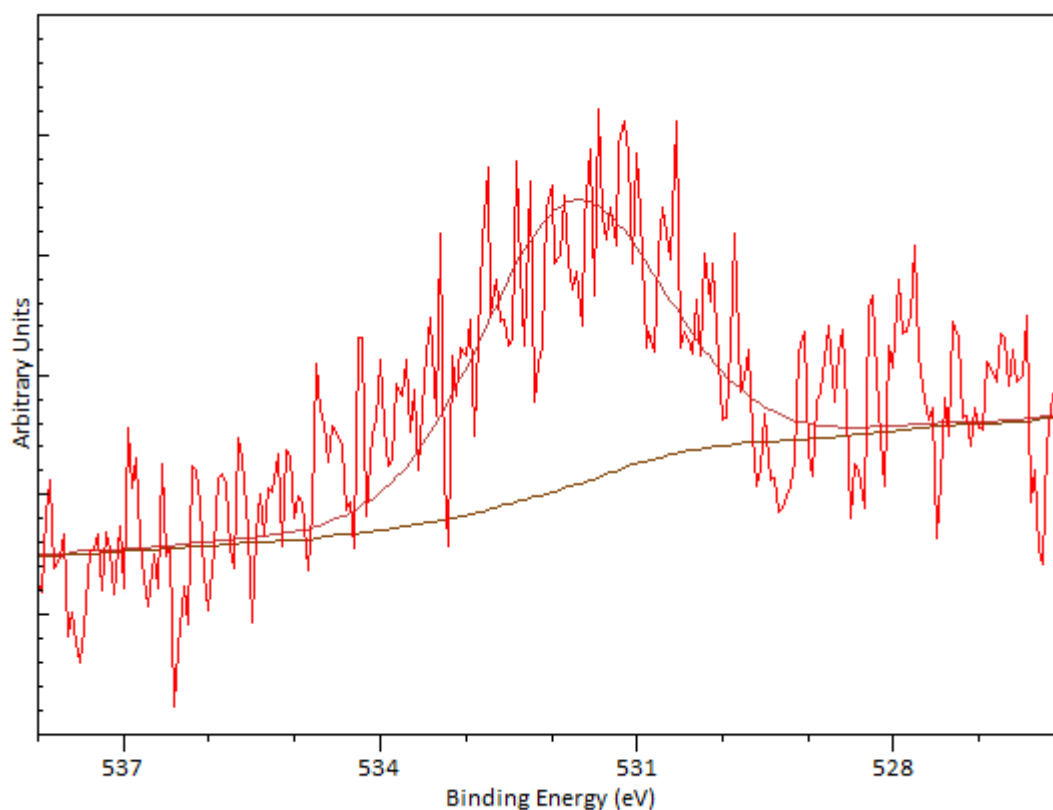


Figure 6-4 – QML TiO – The O 1s core-level spectrum after the 1000 °C anneal.

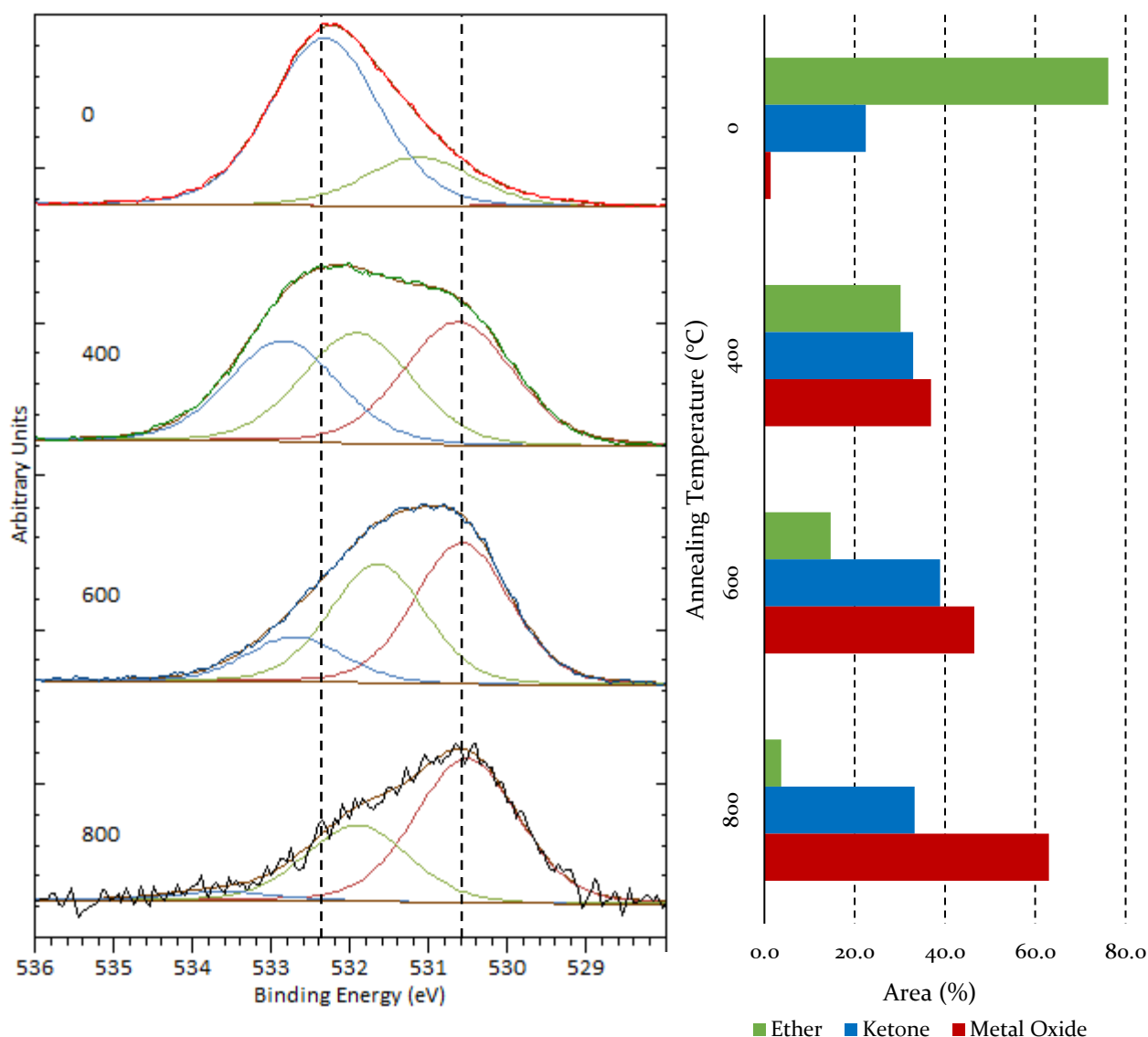


Figure 6-5 – QML TiO – An overlay of the O 1s spectra (left) after the different temperature anneals and the areas of the corresponding component peaks (right). No attempt has been made to colour match the lineshapes used in the spectral fitting with the bars used in the histograms. The components in the spectra from left to right correspond to the bars in the histogram from top to bottom.

ether component at 532.3 eV, a smaller ketone component at 531.1 eV, and a very small metal oxide peak at 529.7 eV. After Ti deposition at 400 °C, it can be immediately seen that the metal oxide component (red) has increased significantly and is now the largest component. This is to be expected after depositing Ti on the O-terminated surface and shows that the Ti has chemically bonded to the O, rather than being physically adsorbed on the surface. After the 600 °C anneal, peak composition shifts even more towards the metal oxide component, and the same applies to the 800 °C anneal.

Figure 6-6 shows an overlay of the C 1s spectra. The bar chart for the component ratios is on a logarithmic scale, because a linear scale would only show the two large C-C components from the diamond substrate. This can be observed from the two spectra overlays in this figure, with the top one being on a linear intensity scale and the bottom one on a logarithmic intensity scale. On the linear scale, only the largest two components, the C-C interactions from the diamond substrate, can be easily observed. But the logarithmic overlay clearly shows the C-O components at around 288 eV decreasing in magnitude while the metal carbide peaks around 282 eV increase in magnitude with increasing temperatures. One interesting aspect is that the second metal carbide component (purple in the bar chart) can only be observed after most of the O has desorbed after 800 °C.

Finally, Figure 6-7 shows an overlay of the Ti 2p spectra from Ti deposition (at 400 °C) to the 1000 °C anneal. Initially the Ti is predominantly in the Ti(IV) and Ti(III) oxidation state. Following the 600 °C anneal, the composition shifts towards the Ti(IV) state at 458.5 eV, but after the 800 °C anneal there is a significant shift to the Ti(II) oxidation state at 455.2 eV binding energy.

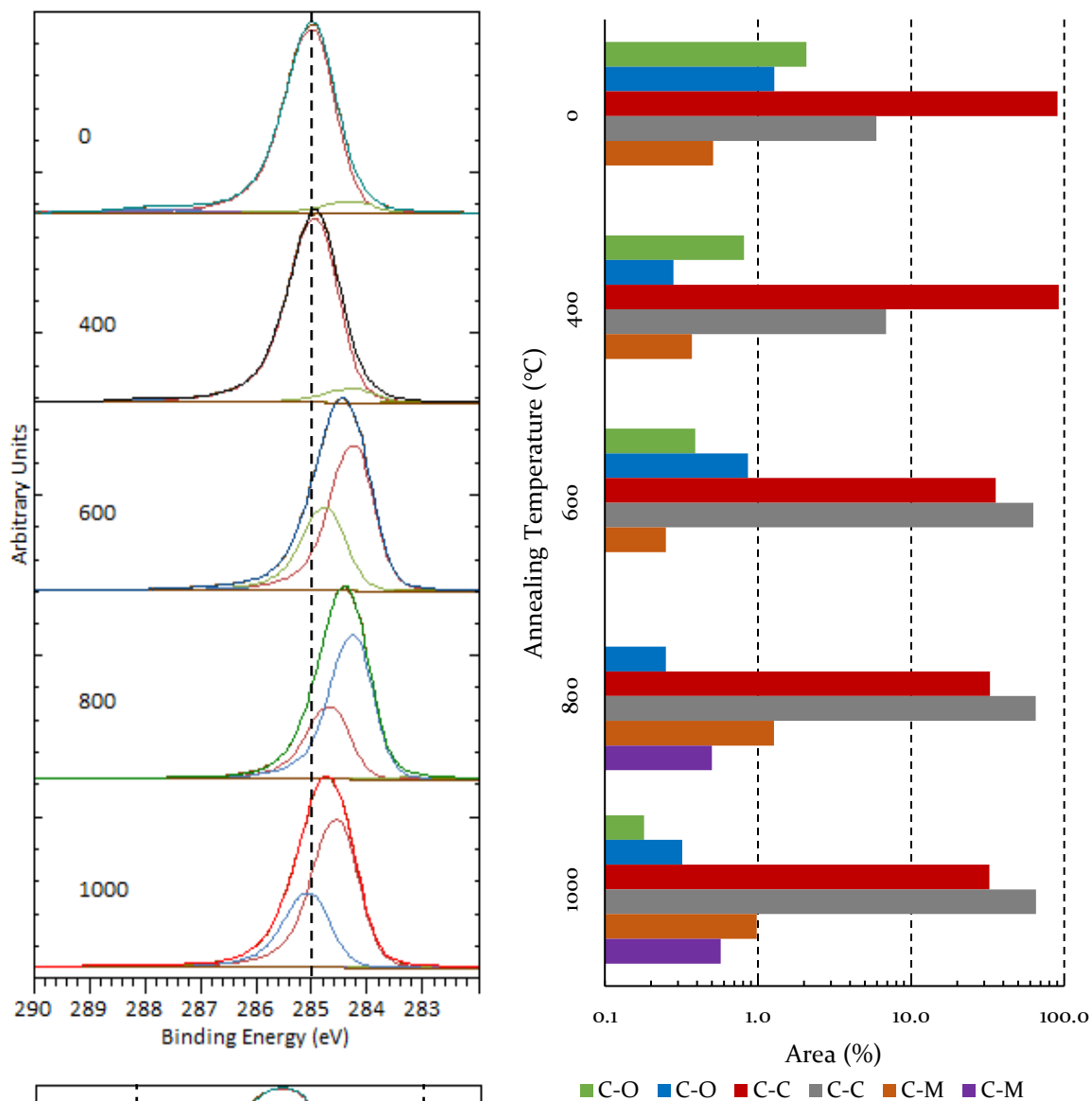


Figure 6-6 – QML TiO – An overlay of the C 1s spectra (top left) after the different temperature anneals, a bar chart of the areas of the corresponding component peaks (top right), and another overlay of the C1s spectra on a logarithmic vertical-axis (bottom right) to enable the visualisation of the smaller components in the shoulders. The bar chart is also on a logarithmic scale for the same reason. No attempt has been made to colour match the lineshapes used in the spectral fitting with the bars used in the histograms. The components in the spectra from left to right correspond to the bars in the histogram from top to bottom.

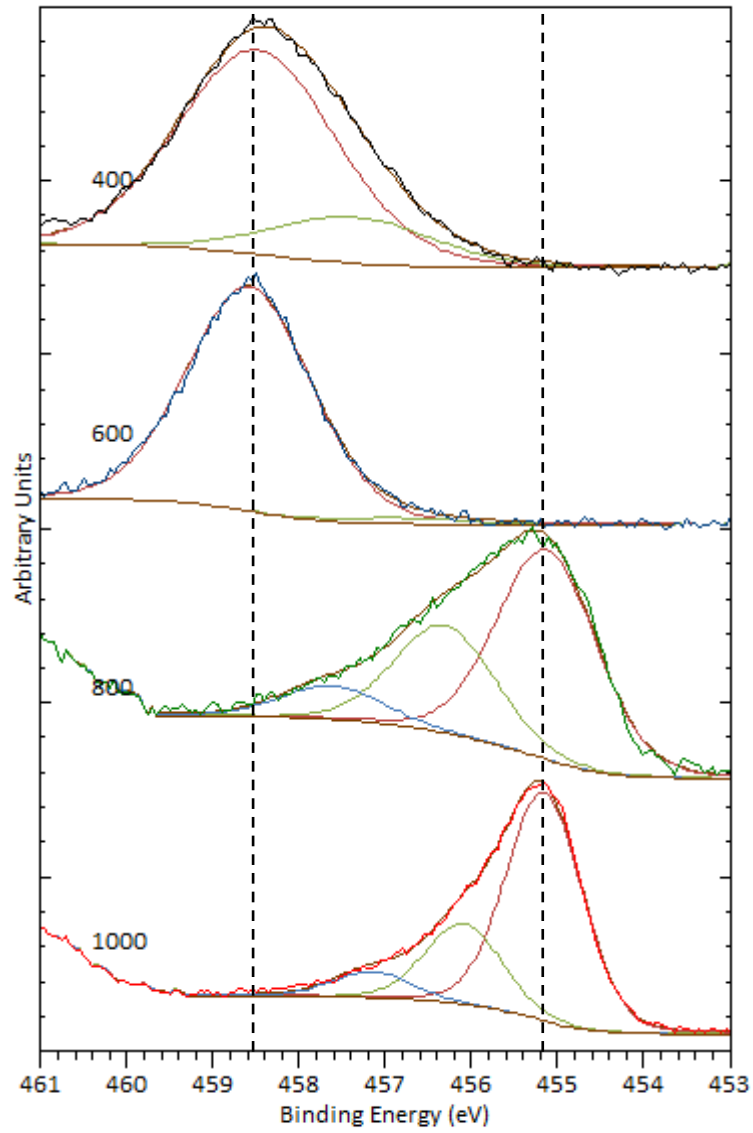


Figure 6-7 – QML TiO – An overlay of the Ti 2p spectra after the different temperature anneals.

### 6.3.2 HML TiO

This sample was prepared to exhibit an HML of Ti on an O-terminated diamond surface. Therefore, 2.0 % Ti was deposited using the e-beam evaporator. Table 6-3 shows the elemental composition of the sample at different stages. To begin with, the sample shows 6.0 % of O on the diamond surface, which is minimally above the  $5.7 \pm 0.1$  % that was determined to be an ML. This can potentially be accounted for by the fluorine and N contamination present on the sample, as discussed in section 3.1.4.7. Ti was then deposited on this sample at 400 °C, resulting in an HML of Ti on O-terminated diamond. As discussed in the previous section, by looking at the Ti 2p spectrum, which has a larger component at 458.9 eV and a smaller component at 457.1 eV, we can see that the Ti coverage is uniform. After deposition, the N contamination was no longer present, but the fluorine contamination has increased, which was consistent with other spectra obtained after using the e-beam evaporator. There was no change in the concentration of O present, which also holds true for the 600 °C anneal. After 800 °C, there was a 0.6% decrease in O concentration, and after 1000 °C, almost no O remains on the surface. As with the QML sample, the O 1s core-level spectrum shows a small peak above the baseline. Additionally, enough O was present to show a small peak in the survey spectrum.

Unlike the QML sample discussed in the previous section, there was no change in the Ti concentration during any of the annealing processes, within the margin of error. This supports the view that the changes in Ti concentration seen for the QML sample were not due the Ti desorbing, but it is currently unknown why this difference in behaviour is observed.

<i>T</i> (°C)	Elemental Composition (%)			
	O 1s	Ti 2p	F 1s	N 1s
0	6.0	-	0.1	0.2
400	5.9	2.0	0.3	-
600	6.0	2.1	-	-
800	5.4	2.0	-	-
1000	0.1	2.0	-	-

Table 6-3 – HML TiO – Summary of the elemental composition after annealing at different temperatures where 0 °C represents before deposition, and 400 °C is after deposition, as this is the deposition temperature.

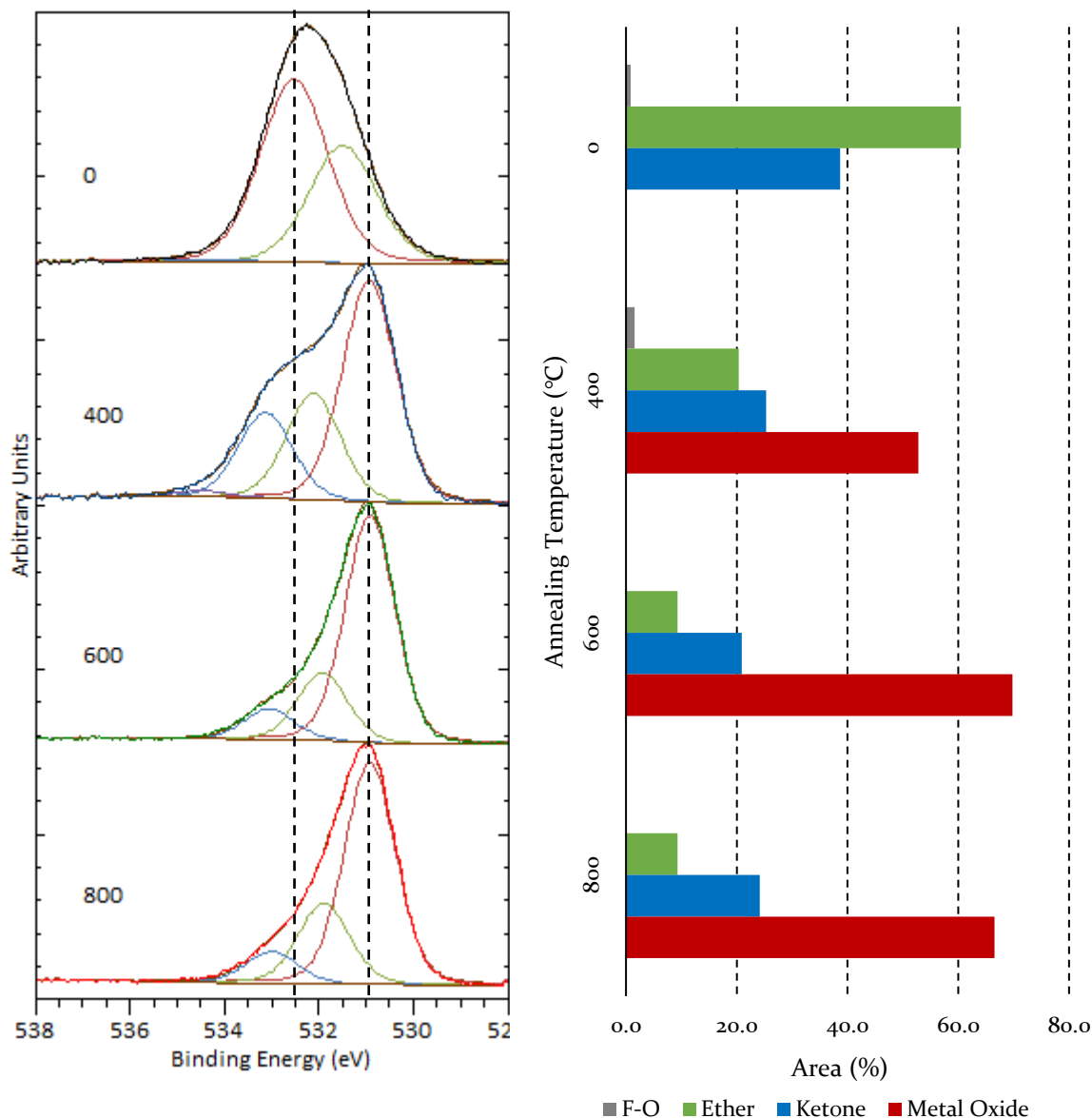


Figure 6-8 – HML TiO – An overlay of the O 1s spectra (left) after the different temperature anneals and the areas of the corresponding component peaks (right). No attempt has been made to colour match the lineshapes used in the spectral fitting with the bars used in the histograms. The components in the spectra from left to right correspond to the bars in the histogram from top to bottom.

Looking at the overlaid O 1s spectra in Figure 6-8, the spectrum before Ti deposition (0 °C) exhibited a large ether component at 532.5 eV, a smaller ketone component at 531.5 eV and a very small fluorine oxide component at 534.2 eV. This is consistent with the O-terminated samples discussed in section 5.3. As with the QML TiO sample, upon Ti deposition at 400 °C a TiO component appeared at 530.9 eV which was larger than the other components. As seen when investigating pure Ti in section 6.2, there was an increase in fluorine contamination which can be seen not only in the survey spectrum, but also in the O 1s spectrum (the grey component in the bar chart). This fluorine

component disappeared after the 600 °C anneal, which again agrees with the lack of fluorine in the survey spectrum (Table 6-3). It should also be noted that the TiO component increased in size while the other components reduced. This was also seen for the QML sample, but was more pronounced here, where the metal oxide component was not only just the largest component, but it was significantly larger than the ketone component. This is due to there being twice as much Ti on the surface of this HML sample.

The C 1s spectra in Figure 6-9 showed a large component at 285.1 eV and a smaller component at 284.4 eV. Additionally, three small components in the shoulders of the peak were observed. After the deposition of an HML onto the O-terminated surface, there was minimal change in the composition of the peak, however the peak shifted by 0.3 eV to a lower binding energy. Upon annealing at 600 °C, this shift was even more pronounced, with the peak being 0.7 eV lower in energy than at 0 °C. The overlay of the spectra on a logarithmic scale again shows the decrease in size for the C-O components. There was a significant metal carbide peak at 282.0 eV after the 1000 °C anneal, once virtually all of the O had desorbed.

The Ti 2p spectra in Figure 6-10 showed that upon Ti deposition at 400 °C, the Ti was predominantly in its Ti(IV) and Ti(III) oxidation state, with the largest component at 458.9 eV. As with the QML sample, there was a shift towards Ti(IV) after 600 °C, followed by a shift towards the lower-energy Ti(II) state after most of the O had desorbed after 1000 °C. This can be explained in terms of the electronegativity of the species involved. Electronegativity is a measure of how readily an atom attracts a pair of electrons to form a chemical bond. A high electronegativity value means the element attracts electrons while a low value indicates the element will readily donate electrons. As can be seen from the periodic table of electronegativity values in Figure 6-11, O has a fairly high electronegativity (3.4), while C has a medium value (2.6), and Ti has a low value (1.5).<sup>152</sup> Therefore, O exerts a greater attraction on the electron of Ti, leading to Ti(IV) when bonded to O. When the O desorbs, the Ti is bonded to the less electronegative C, and forms the Ti(II) oxidation state.

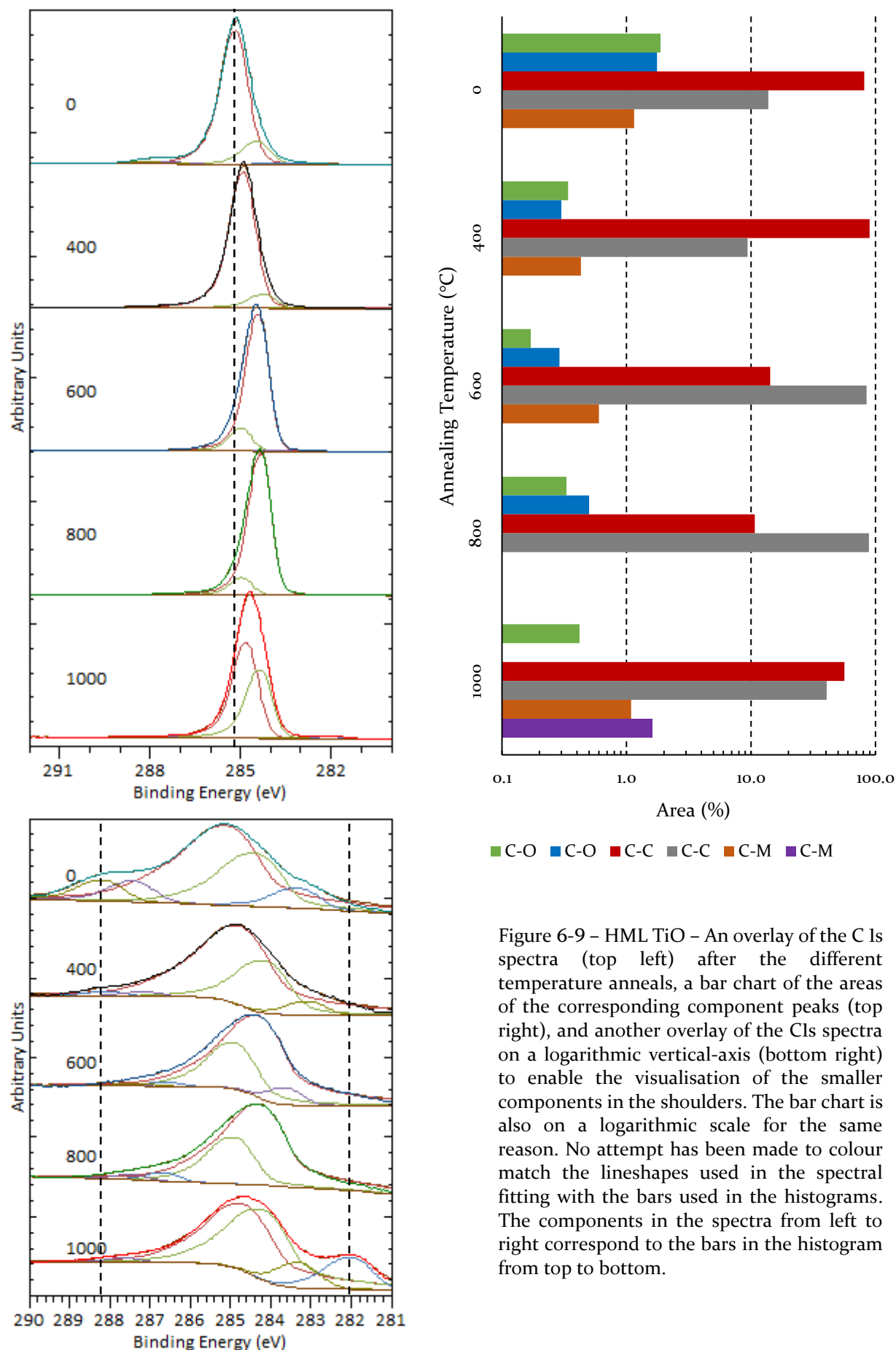


Figure 6-9 – HML TiO – An overlay of the C 1s spectra (top left) after the different temperature anneals, a bar chart of the areas of the corresponding component peaks (top right), and another overlay of the C1s spectra on a logarithmic vertical-axis (bottom right) to enable the visualisation of the smaller components in the shoulders. The bar chart is also on a logarithmic scale for the same reason. No attempt has been made to colour match the lineshapes used in the spectral fitting with the bars used in the histograms. The components in the spectra from left to right correspond to the bars in the histogram from top to bottom.

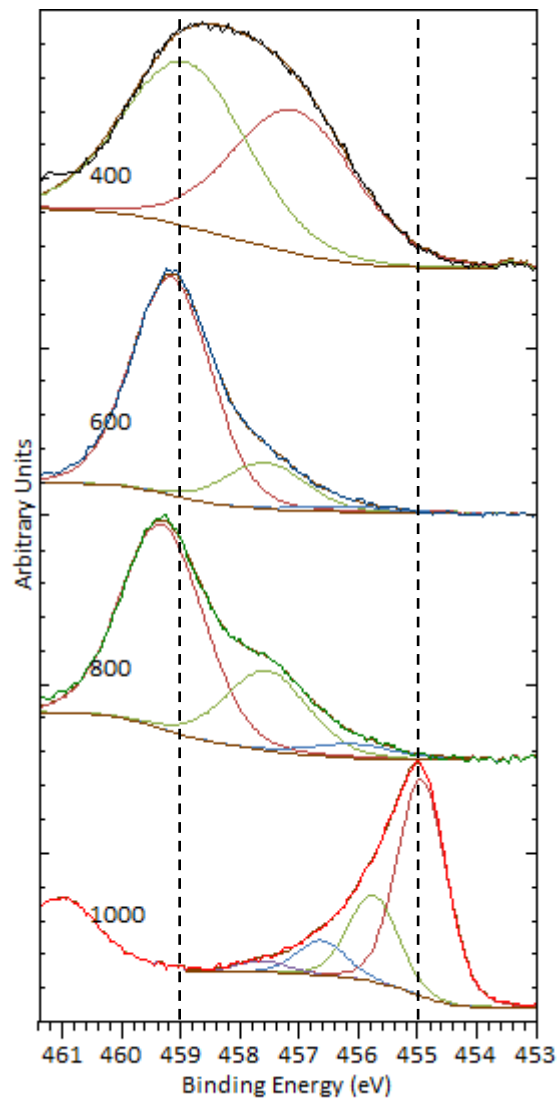


Figure 6-10 – HML TiO – An overlay of the Ti 2p spectra after the different temperature anneals.

### Electronegativity of the Elements

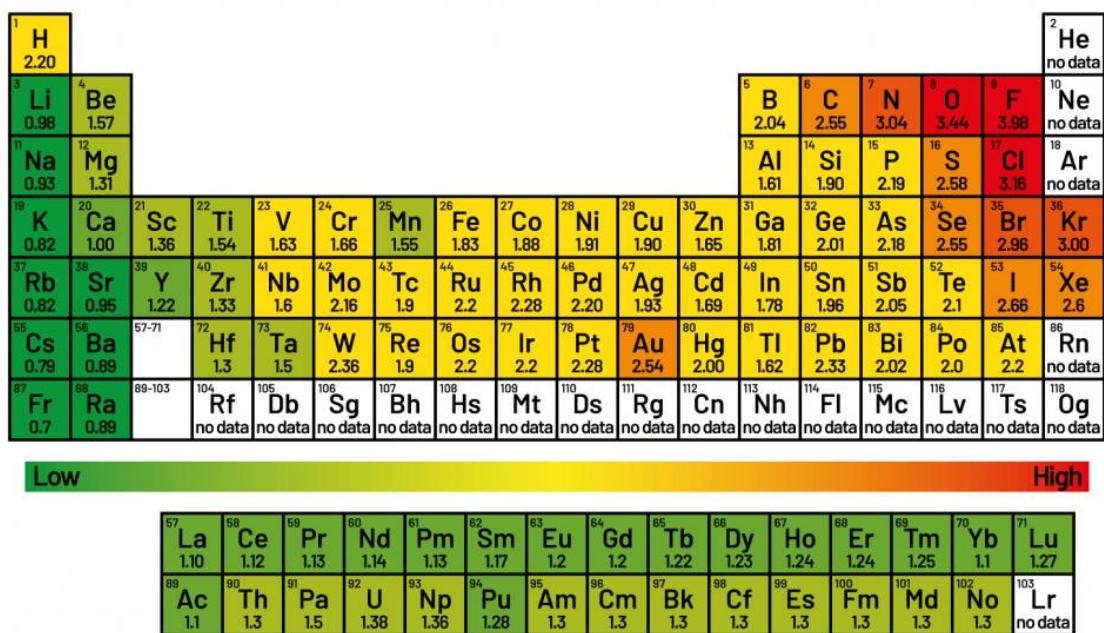


Figure 6-II – Periodic table showing the values and trends in the electronegativity of the elements.<sup>152</sup>

### 6.3.3 FML TiO

In the following section the FML sample, with a desired 4.1 % Ti on O-terminated diamond, is discussed. Before Ti was deposited (0 °C), the sample had an ML of O and trace amounts of N present, as shown in Table 6-4. After deposition of Ti at 400 °C, there was an increase in the quantity of O present, from 5.6 % to 6.4 %, and again to 7.5 % after 600 °C. The amount of Ti deposited was slightly more than an ML, at 4.3 %. Unlike the previous sample, there was no fluorine contamination present at 400 °C, although the trace amounts of fluorine detected after 600 °C and 1000 °C suggest there was a trace amount of fluorine present below the limit of detection.

The concentration of Ti on the surface remained relatively unchanged until 1000 °C, after which a slight decrease was observed. It is not possible to determine from this data alone whether this was because of rearrangement of the Ti atoms on the surface or whether a portion of the Ti had, indeed, desorbed.

Figure 6-12 shows the overlay of the O 1s spectra after the various annealing processes. Before Ti deposition at 0 °C, the O spectrum was similar to the spectra discussed in section 5.3, with a large ether component at 532.4 eV, a smaller ketone component at 531.5 eV and a miniscule fluorine component at 533.5 eV. Upon Ti deposition these components shift to a higher energy, while a fourth component, the metal oxide peak emerged. Unlike the QML and HML samples, there was no significant change in the peak composition after the 600 °C anneal, which may be related to the increase in O concentration between these temperatures, as opposed to the decrease seen for the other samples. After the 800 °C anneal, instead of the metal oxide peak increasing in

<i>T</i> (°C)	Elemental Composition (%)			
	O 1s	Ti 2p	F 1s	N 1s
0	5.6	-	-	<0.1
400	6.4	4.3	-	-
600	7.5	4.4	<0.1	<0.1
800	1.7	4.3	-	-
1000	-	3.9	<0.1	-

Table 6-4 – FML TiO – Summary of the elemental composition after annealing at different temperatures where 0 °C represents before deposition, and 400 °C is after deposition, as this is the deposition temperature.

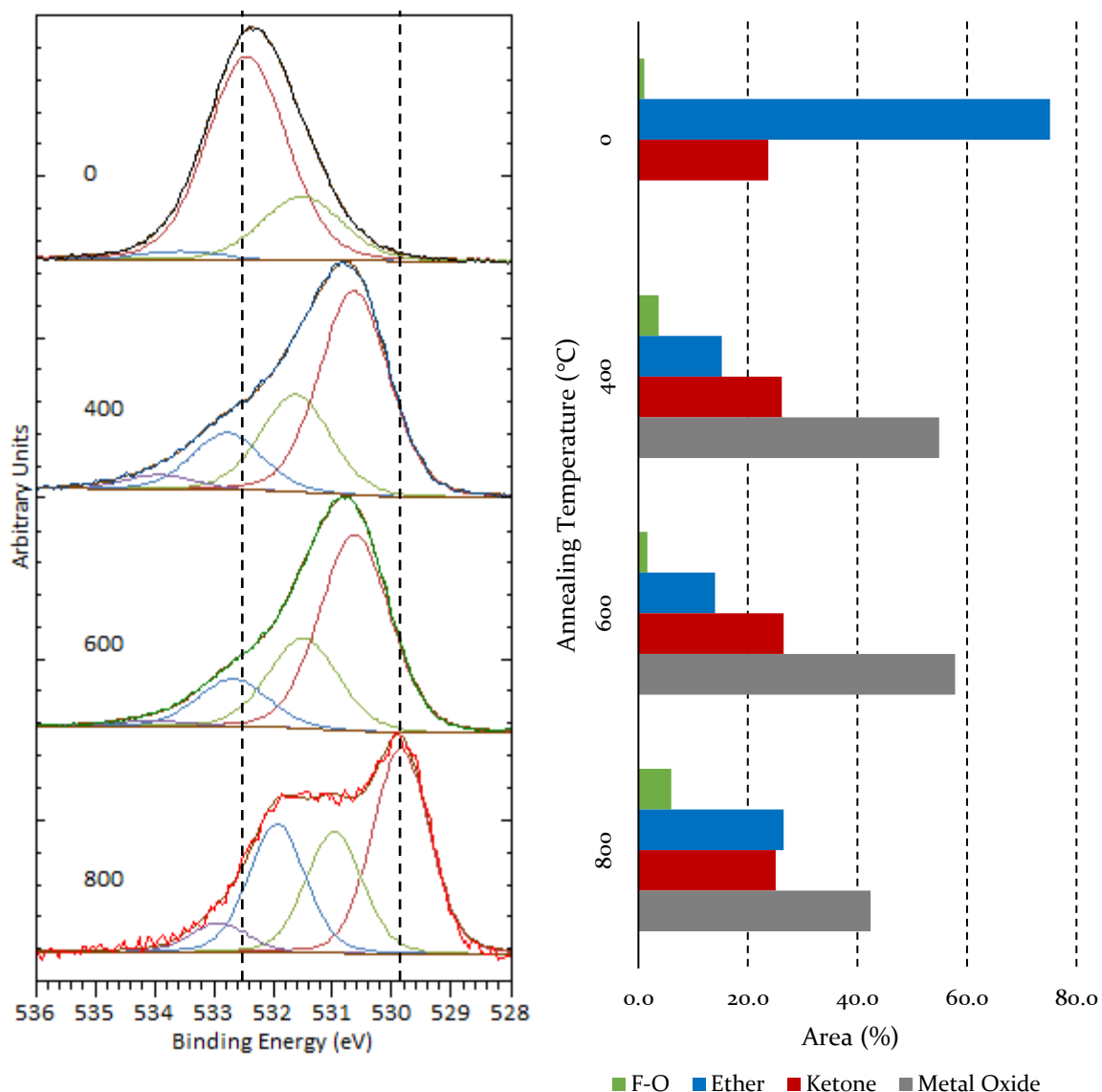


Figure 6-12 – FML TiO – An overlay of the O 1s spectra (left) after the different temperature anneals and the areas of the corresponding component peaks (right). No attempt has been made to colour match the lineshapes used in the spectral fitting with the bars used in the histograms. The components in the spectra from left to right correspond to the bars in the histogram from top to bottom.

size relative to the other components, it decreased in size while shifting to a lower energy. This is most likely due to a significant portion of the O having desorbed at this point. Furthermore, this indicates that the O in the metal oxide environment has desorbed more readily than for the QML and HML samples. This can be accounted for by the fact that the Ti oxidised further upon and after deposition, as can be seen by the aforementioned increase in O concentration after the 400 °C and 600 °C anneals.

The C 1s spectra in Figure 6-13 followed a similar pattern to the previous two samples with the two largest C-C components at 285.1 and 284.4 eV. There is little change with

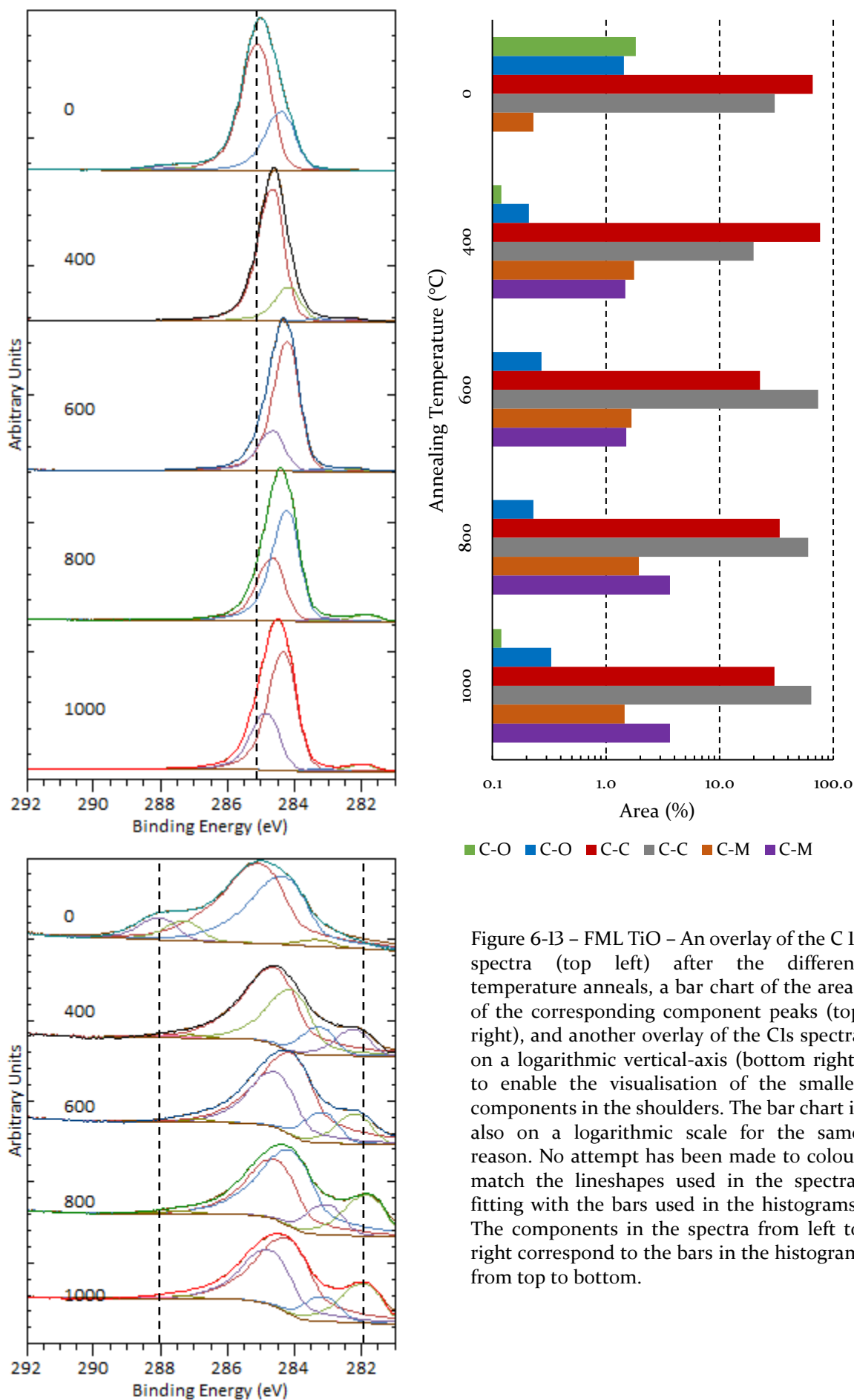


Figure 6-13 – FML TiO – An overlay of the C 1s spectra (top left) after the different temperature anneals, a bar chart of the areas of the corresponding component peaks (top right), and another overlay of the C 1s spectra on a logarithmic vertical-axis (bottom right) to enable the visualisation of the smaller components in the shoulders. The bar chart is also on a logarithmic scale for the same reason. No attempt has been made to colour match the lineshapes used in the spectral fitting with the bars used in the histograms. The components in the spectra from left to right correspond to the bars in the histogram from top to bottom.

these two components after Ti deposition except for a small decrease in binding energy. After the 600 °C anneal, the two largest components swap places, a trend which has also been observed in the QML and HML samples. As this is single crystal diamond, the larger component would typically be assigned to  $sp^3$  carbon while the smaller component originates from the  $sp^2$  carbon.  $Sp^3$  has a higher binding energy than  $sp^2$ , which implies that most of the diamond surface converts to graphitic or amorphous C after the 600 °C anneal. As it can be seen that this is not the case, both by visually inspecting the sample as well as subsequent experiments, one can only conclude that this is mathematical artefact of the fitting procedure. Perhaps there is a change in the asymmetry of the C 1s peak due to the change in the surface composition which complicates the component fitting. Interesting to note is the fact that the second metal carbide component was observed following Ti deposition at 400 °C, rather than after O desorption at 800 or 1000 °C, as was the case for the QML and HML samples. This can be seen on the logarithmic overlay in Figure 6-13, and is most likely due to the larger quantity of Ti present on this sample surface.

Figure 6-14 shows the Ti 2p spectra of the FML sample. For the QML and HML samples, the Ti was predominantly in the Ti(IV) oxidation state upon deposition and shifted towards lower oxidation states with increasing temperature. However, the Ti on the FML sample is predominantly in the Ti(II) oxidation state, even at the deposition temperature of 400 °C. This is most likely related to the decreased coordination of the Ti atoms with increasing Ti coverage, as discussed in more detail in section 6.3.4. Despite the Ti being mainly in Ti(II) oxidation state, even upon deposition, minimal changes to the shape of the peak were noted, with the highest-energy component increasing in size after the 600 °C anneal, relative to the other components. After the 800 °C and 1000 °C anneals, there is a shift towards the lower binding energies. This indicates that the shift toward lower oxidation states was also present in this sample, albeit not as pronounced as with the QML and HML samples.

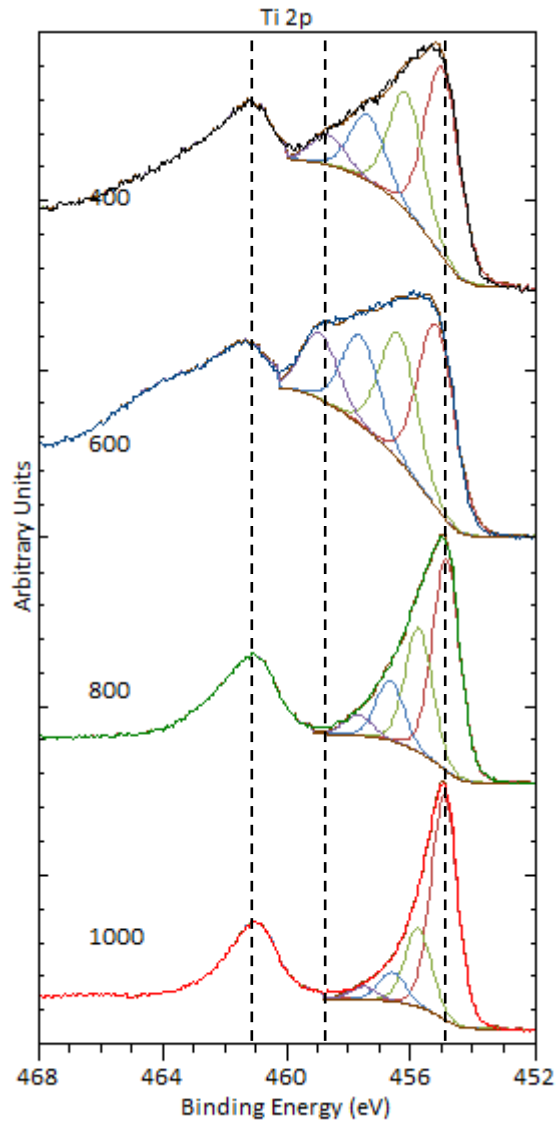


Figure 6-14 – FML TiO – An overlay of the Ti 2p spectra after the different temperature anneals.

### 6.3.4 TiO Work Functions

UPS analysis was performed on the QML, HML and FML samples before and after Ti deposition, as well as following the 600 °C, 800 °C, and 1000 °C anneals. The WF values after these different temperatures are summarised in Figure 6-15. At 0 °C, before Ti deposition, the WF values of all three samples were relatively high (5.3 – 5.5 eV) and consistent with O-terminated diamond as discussed in section 5.3. After Ti deposition at 400 °C, the WF values of all three samples decreased, with the QML sample decreasing significantly less than the other two (0.2 eV versus 1.0 – 1.2 eV). After 600 °C, the WF of the QML sample reduced by a further 0.7 eV to 4.4 eV, which is comparable to the WF of the HML and FML samples after Ti deposition (4.2 eV and 4.5 eV respectively). The WF values of the QML and HML samples increased after 800 and 1000 °C while the WF of the FML sample increased after 600 °C. The final WF values after the 1000 °C anneal were 4.3 – 4.6 eV.

As detailed in Tables 6-1, 6-2, and 6-3, while the Ti concentration only varied by small amounts, the concentration of O on the diamond surface changed significantly, with all three samples showing only trace amounts of O remaining after 1000 °C. Figure 6-16 therefore shows the relationship between the percentage of O present on the sample

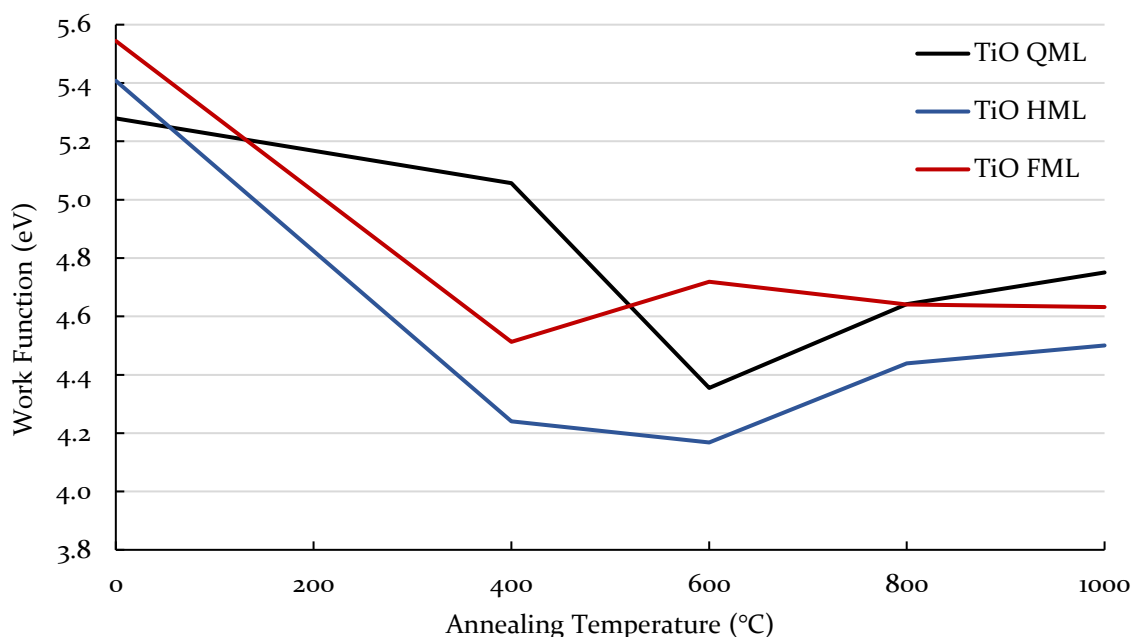


Figure 6-15 - TiO - How the WF of the three TiO-terminated samples evolves as a function of annealing temperature. 0 °C is the O-terminated samples before Ti deposition while 400 °C is the WF after Ti deposition as this is the deposition temperature.

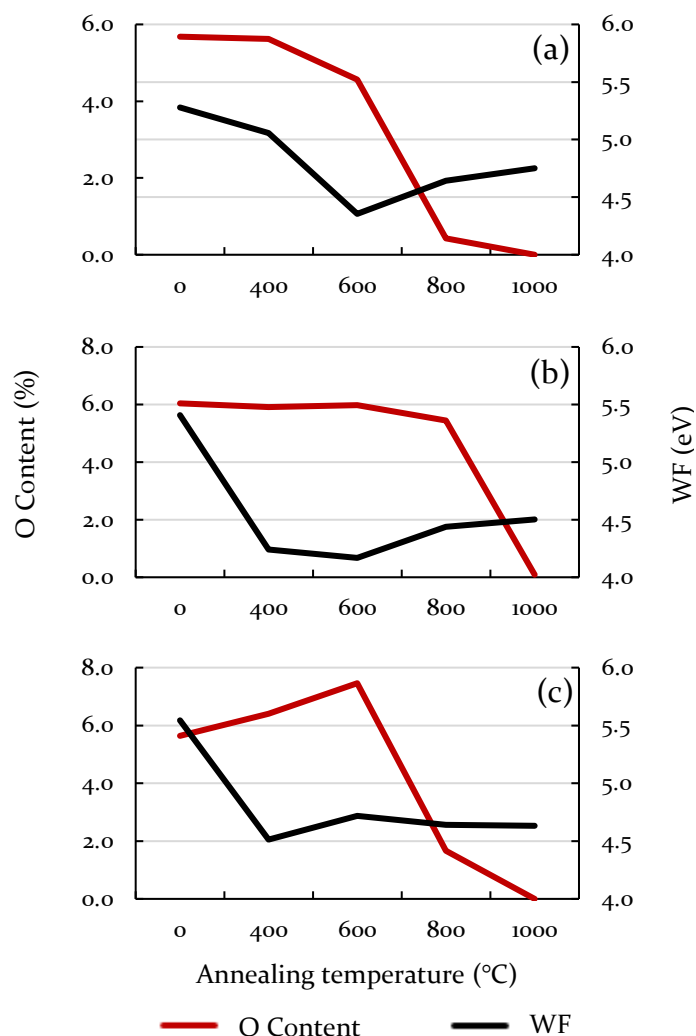


Figure 6-16 – TiO – Evolution of the WFs of the (a) QML, (b) HML, and (c) FML Ti oxide-terminated samples in relation to the O content.

surface and the WF. The QML sample (a) showed a degree of correlation between the WF and O concentration. The largest drop in O concentration corresponded to the largest increase in WF between 600 and 800 °C. For the HML sample on the other hand, the large increase in WF between those temperatures was accompanied by only a small decrease in O concentration.

For the FML sample on the other hand, the largest increase in the WF was between 400 and 600 °C, during which no decrease in O concentration was noted. Instead, the amount of O increases due to the decrease in the coordination of the Ti atoms. The initial amount of O present on each of the sample, as discussed previously, was consistent (5.7 – 6.0 %), while the concentration of Ti increased from QML, to HML, to FML (1.0 %, 2.0 %, and 4.3 % respectively). This means that the resulting metal-to-

oxygen ratio increased causing a decrease in coordination per Ti atom. With the FML coverage, the individual Ti atoms could no longer bond to a sufficient number of O atoms to satisfy its bonding requirements. This resulted in the sample oxidising further after deposition, and the 600 °C anneal. After the 800 °C anneal, the concentration of O decreased as the O desorbed, as observed with the other two samples.

## 6.4 Titanium Nitride

To create TiN-terminated diamond surfaces, several single crystal (100) diamond samples were first N-terminated, using the ammonia plasma method in the Terminator reactor (see section 4.5.2.3). The samples were then characterised in the NanoESCA as discussed in chapter 4, and Ti was then deposited *in situ* in varying quantities.

In the computational study, as discussed in chapter 2, the adsorption energy (surface stability) and EA (electron emission) were calculated. The experimental work presented here aims to replicate this with species desorption as a function of temperature (surface stability) and WF (electron emission). The WF and EA are intrinsically linked as they both define the position of the vacuum level, either relative to the Fermi level or conduction band minimum respectively, discussed in more detail in sections 1.3.1 and 1.4.

To enable a comparison of the experimental data to the computational models, a QML, HML, FML of Ti on N-terminated (100) diamond surfaces were prepared. These equate to 1.0 %, 2.1 %, and 4.1 % of Ti in the survey spectrum, respectively. The sample composition is discussed as a function of the annealing temperature, and the impact this had on the observed WF values.

A key difference between the TiO- and TiN-terminated samples is the contamination present on the TiN surfaces. Despite both O and N terminations being performed in the same reactor, this issue only affects the N-terminated samples. This is because for the O termination, the sample is exposed to the plasma for 7 s, while for the N termination the samples are exposed to the ammonia plasma for 180 s. This increased exposure time leads to significant sputtering of the stainless-steel electrode resulting in significant chromium, iron, and nickel contamination.

### 6.4.1 QML TiN

Table 6-5 shows the elemental composition of the sample according to the survey scans after the various temperature anneals. Before deposition, the sample was N-terminated using an ammonia plasma (see section 4.5.2.3). The sample had 3.0 % N, which equates to  $\sim 0.5$  ML, as discussed in section 5.4. Additionally, extensive iron contamination and more than an ML equivalent of O were present. The iron contamination was sputtered from the stainless-steel electrode used to generate the ammonia plasma. The sample also contained small amounts (0.2 %) of nickel and chromium, also from the stainless-steel electrode, though these are not shown in Table 6-5 as the quantities of these elements are directly related to the amount of iron, which is the largest contaminant. Due to this, care was taken in any conclusions drawn from these data. In particular, the WF values of these surfaces could be affected by the presence of trace metal on the surface. As such, the observed data trends are more significant than the absolute values. At 400 °C, 1.0 % Ti was deposited, which equates to a QML of Ti on the N-terminated surface. Upon Ti deposition, a small decrease in the concentration of N on the surface was observed, the amount of O remained unchanged, while the quantity of iron increased by 0.2 %. As there are neither any iron sources in the chamber, nor has this been observed in other experiments, this increase is likely due to the iron atoms rearranging on the surface.

After the 600 °C anneal, there was a further decrease in the amount of N present, while the quantity of Ti and iron remained the same, within the margin of error. There is also a significant decrease in the concentration of O on the surface, from 6.0 % to 1.9 %, due to desorption.

<i>T</i> (°C)	Elemental Composition (%)				
	O 1s	N 1s	Ti 2p	F 1s	Fe 2p
0	6.1	3.0	-	-	1.9
400	6.0	2.6	1.0	<0.1	2.1
600	1.9	2.0	1.1	0.1	2.1
800	0.3	0.5	1.0	0.1	1.3
1000	<0.1	0.1	0.8	-	<0.1

Table 6-5 – QML TiN – Summary of the elemental composition after annealing at different temperatures where 0 °C represents before deposition, and 400 °C is after deposition, as this is the deposition temperature.

After 800 °C, there was an even larger decrease in the quantity of N present while the O had almost completely desorbed. There was also a significant decrease in the amount of iron on the surface (2.1 % to 1.3 %). After the 1000 °C anneal, virtually all of the O, N, and iron had desorbed leaving only Ti on diamond.

Figure 6-17 shows an overlay of all the O 1s spectra after the different temperature anneals and a bar chart with the relative size of all the component peaks. Unlike the TiO-terminated samples, the O 1s spectrum before Ti deposition does not resemble the O 1s spectra of clean O-terminated diamond discussed in section 5.3, which typically contains a large ether component and a smaller ketone component. The O 1s spectrum in Figure 6-17, however, while exhibiting an ether component that is larger than the ketone component, has a metal oxide peak as its largest component, even before Ti deposition. This indicates that a significant portion of the O originates from the iron contamination being oxidised upon the sample being exposed to atmosphere, rather than O directly on the diamond surface. After Ti deposition, the ratio of ether to ketone resembled the TiO-terminated samples, but the metal-oxide peak was significantly larger, containing contributions from both FeO and TiO.

Figure 6-18 shows the C 1s spectra after the various temperature anneals. On the linear intensity scale, the 0 °C and 400 °C spectra closely resemble those for the TiO samples. After 600 °C, however, while a shift of the peak as a whole to a lower binding energy is observed, there is no reversal in the relative size of the two largest components. Looking at the overlays on a logarithmic scale, the O component at 288.0 eV is smaller than for the TiO-terminated samples, despite there being more O present. This is further evidence that the O is not predominantly bonded directly to the diamond, in agreement with the data from the O 1s spectra. Furthermore, the carbide component peak can be observed after 800 °C, when the majority of the N and almost all of the O has desorbed. It increased in size after the 1000 °C anneal, despite less Ti being observed in the survey spectrum. This again indicates that this decrease is not due to Ti desorbing.

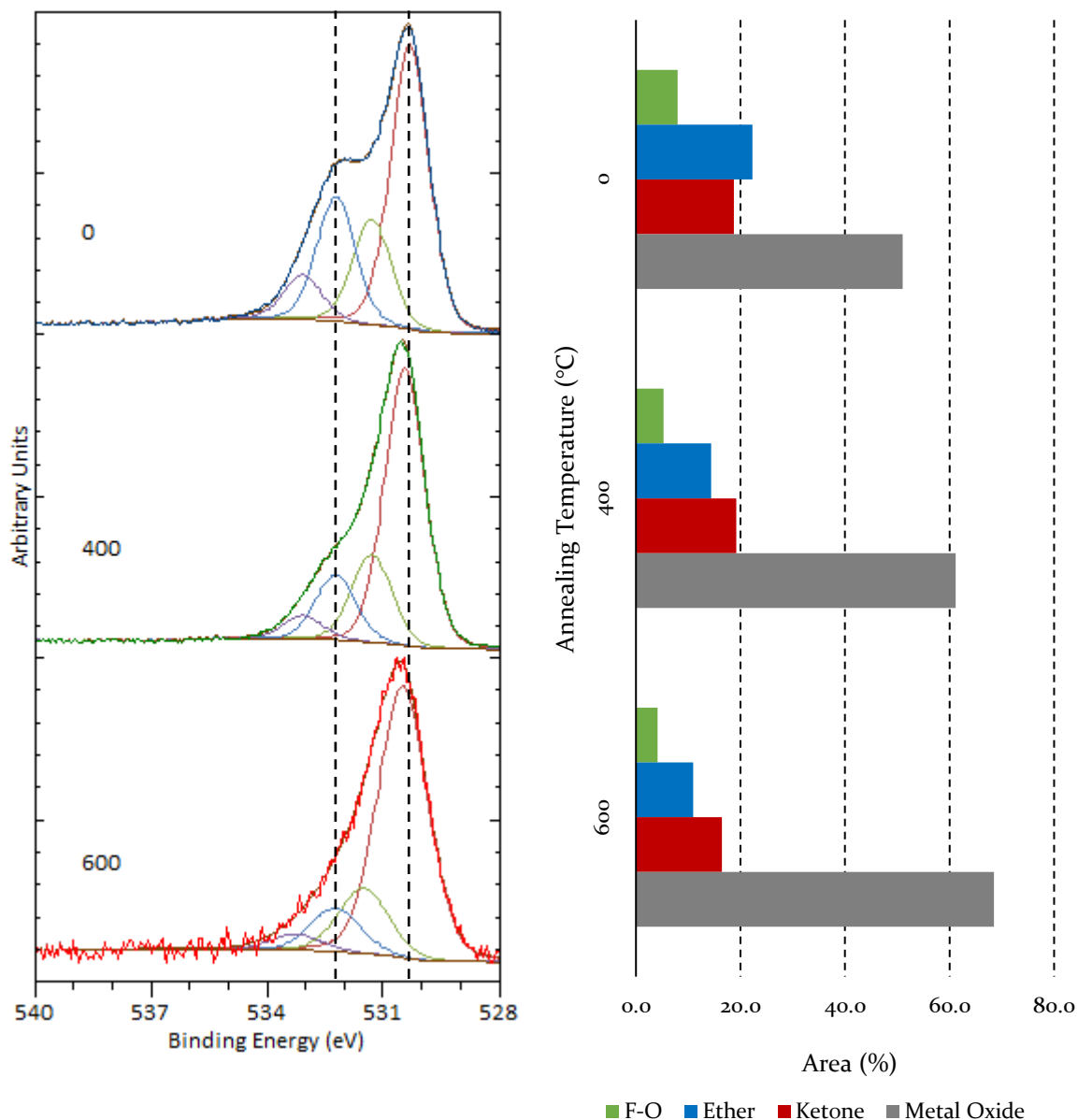


Figure 6-17 – QML TiN – An overlay of the O 1s spectra (left) after the different temperature anneals and the areas of the corresponding component peaks (right). No attempt has been made to colour match the lineshapes used in the spectral fitting with the bars used in the histograms. The components in the spectra from left to right correspond to the bars in the histogram from top to bottom.

Figure 6-19 shows the overlaid N 1s spectra for this sample. Before Ti deposition, the largest component peak corresponds to the C-NH functional group. With increasing annealing temperatures, the composition shifts towards the metal nitride components. This is comparable to the O spectra obtained for the TiO samples. The metal nitride component observed before Ti deposition can be attributed to the iron contamination. Figure 6-20 contains an overlay of the Ti 2p spectra. As seen with previous samples, after deposition, the Ti was predominantly in high oxidation states, and progressively moved towards lower oxidation states with each successive temperature anneal.

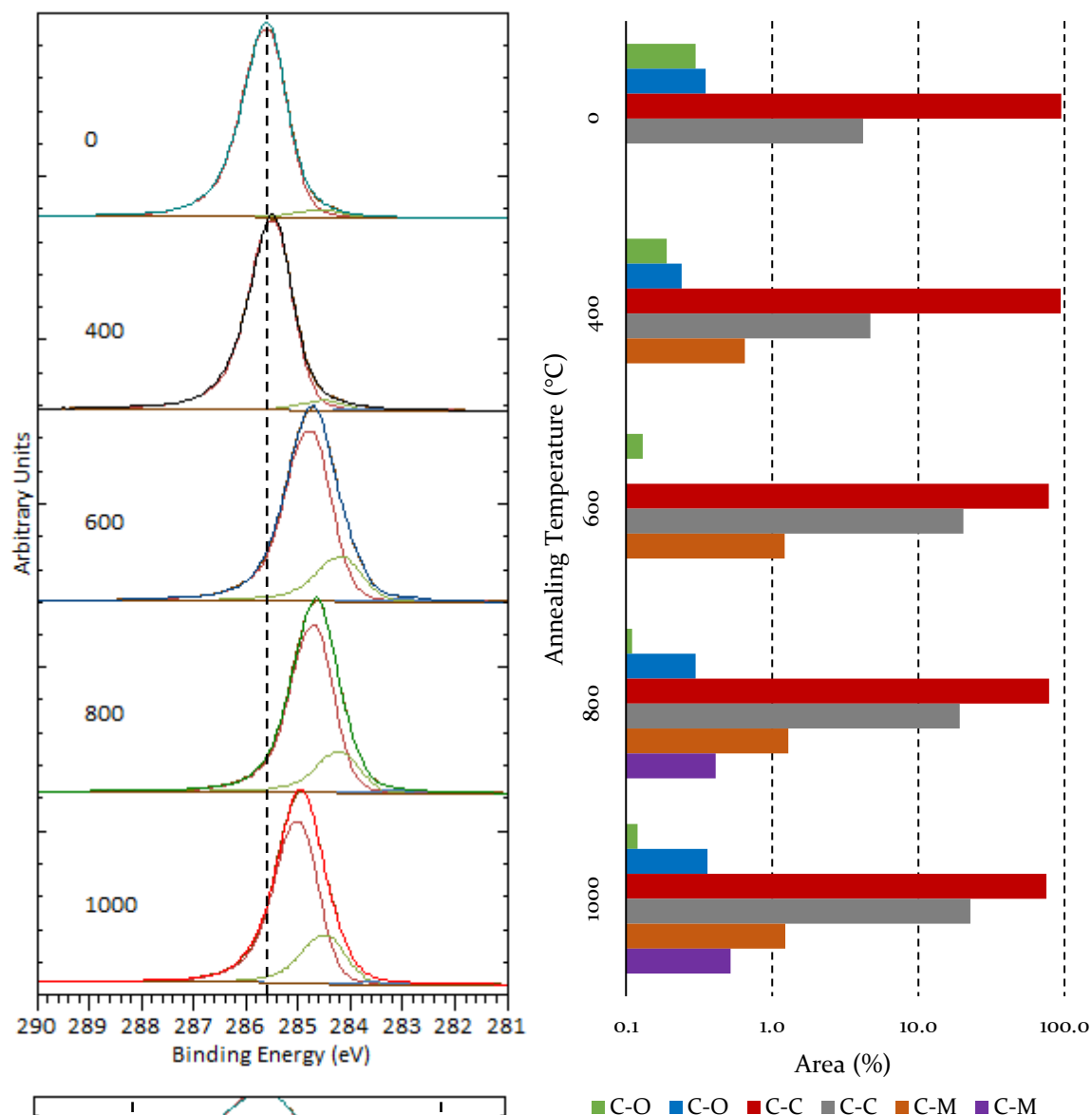


Figure 6-18 – QML TiN – An overlay of the C 1s spectra (top left) after the different temperature anneals, a bar chart of the areas of the corresponding component peaks (top right), and another overlay of the C1s spectra on a logarithmic vertical-axis (bottom right) to enable the visualisation of the smaller components in the shoulders. The bar chart is also on a logarithmic scale for the same reason. No attempt has been made to colour match the lineshapes used in the spectral fitting with the bars used in the histograms. The components in the spectra from left to right correspond to the bars in the histogram from top to bottom.

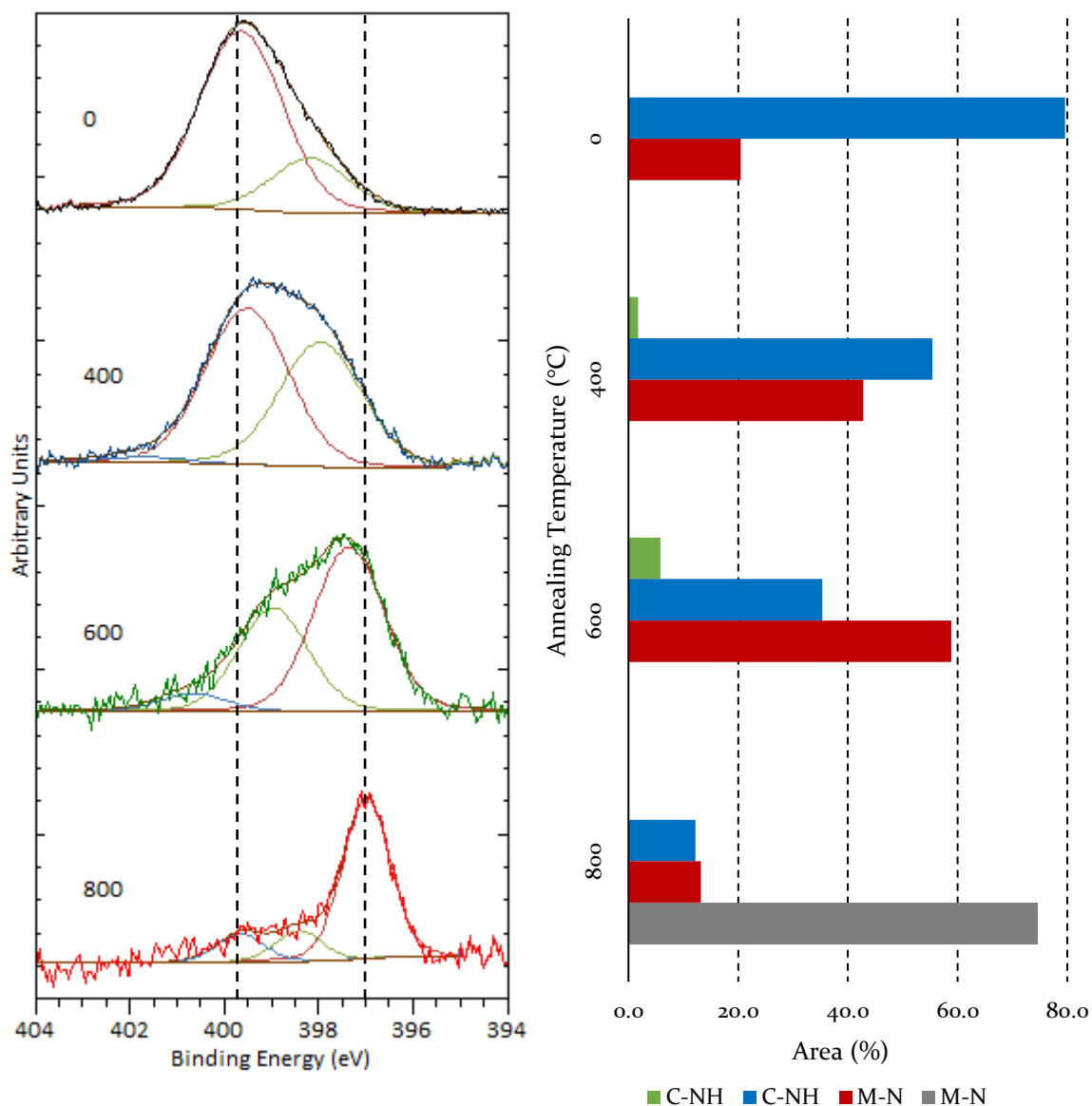


Figure 6-19 – QML TiN – An overlay of the N 1s spectra (left) after the different temperature anneals and the areas of the corresponding component peaks (right). No attempt has been made to colour match the lineshapes used in the spectral fitting with the bars used in the histograms. The components in the spectra from left to right correspond to the bars in the histogram from top to bottom.

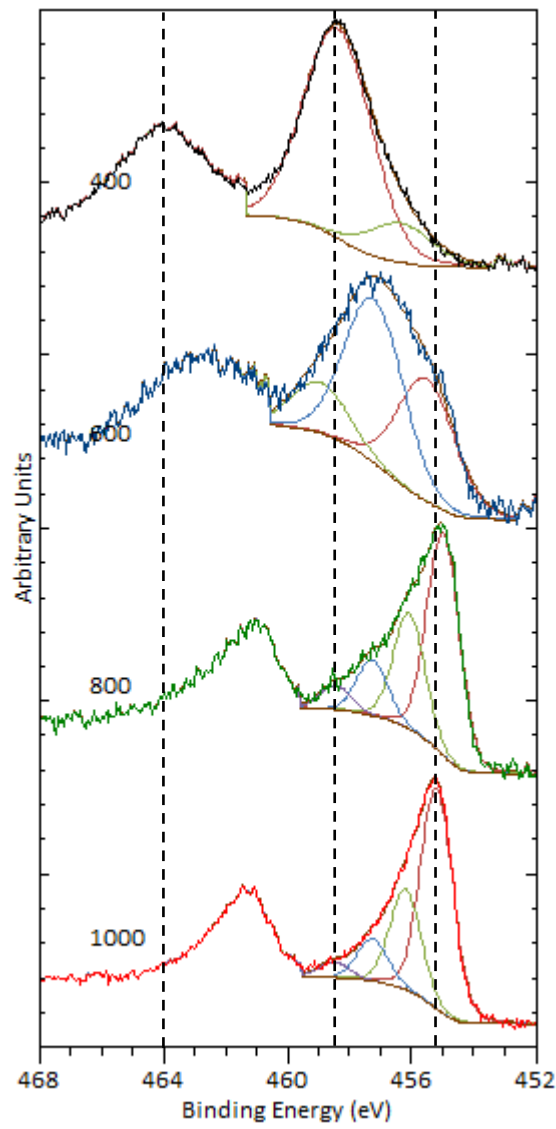


Figure 6-20 – QML TiN – An overlay of the Ti 2p spectra after the different temperature anneals.

### 6.4.2 HML TiN

Table 6-6 shows the elemental composition of the HML TiN sample according to the survey scans. Before Ti deposition, the sample was N-terminated using an ammonia plasma (see section 4.5.2.3) resulting in 2.9 % N on the diamond surface. There was also 2.7 % O and 0.8 % iron present. The fact that there is just under half as much iron contamination present on this samples compared to the QML sample (0.8 vs 1.9 %), as well just under half as much O being present (2.7 % vs 6.1 %), further suggests that the O is primarily due to the iron contamination oxidising.

Following Ti deposition, there was 2.1 % of Ti present, which equates to an HML. There was also a small decrease in the concentration of N (2.9 % to 2.7 %) and an increase in the amount of O (2.7% to 3.7 %) present. This indicates that some of the Ti may have oxidised further following deposition. After the 600 °C anneal, there was another small decrease in the amounts of N, as well as Ti, and a significant decrease in the concentration of O. Following the 800 °C anneal, virtually no O was detected, while the quantity of N had decreased further, with approximately half of the original quantity remaining. There was also a significant decrease in the concentration of iron, and a small decrease in the quantity of Ti present in the survey scan. After the 1000 °C anneal, there was no O or iron present, and only a small amount of N (0.4 %) remained. 75 % of the original Ti remained.

Figure 6-2l shows the overlaid O 1s spectra. Before Ti deposition, the biggest component is the ketone peak, with the metal oxide peak being marginally smaller. As the iron contamination on this sample was lesser, compared to the QML sample, less iron was oxidised and thus yielded a smaller metal oxide component. After Ti deposition, the

<i>T</i> (°C)	Elemental Composition (%)				
	O 1s	N 1s	Ti 2p	F 1s	Fe 2p
0	2.7	2.9	-	-	0.8
400	3.7	2.7	2.1	0.1	0.9
600	2.2	2.3	1.9	0.3	1.0
800	0.1	1.4	1.7	-	0.6
1000	-	0.4	1.6	-	-

Table 6-6 – HML TiN – Summary of the elemental composition after annealing at different temperatures where 0 °C represents before deposition, and 400 °C is after deposition, as this is the deposition temperature.

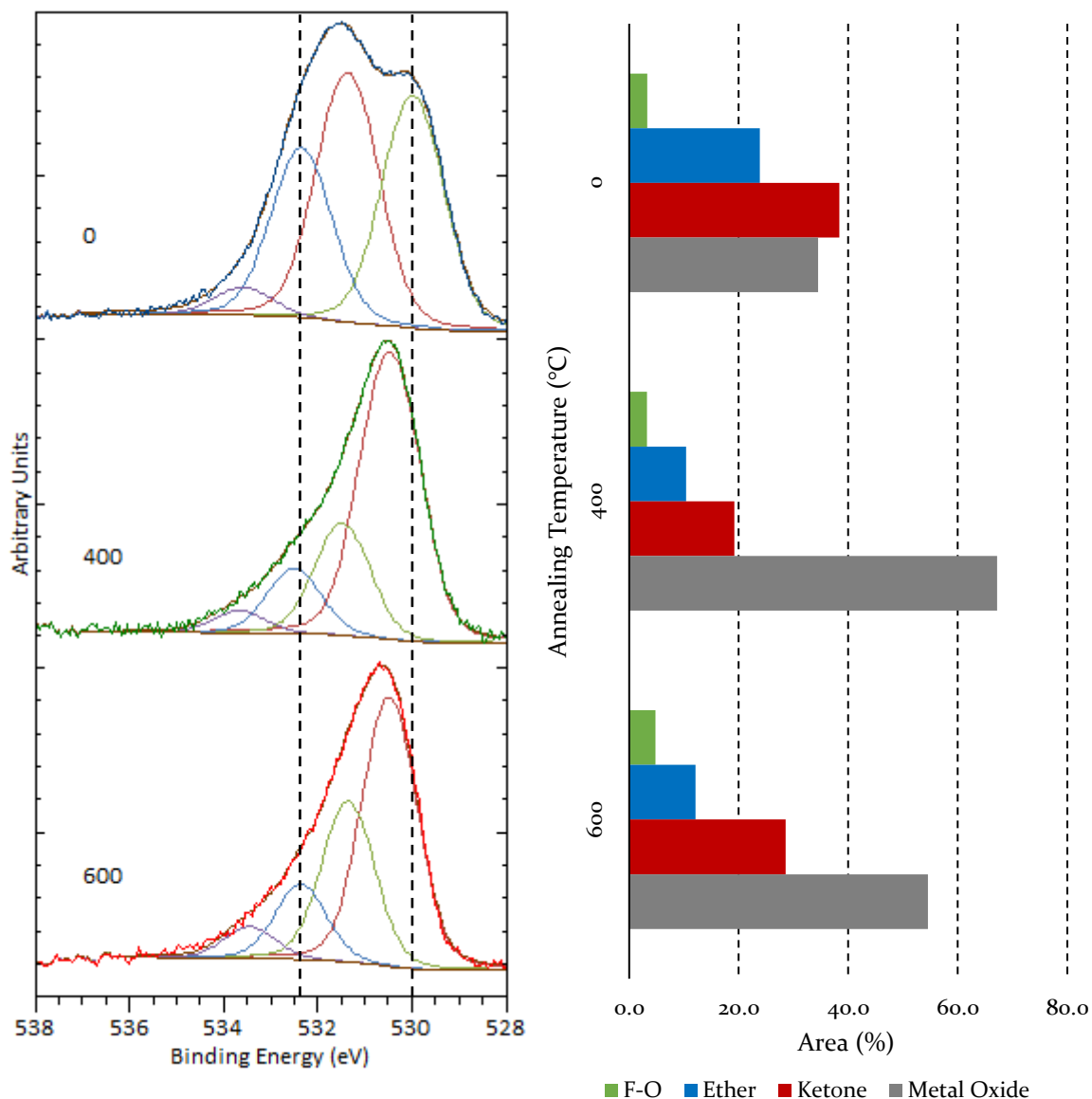


Figure 6-21 – HML TiN – An overlay of the O 1s spectra (left) after the different temperature anneals and the areas of the corresponding component peaks (right). No attempt has been made to colour match the lineshapes used in the spectral fitting with the bars used in the histograms. The components in the spectra from left to right correspond to the bars in the histogram from top to bottom.

metal oxide component increased significantly. However, following the 600 °C anneal, after a portion of the O had desorbed, the metal oxide component actually decreased in size relative to the other components, indicating that the O bonded to metal desorbed more readily than other O environments.

The overlaid C 1s spectra displayed in Figure 6-22 are similar to those of the QML TiN sample. Again, a shift of the peak as a whole to a lower binding energy was observed after the 600 °C anneal, without the reversal of the two largest components as seen for the TiO samples. The spectra overlaid on the logarithmic intensity scale also showed

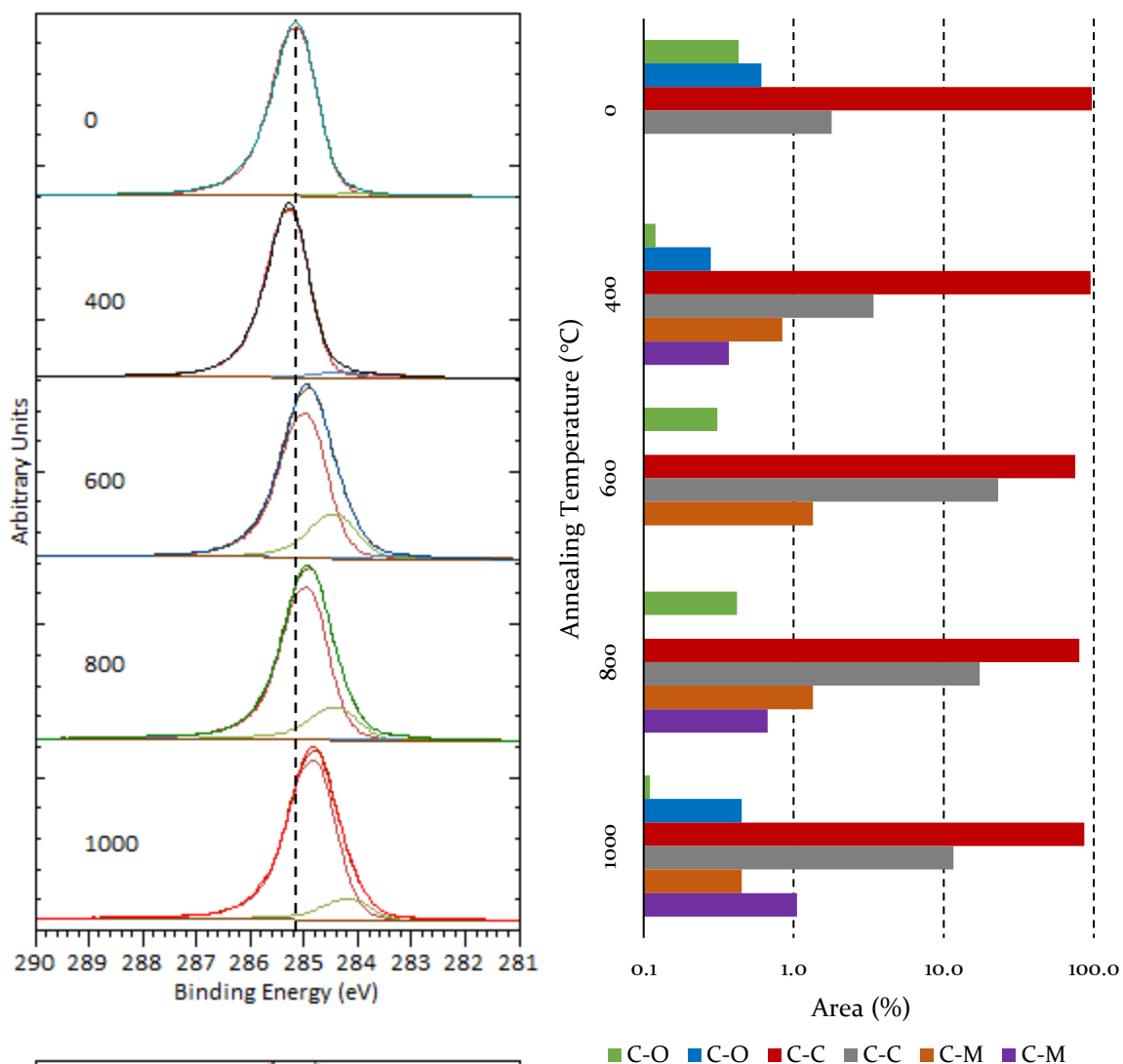


Figure 6-22 – HML TiN – An overlay of the C 1s spectra (top left) after the different temperature anneals, a bar chart of the areas of the corresponding component peaks (top right), and another overlay of the C1s spectra on a logarithmic vertical-axis (bottom right) to enable the visualisation of the smaller components in the shoulders. The bar chart is also on a logarithmic scale for the same reason. No attempt has been made to colour match the lineshapes used in the spectral fitting with the bars used in the histograms. The components in the spectra from left to right correspond to the bars in the histogram from top to bottom.

smaller O environments at 288 eV, while the metal carbide peak can only be detected following complete O desorption at 800 °C.

Figure 6-23 shows the overlaid N 1s spectra for this sample. Prior to Ti deposition, the peak is primarily composed of C-NH, shifting towards the metal nitride components at higher temperature, similar to both the O spectra for the TiO samples and the N 1s spectra of the QML TiN sample. A small metal nitride component can be observed before deposition because of the metal contamination. The N 1s spectrum after the 1000 °C anneal is not included, as almost no N on the sample remained and the

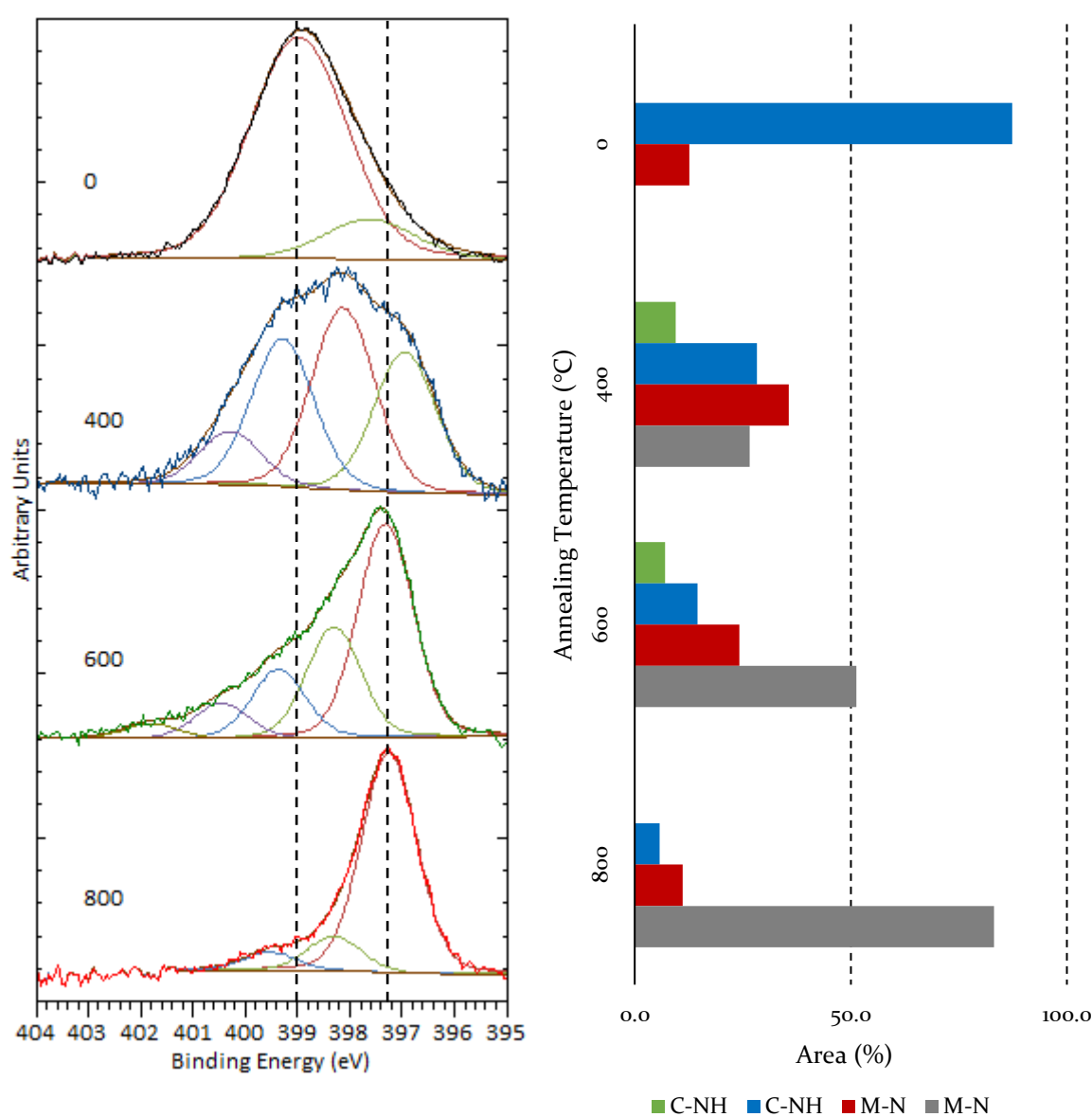


Figure 6-23 – HML TiN – An overlay of the N 1s spectra (left) after the different temperature anneals and the areas of the corresponding component peaks (right). No attempt has been made to colour match the lineshapes used in the spectral fitting with the bars used in the histograms. The components in the spectra from left to right correspond to the bars in the histogram from top to bottom.

spectrum would be inconclusive. Figure 6-24 contains an overlay of the Ti 2p spectra. As seen with previous samples, upon deposition, the Ti was primarily in high oxidation states, and progressively moved towards lower oxidation states with each successive higher temperature anneal.

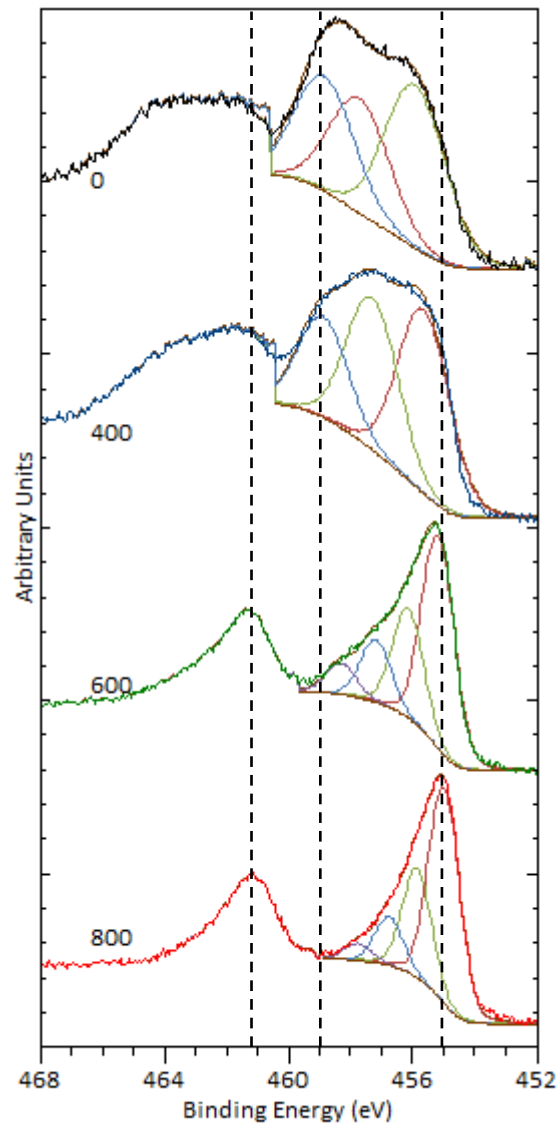


Figure 6-24 – HML TiN – An overlay of the Ti 2p spectra after the different temperature anneals.

### 6.4.3 FML TiN

This sample was intended to be an FML of Ti upon N-terminated diamond to create a TiN termination. Table 6-7 shows the sample composition at various stages. Before Ti deposition, the sample was N-terminated using an ammonia plasma for 3 min. This resulted in 3.1 % N on the diamond surface. There was also 3.7 % O and 0.8 % iron contamination present, as previously discussed.

Following Ti deposition at 400 °C, there was 4.0 % Ti in the survey spectrum which corresponds to an FML of Ti as discussed in section 6.2. Additionally, 0.5 % fluorine was deposited, which, although higher in comparison with other samples, was to be expected considering the longer deposition duration, as discussed in section 6.2. Minimal change in the concentration of N or iron was observed, within the margin of error, although there was a significant increase in the amount of O present. This was due to the deposited Ti oxidising.

Looking back at the structures examined in chapter 2, for the QML scenarios, each Ti atom was bonded to four O atoms, which is optimal. For the HML scenarios however, the Ti atoms were only bonded to two O atoms each or even one atom each for the FML scenarios. This means that in these scenarios, the Ti atoms are capable of creating additional bonds, such as with adsorbate atoms. Because of this, coupled with its high reactivity, Ti oxidises if it is not already fully coordinated, even under ultra-high vacuum conditions, as discussed in section 6.3.4.

After annealing the sample at 600 °C, there was a decrease in the fluorine contamination, as seen in previous samples. There was minimal change in the coverage of iron, Ti or N, while there was a small increase in the O concentration, presumably

<i>T</i> (°C)	Elemental Composition (%)				
	O 1s	N 1s	Ti 2p	F 1s	Fe 2p
0	3.7	3.1	-	-	0.8
400	5.2	3.0	4.0	0.5	0.7
600	5.8	2.8	3.9	0.1	0.6
800	5.5	2.5	3.8	-	0.6
1000	0.4	2.1	3.5	-	0.6

Table 6-7 – FML TiN – Summary of the elemental composition after annealing at different temperatures where 0 °C represents before deposition, and 400 °C is after deposition, as this is the deposition temperature.

due to the Ti oxidising further. Upon annealing the sample at 800 °C, the fluorine had desorbed completely, and there was a small decrease in both the O and N concentrations. Perhaps most interestingly, no decrease in the concentration of the iron contamination was observed. This is also true after the 1000 °C anneal. At this temperature, all previous samples exhibited a clean Ti-terminated surface, with only trace amounts of other elements remaining. For this FML TiN sample, however, not only did most of the initial iron contamination remain, but two thirds of the N was also still present. O was the only species to have mostly desorbed, though even of that, 0.4 % remained.

Figure 6-25 shows the overlaid O 1s spectra after the various annealing processes. As with the previous two TiN-terminated samples, there was a significant metal oxide peak present, even before Ti deposition. As discussed previously, this was due to the iron contamination present from the N termination process. Upon Ti deposition at 400 °C, all the components shifted to a higher binding energy, and the metal-oxide component increased in size, as seen with previous samples. During subsequent higher temperature anneals, there is little change in the O 1s peak, except for the metal oxide component decreasing in size relative to the other components, as the O content decreased. This indicates that the O bonded to metals desorbed more readily than that bonded to the diamond substrate, as mentioned previously.

The overlaid C 1s spectra displayed in Figure 6-26 proceed in a similar fashion to the previous two TiN samples. Initial scans before Ti deposition indicated mostly O components in the shoulders, and upon Ti deposition and subsequent anneals, these decrease in size while the lower energy carbide peaks increased. It should be noted that after the final 1000 °C anneal, the carbide components were larger than those present in the other two TiN-terminated samples, which can be accounted for by the fact that more Ti was deposited on this sample.

The N 1s spectra shown in Figure 6-27, similarly proceed again in the same fashion as previous samples. Upon Ti deposition at 400 °C, both a shift of the components to higher binding energies and a shift away from the C-NH components towards the metal nitride environments was observed. This trend continued as the temperature of the annealing processes increased. Unlike other core level scans, there was little change in

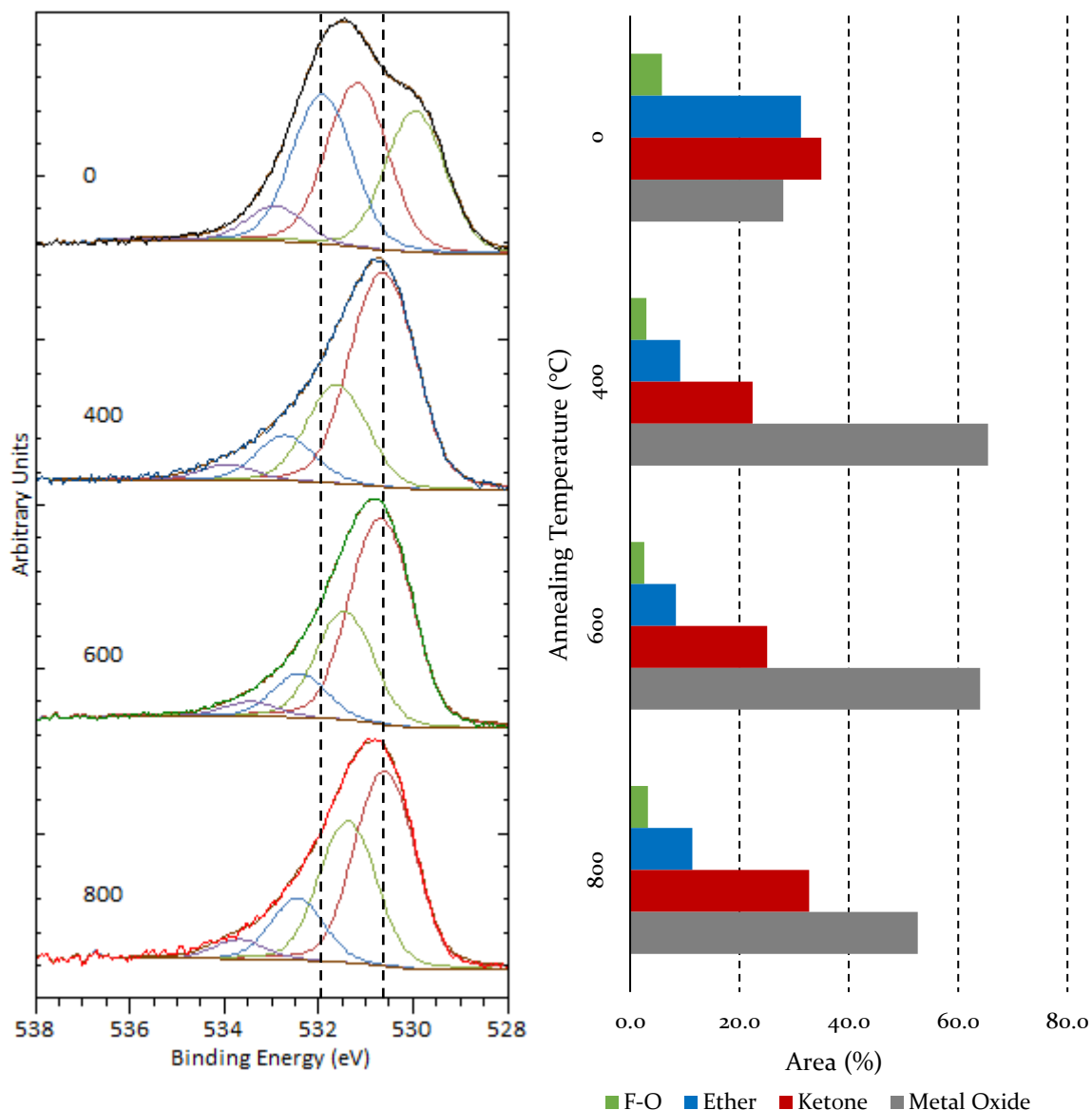


Figure 6-25 – FML TiN – An overlay of the O 1s spectra (left) after the different temperature anneals and the areas of the corresponding component peaks (right). No attempt has been made to colour match the lineshapes used in the spectral fitting with the bars used in the histograms. The components in the spectra from left to right correspond to the bars in the histogram from top to bottom.

the binding energies of the Ti 2p spectra from Figure 6-28. This is most likely because the largest shifts in binding energy for the other elements are typically observed upon Ti deposition, while there is no Ti 2p spectrum before Ti deposition. The shift in component size towards the lower oxidation states observed in previous samples was also seen here.

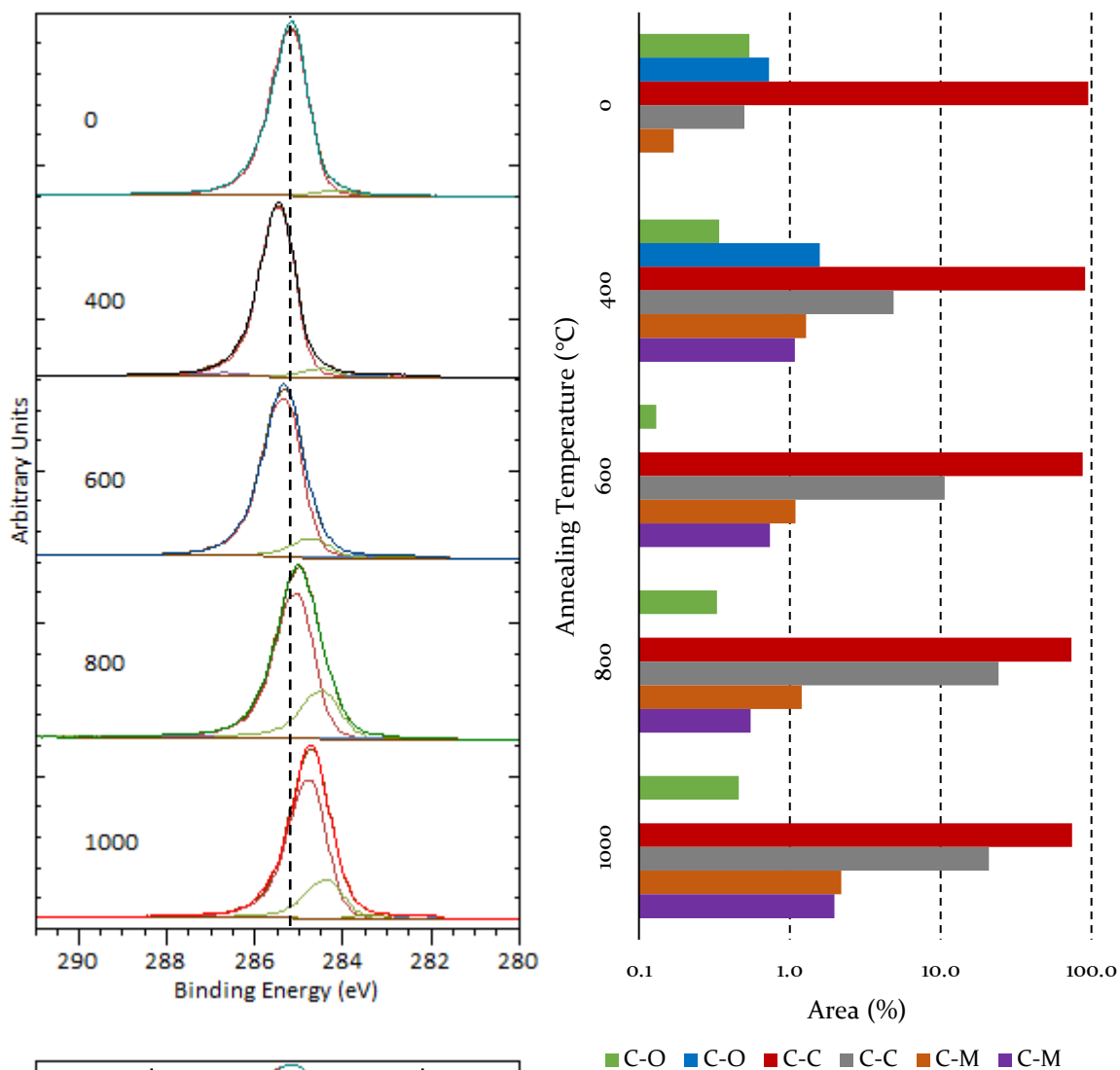


Figure 6-26 - FML TiN – An overlay of the C 1s spectra (top left) after the different temperature anneals, a bar chart of the areas of the corresponding component peaks (top right), and another overlay of the C1s spectra on a logarithmic vertical-axis (bottom right) to enable the visualisation of the smaller components in the shoulders. The bar chart is also on a logarithmic scale for the same reason. No attempt has been made to colour match the lineshapes used in the spectral fitting with the bars used in the histograms. The components in the spectra from left to right correspond to the bars in the histogram from top to bottom.

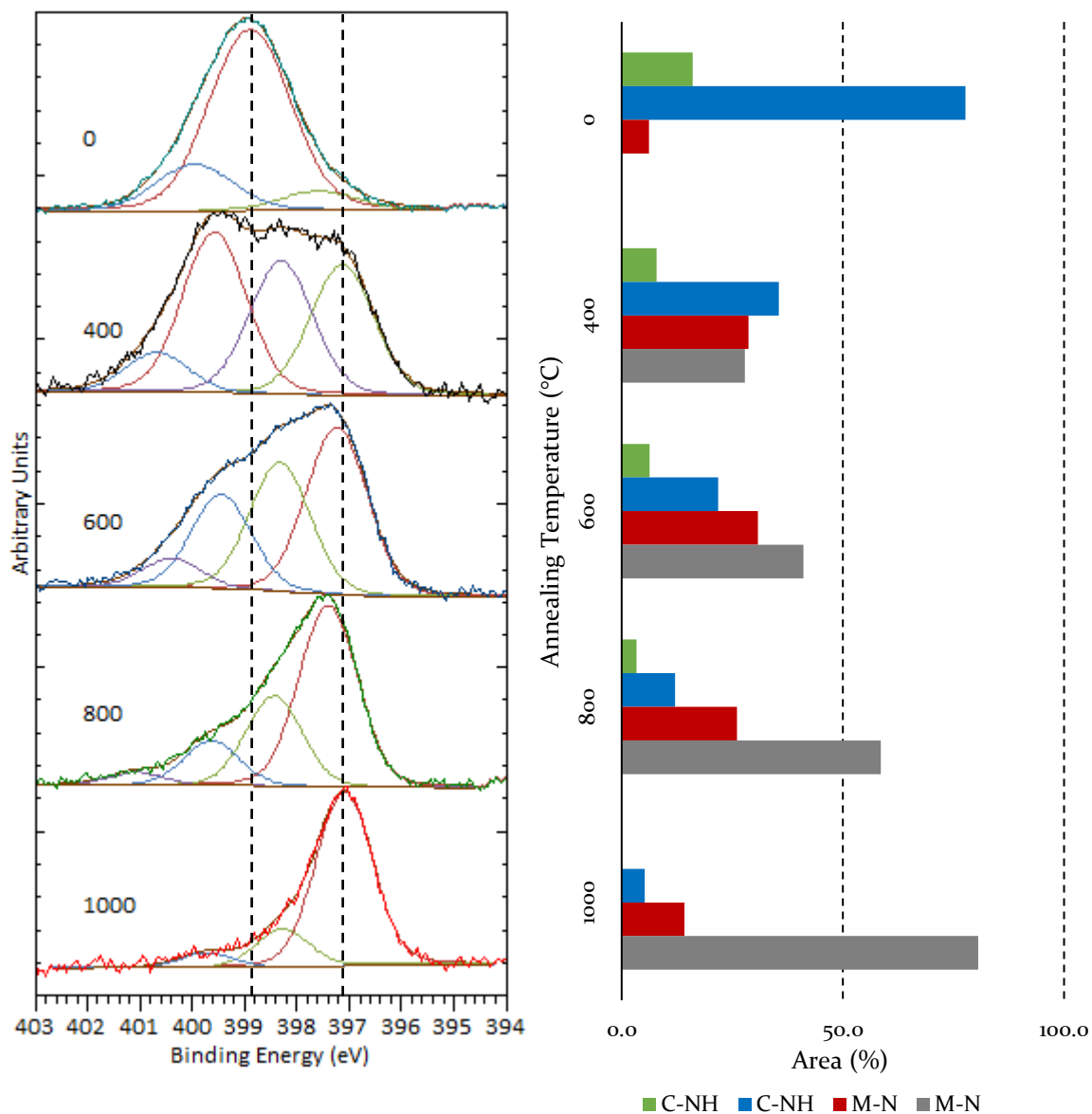


Figure 6-27 - FML TiN - An overlay of the N 1s spectra (left) after the different temperature anneals and the areas of the corresponding component peaks (right). No attempt has been made to colour match the lineshapes used in the spectral fitting with the bars used in the histograms. The components in the spectra from left to right correspond to the bars in the histogram from top to bottom.

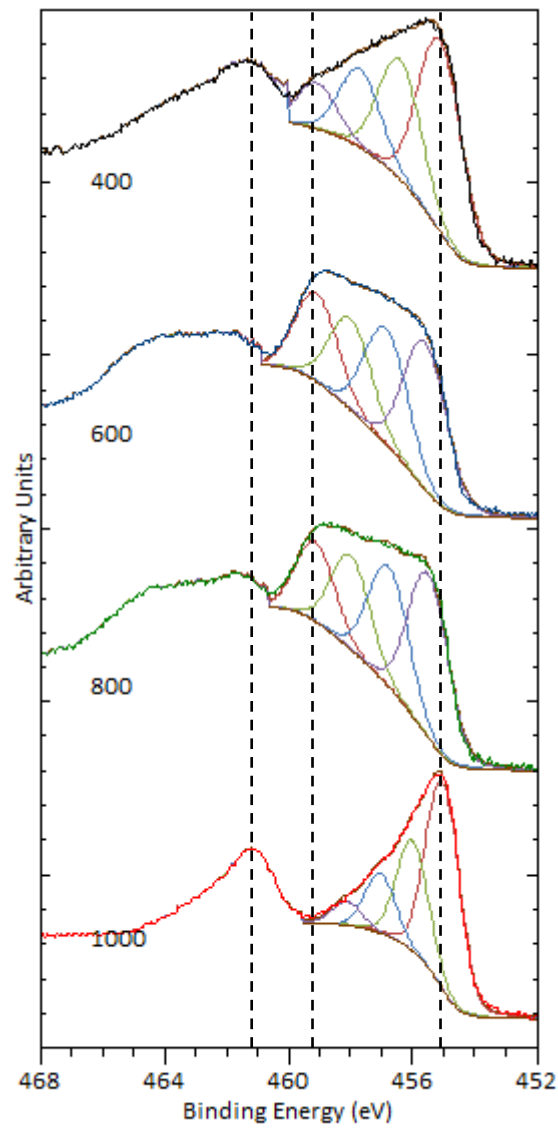


Figure 6-28 – FML TiN – An overlay of the Ti 2p spectra after the different temperature anneals.

#### 6.4.4 TiN Work Functions

Prior to Ti deposition, at 0 °C, the WF values of the N-terminated samples ranged from 4.1 to 4.6 eV. This was lower than the 5.4 eV average WF of the O-terminated surfaces. However, due to the contamination present on the surface, it cannot be determined whether this lower WF was due to the N termination or the iron contamination. Figure 6-29 shows the WF of the three TiN samples as a function of temperature. The WF of these TiN-terminated samples changed little (0.5 eV) over the various annealing temperatures, especially in comparison to TiO-terminated samples (1.2 eV). As such, it was difficult to draw any comparison between the WF values and the sample compositions, especially when considering the complicated nature of the surface due to the contamination present. It should be noted however, that according to the computational calculations in chapter 2, the  $\text{NH}_x$ -terminated diamond surfaces exhibited an NEA, similar to the TiC surfaces. It is therefore possible that the low initial WF was due to the -NH and -NH<sub>2</sub> surface terminations present after ammonia plasma treatment, though further experimental work is required to confirm this.

Figure 6-30 is a visual representation of the data from Figure 6-29 together with data from Table 6-5, Table 6-6, and Table 6-7, displaying how the WF values and the

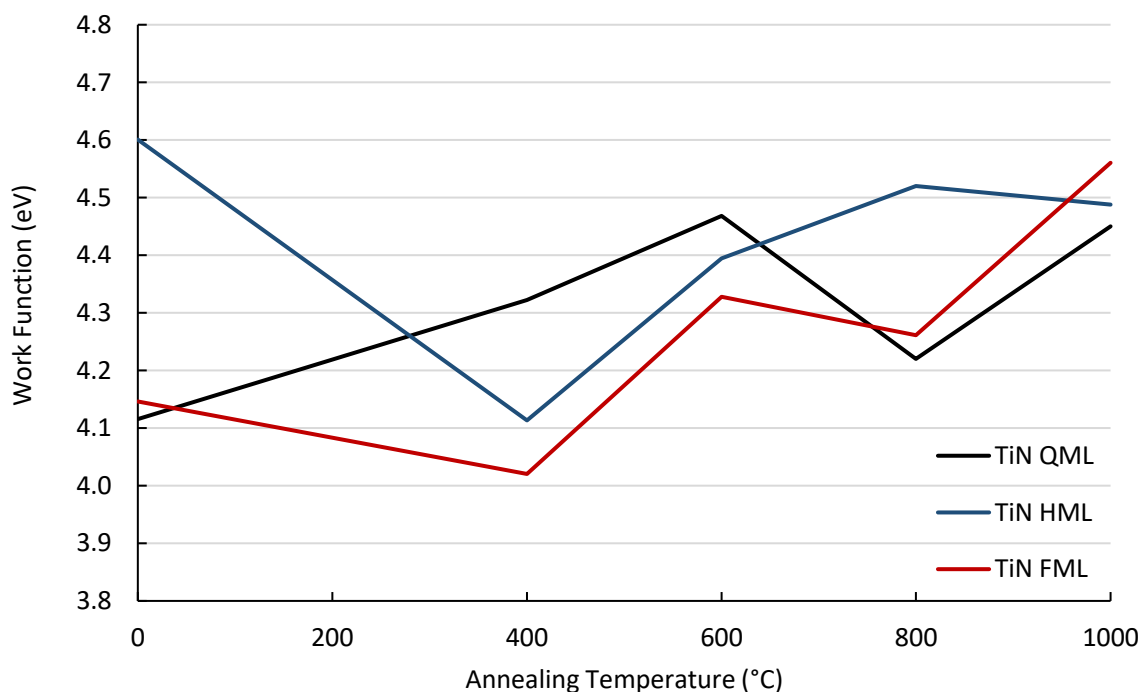


Figure 6-29 – TiN – How the WF of the three TiN-terminated samples evolves as a function of annealing temperature. 0 °C is the O-terminated samples before Ti deposition while 400 °C is the WF after Ti deposition as this is the deposition temperature.

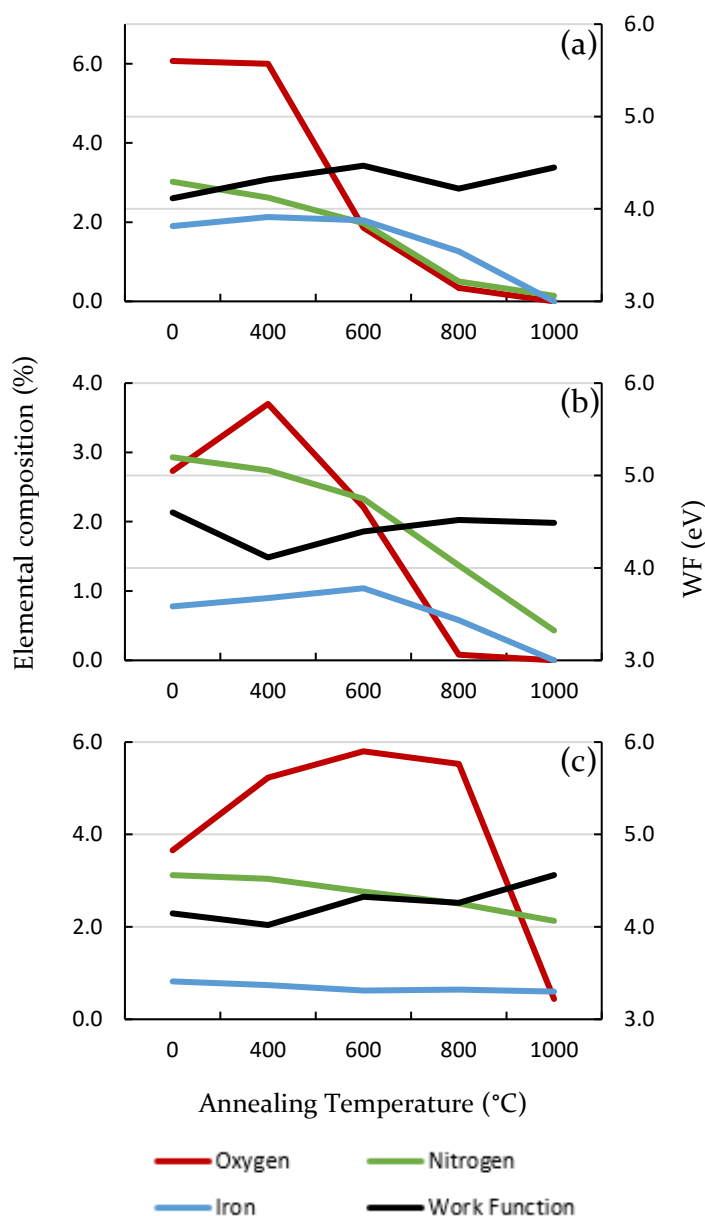


Figure 6-30 – TiN – Showing how the WFs of the (a) QML, (b) HML, and (c) FML TiN-terminated samples evolve in relation to the O content.

concentration of the main surface species varied with annealing temperatures. Unlike the TiO samples discussed in section 6.3.4, little correlation can be drawn between the WF and the concentration of the various surface elements for these TiN samples. This is not only due to the fact that these surfaces are more complicated, but also because the WF does not change significantly. From Figure 6-30(a) it can be seen that the desorption behaviour of the QML TiN sample was similar to that of the three TiO samples, in that the O, N, and iron all desorbed by 1000 °C, leaving only Ti on the

diamond surface. However, unlike the TiO samples, this was not the case for increasing coverages of Ti. For the HML sample shown in Figure 6-30(b), although the oxygen and iron had desorbed by 1000 °C, not all of the N had, with 0.4 % still present. This is even more evident upon increasing the Ti coverage to an FML, Figure 6-30(c), where not only two thirds of the original N were still present, but also some of the O (0.4 %) and most of the iron (0.6 %) still remained, even after the 1000 °C anneal. It is unknown why this is observed for the TiN samples, in contrast to the TiO samples. Further investigation is required to determine the cause of this trend.

## 6.5 Summary

For the TiO samples, the overlaid O spectra all follow a similar pattern. Before Ti deposition, the samples were composed of ether- and ketone-like environments, with a metal oxide component being introduced after Ti deposition at 400 °C. While the HML sample exhibits a relatively larger metal oxide component than the QML (due to the increase in deposited Ti), the relative size of the metal oxide component for the FML is smaller than the HML sample. This may be related to the additional oxidation of the Ti due to the decrease in coordination per Ti atom. For all three samples, there was little change in the O peaks after the 600 °C anneal, apart from a small increase in the size of the metal oxide component. After 800 °C, the relative size of the metal oxide component decreased, which can be attributed to the O in the metal oxide environment desorbing more readily. For the three TiN samples, interpretation of the O 1s spectra was more challenging due to the presence of contamination. As the spectra before Ti deposition showed significant metal oxide components, and the QML sample exhibited twice the amount of iron and O, it supports the view that the O primarily originated from the oxidised metal contamination. For all three samples, there was a significant increase in the relative size of the metal oxide component upon Ti deposition.

The C 1s spectra of the three TiO samples exhibit similar behaviour to each other. After Ti deposition and the 600 °C anneal, the whole peak shifted to a lower binding energy (from ~285 eV to ~284 eV), while there was a reversal in position of the two largest components, as discussed in section 6.3.3. Upon annealing at 1000 °C, the peaks shifted back towards a higher binding energy (~284.5 eV). For the TiN sample, the pattern of the peak positions is similar, except for the shift to a slightly higher binding energy for the HML and FML samples upon Ti deposition. Furthermore, the switch in the binding energy of the two largest components after 600 °C was not seen for the TiN samples, although there was a significant increase in the relative size of the second largest component.

The Ti 2p spectra of the QML and HML TiO samples again exhibit similarities. Following Ti deposition, the Ti was predominantly in the Ti(IV) and Ti(III) oxidation states. After the 600 °C anneal, the Ti shifted more towards Ti(IV), while after O desorption (either after 800 °C or 1000 °C), the Ti was mainly found in the Ti(II)

oxidation state. The FML TiO sample however, is predominantly in the Ti(II) state following Ti deposition. This is most likely due to the decreased coordination of each Ti atom, which is also responsible for the additional oxidation observed for this sample. The Ti 2p spectra of the three TiN samples exhibited a wider variety of oxidation states upon Ti deposition, which is mostly likely due to N being less electronegative than O. All three samples shifted towards the lower Ti(II) oxidation state with increasing temperature anneals. Only the FML TiN sample was predominantly Ti(II) following Ti deposition, as was also seen with the TiO samples. The FML sample was the only TiN surface to exhibit the same shift towards the higher oxidation states after the 600 °C, as observed for the TiO samples.

The N 1s spectra of the TiN samples showed the N to be mostly in a C-NH environment prior to Ti deposition, with a small metal nitride component from the iron contamination. Upon Ti deposition, a new metal nitride component was visible, which significantly increased in size with each subsequent anneal.

The lowest WF values for each of the three TiO-terminated samples were 4.2 – 4.5 eV and occurred after Ti deposition at 400 °C for the FML sample, or after the 600 °C anneal for the QML and HML samples. After the 1000 °C anneal, the three samples showed most of the original Ti remaining, while the O had desorbed leaving only trace amounts behind. These three TiC-terminated samples had WF values of 4.5 – 4.8 eV.

The TiN-terminated samples exhibited their lowest WF values (4.0 – 4.2 eV) after Ti deposition (400 °C) for the HML and FML samples, and after the 800 °C anneal for the QML sample. However, considering the change in WF for the QML sample is less than 0.3 eV across all the anneals, few conclusions can be drawn from this. The WF of the TiN-terminated samples after the 1000 °C anneal was between 4.5 and 4.6 eV. Although all of the surface species except Ti desorbed from the QML TiN sample, leaving it purely TiC-terminated similarly to the TiO samples, the same is not true for the HML and FML samples. Despite this, there is little difference in the WF values of the three TiN samples after 1000 °C. This is most likely due to the similar electronic properties of the -TiC, -NH, and -NH<sub>2</sub> terminations as discussed in chapter 2.

## CHAPTER



# Comparison and Future Work

“I do not feel obliged to believe that the same God who has endowed us with sense, reason, and intellect has intended us to forgo their use.”

Galileo Galilei - Letter to the Grand Duchess Christina

## 7.1 Comparison of Modelling and Experimental Data

Concerning the simple terminations discussed in chapter 5, the H-terminated surface exhibits an NEA, as expected from the literature and the theoretical modelling in chapter 2. The results of the O and NH<sub>x</sub> terminations also agreed with both the literature and theoretical studies, exhibiting a PEA and NEA, respectively. For the deposition of Ti on the O- and N-terminated surface, however, the experimental studies do not necessarily agree with the computational modelling. While depositing Ti on the O-terminated surface did yield a decrease in WF (section 6.3.4), there was little difference in the WF values of the QML, HML and FML samples. This is contrary to the theoretical results (section 2.3.2), where the Ti coverage had significant impact on the EA. This is also observed for the TiN termination. This discrepancy possibly arises due to the difference in how an ML is defined in the experimental and theoretical studies. For the theoretical study, one ML is defined as one Ti atom per surface C atom. This was a convenient way to describe the ML coverage because of how the calculations are constructed. For the experimental study however, one ML was determined using XPS, by depositing small amounts of Ti and observing when the second layer began to grow. It is therefore conceivable that the density of Ti atoms in the theoretical monolayer is not achievable in practice, due the significantly larger size of a Ti atom compared to a C atom (atomic radius of C – 70 pm, atomic radius of Ti – 140 pm).<sup>150</sup> As an example, during the deposition of small amounts of Ti, when the Ti atoms reached the density ascribed to a theoretical QML, i.e. one Ti atom per 4 surface C atoms, and this was the highest density achievable, then further addition of Ti atoms would result in the beginnings of the second layer. Despite only reaching a titanium density equivalent to the theoretical QML, this would be defined as an FML from a practical perspective.

Further comparison can be drawn from the surface stabilities in chapter 2, and the desorption of surface species in chapter 6. For the TiO terminations, all O had desorbed by 1000 °C, leaving only TiC on the surface. Whilst the QML TiN surface behaved similarly, the HML and FML surfaces did not exhibit clean TiC-terminated surfaces after the 1000 °C anneal. These two samples did, however, show a decrease in all surface species except Ti, indicating that with longer annealing times, the surface would also be purely TiC-terminated. This compares favourably with the theoretical study in

chapter 2, as the TiC terminations exhibited more stable surfaces, with median adsorption energies of  $-2.5 \text{ J m}^{-2} \text{ N}^{-1}$ , compared to the TiO ( $-2.3 \text{ J m}^{-2} \text{ N}^{-1}$ ) or TiN ( $-2.0 \text{ J m}^{-2} \text{ N}^{-1}$ ) terminations. Furthermore, the WF of most samples increased with increasing temperature (and hence oxygen and nitrogen desorption) following titanium deposition. This agrees with computational modelling, as the lowest EA of the TiC ( $-1.6 \text{ eV}$ ) termination is higher than that of the TiO ( $-2.9 \text{ eV}$ ) or TiN ( $-2.3 \text{ eV}$ ) terminations.

## 7.2 Conclusion

There is considerable interest within the literature in metal-oxide-terminated diamond surfaces as potentially stable negative electron affinity thermionic emitters. Thermal stability testing of up to  $1000 \text{ }^\circ\text{C}$  performed in this work shows that the titanium terminated (TiC) surface was more stable than the TiO or TiN terminations. This was most likely due to the strength of the titanium carbide bond. Furthermore, while the TiO terminations had slightly more favourable EAs, the titanium carbide termination still exhibited an NEA. This leads the author to conclude that perhaps carbide forming metal terminations are a better avenue of exploration due to the higher stability, while still having the potential to exhibit NEAs, as discussed in section 1.3.1 and Figure 6-II.

## 7.3 Future Work

As has been shown both theoretically and experimentally, the TiC surface termination is more stable than the TiO or TiN terminations, while also showing promising electronic properties. Therefore, future work should primarily focus on investigating these surfaces in greater depth than was possible within this work. In particular, TiC surfaces should be prepared directly on clean or H-terminated diamond, as opposed to the O- or N-terminated surfaces studied here. As there were minimal differences observed in the QML, HML, and FML samples, it would be interesting to determine whether two monolayers of Ti would exhibit any notable differences in terms of electronic properties, and surface stability at elevated temperatures. Furthermore, as the TiC surfaces are more stable, longer annealing times, or higher annealing

temperatures should be investigated to determine long term stability, which is important for device manufacture.

Additionally, the small changes in Ti concentration observed for some of the samples (e.g. QML TiO, section 6.3.1) should be investigated, as it is unlikely to be the result of Ti desorption, because no corresponding decrease is seen at higher temperatures. Therefore, further studies should be carried out to determine whether there is a restructuring of the Ti atoms, or whether the Ti is diffusing into the diamond substrate. Though these surfaces were extensively studied using XPS and UPS, no thermionic emission testing was performed. As such, a next logical step would be to prepare TiC-terminated n-type doped diamond samples with which the thermionic emission behaviour of these surfaces could be characterised. Of particular interest are Richardson constants, emission threshold temperatures, and maximum emission current densities. The eventual goal would be to test these surfaces in an actual device.

The O-terminated surfaces investigated in the theoretical studies in chapter 2 were either ether- or ketone-like oxygen. As seen from the XPS spectra in chapters 5 and 6 however, the actual diamond (100) surface is a mixture of ether- and ketone-like oxygen environments. As such, surfaces with mixed ether- and ketone-like oxygen should be constructed and investigated.

Furthermore, in the interest of improving future experimental studies, the contamination issues presented here should be investigated in more detail, with a view towards eliminating them. The two primary concerns are the fluorine, which was deposited alongside the titanium, and the sputtering of the stainless-steel electrodes during ammonia plasma treatment of diamond surfaces. For the fluorine contamination, firstly the source needs to be determined, whether originating from the e-beam evaporator or another component within the fabrication chamber, e.g. the sample stage. For the ammonia plasma treatment, the effectiveness of shorter deposition times in regard to coverage and contamination should be investigated. Furthermore, modification of the top electrode of the Terminator to allow direct water cooling may aid in the reduction/elimination of the sputtering issue.

Concerning other future candidates for promising terminations for TEC applications, the results in this work would indicate that carbide-forming metals (e.g. vanadium or

chromium) show the most promise due to the strength of the metal-carbide bond. Despite Ti being very reactive towards oxygen, the O atoms desorbed from the TiO-terminated surfaces, leaving only the TiC termination. Whether this trend occurs for other metal-oxides is currently unknown and is another proposed avenue of investigation.

# References

“There’s plenty of room at the bottom.”

Richard Feynman – Lecture at Caltech (29 December 1959)

1. Masson-Delmotte, V. *et al.* *IPCC, 2018: Summary for Policymakers. In: Global Warming of 1.5°C. An IPCC Special Report on the impacts of global warming of 1.5°C above pre-industrial levels and related global greenhouse gas emission pathways, in the context of strengthening the global response to the threat of climate change, sustainable development, and efforts to eradicate poverty* [https://www.ipcc.ch/site/assets/uploads/sites/2/2019/05/SR15\\_SPM\\_version\\_report\\_LR.pdf](https://www.ipcc.ch/site/assets/uploads/sites/2/2019/05/SR15_SPM_version_report_LR.pdf) (2018).
2. The Royal Society. *Keeping global warming to 1.5°C Challenges and opportunities for the UK.* (The Royal Society, 2018).
3. Edenhofer, O. *et al.* *IPCC, 2014: Summary for Policymakers. In: Climate Change 2014: Mitigation of Climate Change. Contribution of Working Group III to the Fifth Assessment Report of the Intergovernmental Panel on Climate Change.* <http://www.gtp89.dial.pipex.com/AR4.htm> (2014).
4. Granatstein, V. L., Parker, R. K. & Armstrong, C. M. Vacuum electronics at the dawn of the twenty-first century. *Proc. IEEE* **87**, 702–716 (1999).
5. May, P. W. *et al.* The effect of diamond surface termination species upon field emission properties. *Diam. Relat. Mater.* **7**, 671–676 (1998).
6. Sowers, A. T., Ward, B. L., English, S. L. & Nemanich, R. J. Field emission properties of nitrogen-doped diamond films. *J. Appl. Phys.* **86**, 3973–3982 (1999).
7. Cui, J. *et al.* Hydrogen termination and electron emission from CVD diamond surfaces: a combined secondary electron emission, photoelectron emission microscopy, photoelectron yield, and field emission study. *Diam. Relat. Mater.* **9**, 1143–1147 (2000).
8. Geis, M. W., Twichell, J. C., Efremow, N. N., Krohn, K. & Lyszczarz, T. M. Comparison of electric field emission from nitrogen-doped, type Ib diamond, and boron-doped diamond. *Appl. Phys. Lett.* **2294**, 2294 (1995).

9. Noord, J. L. Van, Kamhawi, H. & Mcewen, H. K. Characterization of a High Current , Long Life Hollow Cathode. *29th Int. Electr. Propuls. Conf. IEPC-2005-321* (2005).
10. Wilbur, P. J., Jahn, R. G. & Curran, F. C. Space electric propulsion plasmas. *IEEE Trans. Plasma Sci.* **19**, 1167–1179 (1991).
11. Van Noord, J. NEXT Ion Thruster Thermal Model. *43rd Jt. Propuls. Conf. AIAA 2007-5218* (2010).
12. Go, D. B. *et al.* Thermionic Energy Conversion in the Twenty-first Century: Advances and Opportunities for Space and Terrestrial Applications. *Front. Mech. Eng.* **3**, 1–17 (2017).
13. Schlichter, W. Die spontane Elektronenemission glühender Metalle und das glühelektrische Element. *Ann. Phys.* **352**, 573–640 (1915).
14. Gryaznov, G. M. 30th anniversary of the startup of Topaz—The first thermionic nuclear reactor in the world. *At. Energy* **89**, 510–515 (2000).
15. Hatsopoulos, G. N. & Gyftopoulos, E. P. *Thermionic Energy Conversion. Volume I. Processes and Devices.* (The MIT Press, 1973).
16. Hatsopoulos, G. N. & Gyftopoulos, E. P. *Thermionic Energy Conversion. Volume II. Theory, Technology, and Application.* (The MIT Press, 1979).
17. National Research Council. *Thermionics Quo Vadis?* (National Academies Press, 2001).
18. Lin, I. N., Koizumi, S., Yater, J. & Koeck, F. Diamond electron emission. *MRS Bull.* **39**, 533–541 (2014).
19. Abdul Khalid, K. A., Leong, T. J. & Mohamed, K. Review on Thermionic Energy Converters. *IEEE Trans. Electron Devices* **63**, 2231–2241 (2016).
20. Kribus, A. & Segev, G. Solar energy conversion with photon-enhanced thermionic emission. *J. Opt.* **18**, 073001 (2016).
21. Khoshaman, A. H. *et al.* Nanostructured Thermionics for Conversion of Light to Electricity: Simultaneous Extraction of Device Parameters. *IEEE Trans. Nanotechnol.* **14**, 624–632 (2015).
22. Vahdani Moghaddam, M., Yaghoobi, P., Sawatzky, G. A. & Nojeh, A. Photon-

- Impenetrable, Electron-Permeable: The Carbon Nanotube Forest as a Medium for Multiphoton Thermal-Photoemission. *ACS Nano* **9**, 4064–4069 (2015).
23. McCarthy, P. T., Reifenberger, R. G. & Fisher, T. S. Thermionic and Photo-Excited Electron Emission for Energy-Conversion Processes. *Front. Energy Res.* **2**, 1–15 (2014).
  24. Liang, S.-J. & Ang, L. K. Electron Thermionic Emission from Graphene and a Thermionic Energy Converter. *Phys. Rev. Appl.* **3**, 014002 (2015).
  25. Ade, P. A. R. *et al.* Planck 2015 results. *Astron. Astrophys.* **594**, A15 (2016).
  26. Rock, P. A. *Chemical Thermodynamics*. (University Science Books, 1983).
  27. May, P. W. Diamond thin films: a 21st-century material. *Philos. Trans. R. Soc. London. Ser. A* **358**, 473–495 (2000).
  28. Wort, C. J. H. & Balmer, R. S. Diamond as an electronic material. *Mater. Today* **11**, 22–28 (2008).
  29. Koeck, F. A. M., Nemanich, R. J., Lazea, A. & Haenen, K. Thermionic electron emission from low work-function phosphorus doped diamond films. *Diam. Relat. Mater.* **18**, 789–791 (2009).
  30. Paxton, W. F. *et al.* Thermionic emission characterization of boron-doped microcrystalline diamond films at elevated temperatures. *Phys. status solidi* **209**, 1993–1995 (2012).
  31. Paxton, W. F., Howell, M., Kang, W. P. & Davidson, J. L. Influence of hydrogen on the thermionic electron emission from nitrogen-incorporated polycrystalline diamond films. *J. Vac. Sci. Technol. B* **30**, 021202 (2012).
  32. Paxton, W. F. *et al.* The effect of hydrogen desorption kinetics on thermionic emission from polycrystalline chemical vapor deposited diamond. *Appl. Phys. Lett.* **101**, (2012).
  33. Tiwari, A. K. *et al.* Calculated electron affinity and stability of halogen-terminated diamond. *Phys. Rev. B* **84**, 245305 (2011).
  34. Kawarada, H. Hydrogen-terminated diamond surfaces and interfaces. *Surf. Sci. Rep.* **26**, 205–206 (1996).
  35. Koeck, F. A. M. & Nemanich, R. J. Advances in Thermionic Energy Conversion

- through Single-Crystal n-Type Diamond. *Front. Mech. Eng.* **3**, 1–11 (2017).
36. Loh, K. P., Foord, J. S., Egdell, R. G. & Jackman, R. B. Tuning the electron affinity of CVD diamond with adsorbed caesium and oxygen layers. *Diam. Relat. Mater.* **6**, 874–878 (1997).
  37. Petrick, S. & Benndorf, C. Potassium adsorption on hydrogen- and oxygen-terminated diamond (100) surfaces. *Diam. Relat. Mater.* **10**, 519–525 (2001).
  38. Sque, S. J., Jones, R. & Briddon, P. R. Structure, electronics, and interaction of hydrogen and oxygen on diamond surfaces. *Phys. Rev. B* **73**, 1–15 (2006).
  39. Suzuki, M., Ono, T., Sakuma, N. & Sakai, T. Low-temperature thermionic emission from nitrogen-doped nanocrystalline diamond films on n-type Si grown by MPCVD. *Diam. Relat. Mater.* **18**, 1274–1277 (2009).
  40. Koeck, F. A. M. & Nemanich, R. J. Emission characterization from nitrogen-doped diamond with respect to energy conversion. *Diam. Relat. Mater.* **15**, 217–220 (2006).
  41. Kataoka, M., Zhu, C., Koeck, F. A. M. & Nemanich, R. J. Thermionic electron emission from nitrogen-doped homoepitaxial diamond. *Diam. Relat. Mater.* **19**, 110–113 (2010).
  42. Koeck, F. A. M. & Nemanich, R. J. Low temperature onset for thermionic emitters based on nitrogen incorporated UNCD films. *Diam. Relat. Mater.* **18**, 232–234 (2009).
  43. Koeck, F. A. M., Nemanich, R. J. & Sharp, J. Doped diamond thin film electron sources for thermionic energy conversion. *26th Int. Vac. Nanoelectron. Conf.* 1–3 (2013).
  44. Koeck, F. A. M. & Nemanich, R. J. Substrate-diamond interface considerations for enhanced thermionic electron emission from nitrogen doped diamond films. *J. Appl. Phys.* **112**, (2012).
  45. Kato, H. *et al.* Heavily phosphorus-doped nano-crystalline diamond electrode for thermionic emission application. *Diam. Relat. Mater.* **63**, 165–168 (2016).
  46. Diederich, L., Küttel, O. M., Aebi, P. & Schlapbach, L. Electron affinity and work function of differently oriented and doped diamond surfaces determined by photoelectron spectroscopy. *Surf. Sci.* **418**, 219–239 (1998).

47. Zhang, G. J. *et al.* DNA micropatterning on polycrystalline diamond via one-step direct amination. *Langmuir* **22**, 3728–3734 (2006).
48. Nakamura, T. *et al.* Chemical modification of diamond films using photolysis of perfluoroazooctane. *Diam. Relat. Mater.* **13**, 1084–1087 (2004).
49. Nakamura, T. *et al.* Photochemical modification of diamond films: Introduction of perfluorooctyl functional groups on their surface. *Langmuir* **20**, 5846–5849 (2004).
50. Yang, W. *et al.* Electrically addressable biomolecular functionalization of conductive nanocrystalline diamond thin films. *Chem. Mater.* **17**, 938–940 (2005).
51. Rezek, B., Shin, D., Nakamura, T. & Nebel, C. E. Geometric properties of covalently bonded DNA on single-crystalline diamond. *J. Am. Chem. Soc.* **128**, 3884–3885 (2006).
52. Liu, Y. C. & McCreery, R. L. Reactions of Organic Monolayers on Carbon Surfaces Observed with Unenhanced Raman Spectroscopy. *J. Am. Chem. Soc.* **117**, 11254–11259 (1995).
53. Anariba, F., DuVall, S. H. & McCreery, R. L. Mono- and Multilayer Formation by Diazonium Reduction on Carbon Surfaces Monitored with Atomic Force Microscopy “Scratching”. *Anal. Chem.* **75**, 3837–3844 (2003).
54. Rezek, B., Shin, D. & Nebel, C. E. Properties of hybridized DNA arrays on single-crystalline undoped and boron-doped (100) diamonds studied by atomic force microscopy in electrolytes. *Langmuir* **23**, 7626–7633 (2007).
55. Uetsuka, H., Shin, D., Tokuda, N., Saeki, K. & Nebel, C. E. Electrochemical grafting of boron-doped single-crystalline chemical vapor deposition diamond with nitrophenyl molecules. *Langmuir* **23**, 3466–3472 (2007).
56. Ando, T. *et al.* Chemical modification of diamond surfaces using a chlorinated surface as an intermediate state. *Diam. Relat. Mater.* **5**, 1136–1142 (1996).
57. Coffinier, Y. *et al.* Peptide immobilization on amine-terminated boron-doped diamond surfaces. *Langmuir* **23**, 4494–4497 (2007).
58. Raymakers, J., Haenen, K. & Maes, W. Diamond surface functionalization: from gemstone to photoelectrochemical applications. *J. Mater. Chem. C* **7**, 10134–10165

- (2019).
59. Szunerits, S. & Boukherroub, R. Different strategies for functionalization of diamond surfaces. *J. Solid State Electrochem.* **12**, 1205–1218 (2008).
  60. Maier, F., Ristein, J. & Ley, L. Electron affinity of plasma-hydrogenated and chemically oxidized diamond (100) surfaces. *Phys. Rev. B* **64**, 165411 (2001).
  61. Speranza, G. *et al.* XPS and UPS in situ study of oxygen thermal desorption from nanocrystalline diamond surface oxidized by different process. *Diam. Relat. Mater.* **20**, 560–563 (2011).
  62. Stacey, A. *et al.* Nitrogen Terminated Diamond. *Adv. Mater. Interfaces* **2**, 1500079 (2015).
  63. Yamaguchi, H. *et al.* Electron emission from conduction band of diamond with negative electron affinity. *Phys. Rev. B* **80**, 165321 (2009).
  64. Takeuchi, D. *et al.* Direct observation of negative electron affinity in hydrogen-terminated diamond surfaces. *Appl. Phys. Lett.* **86**, 1–3 (2005).
  65. Bandis, C. & Pate, B. B. Photoelectric emission from the negative electron affinity (100) diamond surface - Exciton effects. *Surf. Sci.* **350**, 315–321 (1996).
  66. Diederich, L., Aebi, P., Küttel, O. M. & Schlapbach, L. NEA peak of the differently terminated and oriented diamond surfaces. *Surf. Sci.* **424**, 1–7 (1999).
  67. Robinson, V. S., Show, Y., Swain, G. M., Reifenberger, R. G. & Fisher, T. S. Thermionic emission from surface-terminated nanocrystalline diamond. *Diam. Relat. Mater.* **15**, 1601–1608 (2006).
  68. Wan, G., Cattelan, M. & Fox, N. A. Electronic structure tunability of diamonds by surface functionalization. *J. Phys. Chem. C* **123**, 4168–4177 (2019).
  69. Wang, Y. M. *et al.* Recent studies on diamond surfaces. *Diam. Relat. Mater.* **9**, 1582–1590 (2000).
  70. Koeck, F. A. M. & Nemanich, R. J. Sulfur doped nanocrystalline diamond films as field enhancement based thermionic emitters and their role in energy conversion. *Diam. Relat. Mater.* **14**, 2051–2054 (2005).
  71. Navas, J. *et al.* Oxygen termination of homoepitaxial diamond surface by ozone and chemical methods: An experimental and theoretical perspective. *Appl. Surf.*

- Sci.* **433**, 408–418 (2018).
72. Pehrsson, P. E., Mercer, T. W. & Chaney, J. A. Thermal oxidation of the hydrogenated diamond (100) surface. *Surf. Sci.* **497**, 13–28 (2002).
  73. Ando, T., Yamamoto, K., Ishii, M., Kamo, M. & Sato, Y. Vapour-phase oxidation of diamond surfaces in O<sub>2</sub> studied by diffuse reflectance Fourier-transform infrared and temperature-programmed desorption spectroscopy. *J. Chem. Soc. Faraday Trans.* **89**, 3635–3640 (1993).
  74. John, P., Polwart, N., Troupe, C. E. & Wilson, J. I. B. The oxidation of diamond: The geometry and stretching frequency of carbonyl on the (100) surface. *J. Am. Chem. Soc.* **125**, 6600–6601 (2003).
  75. Rutter, M. J. & Robertson, J. Ab initio calculation of electron affinities of diamond surfaces. *Phys. Rev. B* **57**, 9241–9245 (1998).
  76. Kaviani, M. *et al.* Proper surface termination for luminescent near-surface NV centers in diamond. *Nano Lett.* **14**, 4772–4777 (2014).
  77. Cui, J. B., Ristein, J. & Ley, L. Dehydrogenation and the surface phase transition on diamond (111): Kinetics and electronic structure. *Phys. Rev. B* **59**, 5847–5856 (1999).
  78. O'Donnell, K. M., Martin, T. L., Fox, N. A. & Cherns, D. Ab initio investigation of lithium on the diamond C(100) surface. *Phys. Rev. B* **82**, 115303 (2010).
  79. Thomas, R. E., Rudder, R. A. & Markunas, R. J. Thermal desorption from hydrogenated and oxygenated diamond (100) surfaces. *J. Vac. Sci. Technol. A* **10**, 2451–2457 (1992).
  80. Mackey, B. L. *et al.* Oxygen Adsorption on the (110)-Oriented Diamond Surface. *J. Phys. Chem. B* **105**, 3803–3812 (2001).
  81. Chandran, M., Shasha, M., Michaelson, S. & Hoffman, A. Nitrogen termination of single crystal (100) diamond surface by radio frequency N<sub>2</sub> plasma process: An in-situ x-ray photoemission spectroscopy and secondary electron emission studies. *Appl. Phys. Lett.* **107**, 111602 (2015).
  82. Szunerits, S. *et al.* Direct amination of hydrogen-terminated boron doped diamond surfaces. *Electrochem. commun.* **8**, 1185–1190 (2006).
  83. Yang, J. H. *et al.* Characterization of DNA hybridization on partially aminated

- diamond by aromatic compounds. *Langmuir* **22**, 11245–11250 (2006).
84. Artemenko, A., Kozak, H., Biederman, H., Choukourov, A. & Kromka, A. Amination of NCD Films for Possible Application in Biosensing. *Plasma Process. Polym.* **12**, 336–346 (2015).
  85. Miller, J. B. & Brown, D. W. Photochemical Modification of Diamond Surfaces. *Langmuir* **12**, 5809–5817 (1996).
  86. Takahashi, K., Tanga, M., Takai, O. & Okamura, H. DNA preservation using diamond chips. *Diam. Relat. Mater.* **12**, 572–576 (2003).
  87. Chou, J. P., Retzker, A. & Gali, A. Nitrogen-Terminated Diamond (III) Surface for Room-Temperature Quantum Sensing and Simulation. *Nano Lett.* **17**, 2294–2298 (2017).
  88. Zhu, D., Bandy, J. A., Li, S. & Hamers, R. J. Amino-terminated diamond surfaces: Photoelectron emission and photocatalytic properties. *Surf. Sci.* **650**, 295–301 (2016).
  89. James, M. C., Croot, A., May, P. W. & Allan, N. L. Negative electron affinity from aluminium on the diamond (100) surface: a theoretical study. *J. Phys. Condens. Matter* **30**, 235002 (2018).
  90. Tiwari, A. K. *et al.* Electronic and structural properties of diamond (001) surfaces terminated by selected transition metals. *Phys. Rev. B* **86**, 155301 (2012).
  91. Baumann, P. K. & Nemanich, R. J. Characterization of cobalt-diamond (100) interfaces: electron affinity and Schottky barrier. *Appl. Surf. Sci.* **104–105**, 267–273 (1996).
  92. Baumann, P. K. & Nemanich, R. J. Characterization of copper-diamond (100), (III), and (100) interfaces: Electron affinity and Schottky barrier. *J. Appl. Phys.* **58**, 1643–1654 (1998).
  93. Baumann, P. K. & Nemanich, R. J. Electron emission from metal-diamond (100), (III) and (II0) interfaces. *Diam. Relat. Mater.* **7**, 612–619 (1998).
  94. Schenk, A. *et al.* Formation of a silicon terminated (100) diamond surface. *Appl. Phys. Lett.* **106**, 191603 (2015).
  95. Schenk, A. K. *et al.* The surface electronic structure of silicon terminated (100) diamond. *Nanotechnology* **27**, (2016).

96. Sear, M. J. *et al.* Germanium terminated (100) diamond. *J. Phys. Condens. Matter* **29**, 145002 (2017).
97. Schenk, A. K., Sear, M. J., Tadich, A., Stacey, A. & Pakes, C. I. Oxidation of the silicon terminated (100) diamond surface. *J. Phys. Condens. Matter* **29**, 025003 (2017).
98. Köck, F. A. M., Garguilo, J. M., Brown, B. & Nemanich, R. J. Enhanced low-temperature thermionic field emission from surface-treated N-doped diamond films. *Diam. Relat. Mater.* **11**, 774–779 (2002).
99. Tiwari, A. K. *et al.* Thermodynamic stability and electronic properties of F- and Cl-terminated diamond. *Phys. status solidi* **209**, 1709–1714 (2012).
100. Widmann, C. J., Giese, C., Wolfer, M., Kono, S. & Nebel, C. E. F- and Cl-terminations of (100)-oriented single crystalline diamond. *Phys. status solidi* **211**, 2328–2332 (2014).
101. Tiwari, A. K. *et al.* Bromine functionalisation of diamond: An *ab initio* study. *Phys. status solidi* **209**, 1703–1708 (2012).
102. Pickett, W. E. Negative Electron Affinity and Low Work Function Surface: Cesium on Oxygenated Diamond (100). *Phys. Rev. Lett.* **73**, 1664–1667 (1994).
103. Diederich, L. *et al.* Photoelectron emission from the negative electron affinity caesiated natural diamond (100) surface. *Diam. Relat. Mater.* **7**, 660–665 (1998).
104. Geis, M. W., Twichell, J. C., Macaulay, J. & Okano, K. Electron field emission from diamond and other carbon materials after H<sub>2</sub>, O<sub>2</sub>, and Cs treatment. *Appl. Phys. Lett.* **67**, 1328–1330 (1995).
105. Loh, K. P., Xie, X. N., Yang, S. W., Pan, J. S. & Wu, P. A spectroscopic study of the negative electron affinity of cesium oxide-coated diamond (III) and theoretical calculation of the surface density-of-states on oxygenated diamond (III). *Diam. Relat. Mater.* **11**, 1379–1384 (2002).
106. O'Donnell, K. M. *et al.* Photoelectron emission from lithiated diamond. *Phys. status solidi* **211**, 2209–2222 (2014).
107. O'Donnell, K. M. *et al.* Diamond surfaces with air-stable negative electron affinity and giant electron yield enhancement. *Adv. Funct. Mater.* **23**, 5608–5614 (2013).
108. O'Donnell, K. M., Martin, T. L. & Allan, N. L. Light metals on oxygen-terminated

- diamond (100): Structure and electronic properties. *Chem. Mater.* **27**, 1306–1315 (2015).
109. O'Donnell, K. M. *et al.* Extremely high negative electron affinity of diamond via magnesium adsorption. *Phys. Rev. B* **92**, 035303 (2015).
110. Nie, J. L., Xiao, H. Y., Zu, X. T. & Gao, F. First principles calculations on Na and K-adsorbed diamond(100) surface. *Chem. Phys.* **326**, 308–314 (2006).
111. Tiwari, A. K. *et al.* Unexpected change in the electron affinity of diamond caused by the ultra-thin transition metal oxide films. *EPL* **108**, 46005 (2014).
112. Tiwari, A. K. *et al.* Effect of different surface coverages of transition metals on the electronic and structural properties of diamond. *Phys. Status Solidi* **209**, 1697–1702 (2012).
113. Baumann, P. K. & Nemanich, R. J. Characterization of copper-diamond (100), (111), and (110) interfaces: Electron affinity and Schottky barrier. *Phys. Rev. B* **58**, 1643–1654 (1998).
114. Baumann, P. K. & Nemanich, R. J. Electron affinity and Schottky barrier height of metal–diamond (100), (111), and (110) interfaces. *J. Appl. Phys.* **83**, 2072–2082 (1998).
115. Hohenberg, P. & Kohn, W. Inhomogeneous Electron Gas. *Phys. Rev.* **136**, B864–B871 (1964).
116. Kohn, W. & Sham, L. J. Self-Consistent Equations Including Exchange and Correlation Effects. *Phys. Rev.* **140**, A1133–A1138 (1965).
117. Kurth, S., Perdew, J. P. & Blaha, P. Molecular and solid-state tests of density functional approximations: LSD, GGAs, and Meta-GGAs. *Int. J. Quantum Chem.* **75**, 889–909 (1999).
118. Heyd, J., Scuseria, G. E. & Ernzerhof, M. Hybrid functionals based on a screened Coulomb potential. *J. Chem. Phys.* **118**, 8207–8215 (2003).
119. Heyd, J., Peralta, J. E., Scuseria, G. E. & Martin, R. L. Energy band gaps and lattice parameters evaluated with the Heyd-Scuseria-Ernzerhof screened hybrid functional. *J. Chem. Phys.* **123**, 174101 (2005).
120. Heyd, J. & Scuseria, G. E. Efficient hybrid density functional calculations in solids: Assessment of the Heyd-Scuseria-Ernzerhof screened Coulomb hybrid

- functional. *J. Chem. Phys.* **121**, 1187–1192 (2004).
121. Janesko, B. G., Henderson, T. M. & Scuseria, G. E. Screened hybrid density functionals for solid-state chemistry and physics. *Phys. Chem. Chem. Phys.* **11**, 443–454 (2009).
122. Garza, A. J. & Scuseria, G. E. Predicting Band Gaps with Hybrid Density Functionals. *J. Phys. Chem. Lett.* **7**, 4165–4170 (2016).
123. Dovesi, R. *et al.* Quantum-mechanical condensed matter simulations with CRYSTAL. *Wiley Interdiscip. Rev. Comput. Mol. Sci.* **8**, e1360 (2018).
124. Vilela Oliveira, D., Laun, J., Peintinger, M. F. & Bredow, T. BSSE-correction scheme for consistent gaussian basis sets of double- and triple-zeta valence with polarization quality for solid-state calculations. *J. Comput. Chem.* **40**, 2364–2376 (2019).
125. Laun, J., Vilela Oliveira, D. & Bredow, T. Consistent gaussian basis sets of double- and triple-zeta valence with polarization quality of the fifth period for solid-state calculations. *J. Comput. Chem.* **39**, 1285–1290 (2018).
126. Peintinger, M. F., Oliveira, D. V. & Bredow, T. Consistent Gaussian basis sets of triple-zeta valence with polarization quality for solid-state calculations. *J. Comput. Chem.* **34**, 451–459 (2013).
127. Hoy, A. R. & Bunker, P. R. A precise solution of the rotation bending Schrödinger equation for a triatomic molecule with application to the water molecule. *J. Mol. Spectrosc.* **74**, 1–8 (1979).
128. Stekolnikov, A. A., Furthmüller, J. & Bechstedt, F. Absolute surface energies of group-IV semiconductors: Dependence on orientation and reconstruction. *Phys. Rev. B* **65**, 115318 (2002).
129. Skinner, H. A. The Strengths of Metal-to-Carbon Bonds. *Adv. Organomet. Chem.* **2**, 49–114 (1965).
130. Greenwood, N. N. & Earnshaw, A. *Chemistry of the Elements*. (Butterworth-Heinemann, 1997).
131. Capri, A. Z. *Quips, Quotes and Quanta*. (World Scientific, 2007).
132. Lenard, P. Ueber die lichtelektrische Wirkung. *Ann. Phys.* **313**, 149–198 (1902).

133. Siegbahn, K. & Edvarson, K.  $\beta$ -Ray spectroscopy in the precision range of 1 : 105. *Nucl. Phys.* **1**, 137–159 (1956).
134. Shirley, D. A. High-Resolution X-Ray Photoemission Spectrum of the Valence Bands of Gold. *Phys. Rev. B* **5**, 4709–4714 (1972).
135. Tougaard, S. Background removal in x-ray photoelectron spectroscopy: Relative importance of intrinsic and extrinsic processes. *Phys. Rev. B* **34**, 6779–6783 (1986).
136. Tougaard, S. Practical algorithm for background subtraction. *Surf. Sci.* **216**, 343–360 (1989).
137. Végh, J. The Shirley-equivalent electron inelastic scattering cross-section function. *Surf. Sci.* **563**, 183–190 (2004).
138. Végh, J. The Shirley background revised. *J. Electron Spectros. Relat. Phenomena* **151**, 159–164 (2006).
139. CasaXPS. *Peak Fitting in XPS*. (Casa Software Ltd, 2006).
140. Jain, V., Biesinger, M. C. & Linford, M. R. The Gaussian-Lorentzian Sum, Product, and Convolution (Voigt) functions in the context of peak fitting X-ray photoelectron spectroscopy (XPS) narrow scans. *Appl. Surf. Sci.* **447**, 548–553 (2018).
141. Davisson, C. M. Interaction of  $\gamma$ -Radiation with Matter. *Alpha-, Beta- Gamma-Ray Spectrosc.* **1**, 37–78 (1968).
142. Fornalski, K. W. Simple empirical correction functions to cross sections of the photoelectric effect, Compton scattering, pair and triplet production for carbon radiation shields for intermediate and high photon energies. *J. Phys. Commun.* **2**, 035038 (2018).
143. Wagner, C. D. Sensitivity factors for XPS analysis of surface atoms. *J. Electron Spectros. Relat. Phenomena* **32**, 99–102 (1983).
144. Ruzyllo, J. *et al.* Cleaning Technology in Semiconductor Device Manufacturing. in vols 97–35 614 (1998).
145. Othman, M. Z. Studies of n-type doping and surface modification of CVD diamond for use in thermionic applications. (University of Bristol, 2014).
146. Croot, A. Boron and nitrogen in diamond: an ab initio simulation, plasma

- emission spectroscopy and material deposition & characterisation study. (University of Bristol, 2018).
147. Al-jeda, T. Construction and Operation of a Plasma System to Fluorinate and Aminate the Surfaces of Diamond Thin Films. (University of Bristol, 2018).
  148. Scienta Omicron. NanoESCA. <https://scientaomicron.com/en/productDetailPages/system-solutions/electron-spectroscopy/NanoESCA>.
  149. David, D. G. F., Pinault-Thaury, M.-A., Ballutaud, D. & Godet, C. Sensitivity of photoelectron energy loss spectroscopy to surface reconstruction of microcrystalline diamond films. *Appl. Surf. Sci.* **273**, 607–612 (2013).
  150. Slater, J. C. Atomic Radii in Crystals. *J. Chem. Phys.* **41**, 3199–3204 (1964).
  151. Luo, Y. R. *Comprehensive Handbook of Chemical Bond Energies*. (Taylor and Francis, 2007).
  152. Helmenstine, A. Electronegativity Definition and Trend. <https://sciencenotes.org/electronegativity-definition-and-trend/>.
  153. IPCC. About the IPCC. <https://www.ipcc.ch/about/>.
  154. Anthony, T. R. *et al.* Thermal diffusivity of isotopically enriched C12 diamond. *Phys. Rev. B* **42**, 1104–1111 (1990).
  155. Perdew, J. P. Jacob's ladder of density functional approximations for the exchange-correlation energy. *AIP Conf. Proc.* **577**, 1–20 (2001).
  156. Dolenko, G. N., Poleshchuk, O. K. & Latośńska, J. N. X-ray Emission Spectroscopy, Methods. in *Encyclopedia of Spectroscopy and Spectrometry* 2463–2467 (Elsevier, 1999).
  157. Moulder, J. F., Stickle, W. F., Sobol, P. E. & Bomben, K. D. *Handbook of X-ray Photoelectron Spectroscopy*. (Perkin-Elmer Corp., Physical Electronics Division, 1992).
  158. Wanger, C. D., Riggs, W. M., Davis, L. E., Moulder, J. F. & E. Muilenberg, G. *Handbook of X-ray Photoelectron Spectroscopy*. (Perkin-Elmer Corp., Physical Electronics Division, 1981).
  159. Miller, D. J., Biesinger, M. C. & McIntyre, N. S. Interactions of CO<sub>2</sub> and CO at

- fractional atmosphere pressures with iron and iron oxide surfaces: one possible mechanism for surface contamination? *Surf. Interface Anal.* **33**, 299–305 (2002).
160. Thermo Scientific. XPS Interpretation of Carbon. <https://xpssimplified.com/elements/carbon.php>.
161. University of Western Ontario. X-ray Photoelectron Spectroscopy (XPS) Reference Pages - Carbon. <http://www.xpsfitting.com/search/label/carbon>.
162. Arezzo, F., Severini, E. & Zacchetti, N. An XPS study of diamond films grown on differently pretreated silicon substrates. *Surf. Interface Anal.* **22**, 218–223 (1994).
163. Biesinger, M. C., Payne, B. P., Lau, L. W. M., Gerson, A. & Smart, R. S. C. X-ray photoelectron spectroscopic chemical state quantification of mixed nickel metal, oxide and hydroxide systems. *Surf. Interface Anal.* **41**, 324–332 (2009).
164. Thermo Scientific. XPS Interpretation of Oxygen. <https://xpssimplified.com/elements/oxygen.php>.
165. University of Western Ontario. X-ray Photoelectron Spectroscopy (XPS) Reference Pages - Oxygen. <http://www.xpsfitting.com/search/label/oxygen>.
166. Mohtasebi, A., Chowdhury, T., Hsu, L. H. H., Biesinger, M. C. & Kruse, P. Interfacial Charge Transfer between Phenyl-Capped Aniline Tetramer Films and Iron Oxide Surfaces. *J. Phys. Chem. C* **120**, 29248–29263 (2016).
167. Saha, N. C. & Tompkins, H. G. Titanium nitride oxidation chemistry: An x-ray photoelectron spectroscopy study. *J. Appl. Phys.* **72**, 3072–3079 (1992).
168. Jaeger, D. & Patscheider, J. A complete and self-consistent evaluation of XPS spectra of TiN. *J. Electron Spectros. Relat. Phenomena* **185**, 523–534 (2012).
169. Thermo Scientific. XPS Interpretation of Nitrogen. <https://xpssimplified.com/elements/nitrogen.php>.
170. University of Western Ontario. X-ray Photoelectron Spectroscopy (XPS) Reference Pages - Nitrogen. <http://www.xpsfitting.com/search/label/nitrogen>.
171. Biesinger, M. C., Lau, L. W. M., Gerson, A. R. & Smart, R. S. C. Resolving surface chemical states in XPS analysis of first row transition metals, oxides and hydroxides: Sc, Ti, V, Cu and Zn. *Appl. Surf. Sci.* **257**, 887–898 (2010).
172. Biesinger, M. C. *et al.* Quantitative chemical state XPS analysis of first row

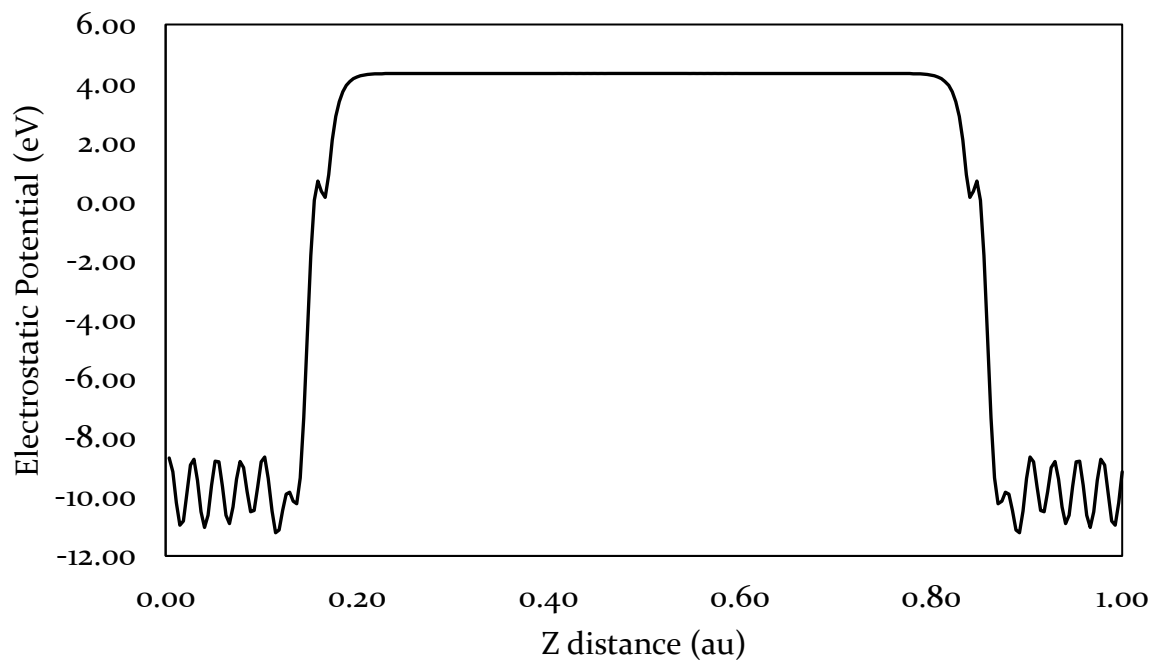
- transition metals, oxides and hydroxides. *J. Phys. Conf. Ser.* **100**, 012025 (2008).
173. Thermo Scientific. XPS Interpretation of Titanium. <https://xpssimplified.com/elements/titanium.php>.
174. University of Western Ontario. X-ray Photoelectron Spectroscopy (XPS) Reference Pages - Titanium. <http://www.xpsfitting.com/search/label/titanium>.
175. Gautama, P. *et al.* Synthesizing diamond film on Cu, Fe and Si substrate by in-liquid microwave plasma CVD. *Precis. Eng.* **49**, 412–420 (2017).

# Appendix A – Electrostatic Potentials

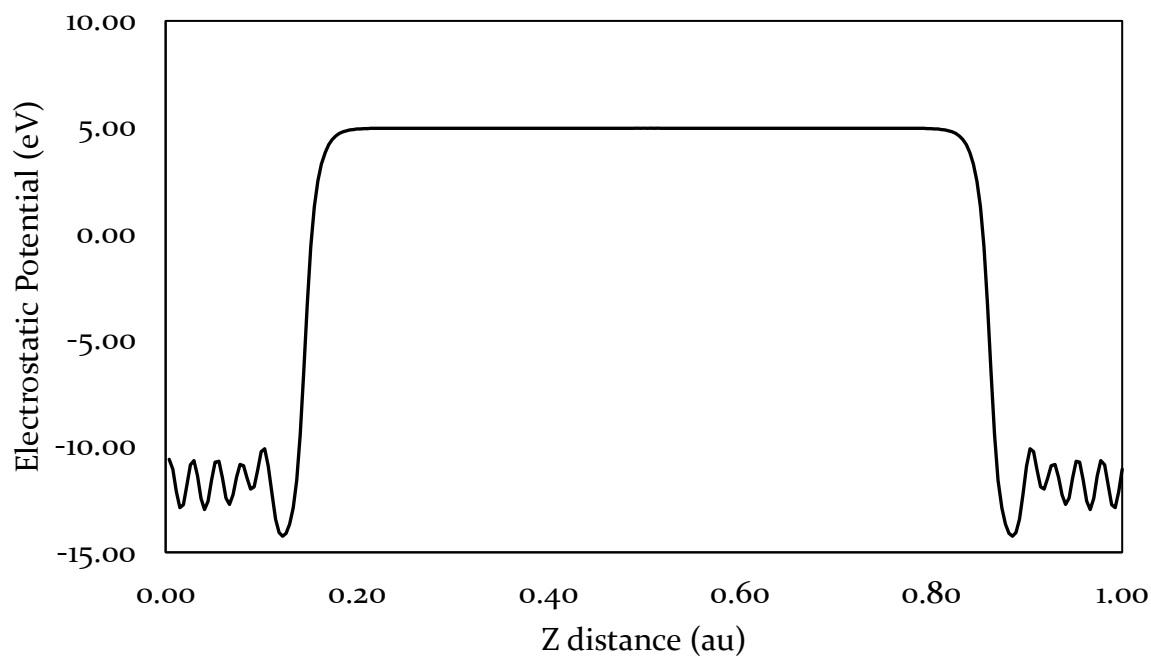
## Graphs

TiC Section 2.3.1

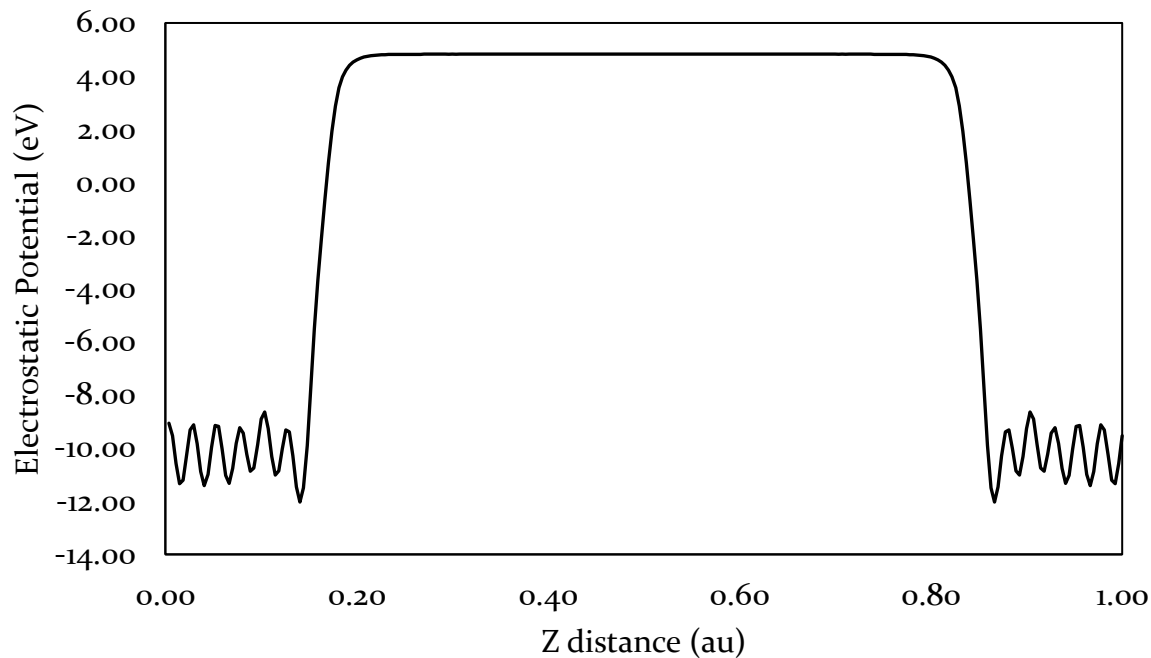
(a) C-H



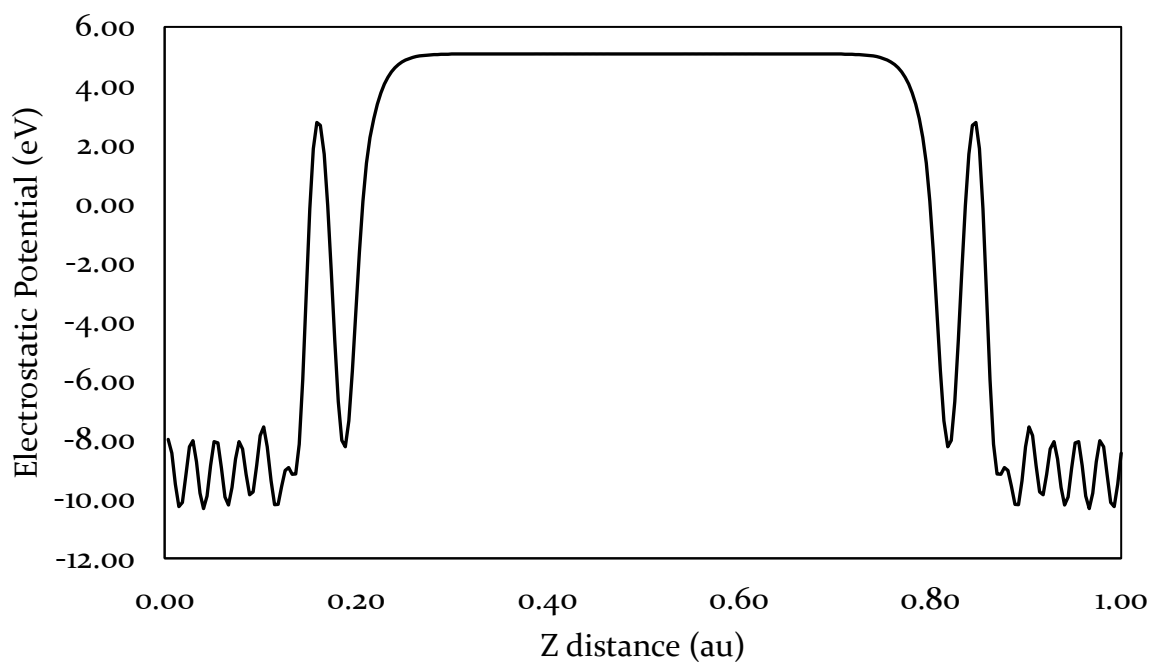
(b) Clean



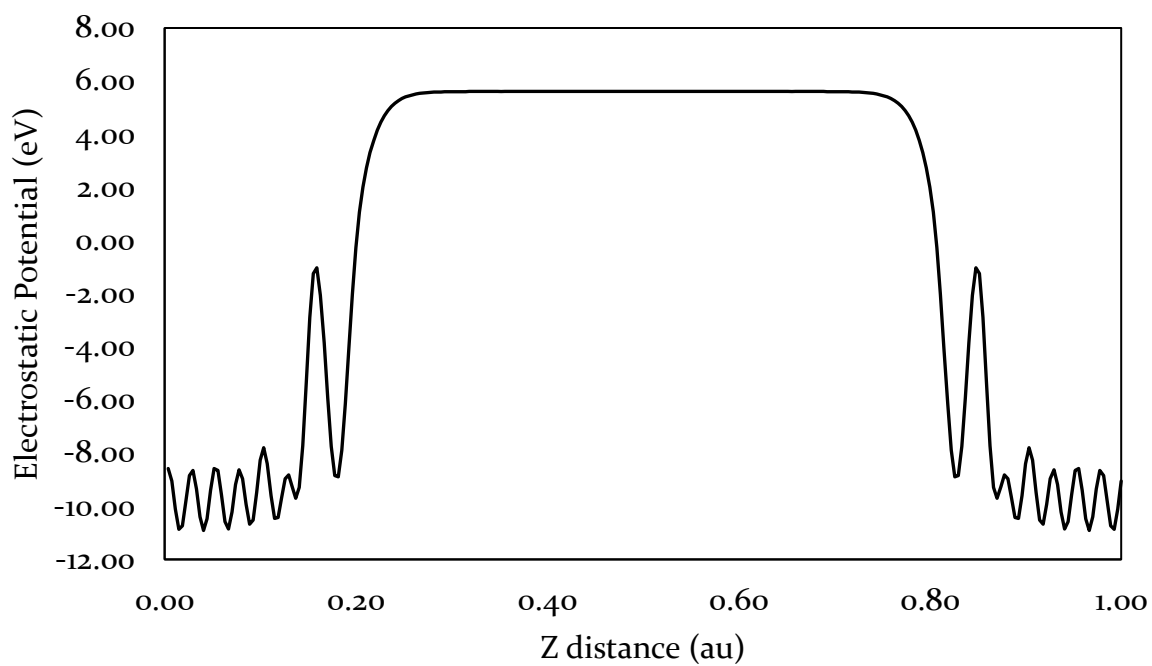
(c) C-Til



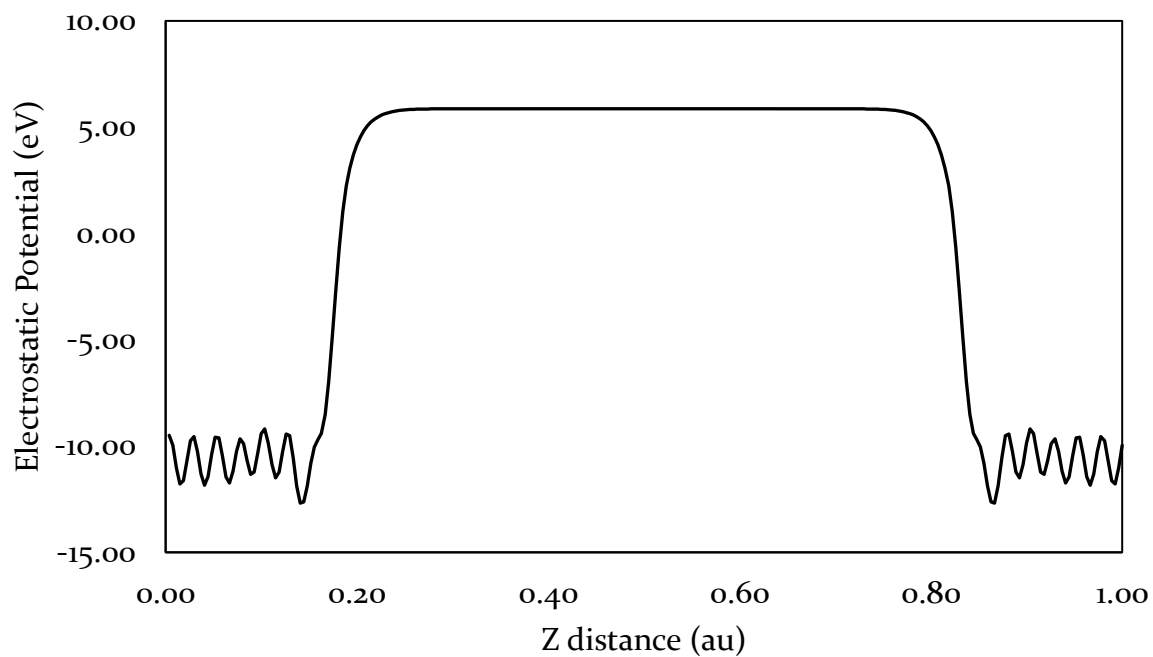
(d) C-Ti2br



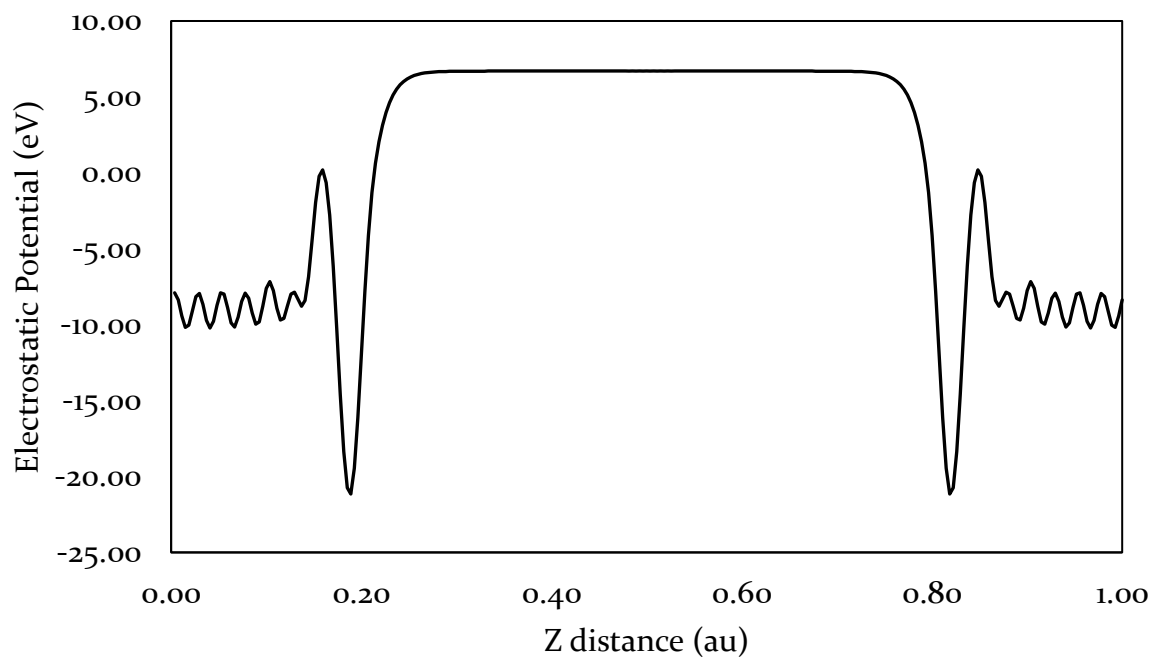
(e) C-Ti2t



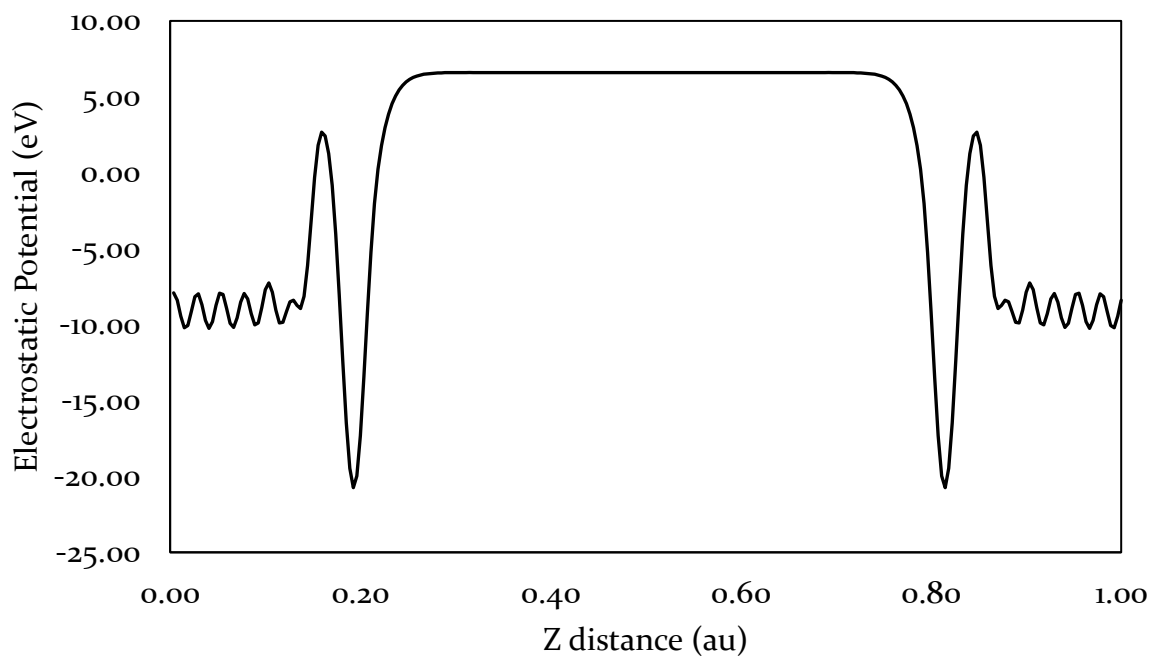
(f) C-Ti2b4



(g) C-Ti4br

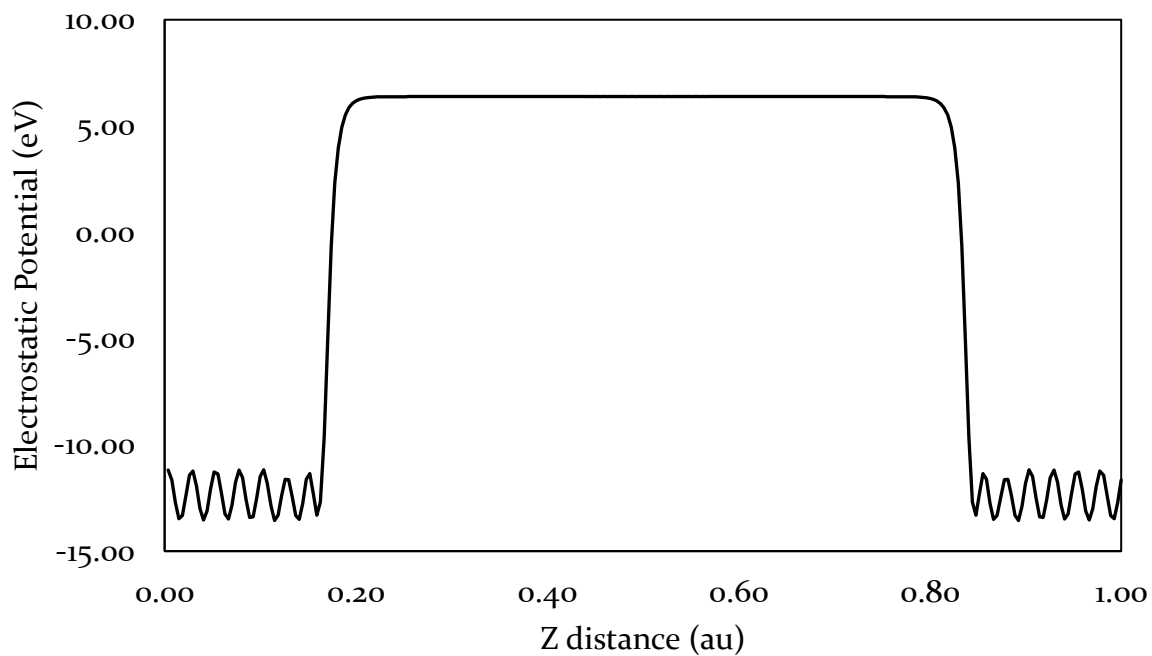


(h) C-Ti4t

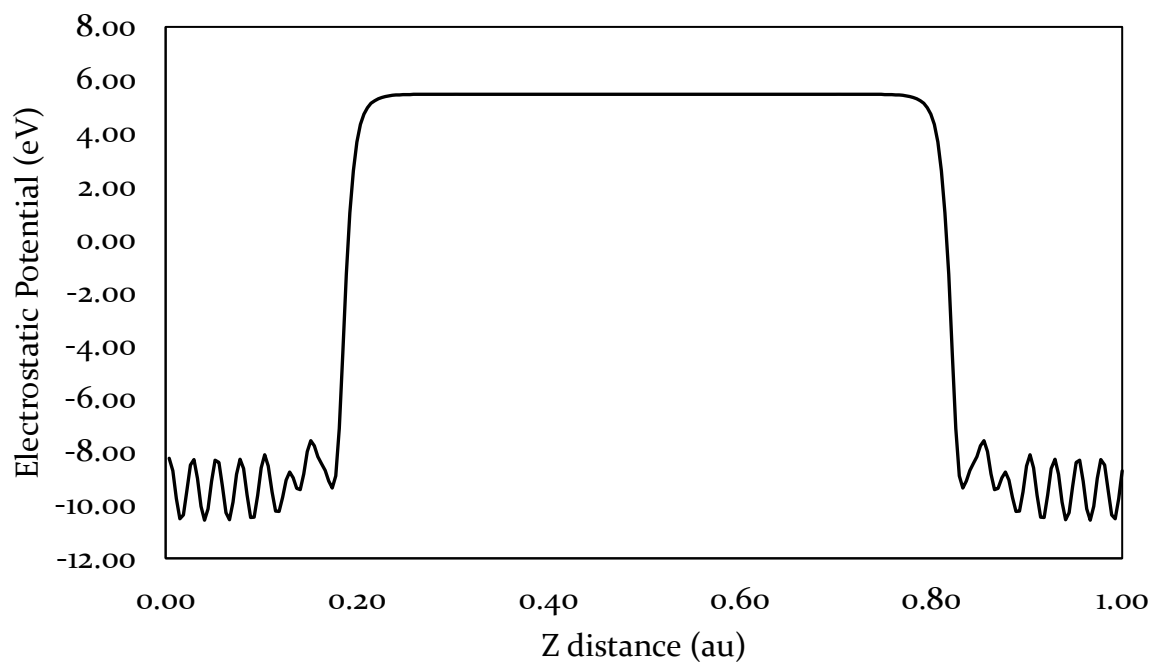


TiO Section 2.3.2

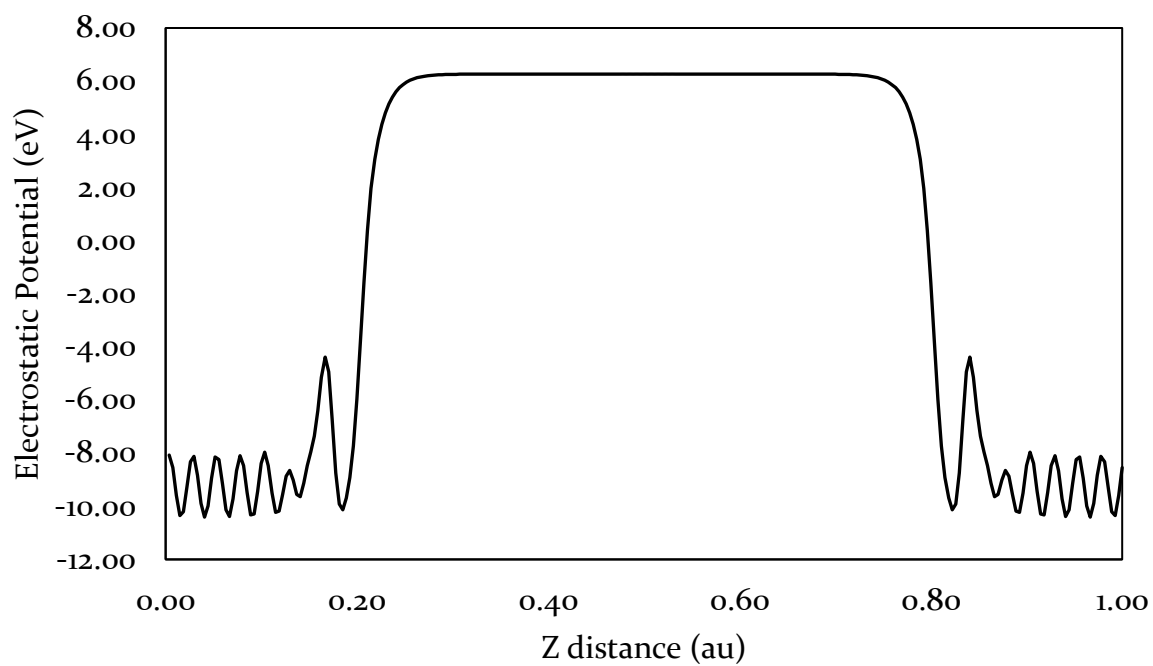
(a) Oe



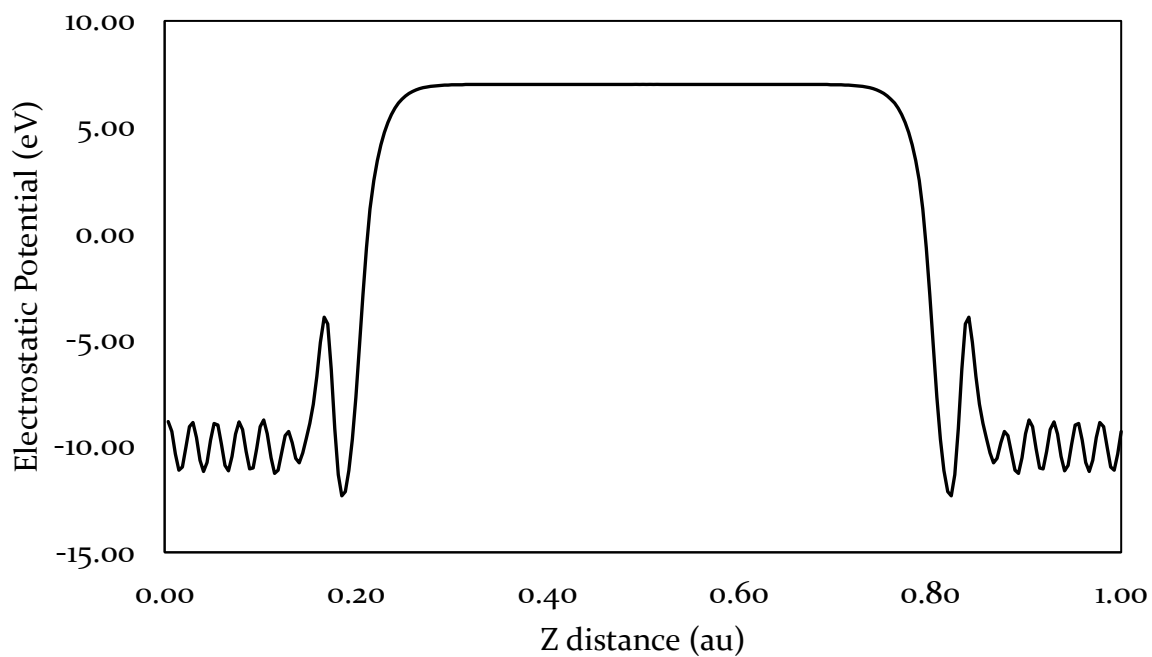
(b) Oe-TiI



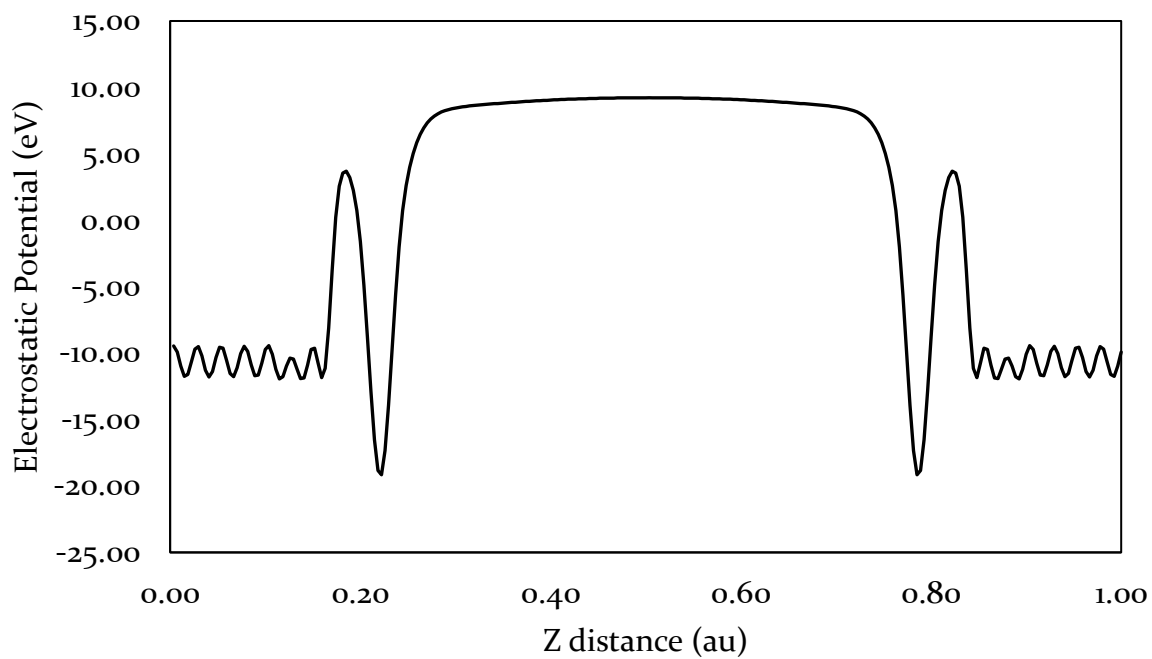
(c) Oe-Ti2br



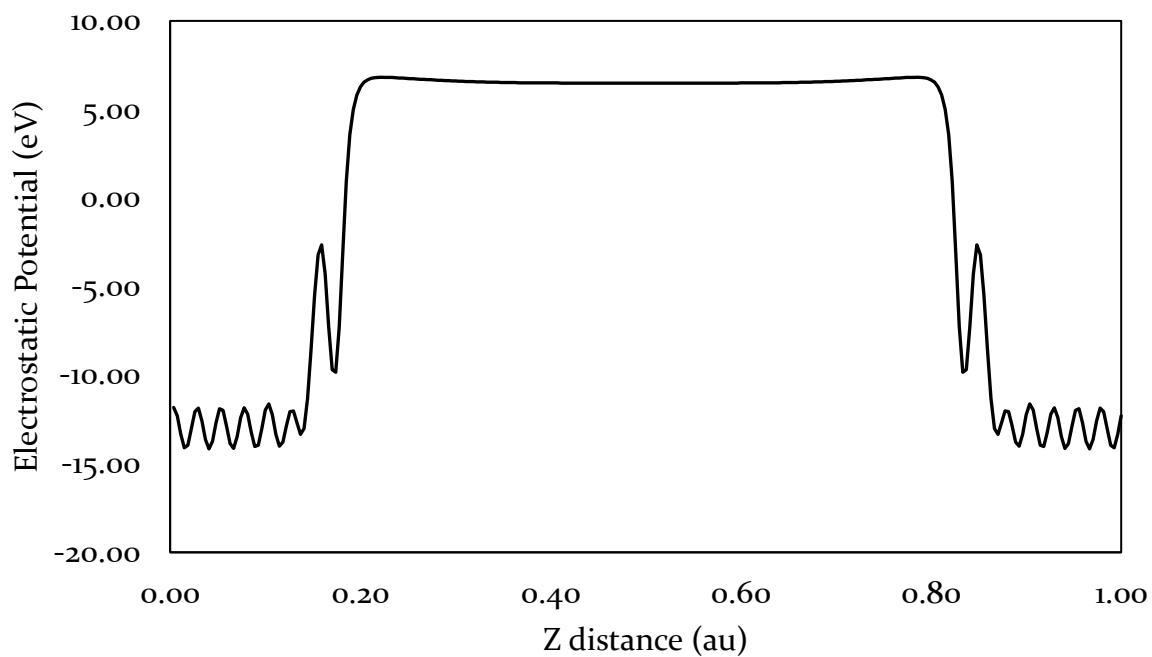
(d) Oe-Ti2t



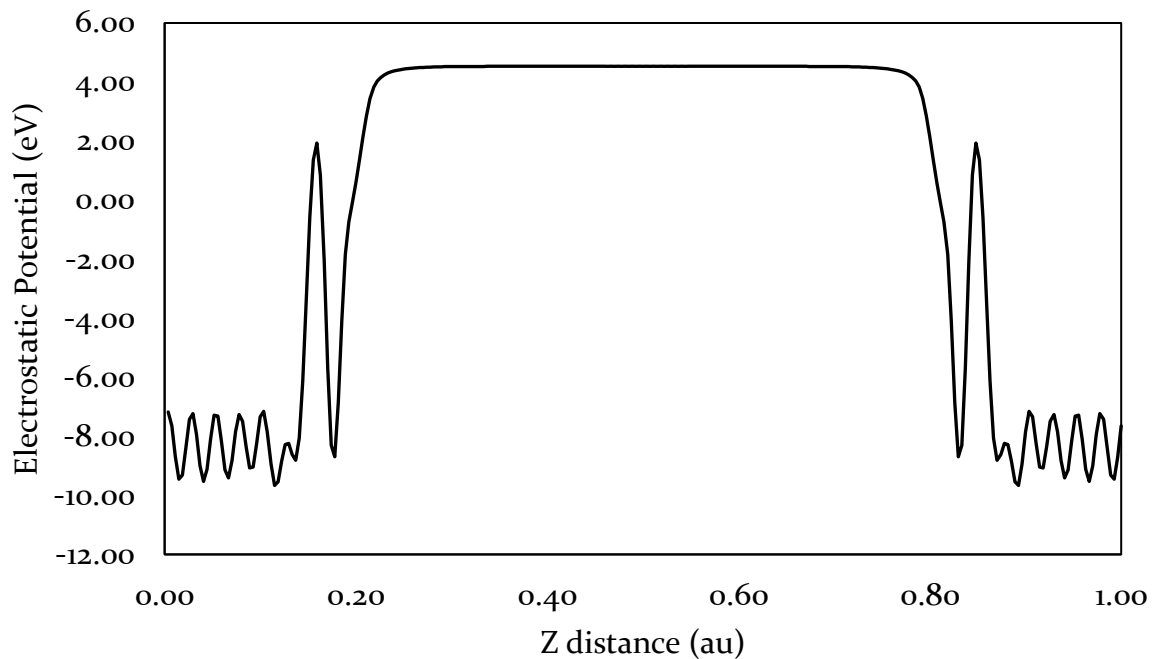
(e) Oe-Ti4



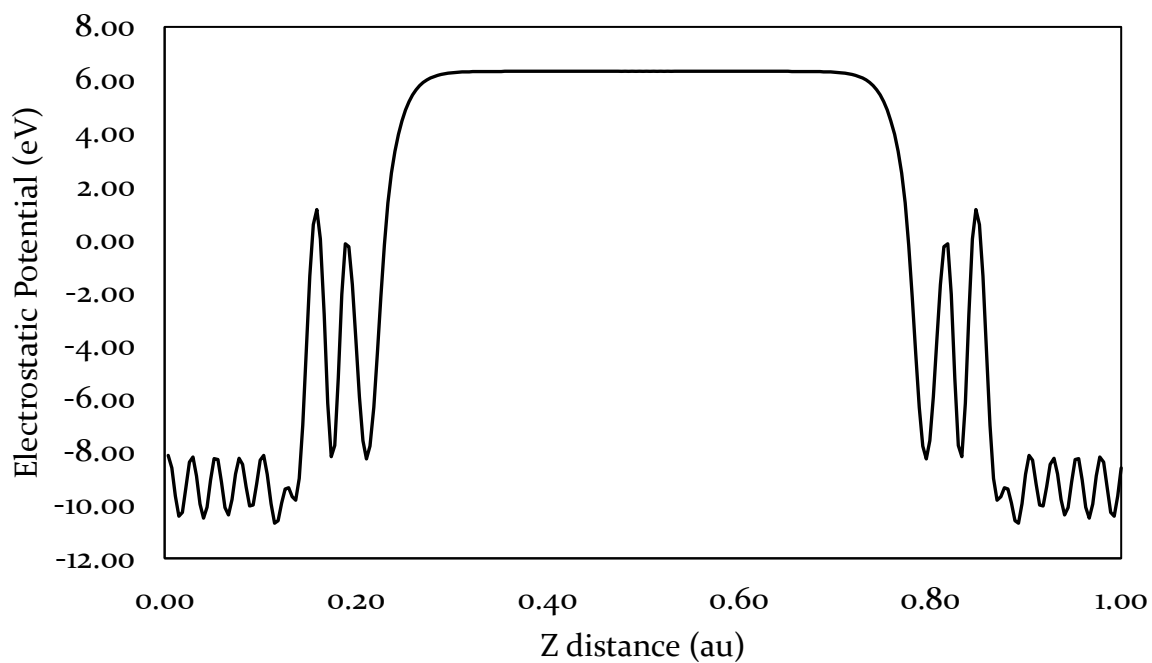
(f) Ok



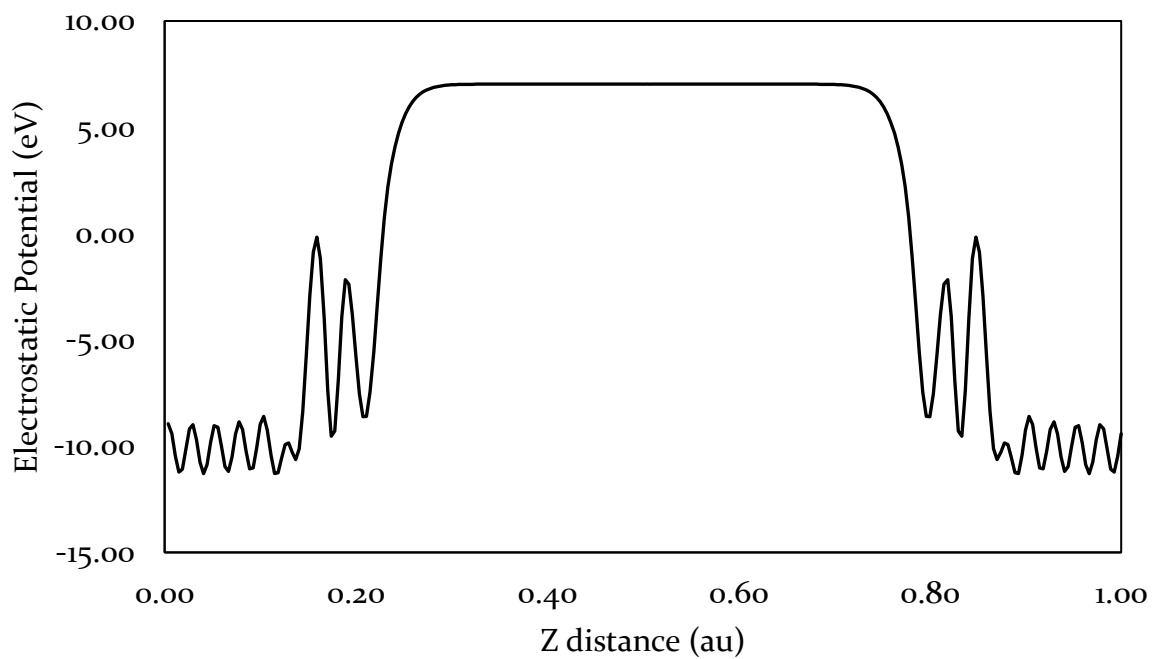
(g) Ok-Til



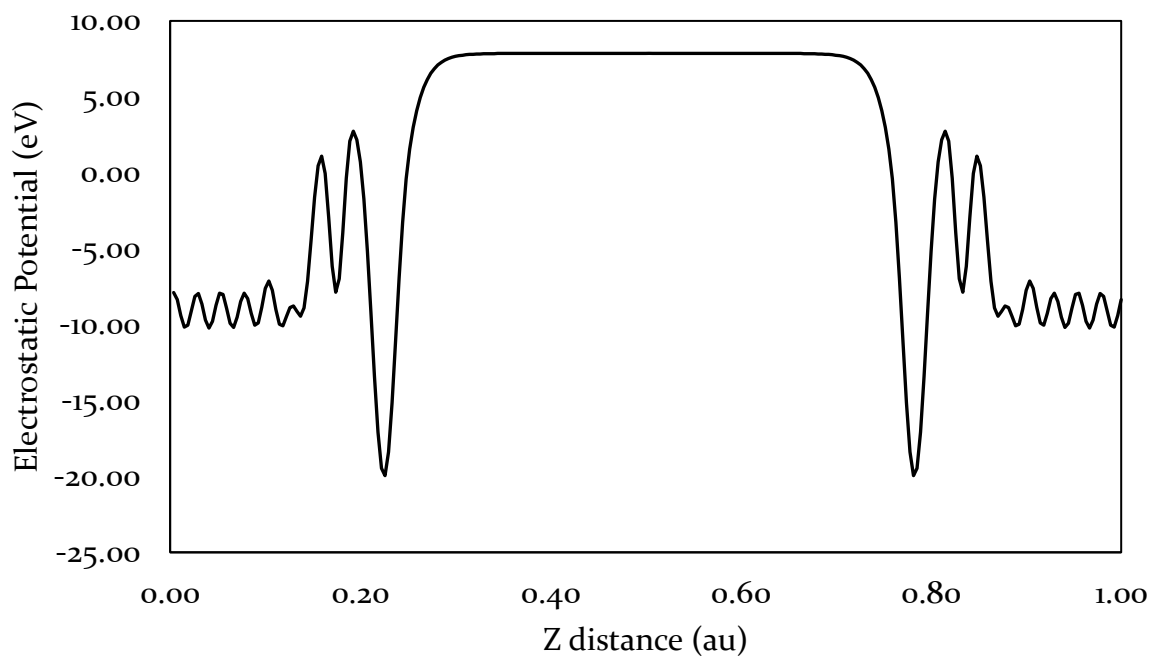
(h) Ok-Ti2br



(i) Ok-Ti2t

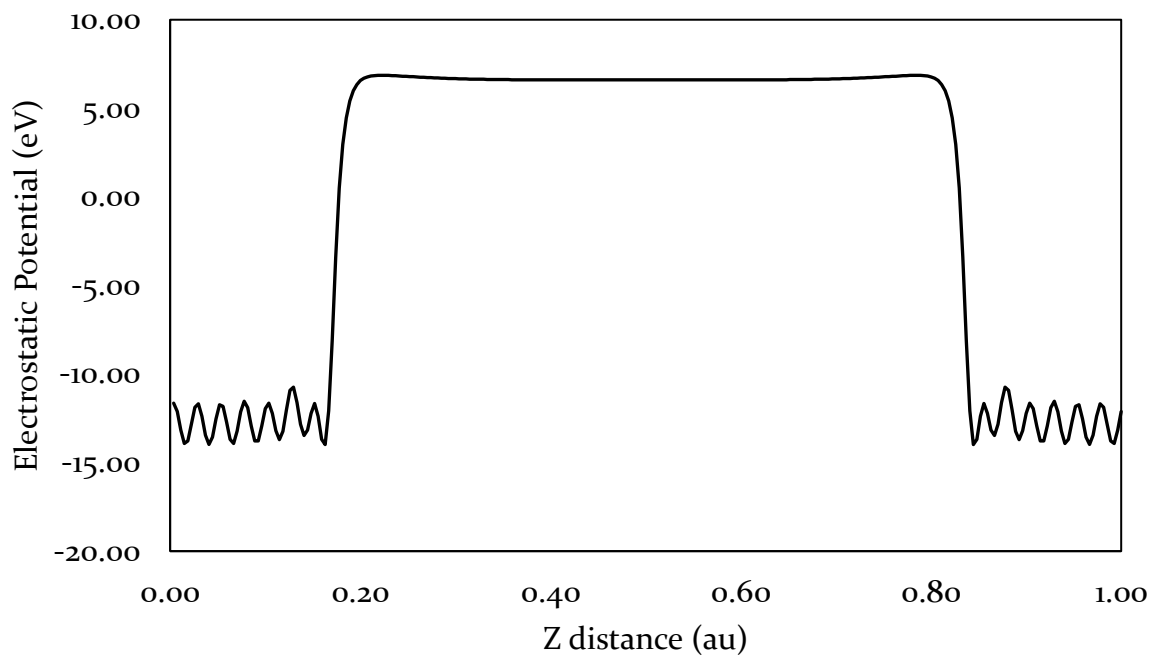


(j) Ok-Ti4

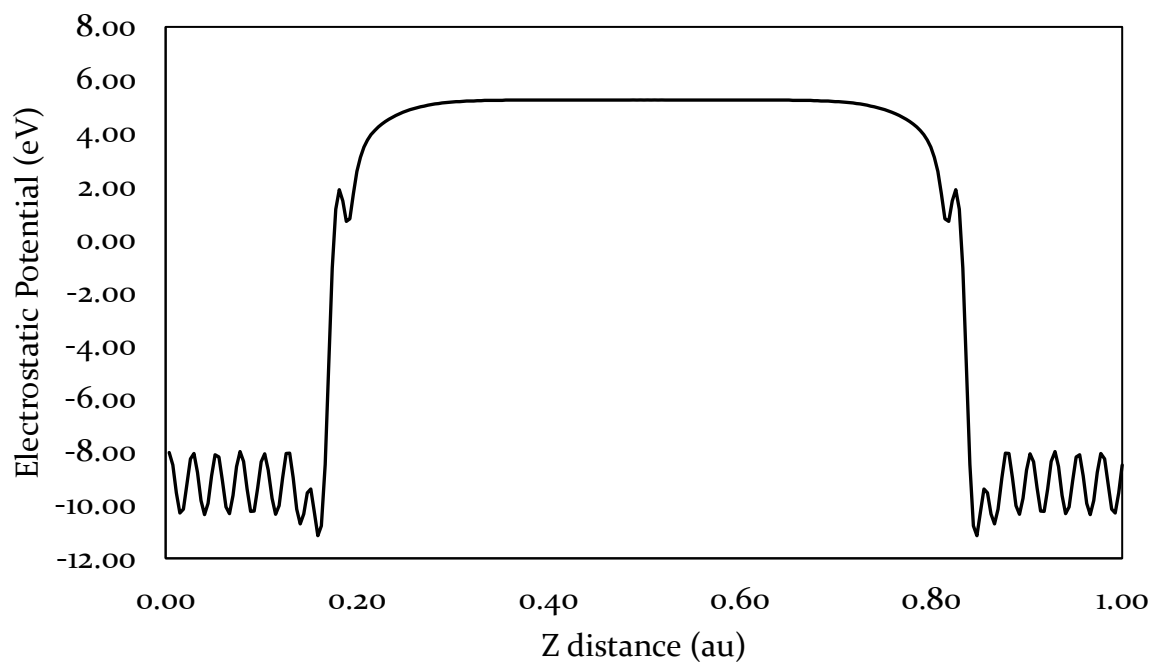


TiN Section 2.3.3

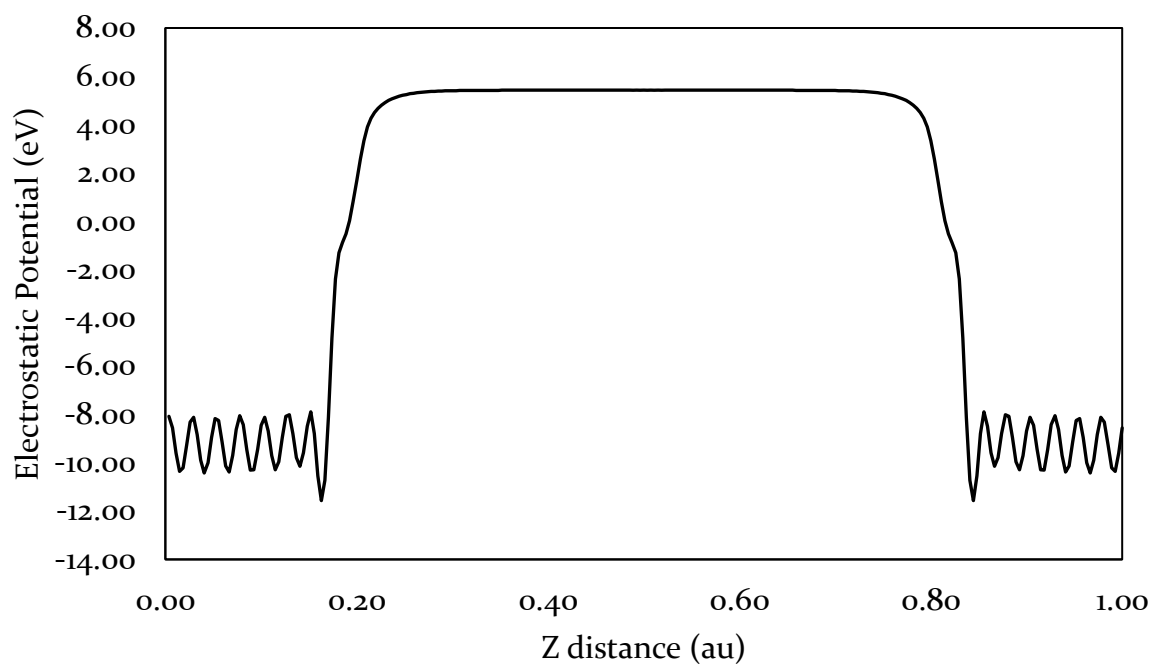
(a) Ne



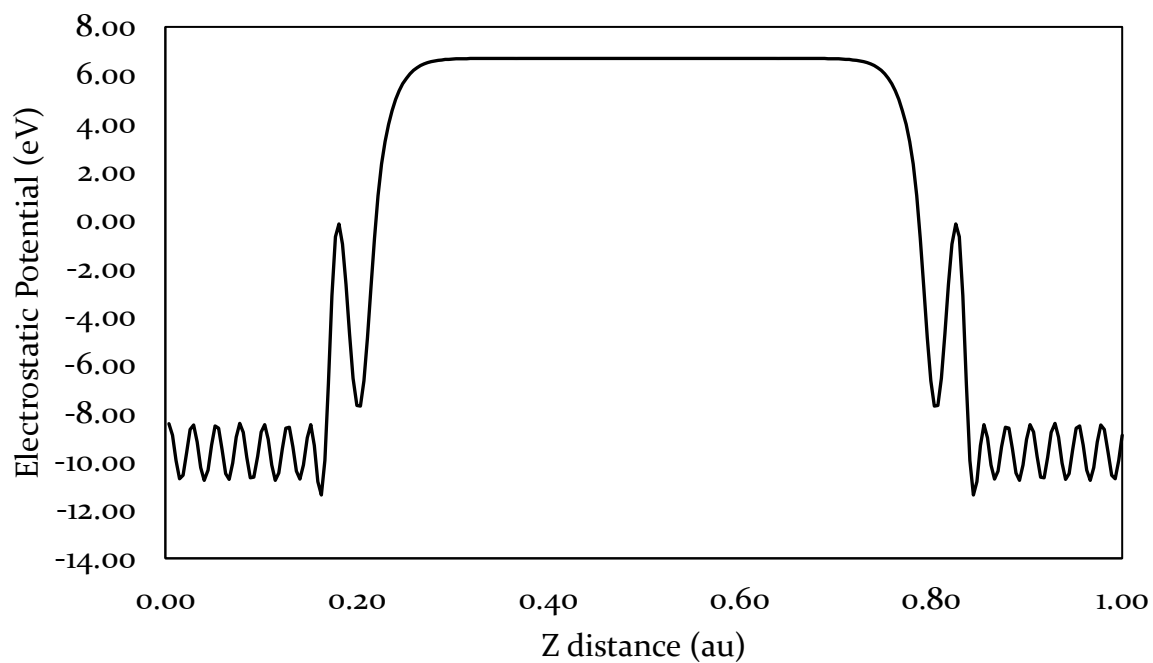
(b) Ne-H



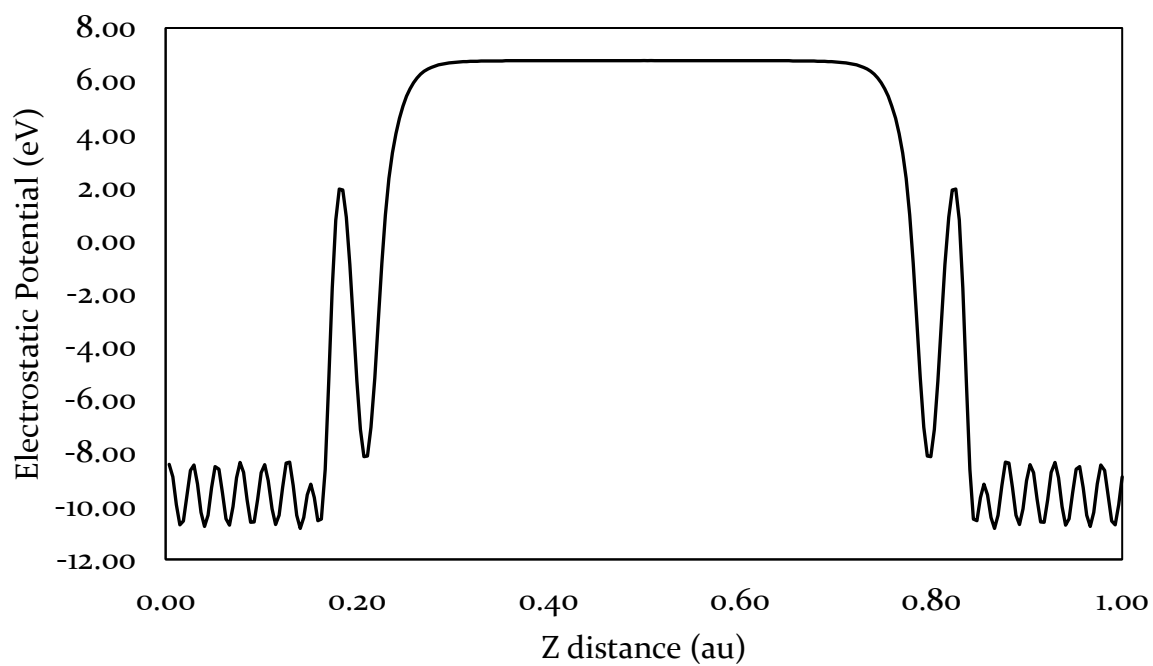
(c) Ne-TiI



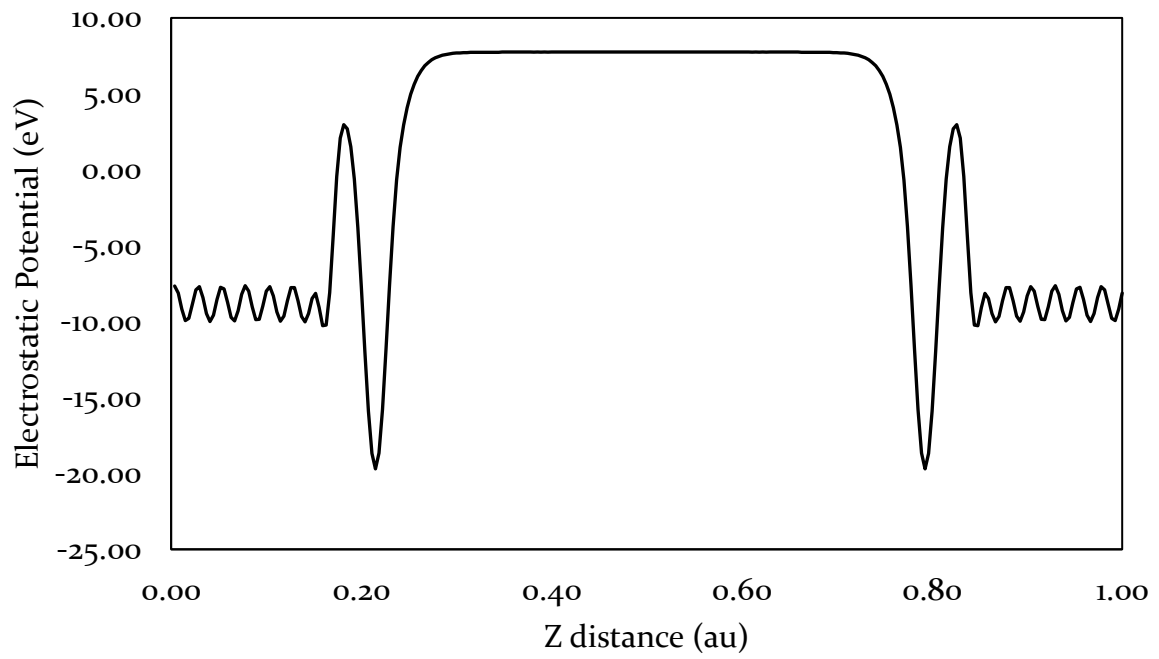
(d) Ne-Ti2br



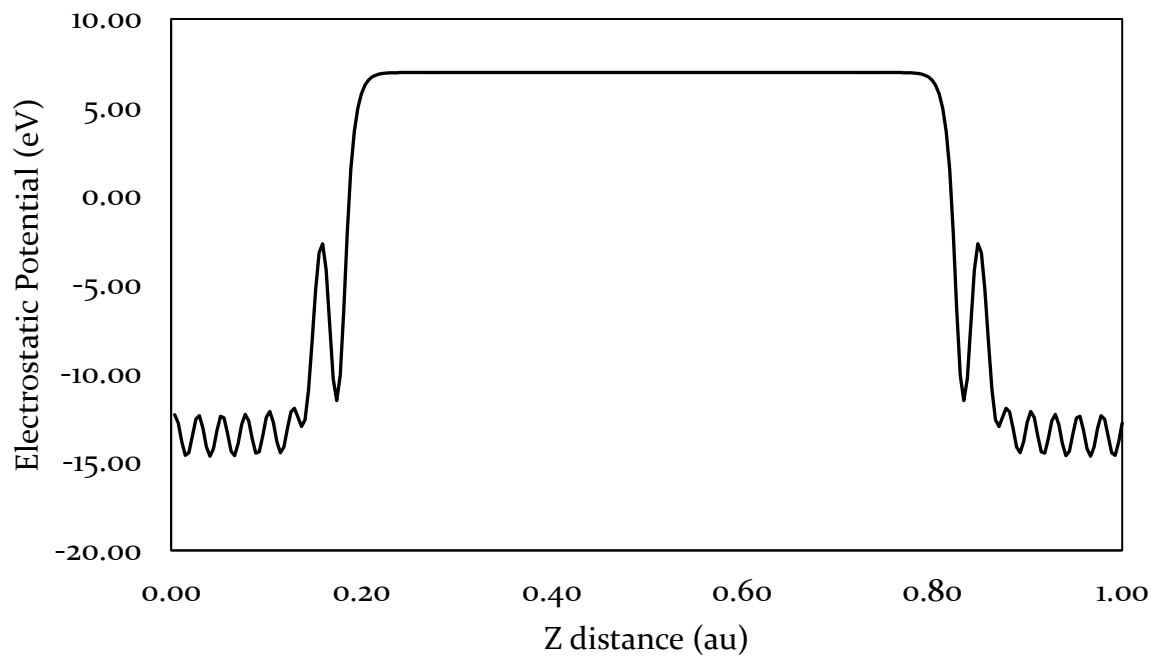
(e) Ne-Ti2t



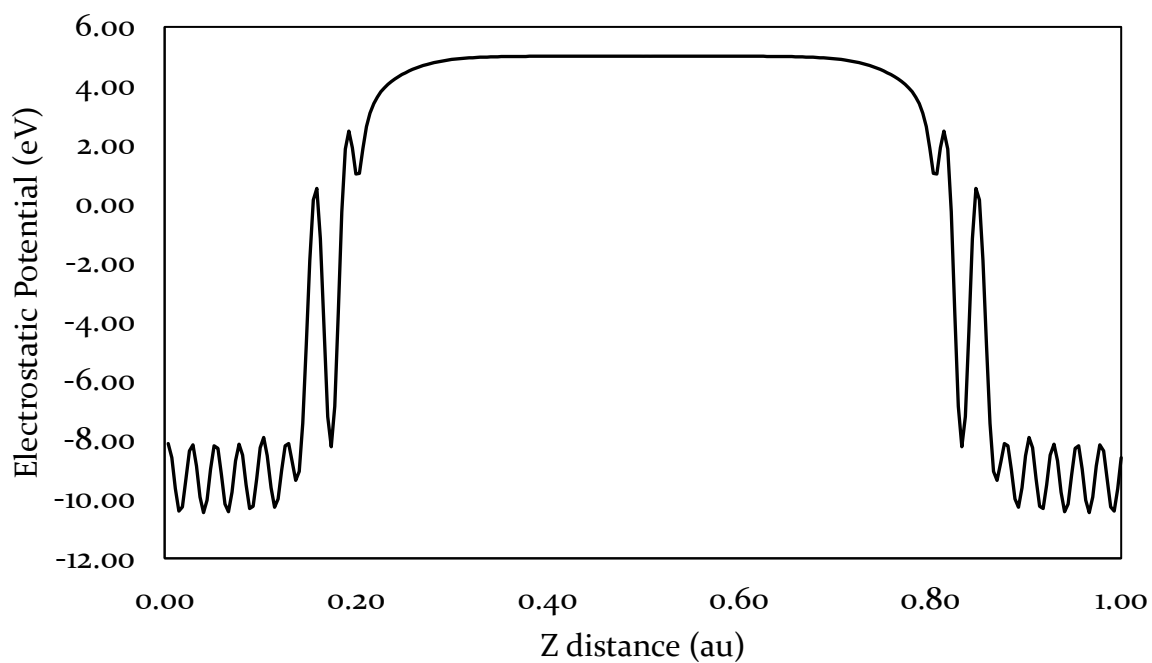
(f) Ne-Ti4



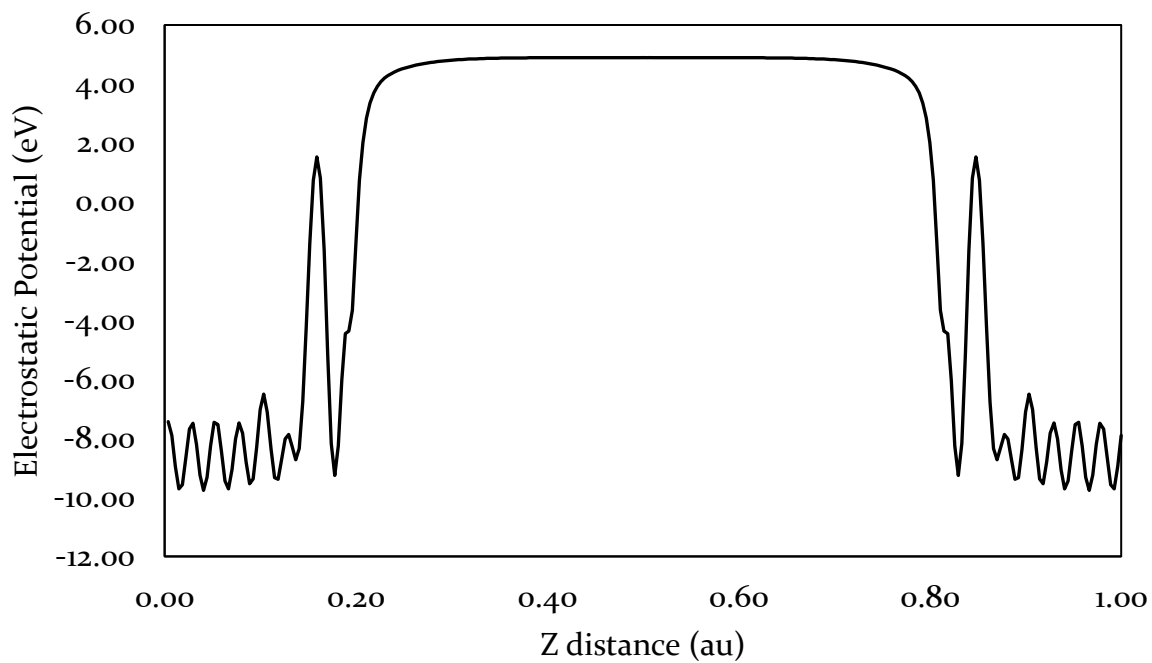
(g) Nk



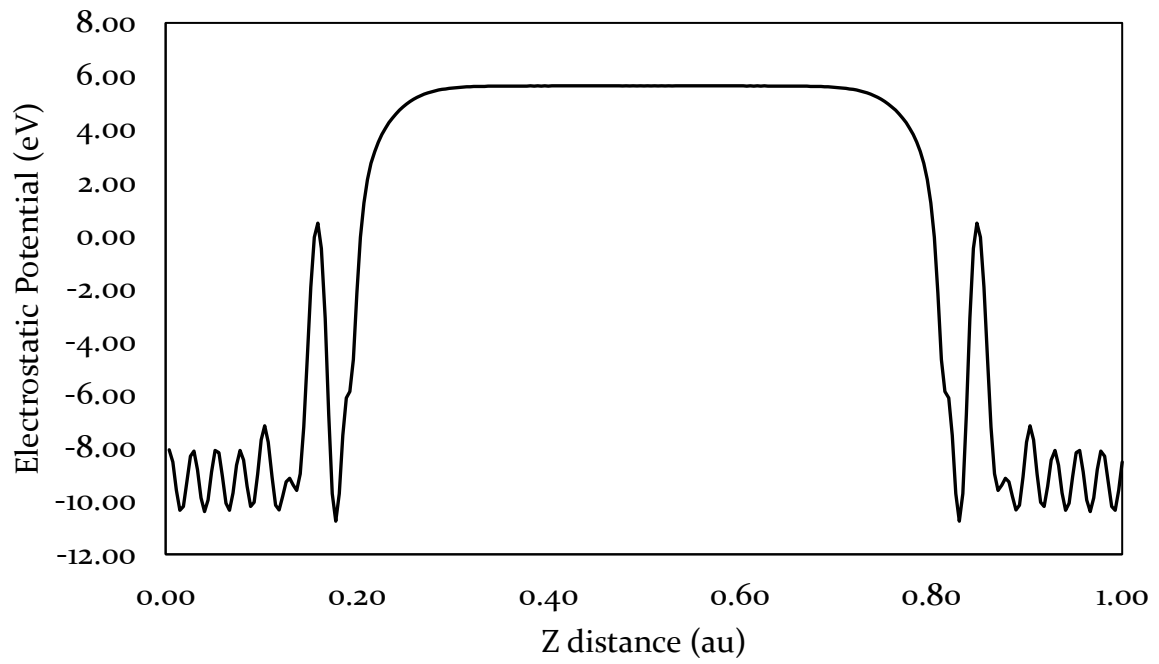
(h) Nk-HI



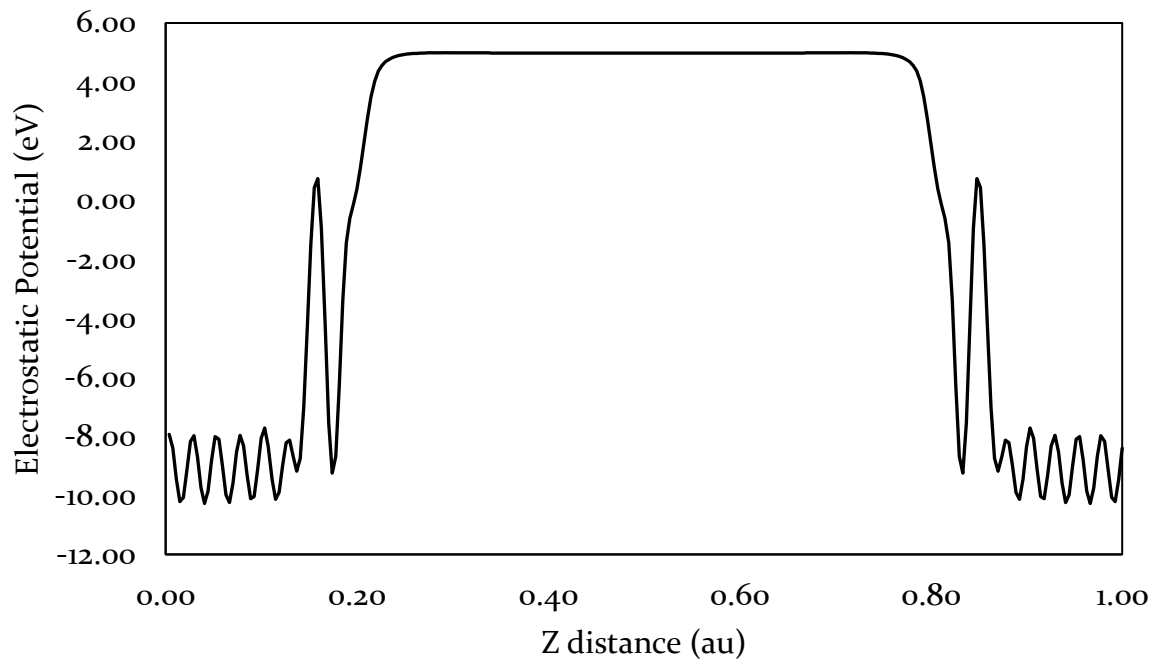
(i) Nk-H2x



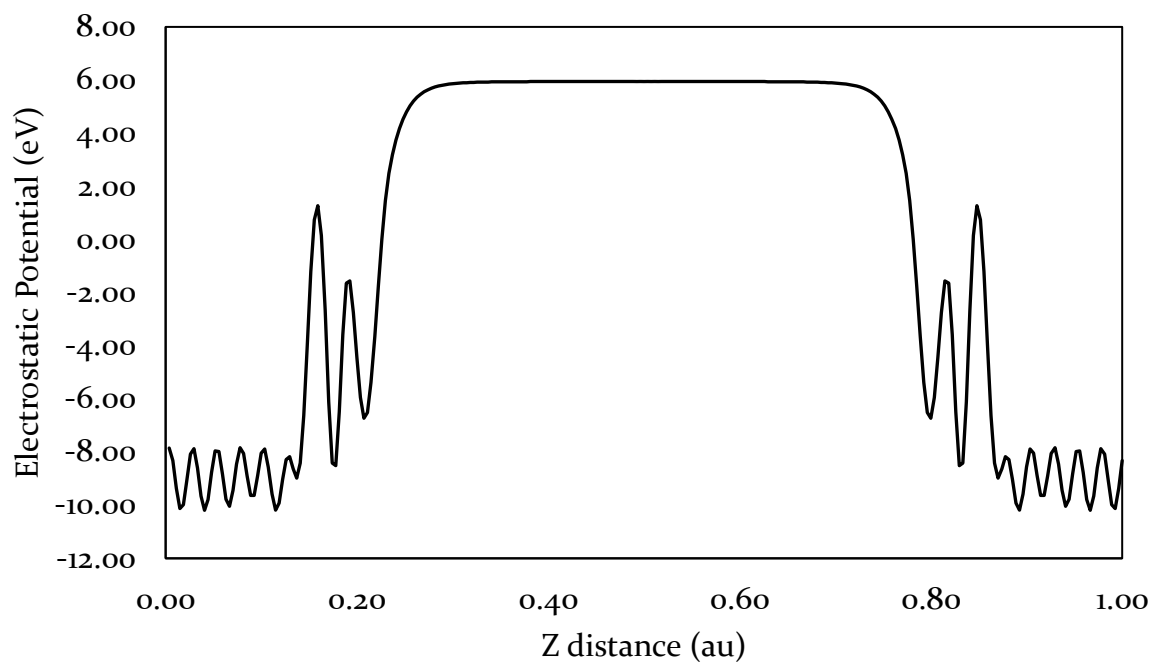
(j) Nk-H2y



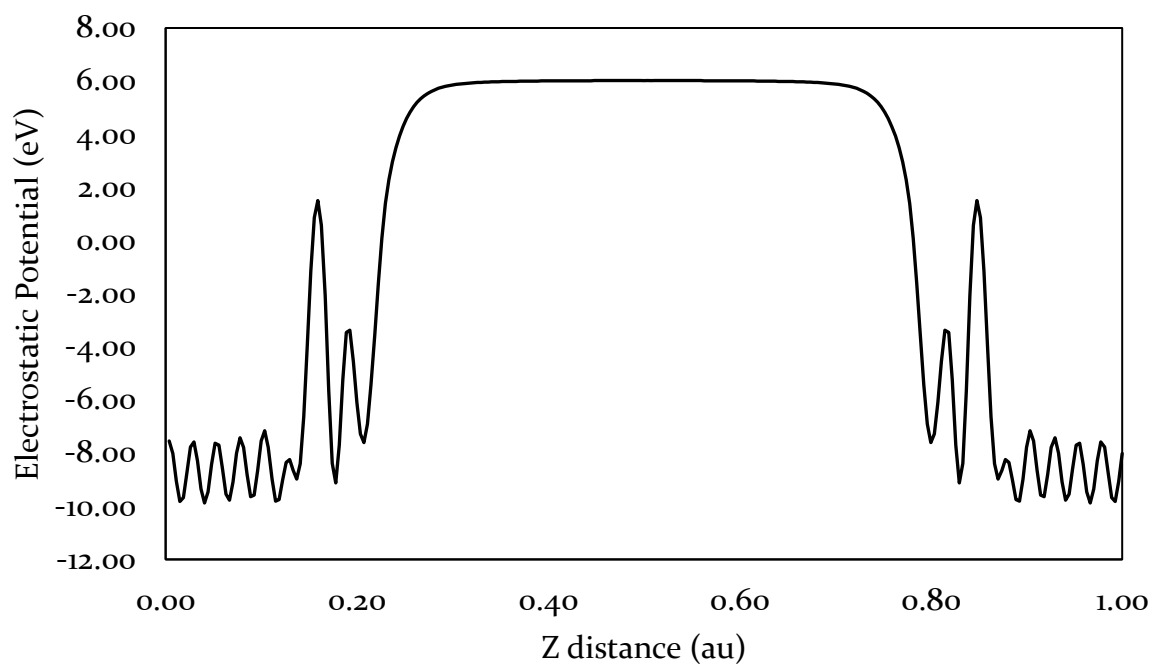
(k) Nk-TiI



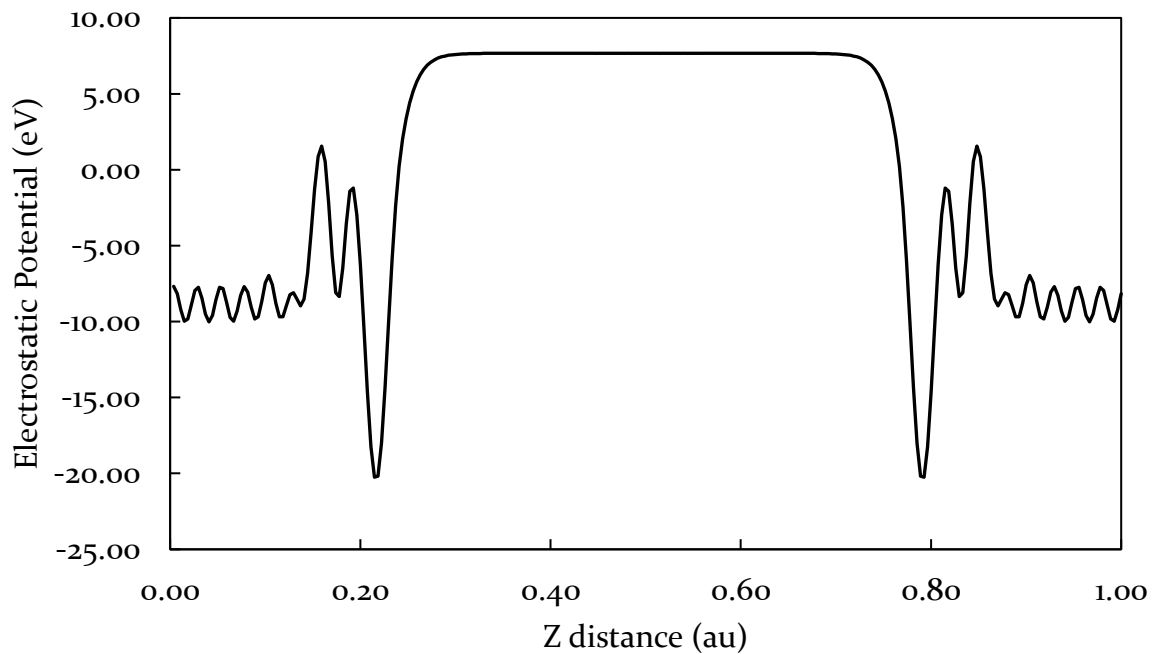
(l) Nk-Ti2br



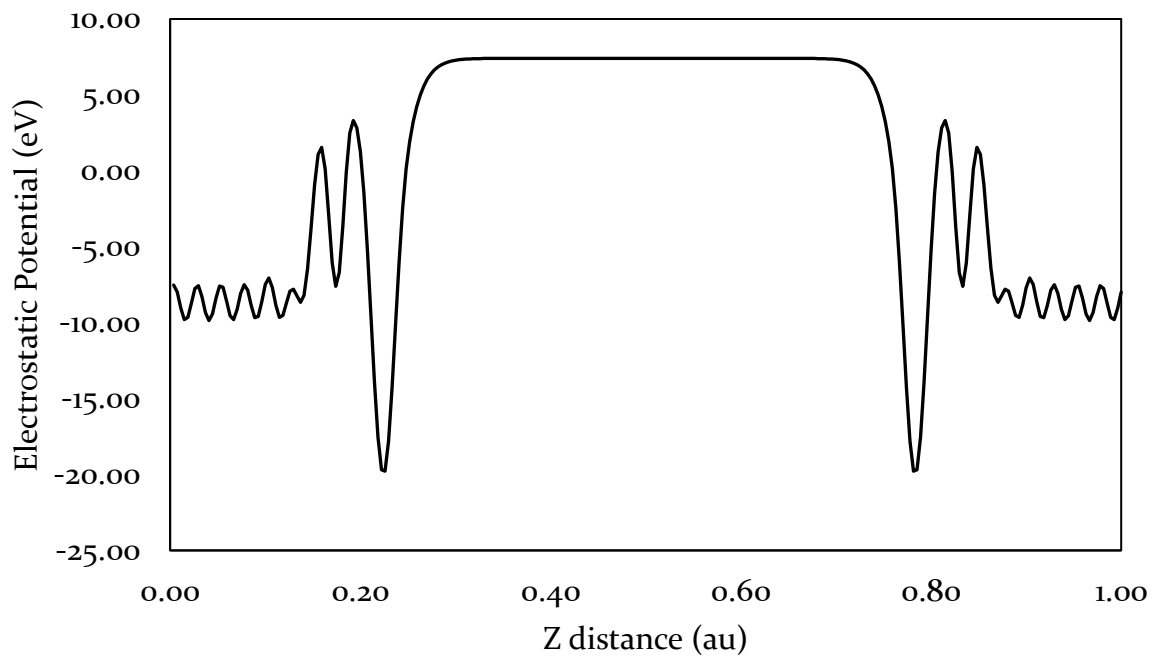
(m) Nk-Ti2t



(n) Nk-Ti4br

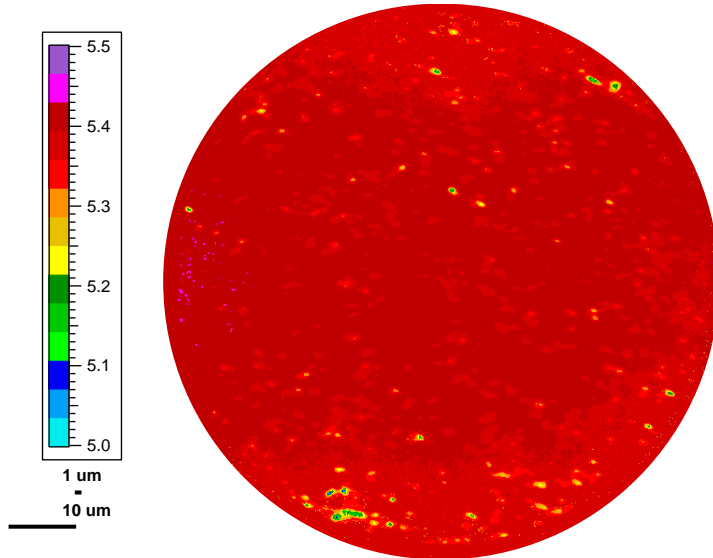


(o) Nk-Ti4t

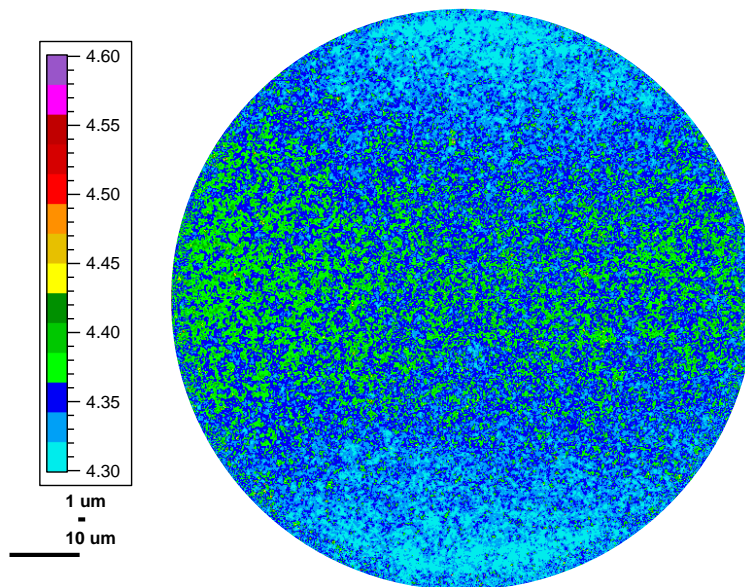


# Appendix B – Work Function Maps

Sample #2.7, section 6.2

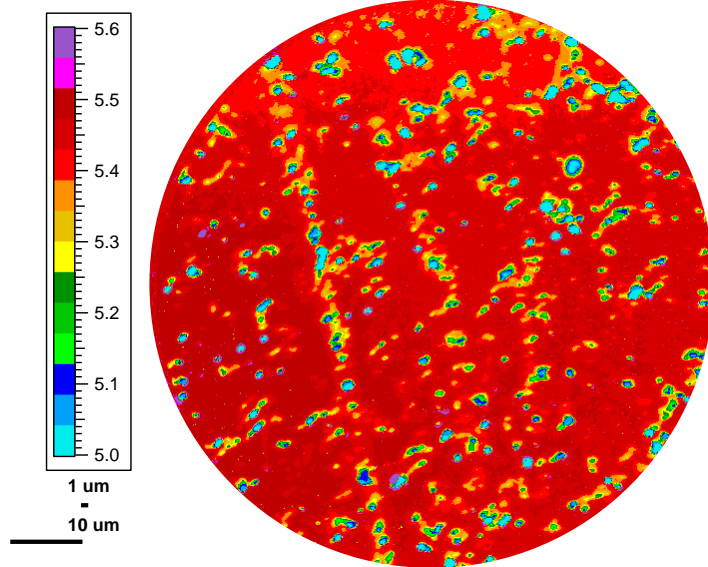


Titanium sample, section 6.2

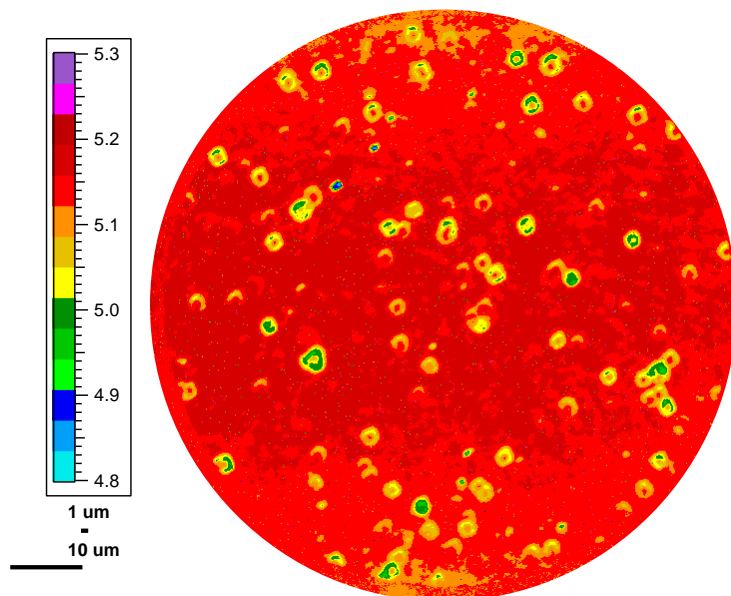


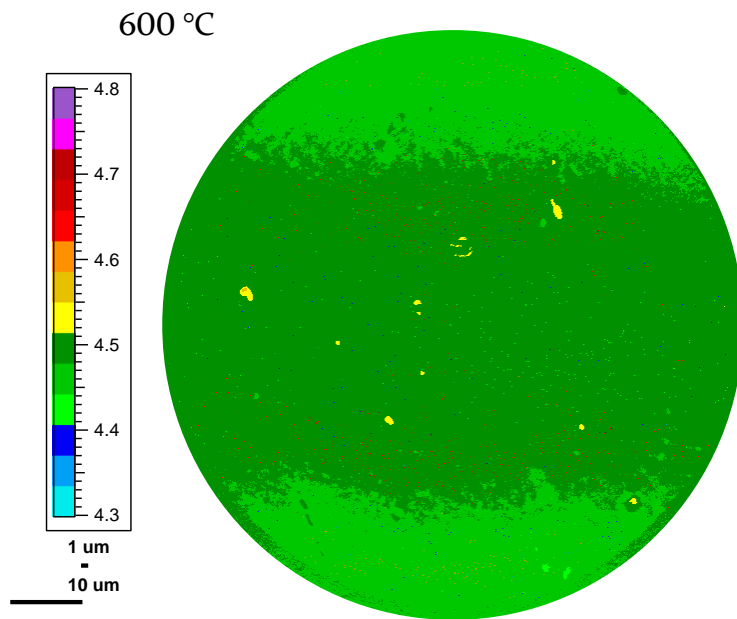
TiO QML, section 6.3.1

0 °C

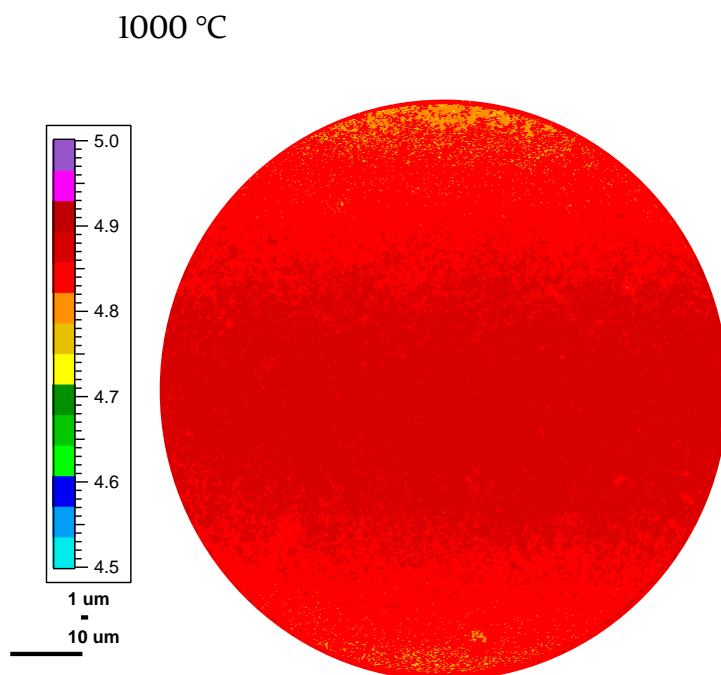


400 °C



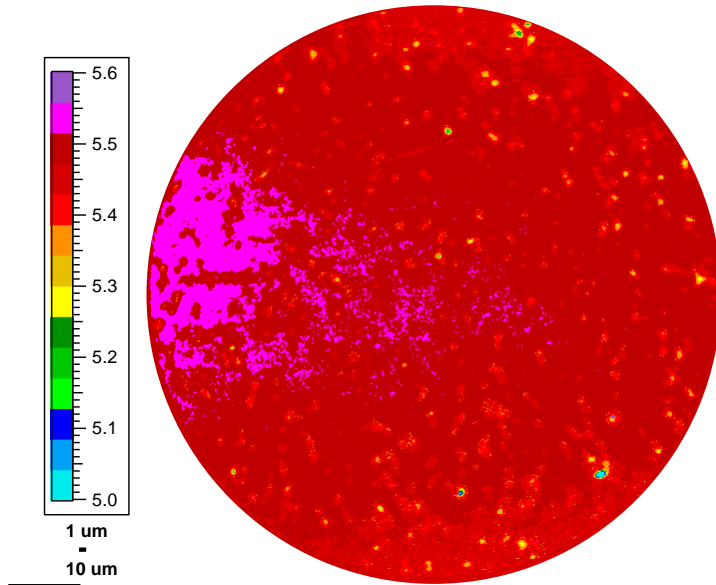


800 °C  
File not found.

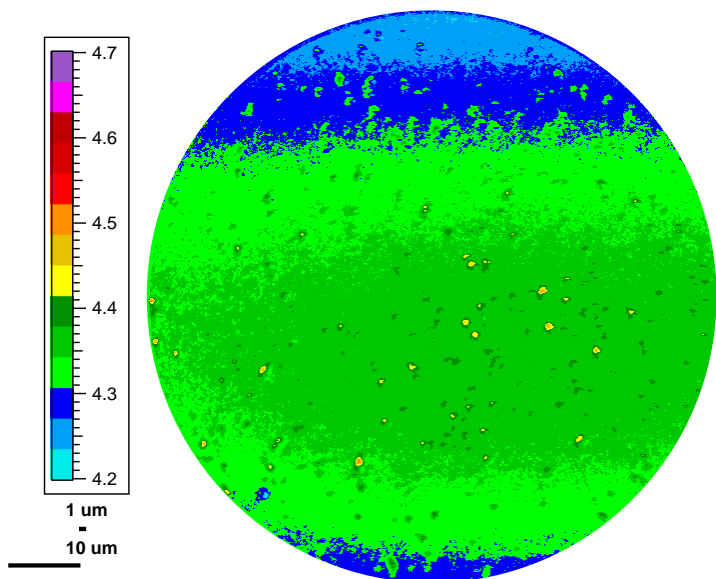


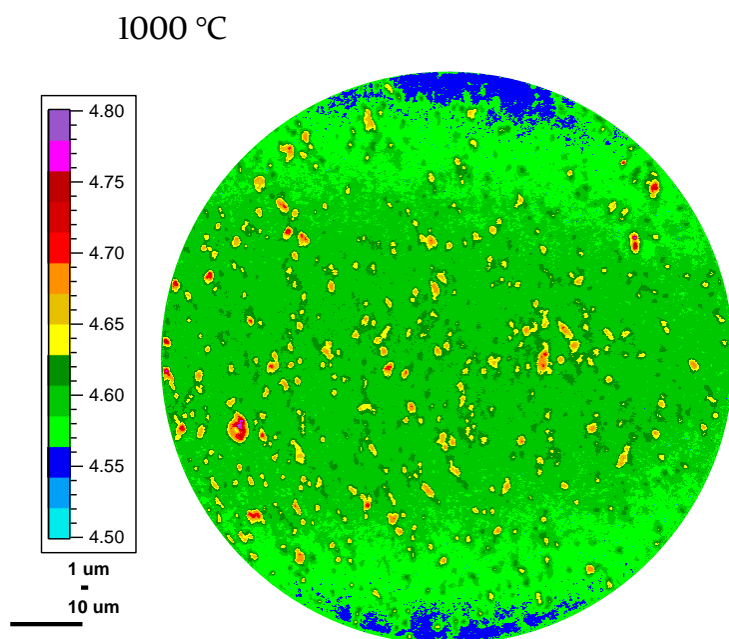
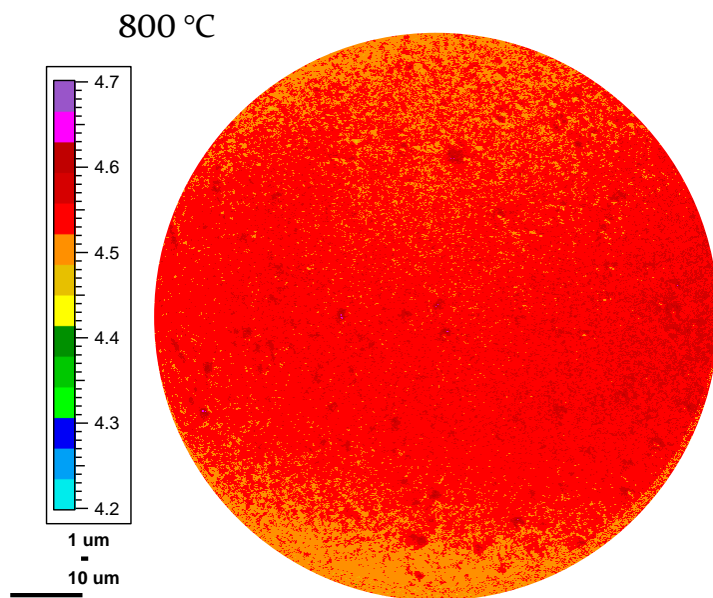
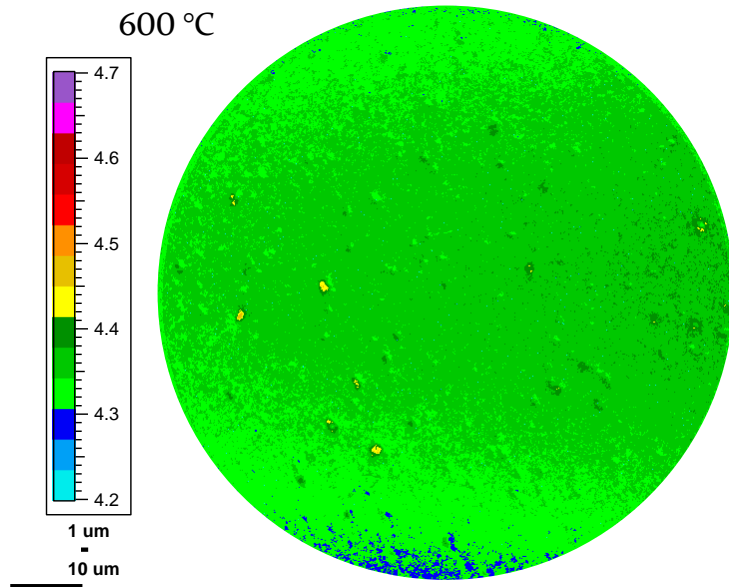
TiO HML, section 6.3.2

0 °C

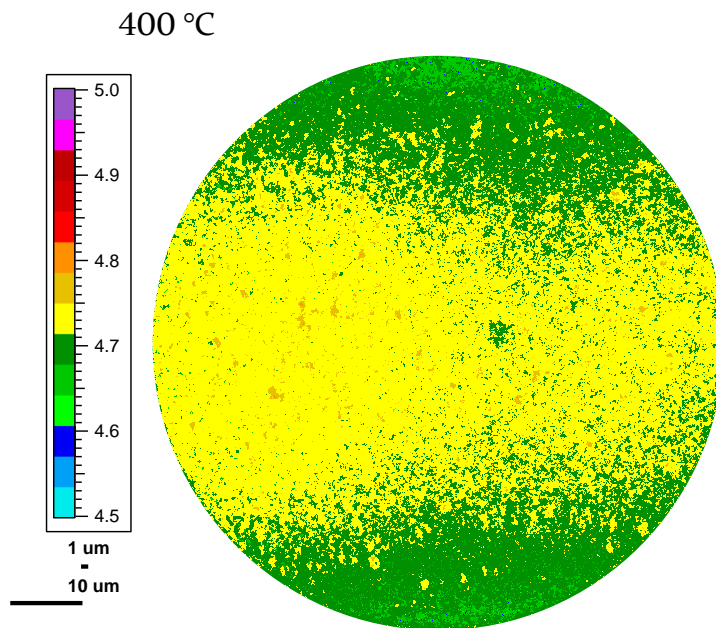
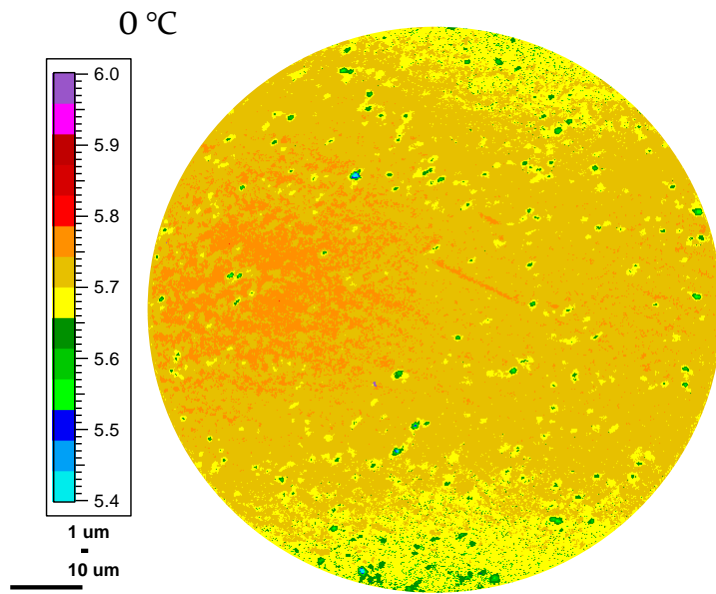


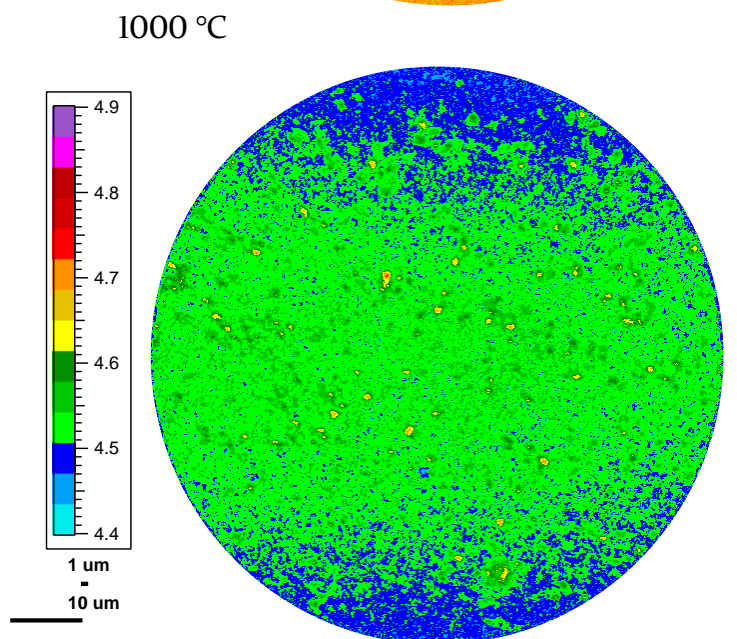
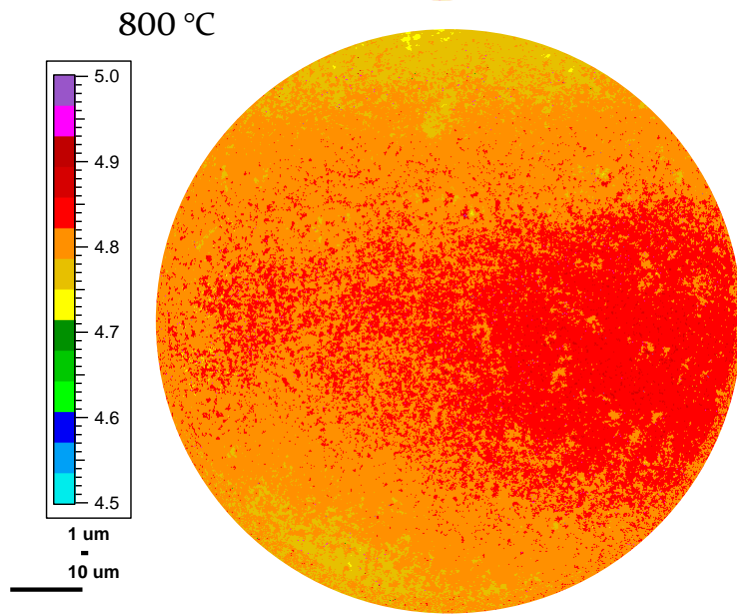
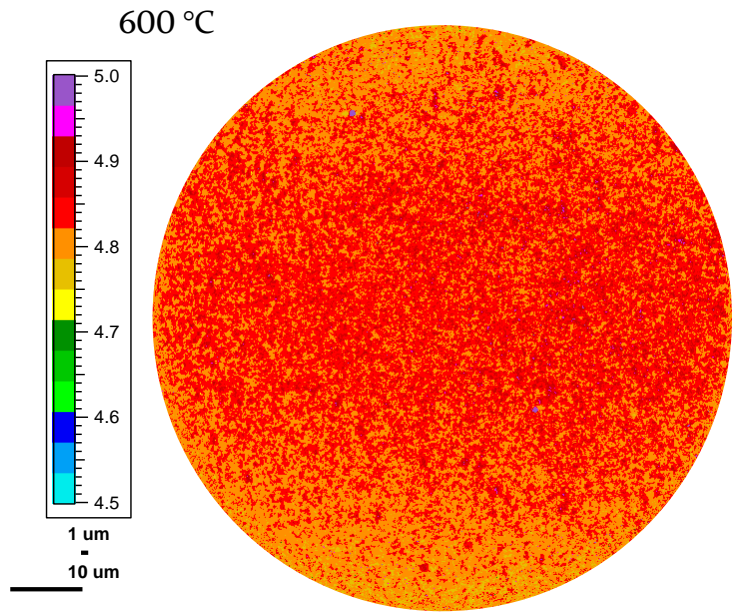
400 °C



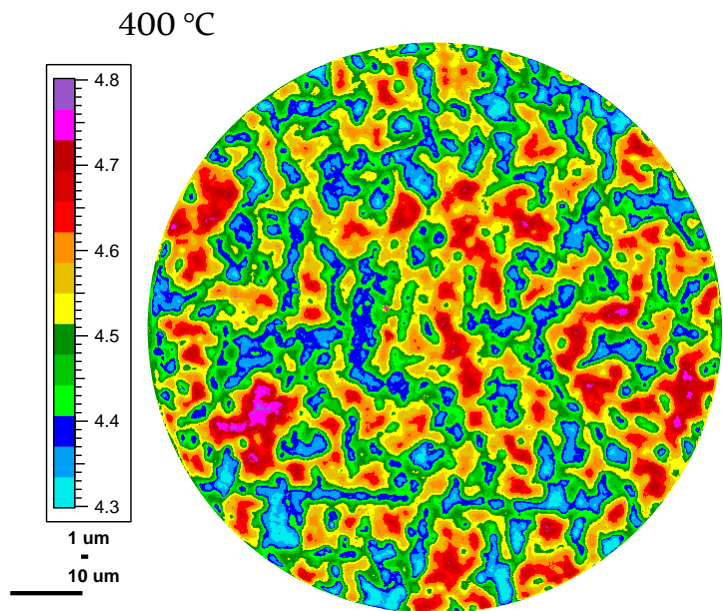
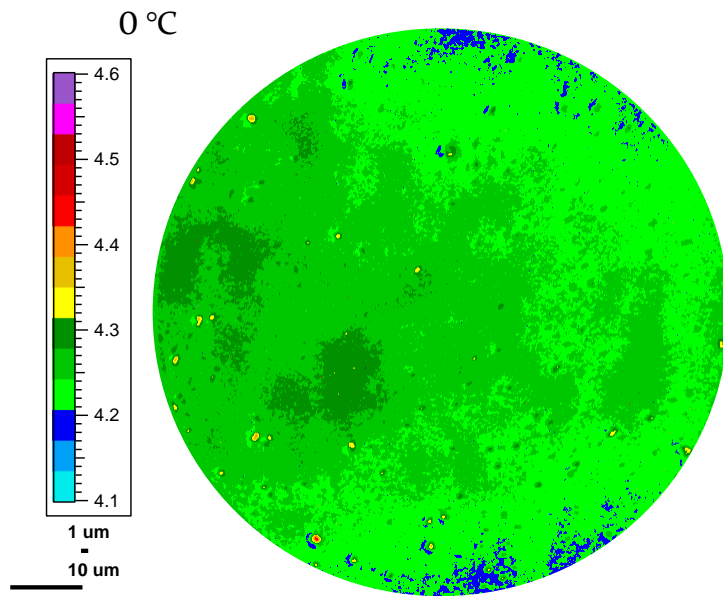


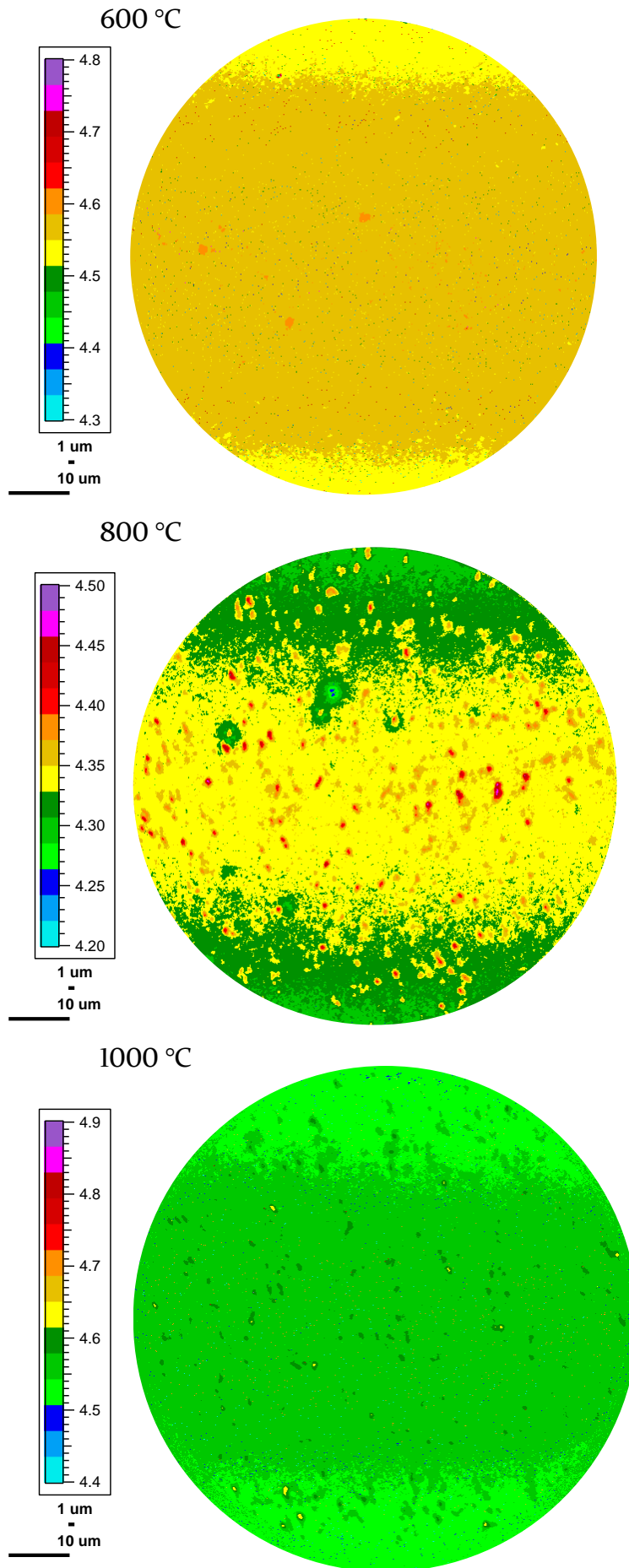
TiO FML, section 6.3.3



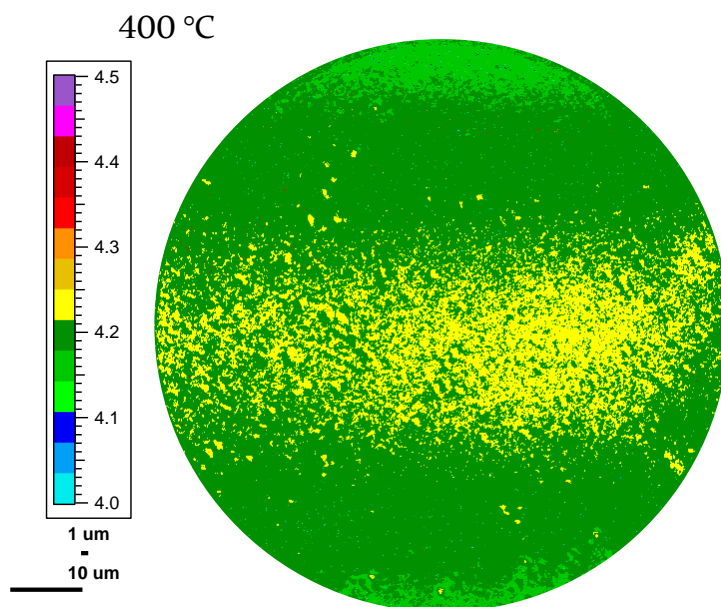
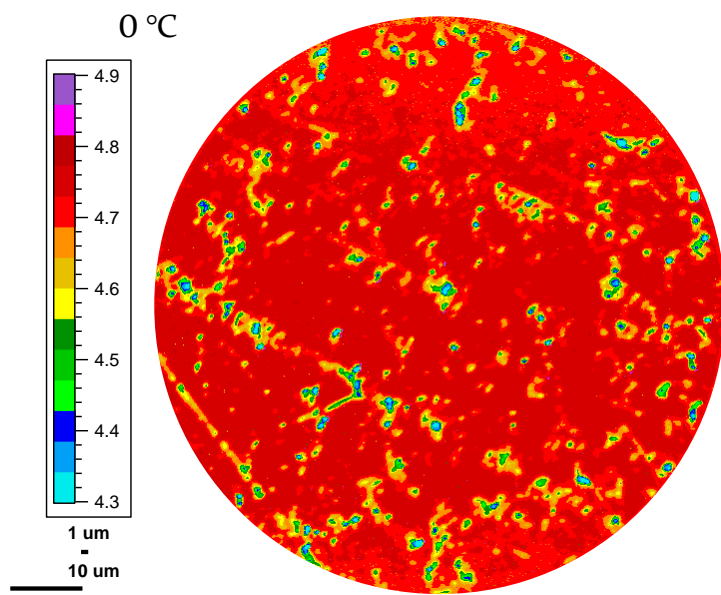


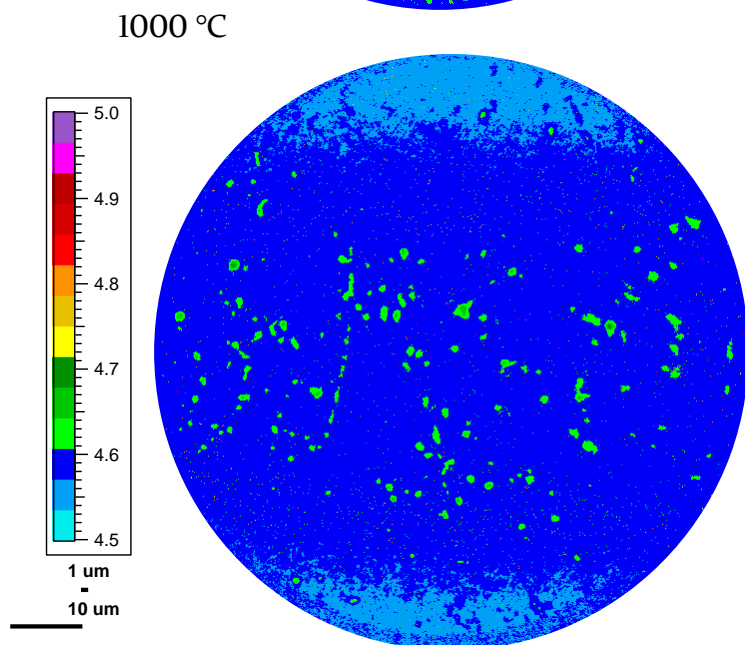
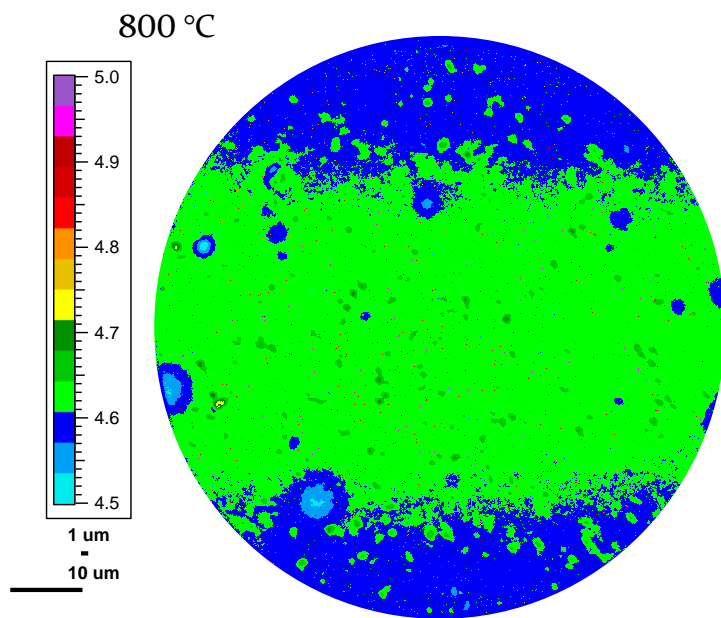
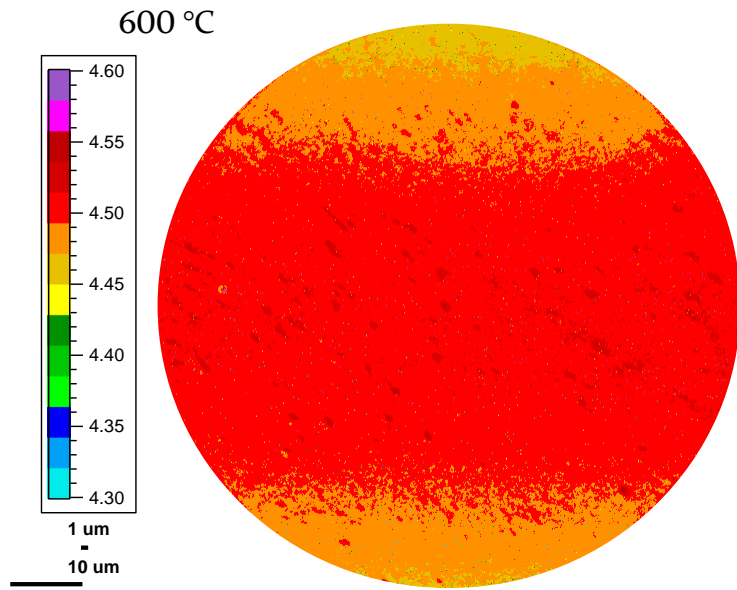
TiN QML, section 6.4.1



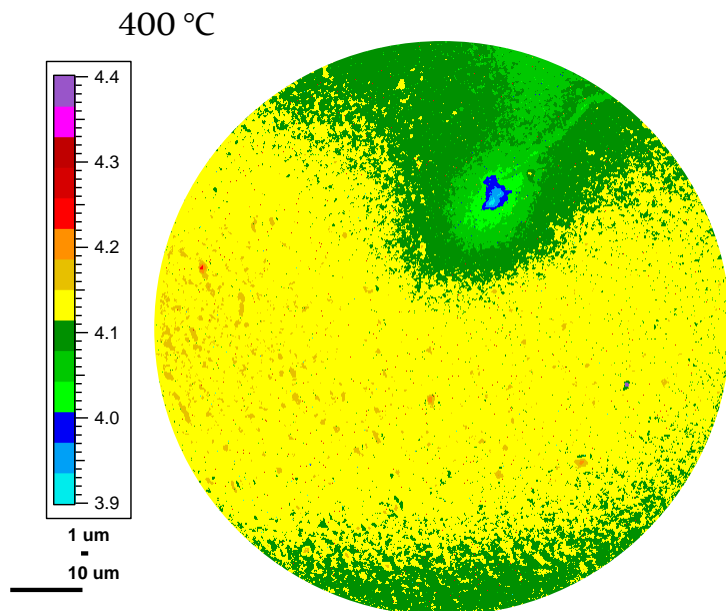
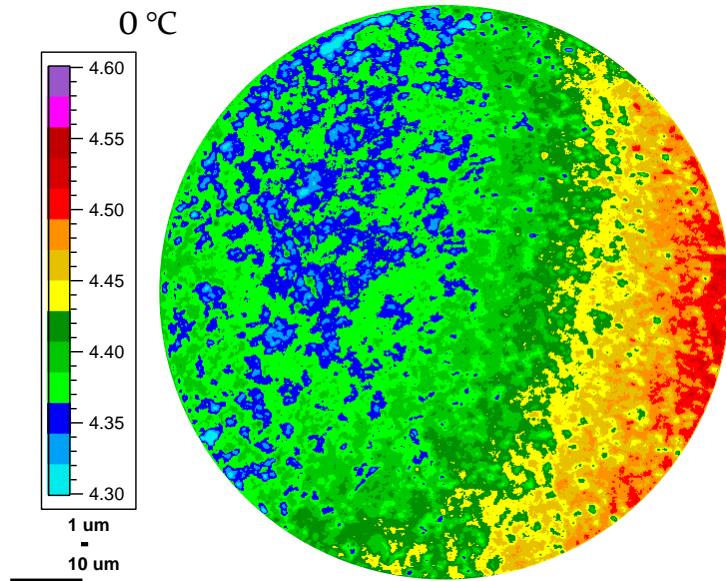


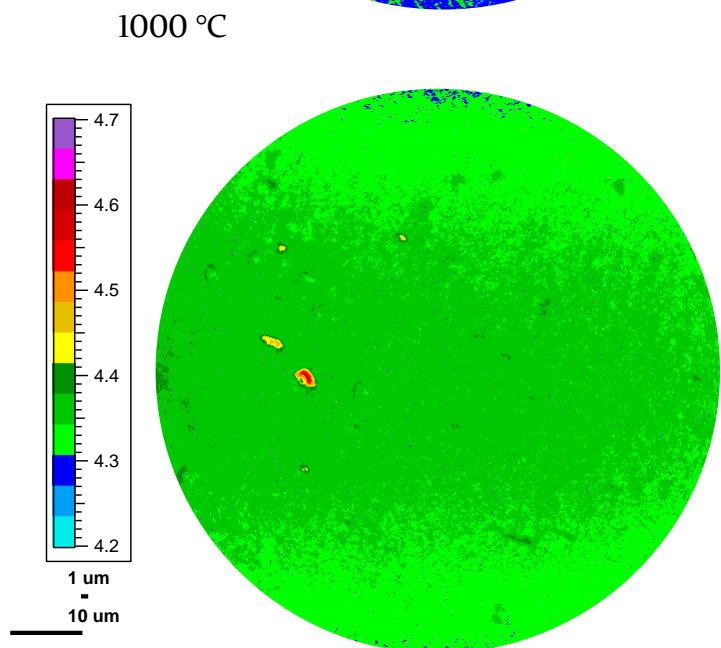
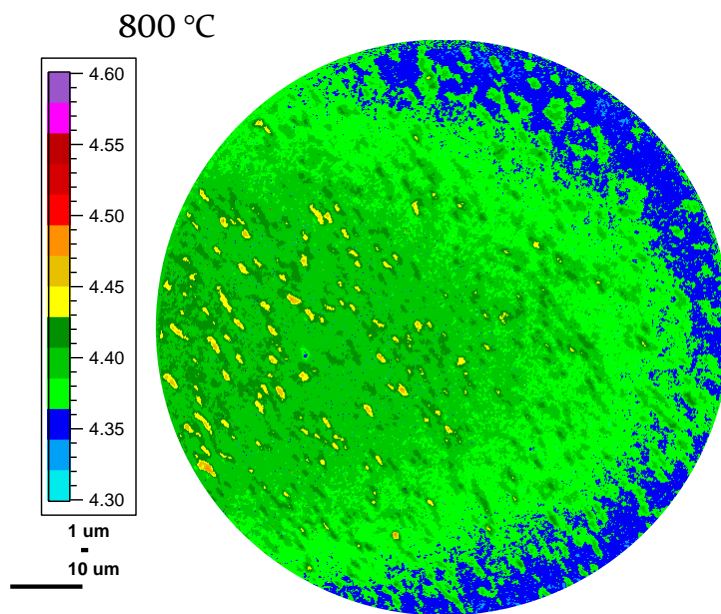
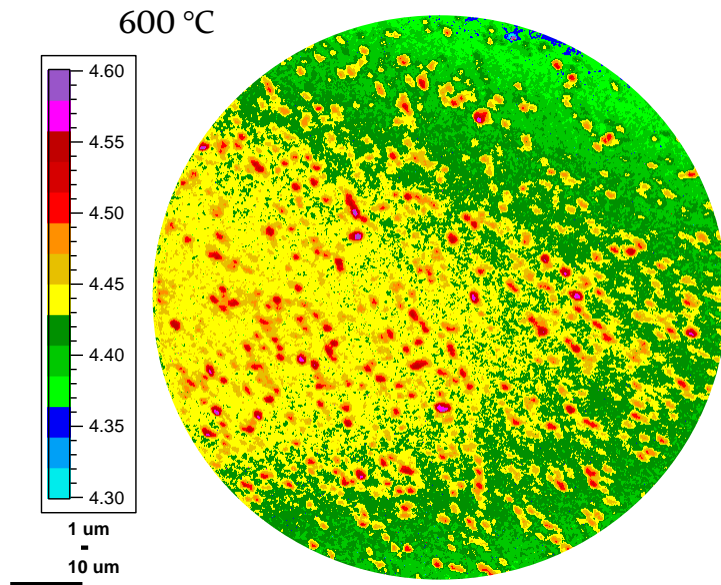
TiN HML, section 6.4.2





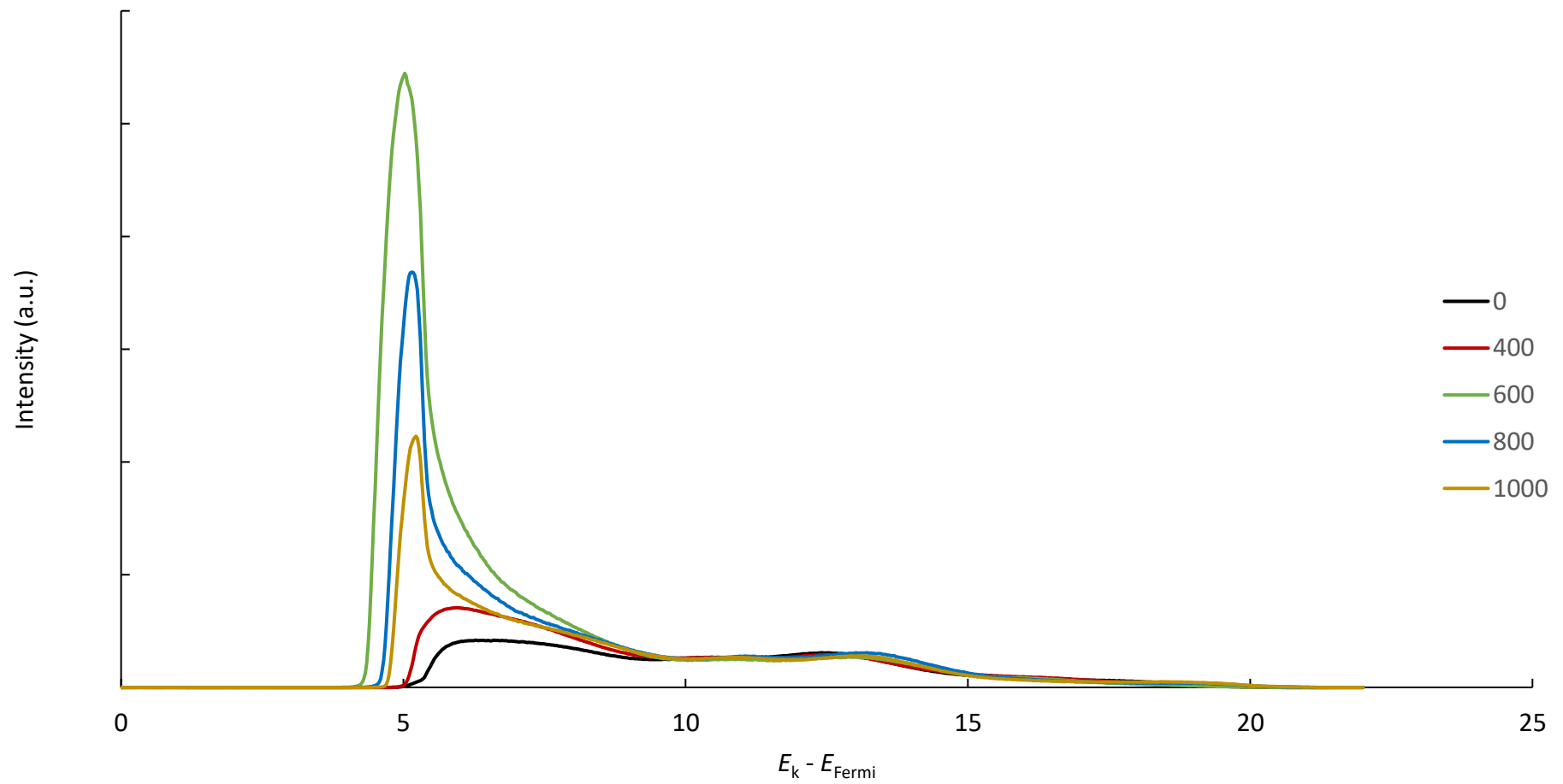
TiN FML, section 6.4.3



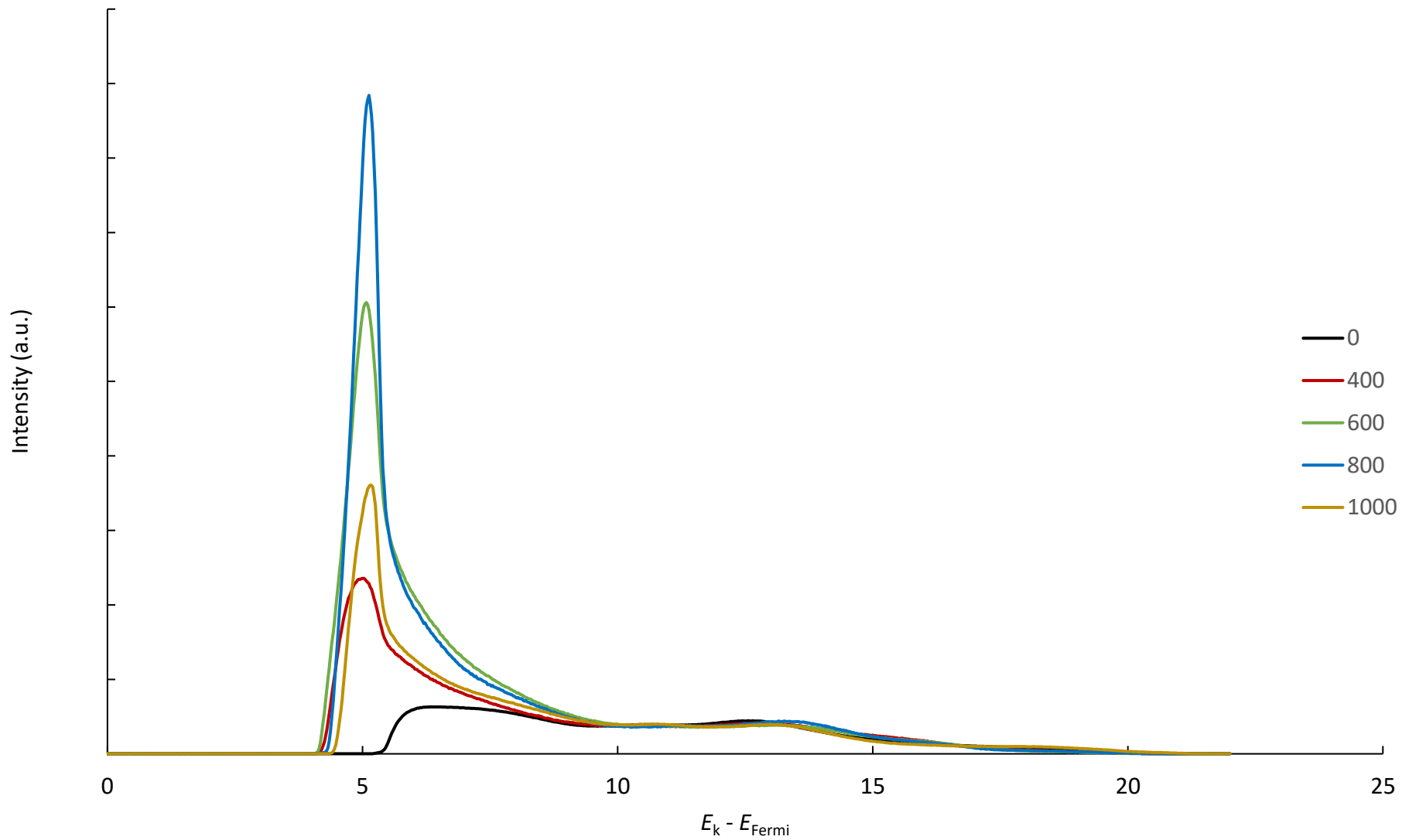


# Appendix C – UPS Spectra

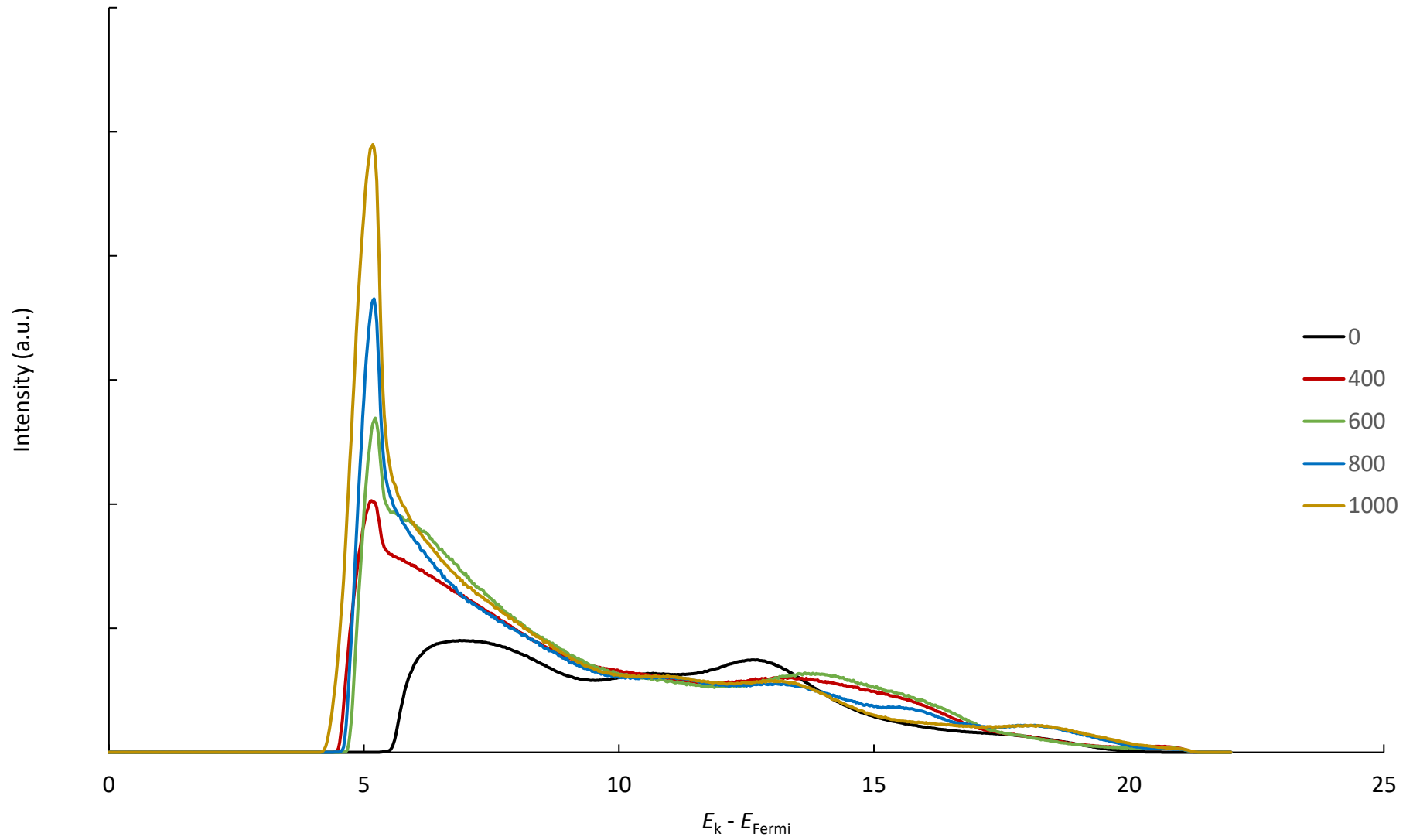
TiO QML, section 6.3.1



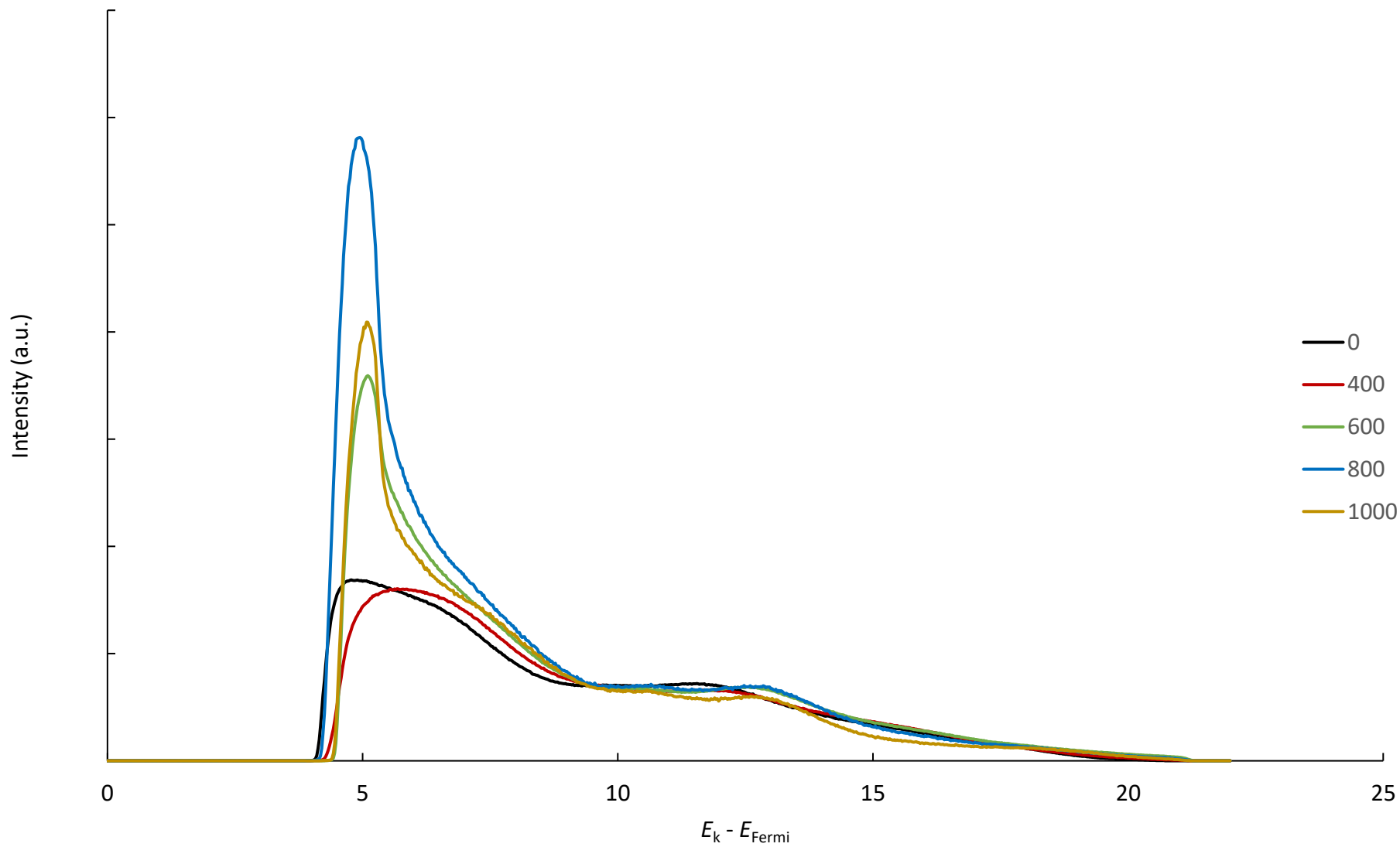
TiO HML, section 6.3.2



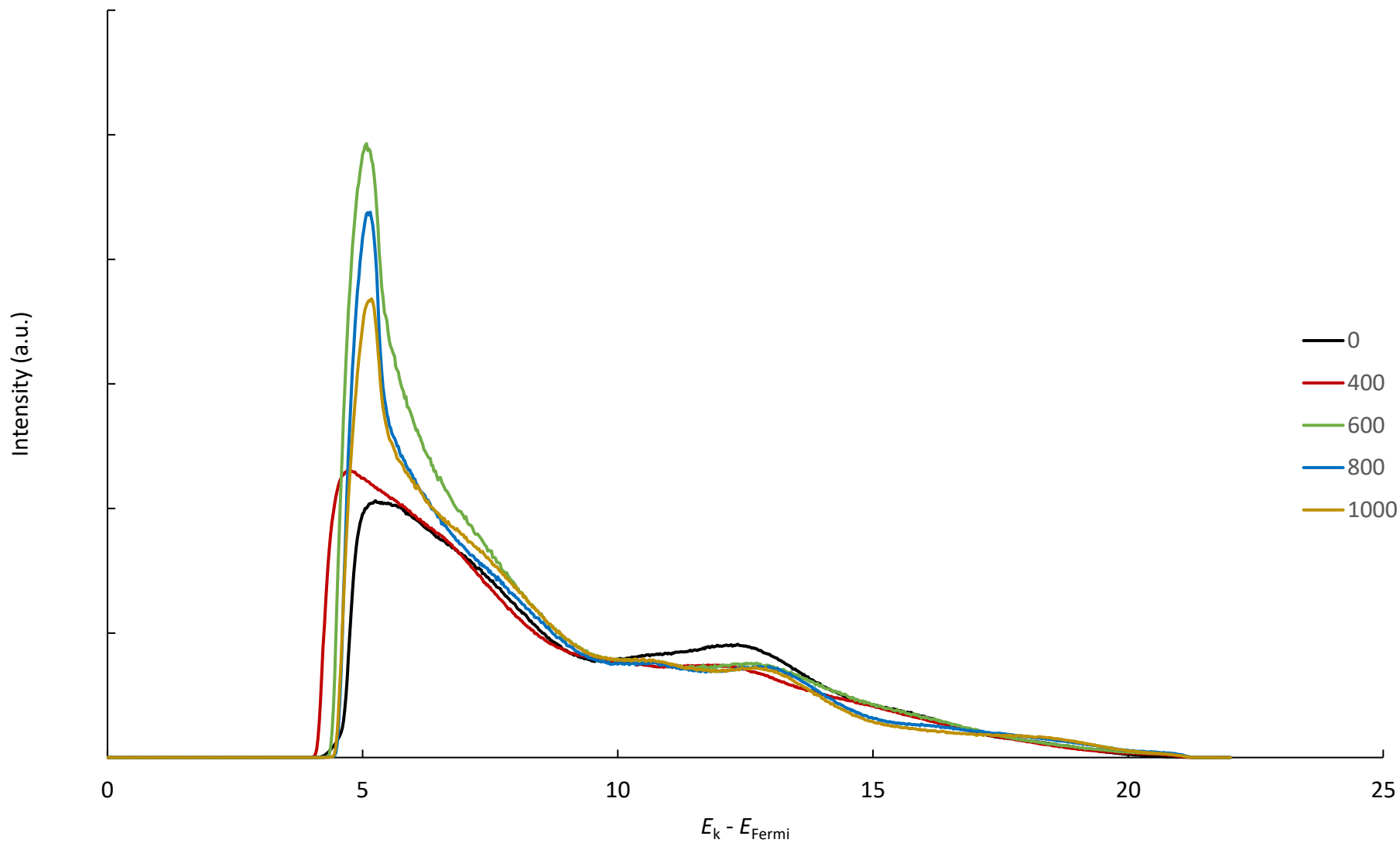
TiO FML, section 6.3.3



TiN QML, section 6.4.1



TiN HML, section 6.4.2



TiN FML, section 6.4.3

